Diplomarbeit

Search for $\mathrm{H} \to \mathrm{W}^{\pm}\mathrm{W}^{\mp(*)} \to \ell^{+}\nu\ell'^{-}\bar{\nu}'$ Decays in the Gluon Fusion and Vector-Boson Fusion Production Modes at the LHC

Andreas Walz

Fakultät für Mathematik und Physik
Albert-Ludwigs-Universität Freiburg

Search for $\mathrm{H} \to \mathrm{W}^{\pm}\mathrm{W}^{\mp(*)} \to \ell^{+}\nu\ell'^{-}\bar{\nu}'$ Decays in the Gluon Fusion and Vector-Boson Fusion Production Modes at the LHC

DIPLOMARBEIT

vorgelegt von

Andreas Walz

Prof. Dr. Karl Jakobs

Fakultät für Mathematik und Physik der

Albert-Ludwigs-Universität

Freiburg im Breisgau

2. November 2012

Abstract

The Higgs boson is the only remaining particle of the Standard Model of particle physics to be established experimentally. It is the phenomenological imprint of the most popular implementation of electroweak symmetry breaking, the Higgs mechanism. After almost 50 years of extensive search at various high-energy experiments the LHC experiments ATLAS and CMS discovered a new particle which is compatible with the hypothesized Higgs boson. This thesis presents a search for the Standard Model Higgs boson in the mass range 110 GeV $\leq m_H \leq$ 300 GeV in the $H \to W^{\pm}W^{\mp(*)} \to \ell^{+}\nu\ell'^{-}\bar{\nu}'$ decay mode using in total approximately 10.5 fb^{-1} of proton-proton collision data collected at center-of-mass energies of $\sqrt{s} = 7$ TeV and 8 TeV with the ATLAS detector in the years 2011 and 2012, respectively. The $H \to W^{\pm}W^{\mp(*)} \to \ell^{+}\nu\ell'^{-}\bar{\nu}'$ analysis, besides searches in the channels $H \to \gamma\gamma$ and $H \to ZZ^{(*)} \to 4\ell$, entered the publication of the ATLAS Collaboration reporting about the observation of the new particle. In the $H \to W^{\pm}W^{\mp(*)} \to \ell^{+}\nu\ell'^{-}\bar{\nu}'$ search, the most significant deviation of the data from the background-only hypothesis is observed for a hypothesized Higgs boson mass of $m_H = 125$ GeV and corresponds to a background fluctuation probability p_0 equivalent to 2.8 standard deviations. In this thesis three sub-channels are used placing emphasis on the gluon fusion and the vector-boson fusion Higgs boson production modes. For the sub-channels focusing on the gluon fusion, an optimal event selection exploiting the spin-induced signal event topology is proposed. In the sub-channel focusing on the vector-boson fusion, the performance of the event selection is investigated and a modification enhancing the sensitivity to the signal process is identified.

Zusammenfassung

Das Higgs-Boson ist das letzte Elementarteilchen des Standardmodells der Teilchenphysik, dessen Existenz experimentell noch zu bestätigen ist. Es stellt das phänomenologische Merkmal der populärsten Variante dar, die elektroschwache Symmetrie zu brechen: des Higgs-Mechanismus. Nach nahezu 50 Jahren intensiver Suche an verschiedenen Hochenergieexperimenten haben die LHC Experimente ATLAS und CMS ein neues Teilchen entdeckt, das mit dem erwarteten Higgs-Boson kompatibel ist. Die vorliegende Diplomarbeit präsentiert eine Suche nach dem Higgs-Boson des Standardmodells im Massenbereich 110 GeV $\leq m_H \leq$ 300 GeV im $H \to W^{\pm}W^{\mp(*)} \to \ell^+\nu\ell'^-\bar{\nu}'$ Zerfallskanal basierend auf ungefähr 10.5 fb^{-1} Proton-Proton-Kollisionsdaten, die bei Schwerpunktsenergien von $\sqrt{s} = 7$ TeV und 8 TeV mit dem ATLAS-Detektor jeweils in den Jahren 2011 und 2012 aufgezeichnet wurden. Neben den Kanälen $H \to \gamma\gamma$ und $H \to ZZ^{(*)} \to 4\ell$ trug die Analyse im $H \to W^{\pm}W^{\mp(*)} \to \ell^+\nu\ell'^-\bar{\nu}'$ Kanal zur Veröffentlichung der ATLAS-Kollaboration über die Entdeckung des neuen Teilchens bei. Im $H \to W^{\pm}W^{\mp(*)} \to \ell^+\nu\ell'^-\bar{\nu}'$ Kanal wird die signifikanteste Abweichung der Daten von der Untergrund-Hypothese bei einer hypothetischen Higgs-Masse von $m_H = 125$ GeV beobachtet. Hierbei ist die Wahrscheinlichkeit einer Fluktuation des Untergrundes p_0 äquivalent zu 2.8 Standardabweichungen. In der vorliegenden Arbeit werden drei Kanäle genutzt, die auf die Higgs-Produktion mittels Gluon-Fusion und Vektorboson-Fusion ausgrichtet sind. Für die auf die Gluon-Fusion ausgerichteten Känale wird eine optimale Ereignissselektion vorgeschlagen, die die spin-induzierte Topologie von Signalereignissen ausnutzt. In dem auf die Vektorboson-Fusion ausgerichteten Kanal wird die Leistung der Ereignisselektion untersucht und eine Modifikation erarbeitet, die die Sensitivität auf den Signalprozess erhöht.

Preface

Modern high-energy physics is all but impossible without a very large number of people supporting the project. From devising, building up, and operating the experiment and its infrastructure to organizing and maintaining resources to prepare, store, simulate, and analyze the data a good deal of expertise is indispensable. With its technical and intellectual infrastructure the *European Organization for Nuclear Research* (CERN) near Geneva, Switzerland, is an excellent place to host an ambitious experiment like ATLAS. The ATLAS Collaboration is made up of more than 3,000 people from 38 countries, and every single person has a share in the efficient operation and maintenance of the experiment. Within the ATLAS Collaboration approximately 100 people are directly involved in the search for the Standard Model Higgs boson in the $H \to W^{\pm}W^{\mp(*)} \to \ell^{+}\nu\ell'^{-}\bar{\nu}'$ channel as presented in this thesis. It would not at all have been possible without the contribution of many of them.

During the time of this thesis the search for the Standard Model Higgs boson at the LHC evolved from a collection of early data analyses based on an integrated luminosity of a few tens of inverse picobarn to a successful discovery. Having the unique opportunity to sit in on these highly exciting times working on the $H \to W^{\pm}W^{\mp(*)} \to \ell^{+}\nu\ell'^{-}\bar{\nu}'$ analysis, I joined in the very first weeks of my thesis the effort producing official results for the publication that is based on the first half of the 2011 dataset. Though this thesis initially was intended to focus on the vector-boson fusion (VBF) analysis, in the course towards a discovery the analyses in the other sub-channels was taking as much manpower as available and the center of my activity more and more shifted.

Thanks to several people supporting my proposal, the private analysis software I was developing and using for studies related to this thesis got accepted as an official tool and became an essential part of the official Common Analysis Framework (CAF), which the Higgs-to-WW sub-group decided to set up in October, 2011. Seizing the opportunity to contribute to the analysis at the sharp end, it implicated a huge amount of work for a general benefit of the official analysis as well as of my personal gratification. Assisting the rapid and successful evolution of the CAF, which finally has become a comprehensive software package driving the entire official $H \to W^{\pm}W^{\mp(*)} \to \ell^{+}\nu\ell'^{-}\bar{\nu}'$ analysis, I have worked not only on the code producing official plots and tables but also on incorporating an early version of the treatment of experimental systematic uncertainties in the latter and eventually on the implementation of data-driven estimation techniques. In the first half of the year 2012 I gave a two-afternoon tutorial at CERN introducing to that component of the CAF which has been developed by me.

Apart from the work related to the CAF, I performed several studies, most of them aiming for an optimization of the event selection. The results obtained in the context of the optimization of the topological selection have been taken as a guideline for the official event selection. Furthermore, serving the original topic, I investigated the performance of the VBF candidate event selection and proposed an improvement. Unfortunately, in view of the *July schedule* forcing the entire analysis to be settled end of May it was not possible to fully incorporate the proposal in time.

Im Gedenken an meine Mama

Table of Contents

Introduction

On July 4$^{\text{th}}$, 2012, not only the whole particle physicists community but also the general public concentrated its attention on an extraordinary event which was taking place at the *European Organization for Nuclear Research* (CERN) near Geneva, Switzerland. Rolf-Dieter Heuer, *Director General* of CERN, had invited to a scientific seminar to deliver the latest update in the search for the Standard Model Higgs boson [1]. The *Higgs boson*, a particle postulated by Peter Higgs and others in 1964 [2] to solve an importunate theoretical problem, had been hunted for decades but despite tremendous efforts had successfully eluded experimental confirmation so far. Since its appearance on the agenda of particle physics, though, the Higgs boson's potential harbors had been narrowed down significantly and the recent past had come up with auspicious hints [3–5]. Awaiting a singular moment in physics' history, a dignified audience of the world's most distinguished physicists as well as numerous journalists gathered at CERN and in Melbourne, Australia, where a video live transmission from CERN was opening the 36$^{\text{th}}$ *International Conference on High Energy Physics* (ICHEP).

In the scope of this seminar, the spokespersons of the ATLAS and the CMS experiments, the two general purpose detectors installed at the *Large Hadron Collider* (LHC) at CERN, presented results of analyses of proton-proton collision data collected in the years 2011 and 2012 [6,7]. Physicists of both experiments had searched billions of collision events for a signature of the Higgs boson. In fact, substantiating a long-standing conjecture, both experiments individually were able to claim the observation of a new particle whose signature is compatible with the long sought-for Higgs boson. Even though at the time of writing it still remains to be confirmed that the newly discovered boson exactly features what is predicted by theory, it can be considered as an undoubted fact that it is closely related to what Peter Higgs' postulation was targeting at almost half a century ago. Paying tribute to his pioneering ideas, it was a moving matter that 83-year old Peter Higgs could attend this great announcement in person.

Shortly after, on July 31$^{\text{st}}$, the ATLAS and the CMS Collaborations simultaneously submitted two papers to *Physics Letters B* summarizing details of the discovery [8,9]. It is the conclusion of thousands of physicists and engineers working towards this goal and it certainly constitutes a deserved acknowledgment of their long-lasting endeavors.

The extent to which the quest for the Higgs boson has been and still is drawing the attention of scientists has to be interpreted in an appropriate historical and theoretical context. The Standard Model of particle physics (SM) [10–13] has been developed since the early sixties of the twentieth century and condenses physicists' knowledge of fundamental particles and their interactions. Having been subject to experimental trials for decades, it has proven to be very successful and no significant deviation of observations from its predictions could be established. However, in order to incorporate masses for elementary particles it requires a mechanism spontaneously breaking an underlying symmetry of the theory. The *Higgs mechanism* [14–19], being the most popular implementation of it, constitutes a centerpiece of the SM, but also implicates the existence of an additional particle: the Higgs boson. Lingering as a hypothetical construct, the Higgs boson has been the last fundamental particle awaiting

detection since the discovery of the top quark in the year 1995 [20, 21]. However, unless the theoretical framework of high-energy physics is fundamentally wrong, the non-existence of the Higgs boson implicates the need for either a modification of or an extension to the SM, undertaking the task of explaining masses of fundamental particles.

In order to elicit nature the momentous answer of the true origin of mass, and in particular of the existence of the Higgs boson, physicists have spared no effort designing and building ambitious experiments at the cutting edge of technology [2]. Unfortunately, the theoretical framework of the SM allows to predict all properties of the Higgs boson except its mass m_H, which strongly affects experimental search strategies. Both indirect analyses taking advantage of a dependence of measurable SM parameters on m_H as well as direct searches scanning high-energy collisions for characteristic decay products of the Higgs boson have been performed in the past. Electroweak precision measurements have been used to indirectly exclude a SM Higgs boson with a mass[1] of $m_H < 158$ GeV at 95 % confidence level (CL) [22]. Direct searches at the *Large Electron-Positron Collider* (LEP) have excluded at 95 % CL a SM Higgs boson with a mass $m_H < 114.4$ GeV [23] and at the *Tevatron* additionally with 147 GeV $< m_H <$ 180 GeV [5].

Certainly, the search for the Higgs boson has also been one of the driving objectives for building the next generation's particle collider, the LHC. The LHC started its nominal operation in 2009 and, as mentioned in the beginning, presumably provided closure on the question of the Higgs boson's existence in its early years.

This thesis presents a search for the SM Higgs boson in the $H \to W^{\pm}W^{\mp(*)} \to \ell^{+}\nu\ell'^{-}\bar{\nu}'$ decay mode with the ATLAS experiment at the LHC, considering any combination of $W \to e\nu$ and $W \to \mu\nu$ decays (throughout this document referred to as $H \to WW^{(*)} \to \ell\nu\ell\nu$). The analysis is performed in the mass range 110 GeV $\leq m_H \leq$ 300 GeV using in total approximately 10.5 fb^{-1} of proton-proton collision data collected at center-of-mass energies of $\sqrt{s} = 7$ TeV and $\sqrt{s} = 8$ TeV in the years 2011 and 2012, respectively. At the LHC, the $H \to WW^{(*)} \to \ell\nu\ell\nu$ channel is the most sensitive one over a broad range of hypothesized Higgs boson masses m_H. The search in this channel featured an important contribution to the observation of the new boson as published by the ATLAS Collaboration in Ref. [8]. The work related to this thesis has been carried out within the Higgs-to-WW sub-group of the ATLAS Collaboration and is closely related to the publications of Refs. [24] and [25].

The outline of this thesis is the following: Chapter 1 provides an overview of the theoretical framework of particle physics and the Higgs mechanism, but also the general phenomenology at a hadron collider like the LHC. Chapter 2 introduces to the experimental environment, the LHC and the ATLAS detector. The expected phenomenology of the SM Higgs boson is outlined in Chapter 3. Setting the scene for the $H \to WW^{(*)} \to \ell\nu\ell\nu$ analysis, Chapter 4 presents the physics processes involved in the search, while the experimental input as well as the corresponding simulated data are defined and described in Chapter 5. Chapter 6 is dedicated to the Common Analysis Framework, a collective analysis software project driving the $H \to WW^{(*)} \to \ell\nu\ell\nu$ analysis. Following a physically well-motivated distinction, the $H \to WW^{(*)} \to \ell\nu\ell\nu$ analysis in the $H + 0/1$ jet and the $H + 2$ jets channels are detailed in Chapters 7 and 8, respectively. These chapters are followed by Chapter 9 reporting on studies aiming for the optimization of the event selection. Finally, Chapter 10 provides a summary and concludes this thesis. Auxiliary material concerning several topics covered in the main part of the thesis is provided in Appendices A and B.

[1] Throughout this thesis masses are expressed in terms of energy (see Chapter 1).

1 Theoretical Overview

The objective of this chapter is to provide a coherent overview of the theoretical fundamentals of particle physics and high-energy experiments. After introducing the Standard Model of particle physics in Section 1.1 and the Higgs mechanism in Section 1.2, the physics and the phenomenology at hadron colliders, in particular at the LHC, are summarized in Section 1.3.

Throughout this document, the usual units of particle physics are used. That is, $\hbar = c = 1$ and both momenta and masses are given in terms of energy (e.g. GeV).

1.1. The Standard Model of Particle Physics

The *Standard Model of particle physics* [10–13] (in the following referred to as *the* Standard Model or SM) is a framework of relativistic quantum field theories describing three of the four known fundamental forces between all to date known elementary particles. It comprises the *strong*, the *weak* and the *electromagnetic* interaction. Up to now, the fourth fundamental force, the gravitation, has refused its incorporation into a quantum field theoretical framework. However, gravitation is of negligible impact at present particle collider energies anyway.

The SM has been developed since the early sixties of the twentieth century and has passed a plethora of experimental test with a startling accuracy. It is based on the fundamental principle of postulating *local gauge invariance* with respect to a certain symmetry group. In the case of the SM the symmetry group is $SU(3) \times SU(2) \times U(1)$, where the strong interaction is represented by $SU(3)$ (see Section 1.1.3) and the *electroweak* interaction, the unification of the weak and the electromagnetic interaction, is represented by $SU(2) \times U(1)$ (see Section 1.1.4). Masses of elementary particles are incorporated in the SM through the *Higgs mechanism* [14–19] spontaneously breaking the electroweak symmetry (see Section 1.2).

The SM and corresponding theoretical details are extensively covered in the literature. The following summary of the most important aspects of the SM and the Higgs mechanism is inspired by Refs. [26–28].

1.1.1. Particle Content

The SM distinguishes two fundamentally different types of elementary particles according to their spin. *Fermions* have half-integer spin and constitute *matter particles*, whereas *bosons* have an integer spin and constitute *force mediators*. Fermions are furthermore divided into *leptons* and *quarks*, where the discrimination is driven by the fact that quarks are subject to the strong interaction, whereas leptons are not. Table 1.1 provides an overview of leptons and quarks of the SM.

Both leptons and quarks have spin $1/2$ and are grouped into three *generations*, with each generation comprising a pair of leptons or quarks, in total resulting in six types (*flavors*) of leptons and six types of quarks. Furthermore, each lepton and each quark has a corresponding *anti-particle* with the same properties but opposite electric charge.

All interactions of the SM are mediated by *gauge bosons* of spin 1, which couple to a corresponding charge. The electromagnetic interaction is mediated by the massless photon

Generation	Leptons			Quarks		
	Name	Symbol	Charge [e]	Name	Symbol	Charge [e]
1st	Electron	e	-1	Up	u	$2/3$
	e-neutrino	ν_e	0	Down	d	$-1/3$
2nd	Muon	μ	-1	Charm	c	$2/3$
	μ-neutrino	ν_μ	0	Strange	s	$-1/3$
3rd	Tau	τ	-1	Top	t	$2/3$
	τ-neutrino	τ_ν	0	Bottom	b	$-1/3$

Table 1.1: Overview of the SM quarks and leptons. The electric charge is given in units of the electric charge of the positron, the anti-particle of the electron.

(γ) coupling to electrically charged particles, whereas the strong interaction is mediated by eight types of massless gluons (g) coupling to the *color charge* of quarks. The weak interaction is mediated by three types of massive bosons, denoted as $W^\pm$ and Z, which couple to *weak isospin* and *weak hypercharge*. Table 1.2 summarizes the fundamental interactions and the corresponding force mediators of the SM.

1.1.2. Gauge Interactions

In quantum field theory, the behavior of fields (particles) as well as their interactions are described by means of a *Lagrange density* $\mathscr{L}$ (in the following referred to as *Lagrangian*). Based on a Lagrangian $\mathscr{L}_0$ describing a freely propagating field, the structure of the Lagrangian including gauge interactions can be derived by postulating local gauge invariance of the Lagrangian with respect to a particular symmetry transformation. The basic principle is briefly outlined in the following.

A freely propagating fermion field of spin $1/2$ and mass m is described by a *Dirac spinor* ψ and obeys the *Dirac equation*

$$(i\gamma^\mu \partial_\mu - m)\,\psi = 0,$$

where γ^μ denotes the *Dirac γ-matrices*. This description is equivalent to the one based on the Lagrangian

$$\mathscr{L}_0 = \bar{\psi}\,(i\gamma^\mu \partial_\mu - m)\,\psi, \tag{1.1}$$

where $\bar{\psi} = \psi^\dagger \gamma^0$ is the adjoint of ψ. $\mathscr{L}_0$ is invariant under a *global* $U(1)$ gauge transformation

$$\psi(x) \to \psi'(x) = e^{i\alpha}\psi(x) \quad \text{with} \quad \alpha \in \mathbb{R}.$$

Interaction	Mediator	Symbol	Mass [GeV]	el. Charge [e]
Electromagnetic	Photon	γ	0	0
Strong	8 Gluons	g	0	0
Weak	Weak bosons	$W^\pm$	80.4	± 1
		Z	91.2	0

Table 1.2: Overview of the SM interactions and the corresponding force mediators [29].

However, this invariance does no longer hold if $\alpha = \alpha(x)$ becomes a function of the space-time coordinate x (*local* gauge transformation). The principle of local gauge invariance explicitly requires the Lagrangian to be invariant not only under global but also under local gauge transformations. This can be achieved by applying uniquely defined *minimal modifications* which involve the introduction of a new vector field $A_\mu(x)$ with a certain behavior under gauge transformations and the replacement of the covariant derivative $\partial_\mu\psi$ by

$$D_\mu\psi = (\partial_\mu + ieA_\mu)\,\psi.$$

Here, e has the role of a *coupling constant* determining the strength of the interaction. The modifications yield a new Lagrangian $\mathscr{L}$ which is invariant under local gauge transformations but contains an additional term with respect to $\mathscr{L}_0$,

$$\mathscr{L} = \mathscr{L}_0 - eA_\mu\bar{\psi}\gamma^\mu\psi.$$

The additional term reflects an interaction between the fermion described by ψ and a new boson of spin 1 described by the vector field A_μ. To make A_μ itself a propagating field, one has to add a further term $\mathscr{L}_{\text{kin}}$ to the Lagrangian reflecting the kinetic energy of A_μ,

$$\mathscr{L}_{\text{kin}} = -\frac{1}{4}F_{\mu\nu}F^{\mu\nu} \quad \text{with} \quad F_{\mu\nu} = \partial_\mu A_\nu - \partial_\nu A_\mu.$$

It is of great importance to emphasize that the inherent feature of gauge interactions prevents an incorporation of masses for the mediating bosons. Adding a mass term

$$\mathscr{L}_{m_A} = \frac{1}{2}m_A^2 A^\mu A_\mu$$

to the Lagrangian $\mathscr{L}$, rendering the force mediator massive with mass m_A, would explicitly violate the gauge symmetry and make the theory being no longer *renormalizable*, that is, incapable of making meaningful predictions.

1.1.3. Quantum Chromodynamics

Quantum Chromodynamics (QCD) is the gauge theory of the strong interaction between quarks. Since experiments suggest that quarks exist in three different states, which are referred to as *color states*, QCD is based on the principle of local gauge invariance using the special unitary symmetry group $SU(3)$ on quark triplets

$$q = \begin{pmatrix} q_1 \\ q_2 \\ q_3 \end{pmatrix} \quad \text{with} \quad q = u, d, s, c, b, t,$$

where q_1 to q_3 denote the spinors corresponding to the three color states of a quark. Applying the minimal modifications explained in the previous section, one has to introduce eight gauge fields G_μ^a $(a = 1, \ldots, 8)$ and the covariant derivative

$$D_\mu = \partial_\mu - ig_s\frac{\lambda^a}{2}G_\mu^a,$$

where g_s refers to the *strong coupling constant* and λ^a to the *generators* of the $SU(3)$ symmetry group. The new gauge fields G_μ^a give rise to eight different color states of gluons mediating the strong interaction between quarks. The final Lagrangian of QCD is then given by

$$\mathscr{L}_{\text{QCD}} = \sum_q i\bar{q}\gamma^\mu\partial_\mu q - g_s\sum_q \bar{q}\gamma^\mu\frac{\lambda^a}{2}G_\mu^a q - \frac{1}{4}G_{\mu\nu}^a G^{a,\mu\nu}$$

where the sums run over all quark flavors q. The field tensors $G^a_{\mu\nu}$ are given by

$$G^a_{\mu\nu} = \partial_\mu G^a_\nu - \partial_\nu G^a_\mu + g_s f^{abc} G^b_\mu G^c_\nu,$$

where f^{abc} denotes the *structure constants* of $SU(3)$.

Applying the principle of local gauge invariance introduces two new terms to the Lagrangian, which describe the interaction between quarks and the corresponding gauge bosons (gluons) as well as a self-interaction between the gluons. The self-interaction between gluons is a result of the non-Abelian structure of $SU(3)$.

Even though it is described by an apparently simple Lagrangian, QCD exhibits a manifold phenomenology with non-trivial dynamics. One prominent feature of QCD is referred to as *asymptotic freedom* [30,31] and denotes the behavior of the strong coupling to decrease with increasing energy scale (decreasing length scale). On the other hand, the strong interaction becomes arbitrarily strong for increasing length scales and thereby prevents quarks and gluons as carriers of color charge from being observable as free particles (referred to as *confinement*).

1.1.4. Electroweak Unification

The weak interaction has experimentally been found to discriminate between *left-handed* and *right-handed* chiral states $\psi_{L,R}$ of fermions, which are given by the projections

$$\psi_{L,R} = \frac{1}{2}\left(1 \mp \gamma^5\right)\psi,$$

for a Dirac field ψ, whereas the electromagnetic interaction does not discriminate between these states. However, Glashow, Weinberg, and Salam showed that the electromagnetic and the weak interaction can be unified and collectively described by a $SU(2) \times U(1)$ gauge symmetry (*Glashow-Weinberg-Salam model*, GWS model) [10–12]. For this purpose, the particles of the SM are assigned two new quantum numbers, the *weak isospin* I and the *weak hypercharge* Y. The left-handed chiral states of quarks and leptons are arranged in *isospin* doublets χ_L with $I = 1/2$, whereas the right-handed chiral states are arranged in isospin singlets ψ_R with $I = 0$. The third component I_3 of the isospin I, the hypercharge Y, and the electric charge Q obey the *Gell-Mann-Nishijima* relation

$$Q = I_3 + \frac{Y}{2}.$$

Table 1.3 summarizes the fermions and their corresponding quantum numbers in the Glashow-Weinberg-Salam model. For quarks, the eigenstates d', s', b' of the electroweak interaction are orthogonal superpositions of the mass eigenstates d, s, b, where the mixing is described by the *CKM-matrix* U_{CKM} [32]

$$\begin{pmatrix} d' \\ s' \\ b' \end{pmatrix} = U_{\mathrm{CKM}} \cdot \begin{pmatrix} d \\ s \\ b \end{pmatrix}. \tag{1.2}$$

Gauge transformations in $SU(2) \times U(1)$ are generated by the generators T_a and Y of the $SU(2)$ and $U(1)$ groups, respectively. The gauge transformation of isospin doublets and singlets is given by

$$\begin{aligned} \chi_L \to \chi'_L &= e^{i\alpha^a T_a} e^{i\beta Y} \chi_L, \quad a = 1,2,3, \\ \psi_R \to \psi'_R &= e^{i\beta Y} \psi_R, \end{aligned}$$

	Generation			Quantum numbers			
	1st	2nd	3rd	I	I_3	Y	$Q[e]$
Quarks	$\begin{pmatrix} u \\ d' \end{pmatrix}_L$	$\begin{pmatrix} c \\ s' \end{pmatrix}_L$	$\begin{pmatrix} t \\ b' \end{pmatrix}_L$	$1/2$ $1/2$	$1/2$ $-1/2$	$1/3$ $1/3$	$2/3$ $-1/3$
	u_R	c_R	t_R	0	0	$4/3$	$2/3$
	d_R	s_R	b_R	0	0	$-2/3$	$1/3$
Leptons	$\begin{pmatrix} \nu_e \\ e^- \end{pmatrix}_L$	$\begin{pmatrix} \nu_\mu \\ \mu^- \end{pmatrix}_L$	$\begin{pmatrix} \nu_\tau \\ \tau^- \end{pmatrix}_L$	$1/2$ $1/2$	$1/2$ $-1/2$	-1 -1	0 -1
	e_R^-	μ_R^-	τ_R^-	0	0	-2	-1

Table 1.3: Overview of the fermions in the Glashow-Weinberg-Salam model as well as their quantum numbers. For quarks, the eigenstates d', s', b' of the electroweak interaction are orthogonal superpositions of the mass eigenstates d, s, b, where the mixing is described by the CKM-matrix (see Equation 1.2). Right-handed neutrinos are decoupled from interactions of the SM and are therefore not considered.

where $\alpha^a = \alpha^a(x)$ and $\beta = \beta(x)$ reflect local phases. Following the principle of local gauge invariance, the covariant derivative is given by

$$D_\mu = \partial_\mu + i\frac{g}{2}W_\mu^a T_a + i\frac{g'}{2}B_\mu Y,$$

with two coupling constants g and g' as well as four new gauge fields W_μ^a and B_μ. This yields the final Lagrangian $\mathscr{L}_{\mathrm{EW}}$ describing the electroweak interactions,

$$\mathscr{L}_{\mathrm{EW}} = \sum_j i\bar{\chi}_L^j \gamma^\mu D_\mu \chi_L^j + \sum_k i\bar{\psi}_R^k \gamma^\mu D_\mu \psi_R^k - \frac{1}{4}W_{\mu\nu}^a W_a^{\mu\nu} - \frac{1}{4}B_{\mu\nu}B^{\mu\nu}.$$

Here, the sums in j and k run over all doublets and singlets listed in Table 1.3. The field tensors $W_a^{\mu\nu}$ and $B_{\mu\nu}$ are given by

$$\begin{aligned} W_a^{\mu\nu} &= \partial_\mu W_\nu^a - \partial_\nu W_\mu^a - g\varepsilon_{abc}W_\mu^b W_\nu^c, \\ B_{\mu\nu} &= \partial_\mu B_\nu - \partial_\nu B_\mu, \end{aligned}$$

where ε_{abc} denotes the *totally antisymmetric tensor*. The four gauge fields W_μ^a and B_μ are related to the four physical bosons $W^\pm, Z$, and γ of the weak and the electromagnetic interaction. However, as outlined in the following section, the physical fields $W_\mu^\pm, Z_\mu$, and A_μ are given by orthogonal linear combinations of W_μ^a and B_μ,

$$\begin{aligned} W_\mu^\pm &= \frac{1}{\sqrt{2}}\left(W_\mu^1 \mp iW_\mu^2\right), \\ Z_\mu &= \cos\theta_W W_\mu^3 - \sin\theta_W B_\mu, \\ A_\mu &= \sin\theta_W W_\mu^3 + \cos\theta_W B_\mu, \end{aligned} \tag{1.3}$$

where θ_W denotes the *weak mixing angle*.

1.2. Higgs Mechanism

The gauge bosons introduced by the principle of local gauge invariance are required to be massless since corresponding mass terms in the Lagrangian violate the gauge symmetry and render the theory non-renormalizable. The fermions being subject to the gauge interactions are not explicitly prevented from being massive by local gauge invariance. However, mass terms for fermions do violate the electroweak symmetry $SU(2) \times U(1)$ due to the discrimination of the weak interaction between left and right-handed chiral states.

It is an experimental fact that fermions do have mass. Furthermore, in particular the gauge bosons $W^{\pm}$ and Z corresponding to the weak interaction are massive with $m_W \simeq 80.4$ GeV and $m_Z \simeq 91.2$ GeV. The *Higgs mechanism* [14–19] is one way of incorporating masses for gauge bosons and fermions in the SM while keeping the gauge structure of the interaction and thereby retaining renormalizability [33].

This section briefly summarizes the fundamental concept of spontaneous electroweak symmetry breaking and the Higgs mechanism. Details are extensively covered e.g. in Ref. [34].

1.2.1. Spontaneous Symmetry Breaking

The Higgs mechanism is based on the postulation of a new weak isospin doublet Φ of complex scalar fields,

$$\Phi = \begin{pmatrix} \phi^+ \\ \phi^0 \end{pmatrix}, \quad \phi^+, \phi^0 \in \mathbb{C},$$

with hypercharge $Y = 1$, a gauge invariant potential

$$V(\Phi) = -\mu^2 \Phi^\dagger \Phi + \lambda \left(\Phi^\dagger \Phi\right)^2, \qquad (\lambda > 0), \tag{1.4}$$

and a Lagrangian

$$\mathscr{L}_H = (D_\mu \Phi)^\dagger (D_\mu \Phi) - V(\Phi). \tag{1.5}$$

Depending on the parameter μ^2, the potential $V(\Phi)$ exhibits two qualitatively different behaviors. For $\mu^2 < 0$ the potential has a global minimum at $\Phi = 0$ (see Figure 1.1(a)), whereas for $\mu^2 > 0$ the minimum degenerates and constitutes a manifold of equivalent points given by any field configuration with $\Phi^\dagger \Phi = \mu^2/2\lambda$ (see Figure 1.1(b)). The vacuum ground state has to correspond to one specific value of Φ, which can be chosen as

$$\Phi_0 = \frac{1}{\sqrt{2}} \begin{pmatrix} 0 \\ v \end{pmatrix} \quad \text{with} \quad v = \sqrt{\frac{\mu^2}{\lambda}},$$

where $v/\sqrt{2}$ denotes the *vacuum expectation value*. Obviously, this ground state is no longer gauge invariant. The vacuum being forced to chose one ground state out of a manifold of equivalent possible choices is what is referred to as *spontaneous symmetry breaking*, since the Lagrangian itself still obeys the full symmetry.

In accordance with perturbation theory, excitations correspond to small deviations of the field from its ground state. Exploiting the gauge invariance, these deviations can be parametrized without affecting generality as

$$\Phi(x) = \frac{1}{\sqrt{2}} \begin{pmatrix} 0 \\ v + H(x) \end{pmatrix}. \tag{1.6}$$

Expanding the potential $V(\Phi)$, one finds that $H(x)$ corresponds to an electrically neutral scalar particle with mass

$$m_H = \sqrt{2}\mu,$$

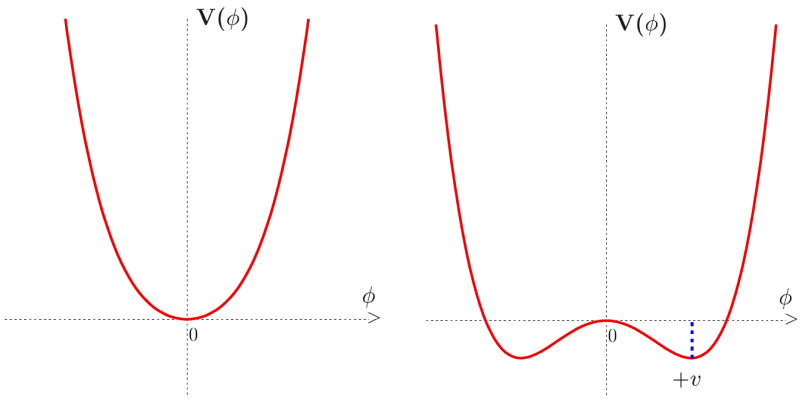

(a) $\mu^2 < 0$ (b) $\mu^2 > 0$

Figure 1.1: A one-dimensional projection of the potential $V(\Phi)$ of Equation (1.4) (adopted from Ref. [34]). (a) For $\mu^2 < 0$ the potential has one global minimum at $\Phi = 0$. (b) For $\mu^2 > 0$ the global minimum of the potential degenerates and constitutes a manifold of equivalent points given by any field configuration with $\Phi^\dagger\Phi = \mu^2/2\lambda$.

which is referred to as the *Standard Model Higgs boson*.

There are further implications of the symmetry breaking, which are revealed by plugging Equation (1.6) into Equation (1.5). Apart from couplings of the Higgs boson to the electroweak gauge fields W_μ^a and B_μ, one also finds terms corresponding to self-couplings of the Higgs boson

$$\frac{1}{2}\left(\frac{g}{2}v\right)^2 \left(W_\mu^1 W^{1,\mu} + W_\mu^2 W^{2,\mu}\right) + \frac{1}{2}\left(\frac{1}{2}v\right)^2 \left(W_\mu^3, B_\mu\right) \begin{pmatrix} g^2 & gg' \\ gg' & g'^2 \end{pmatrix} \begin{pmatrix} W^{3,\mu} \\ B^\mu \end{pmatrix}.$$

These terms can be diagonalized and thereby yield mass terms for the physical fields $W_\mu^\pm, Z_\mu$, and A_μ given in Equation (1.3) which correspond to the weak bosons $W^\pm$, Z, and the photon, respectively. That is, the three remaining degrees of freedom of Φ are absorbed to become the third polarization states of the gauge bosons $W^\pm$ and Z, which thereby acquire mass, whereas the photon stays massless in accordance with experiments.

The weak mixing angle θ_W, the masses of the weak gauge bosons m_W, m_Z and the coupling constants g and g' obey the relations

$$m_W = \frac{g}{2}v, \quad m_Z = \frac{\sqrt{g^2 + g'^2}}{2}v \quad \text{and} \quad \cos\theta_W = \frac{m_W}{m_Z}.$$

These relations allow to determine all parameters of the electroweak model from basic measurements, however, except for the mass m_H of the Higgs boson.

In order to allow fermions to acquire mass without violating the electroweak gauge symmetry, additional terms in the Lagrangian reflecting *Yukawa interactions* between the fermions and the Higgs field are postulated. For a single generation of leptons and quarks it has the form

$$\mathscr{L}_{\text{Yukawa}} = -y_\ell \bar{L}_L \Phi \ell_R - y_d \bar{Q}_L \Phi d_R - y_u \bar{Q}_L \Phi^c u_R + \text{h.c.}$$

Here, y_ℓ, y_d and y_u denote the Yukawa coupling constants of the charged lepton ℓ, the *down-type* quark and the *up-type* quark, respectively. $\bar{L}_L$ and $\bar{Q}_L$ represent the lepton and quark

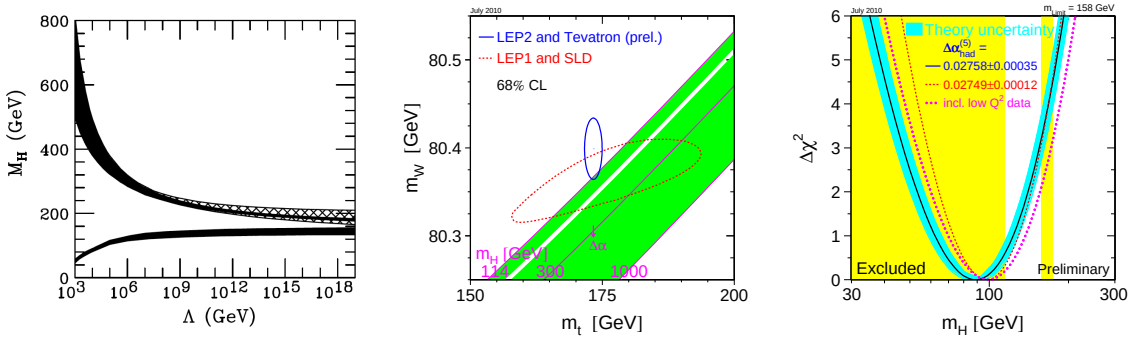

(a) (b) (c)

Figure 1.2: Illustration of constraints on the SM Higgs boson mass m_H. (a) Theoretical constraints (taken from Ref. [35]). The upper edge corresponds to Higgs boson masses for which the couplings of the SM Higgs boson diverge at scale Λ. The lower bound can be derived from requiring the vacuum to be stable. The solid and hatched areas indicate theoretical uncertainties on the Higgs boson mass bounds. (b) 68 % CL contour in the (m_t, m_W)-plane obtained from measurements at LEP, the Tevatron, and SLD as well as the SM relationship for these masses as a function of the Higgs boson mass m_H (taken from Ref. [36]). (c) $\Delta\chi^2$ curve derived from high-Q^2 precision electroweak measurements performed at LEP and by SLD, CDF, and DØ as a function of the Higgs boson mass m_H, assuming the SM to be the correct theory of nature (taken from Ref. [36]).

weak isospin doublets, respectively. $\Phi^c = iT_2\Phi$ is the charge conjugate of the Higgs doublet Φ and "h.c." refers to the hermitian conjugate of the full expression. As a consequence of the mechanism, the couplings of the SM Higgs boson to fermions, but also to gauge bosons, is proportional to their masses.

1.2.2. Constraints on the Higgs Boson Mass

The SM and the theory of electroweak symmetry breaking do not allow a theoretical prediction of the Higgs boson mass m_H. However, theoretical arguments allow to place constraints on m_H derived from internal consistency conditions and extrapolations of the model to high energies [27].

One crucial effect of the Higgs mechanism is to restore *unitarity* in the scattering of two longitudinally polarized W bosons, which is no longer accomplished if the Higgs boson mass m_H exceeds approximately 1 TeV. Furthermore, from requiring the couplings of the SM Higgs boson to be finite up to a hypothetical energy (*cut-off*) scale Λ, one can obtain an upper bound on m_H [35]. A lower bound on m_H can be derived from the requirement of vacuum stability. Figure 1.2(a) illustrates the dependence of theoretical upper and lower bounds on m_H as a function of Λ.

Stringent limits on the Higgs boson mass m_H have been derived from electroweak precision measurements at LEP and the Tevatron [36]. Through loop corrections the Higgs boson mass is indirectly related to the mass of the top quark m_t and the W boson m_W. Assuming the SM is the correct theory of nature, this relation can be determined and compared with measurements. As illustrated in Figure 1.2(b), these measurements prefer a small Higgs boson mass of the order of 100 GeV.

Furthermore, a global fit to electroweak precision data can be used to assess the compatibil-

ity of the data with different Higgs boson mass hypotheses m_H, as illustrated in Figure 1.2(c). This has been used to derive an upper bound on the Higgs boson mass at 95 % confidence level (CL) of $m_H < 158$ GeV [22].

1.3. Phenomenology at Hadron Colliders

High-energy particle colliders have proven to be very successful in probing nature's basic concepts. The types of particles brought to collision determine the types of questions a collider experiment is most suitable to answer, bearing a complementarity of hadron-hadron, hadron-lepton and lepton-lepton colliders. While lepton-lepton colliders are an appropriate experimental environment for high-precision measurements, lepton-hadron colliders conveniently allow to probe the structure of hadrons. Finally, hadron-hadron colliders can be considered as *discovery machines*, reflecting their potential to reveal unknown or yet unobserved phenomena by exploring new energy regimes.

Modern high-energy particle colliders, including the LHC, employ bunched particle beams, where the colliding particles are packed into numerous *bunches*. That is, collisions do not take place continuously but with a certain frequency, which is determined by the *bunch spacing* and the revolution frequency of the bunches.

1.3.1. Cross Sections, Luminosity, and Event Rates

Particle colliders and corresponding detectors are experimental setups to probe physics processes as they appear in nature, whereas a theory of fundamental interactions like the SM is a mathematical framework to describe these physics processes independently of any experiment. The bridging between experiment and theory is accomplished by the equation

$$R = \frac{\mathrm{d}N}{\mathrm{d}t} = \sigma \cdot L, \tag{1.7}$$

where σ denotes the *cross section*[1] of the corresponding physics process and L refers to the *instantaneous luminosity*[2] delivered by the collider. L can be determined from parameters of the colliding particle bunches. If two bunches containing n_1 and n_2 particles collide head-on with frequency f, then L is given by [29]

$$L = f \frac{n_1 n_2}{4\pi \sigma_x \sigma_y},$$

where σ_x and σ_y refer to the root-mean-squares of the transverse beam sizes in the horizontal and vertical direction, respectively.

Except for the initial state of the particle collision, the cross section σ is independent of the experimental setup and can be calculated within the mathematical framework of the SM. For elementary particles in the initial state the cross section σ of a certain physics process is given by [26]

$$\sigma = \int \mathrm{d}\sigma = \int \frac{|\mathcal{M}|^2}{F} \mathrm{d}Q, \tag{1.8}$$

where $\mathcal{M}$ denotes the *matrix element* of the corresponding transition between the initial and the final state. F and $\mathrm{d}Q$ denote quantities corresponding to the kinematic properties of the process and reflect the incident flux in the laboratory frame and the *Lorentz-invariant phase space factor*, respectively.

[1] $[\sigma] = \mathrm{barn} = 10^{-24}\mathrm{cm}^2$
[2] $[L] = \mathrm{cm}^{-2}\mathrm{s}^{-1}$

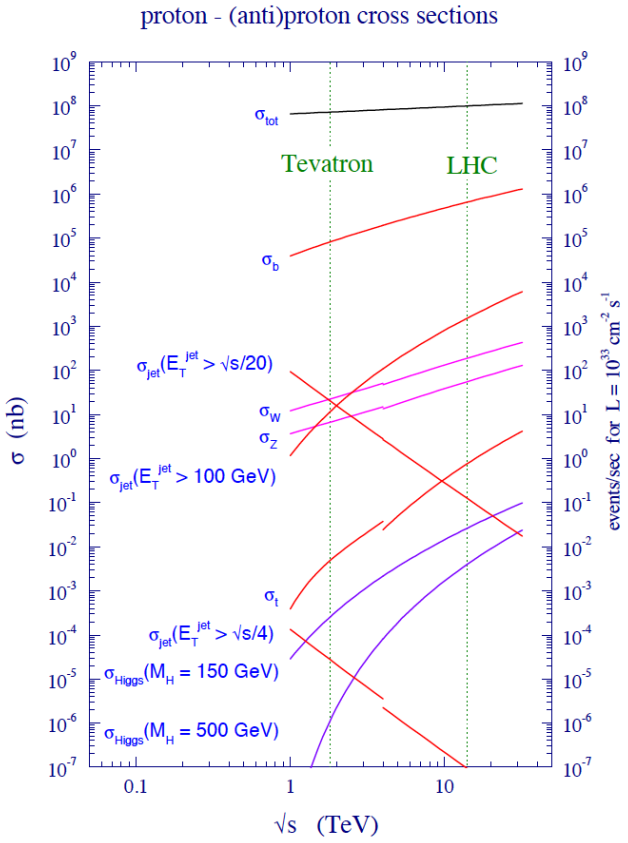

Figure 1.3: Predictions of the cross sections of several SM processes in hadron collisions as a function of the center-of-mass energy $\sqrt{s}$ (taken from Ref. [37]). Proton/anti-proton collisions at the Tevatron at $\sqrt{s} = 1.96$ TeV and proton-proton collisions at the LHC at $\sqrt{s} = 14$ TeV are indicated as vertical lines.

The matrix element $\mathcal{M}$ is determined from the Lagrangian describing the interactions of the theory. Even though it is not possible to derive an analytical expression for $\mathcal{M}$, one can use perturbation theory to obtain an approximative expansion in powers of the corresponding coupling constants. The *leading order* (LO) term reflects an interaction at *tree-level*, whereas higher-order terms, referred to as *next-to-leading order* (NLO), *next-to-next-to-leading order* (NNLO), etc., reflect particle loops as well as initial and final state radiation.

Higher-order corrections induce infinities in the calculations, which have to be absorbed in a redefinition of the coupling constants (referred to as *renormalization*). This comes at the expense of the need for the introduction of energy scale parameters, which the renormalized couplings depend on. This unphysical dependence can be used to assess the theoretical uncertainty on finite-order calculations.

The calculation of cross sections involving hadrons in the initial state has to account for their compositeness (see next section). Figure 1.3 presents the predictions of cross sections of several SM processes in proton-proton and proton/anti-proton collisions as a function of the center-of-mass energy.

The *integrated luminosity*[3] $\mathcal{L}$, reflecting the amount of recorded collision data, and the

[3] $[\mathcal{L}] = \text{cm}^{-2} = 10^{-24}\text{barn}^{-1}$

total number of expected events[4] N of a certain physics process after operating the collider experiment for a given period of time are obtained by integrating Equation (1.7)

$$N = \int R\mathrm{d}t = \sigma \cdot \mathcal{L} \quad \text{where} \quad \mathcal{L} = \int L\mathrm{d}t.$$

1.3.2. Parton Distribution Functions

The formalism of Equation (1.8) assumes interactions between free, elementary particles. Since hadrons have a sub-structure and are composed of quarks and gluons (partons) they cannot be treated as fundamental. A schematic of a generic hard-scattering process in hadron collisions is presented in Figure 1.4(a).

The calculation of cross sections in hadronic initial states involves short-distance effects where the involved partons can be treated as free particles, but also long-distance effects that cannot be dealt with in perturbative QCD. According to the *factorization theorem* [38], these effects can be absorbed in *parton distribution functions* (PDFs) $f_{a/A}(x, Q^2)$, which reflect the probability to "find" a parton a inside a hadron A with momentum fraction x at a momentum transfer Q^2. The x-dependence of PDFs cannot be derived from first principles but can be determined experimentally mainly using results from hadron-lepton collisions. The evolution with Q^2 can be calculated using the *Dokshitzer-Gribov-Lipatov-Altarelli-Parisi* (DGLAP) equations. Figure 1.4(b) displays PDFs of the proton at two different momentum scales Q^2 corresponding to the MSTW2008 PDF set [39].

The cross section for a scattering process $AB \to X$ involving two hadrons A, B in the initial state is then given by

$$\sigma(AB \to X) = \sum_{a,b} \int \mathrm{d}x_a \mathrm{d}x_b f_{a/A}(x_a, Q^2) f_{b/B}(x_b, Q^2) \hat{\sigma}(ab \to X).$$

Here, the sum runs over all partons a, b that can contribute to the final state. $\hat{\sigma}(ab \to X)$ denotes the parton cross section involving the initial state partons a, b, which can be determined by means of Equation (1.8).

1.3.3. Hadronization

Quarks and gluons produced as final state objects of a hard-scattering event are colored objects and undergo a complex process before being observable as colorless hadrons in the detector (see also Section 1.1.3). This transition is referred to as *hadronization* and is not amenable to perturbative calculations in QCD. However, like the structure of hadrons is parametrized in PDFs, the hadronization can be parametrized by *fragmentation functions* $D_{h \to H}(z, \mu_F^2)$, which reflect the probability of a parton h to hadronize into a hadron H, carrying a fraction z of the parton's momentum. Fragmentation functions have to be determined experimentally, which was mainly done in e^+e^- collisions at LEP.

1.3.4. Underlying Event and Pile-Up

At hadron colliders not the entire incoming particles are subject to hard interactions but usually only one single parton each. The remnants of the hadrons that were not subject to the hard interaction give rise to additional activity in the detector, which is referred to as the *underlying event*.

[4] Throughout this thesis, the term "event" refers to a high-energy collision event unless the context reveals something different.

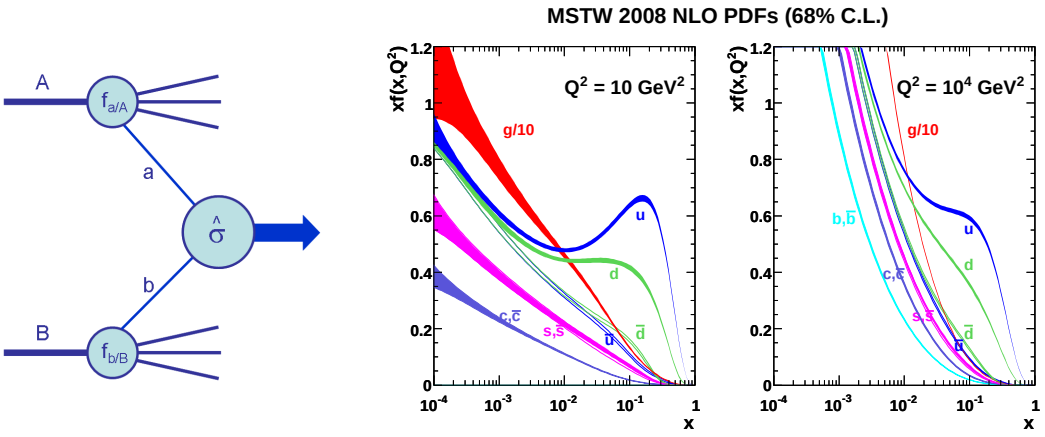

(a) (b)

Figure 1.4: (a) Illustration of the structure of a generic hard-scattering process in hadron-hadron collisions (taken from Ref. [37]). (b) MSTW2008 NLO parton distribution functions of the proton at momentum transfer scales $Q^2 = 10$ GeV^2 and $Q^2 = 10^4$ GeV^2, respectively (taken from Ref. [39]). The bands reflect the 68 % CL intervals.

Another source of additional activity in the detector is referred to as *pile-up* and denotes two different effects. *In-time* pile-up refers to multiple particle interactions simultaneously taking place during one single bunch crossing. The impact of in-time pile-up increases with the particle density inside the bunches and can severely affect the reconstruction of the hard-scattering event, which is of primary interest. In-time pile-up mainly contributes through soft jet production via QCD processes.

Out-of-time pile-up is caused by a temporal spacing between two bunch crossings which is less than the response time of the detector. That is, particles and the corresponding detector response stemming from a certain bunch crossing are overlaid with the ones stemming from a previous bunch crossing, thereby affecting the reconstruction of the current collision event.

1.3.5. Event Simulation

According to the principles of quantum mechanics, the mathematical framework of the SM only allows to predict probabilities for certain events to occur, measured in terms of cross sections, or the probability distributions for event properties of a certain physics process. In the context of an analysis, the predictions have to be confronted with the observed data. Since the interplay between final state particles and the detector is an extremely complex process which is not amenable to an analytical description, the predictions have to be determined by generating a finite number of simulated events. The generation of events is performed by dedicated computer programs using a *Monte Carlo method* to provide *Monte Carlo events* whose properties follow the theoretically determined distributions. Therefore, these tools are referred to as *Monte Carlo generators* and a large variety of different implementations is available [40,41]. Pythia [42,43], for instance, implements LO matrix elements to obtain probability distributions, whereas, for instance, MC@NLO [44] includes NLO QCD corrections.

After the generation of the hard-scattering events and the simulation of other relevant physical effects like parton showering, hadronization, underlying event, and pile-up the event data is passed to a detailed detector simulation [45, 46].

2 The ATLAS Experiment at the Large Hadron Collider

This chapter provides an overview of the experimental setup used to perform the $H \to WW^{(*)} \to \ell\nu\ell\nu$ analysis as presented in this thesis. The analysis is based on proton-proton collision data recorded with the ATLAS experiment installed at the *Large Hadron Collider* (LHC). The LHC is briefly introduced in Section 2.1, followed by a more detailed summary of the integral components of the ATLAS detector in Section 2.2. Procedures and algorithms related to the identification and reconstruction of physical objects within the ATLAS experiment are outlined in Section 2.3.

2.1. The Large Hadron Collider

The LHC is the world's most modern and powerful particle accelerator. It is located at the *European Organization for Nuclear Research* (CERN[1]) near Geneva, Switzerland. The LHC is built about one hundred meters underground inside a tunnel of approximately 27 kilometers circumference, which formerly hosted the *Large Electron Positron collider* (LEP) before its final shut down in the year 2000. The LHC is designed to operate in two different modes: it can store and collide either two proton beams (pp physics) at four interaction points with a maximum center-of-mass energy of $\sqrt{s} = 14$ TeV and an instantaneous luminosity of $L = 10^{34}$ cm^{-2}s^{-1}, considerably outperforming previous colliders. Alternatively, it can store and collide two heavy ion beams (HI physics), specifically lead (Pb) nuclei, at a maximum center-of-mass energy of $\sqrt{s} = 5.6$ TeV and an instantaneous luminosity of $L = 10^{27}$ cm^{-2}s^{-1} [47].

The LHC started successful operation in the year 2009. First pp collisions for physics analyses have been accomplished in the year 2010 at a center-of-mass energy of $\sqrt{s} = 7$ TeV. In the year 2012 the LHC has been operated at a center-of-mass energy of $\sqrt{s} = 8$ TeV and an instantaneous luminosity close to its design parameters. Nominal operation is expected to be achieved after a shut down, which aims for technical improvements and an upgrade of the accelerator hardware.

Along the LHC accelerator ring four main experiments are installed around four interactions points. These are two multi-purpose experiments, the ATLAS and the CMS experiment, as well as two specialized experiments with more specialized physics programs, the LHCb and the ALICE experiment.

The search for the Higgs boson clearly has been one decisive incitement for building the LHC and its experiments, though by far not the only one. Besides Higgs boson physics, the physics programs of the main experiments at the LHC involve the search for supersymmetric particles, new heavy gauge bosons and many other new physics phenomena as well as precision measurements of the parameters of the SM.

[1] French: Conseil Européen pour la Recherche Nucléaire.

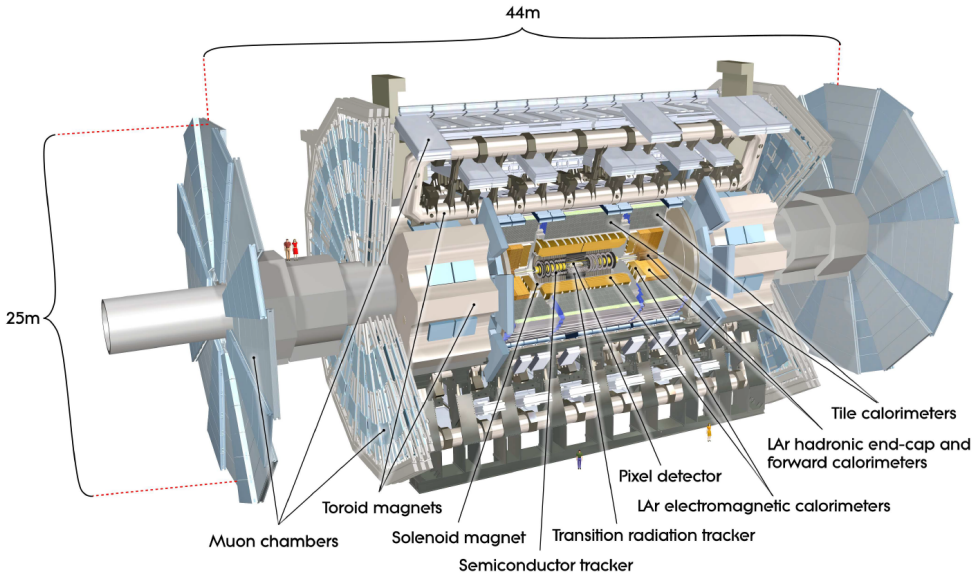

Figure 2.1: Cut-away view of the ATLAS detector (taken from Ref. [48]). Going from the interaction point to the outside, the ATLAS detector consists of the Inner Detector (ID), the Electromagnetic (EM) calorimeter, the hadronic calorimeter and the Muon System (MS).

2.2. The ATLAS Detector

The ATLAS detector is one of the two general purpose particle detectors installed at the LHC. It allows to identify all relevant final state objects like electrons, muons, photons, jets and the reconstruction of missing transverse energy. This section provides an overview of the ATLAS detector and thereby very closely follows Refs. [48] and [49].

The high instantaneous luminosity and energy of the particle collisions provided by the LHC enable a large variety of physics analyses at the ATLAS experiment, in particular searches for processes with very low cross sections, e.g. the production of Higgs bosons or supersymmetric particles. However, the machine parameters making new and interesting physics processes accessible experimentally also pose a challenge on both the detector hardware and the reconstruction software of the ATLAS experiment. If the LHC is operated at its design parameters, the inelastic proton-proton cross section of $\sigma_{pp} = 80$ mb results in a total rate of the order of 10^9 inelastic scattering events per second [48].

The ATLAS detector has an onion-like, forward-backward-symmetric structure with several detector sub-systems built as different concentric and approximately cylindrical layers, providing an almost hermetic coverage. A cut-away view of the ATLAS detector is presented in Figure 2.1. With the beam pipe in the center, the innermost sub-detector is a high-resolution tracking and vertexing detector (see Section 2.2.1), surrounded by electromagnetic and hadronic calorimeters (see Section 2.2.2) and a muon spectrometer system as the outermost part of the ATLAS detector (see Section 2.2.3). The luminosity delivered to the ATLAS experiment is measured by two dedicated sub-detectors (Lucid[2] and Alfa[3]) located in the forward regions.

[2] LUminosity measurement using Cerenkov Integrating Detector
[3] Absolute Luminosity For Atlas

The ATLAS experiment uses a right-handed coordinate system with its origin defined as the nominal interaction point. The x-axis points to the center of the LHC ring, the y-axis points upwards and the z-direction is given by the direction of the beam axis. The *azimuthal angle* ϕ is measured in the x-y-plane with respect to the x-axis ($\tan\phi = y/x$) and the *polar angle* θ is measured with respect to the beam-line. The *pseudo-rapidity* η is defined as

$$\eta = -\ln\tan\left(\frac{\theta}{2}\right). \tag{2.1}$$

2.2.1. Inner Detector

The physics analyses to be performed with the ATLAS experiment require a very high resolution and accuracy in energy and momentum measurements of the particles emerging from the collision point. The momentum of a charged particle is determined by measuring its trajectory in a bending magnetic field of known strength, translating momentum resolution requirements into spatial resolution requirements of the tracking detector. Furthermore, there is the need for an efficient reconstruction of primary interaction and secondary decay vertices, which constitutes an important ingredient to the rejection of objects produced in simultaneous collision events (*pile-up events*) or of heavy quark flavor tagging. If the LHC is operated at its design luminosity, the ATLAS detector will have to handle of the order of one thousand charged particle tracks per bunch crossing [49].

The *Inner Detector* (ID) is designed to meet the requirements mentioned above and is built up from three independent sub-systems: the *Pixel detector*, the *Semiconductor Tracker* (SCT) and the *Transition Radiation Tracker* (TRT). Figure 2.2 shows a plan view of a quarter-section of the ID. It is entirely contained in a cylindrical envelope of approximately 3.5 m length and 2.3 m diameter and immersed in a solenoidal magnetic field of 2 T to provide bending of charged particle tracks. The intrinsic momentum resolution of the IDis $\sigma_{p_\mathrm{T}}/p_\mathrm{T} = 0.05\ \% \cdot p_\mathrm{T} \oplus 1\ \%$ [48].

Pixel Detector

The pixel detector consists of silicon pixel detectors arranged in three cylindrical layers in the barrel region and two times three disks perpendicular to the beam axis in the end-cap regions, where the innermost barrel layer is as close as 51 mm to the beam axis. All pixel sensor modules are identical with a minimum pixel size of $50 \times 400\ \mu\mathrm{m}^2$, resulting in an accuracy of 10 μm for $(R-\phi)$ in both the barrel and the end-cap regions and 115 μm for z in the barrel and R in the end-cap disks. In total, the pixel detector covers the region of $|\eta| < 2.5$ and features more than 80 million readout channels. Given the geometry of the pixel detector, each particle track inside its fiducial region will typically traverse three pixel layers.

The Pixel detector is a crucial instrument for measurements based on particle tracking, e.g. the reconstruction of primary interaction and secondary decay vertices (see Section 2.3.1).

Semiconductor Tracker

Together with the pixel detector the SCT makes up the precision tracking instrument of the ATLAS detector. The SCT uses double layers of silicon strip detectors arranged in a small stereo angle of approximately 40 mrad to provide two-dimensional position measurements of particle hits. In the barrel region the SCT consists of four double layers with cylindrical arrangement and one set of strips running parallel to the beam axis. The innermost SCT layer is mounted at a radius of approximately 30 cm from the interaction point. In the end-cap

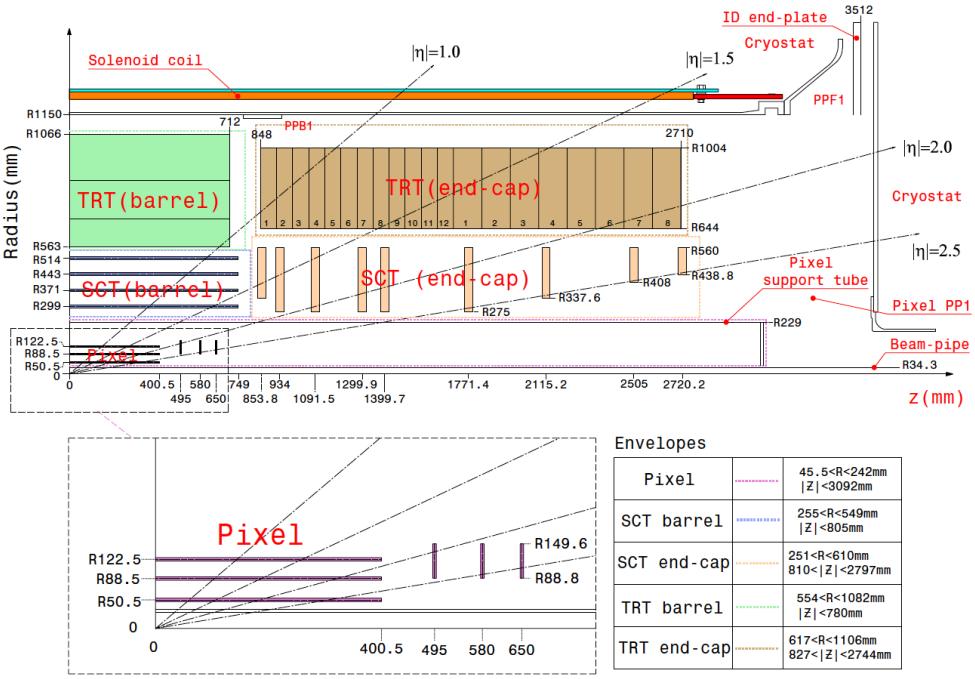

Figure 2.2: Plan view of a quarter-section of the ATLAS Inner Detector (taken from Ref. [48]).

region the SCT consists of two times nine disks of double layers installed perpendicular to the beam axis, with one set of strips running radially. The average strip pitch is approximately 80 μm. In total, the SCT has approximately 6.3 million readout channels, and with $|\eta| < 2.5$ its coverage matches the one of the pixel detector.

Transition Radiation Tracker

The TRT is the outermost sub-detector of the IDand is consists of straw tubes of 4 mm diameter. In the barrel region, the tubes are arranged parallel to the beam axis with a length of 144 cm each and radially with a length of 37 cm each in the end-cap region. By construction, the TRT is only capable of providing R and ϕ coordinates of particle hits with an intrinsic accuracy of 130 μm per straw tube. The deficiency of the missing η coordinate is compensated by the large number of hits per track, which typically is of the order of 36. In contrast to the high precision silicon detectors, the TRT only covers the region of $|\eta| < 2$. The total number of readout channels of the TRT is approximately 351,000.

2.2.2. Calorimeter System

The calorimeter system is designed to determine the energy of particles like electrons, photons and hadrons. The measurement is based on the interaction of these particles with the calorimeter material and the deposition of energy while traversing the calorimeter system. In order to allow for a high resolution energy measurement, the calorimeter system has to provide good containment for electromagnetic and hadronic showers and must limit punch-through into the muon system, rendering the calorimeter depth one crucial parameter of the system.

The calorimeter system of the ATLAS detector encapsulates the IDand covers the region

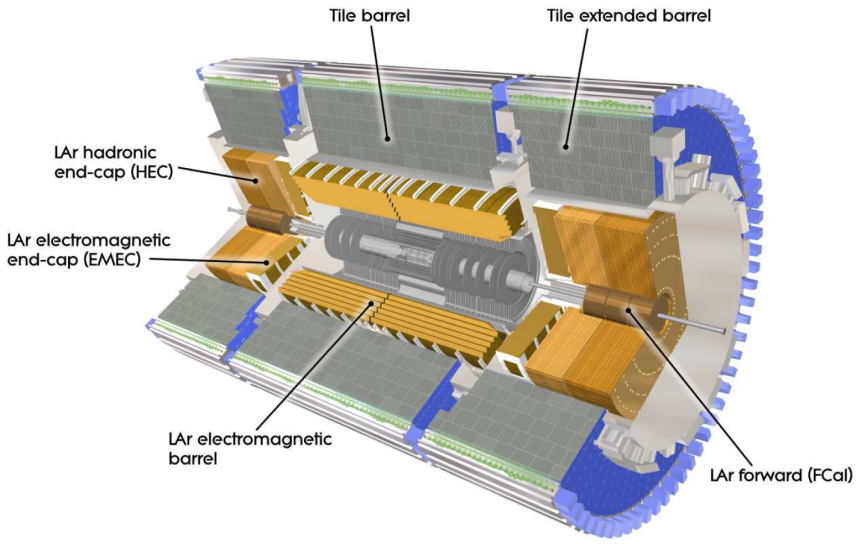

Figure 2.3: Cut-away view of the ATLAS calorimeter system (taken from Ref. [48]). The calorimeter system surrounds the IDand is built from several sub-systems using different calorimeter technologies.

up to $|\eta| < 4.9$ using different technologies. Figure 2.3 shows a cut-away view of the full ATLAS calorimeter system.

LAr Electromagnetic Calorimeter

The electromagnetic (EM) calorimeter is composed of a barrel component covering the region $|\eta| < 1.475$ and two end-cap components covering the region $1.375 < |\eta| < 3.2$. Each end-cap calorimeter component in turn consists of two coaxial wheels, with the outer wheel's coverage of $1.375 < |\eta| < 2.5$ overlapping with the one of the ID, and an inner wheel covering the region $2.5 < |\eta| < 3.2$. The EM calorimeter uses liquid argon (LAr) as the active medium, lead as the absorber material and accordion-shaped kapton electrodes for readout to allow for a full ϕ-symmetry without azimuthal cracks.

The barrel and the outer end-cap wheel of the EM calorimeter are longitudinally divided into three, and the inner end-cap wheel into two layers with decreasing granularity viewed radially from the interaction point. A schematic drawing of a barrel module of the EM calorimeter is shown in Figure 2.4. The first layer (η *strip layer*) has a fine granularity of up to $\Delta\eta \times \Delta\phi = 0.0031 \times 0.1$ depending on $|\eta|$. The second layer (*middle layer*), where most of the energy of electrons and photons is deposited, has a granularity of up to $\Delta\eta \times \Delta\phi = 0.025 \times 0.025$. The third layer (*back layer*), collecting the tails of high-energy electromagnetic showers, has a granularity of up to $\Delta\eta \times \Delta\phi = 0.05 \times 0.025$. The intrinsic energy resolution of the EM calorimeter is $\sigma_E/E = 10\ \%/\sqrt{E/\mathrm{GeV}} \oplus 0.7\ \%$ [48].

Hadronic Tile and End-Cap Calorimeters

The energy measurement of hadronic particles and showers is performed using the hadronic calorimeter consisting of a tile calorimeter and the *Hadronic End-cap* (HEC) calorimeter. The tile component, in total covering the region $|\eta| < 1.7$, is subdivided into a central barrel enclosing the barrel component of the EM calorimeter and an extended barrel component enclosing the end-cap calorimeters. The hadronic end-cap calorimeter is placed behind the

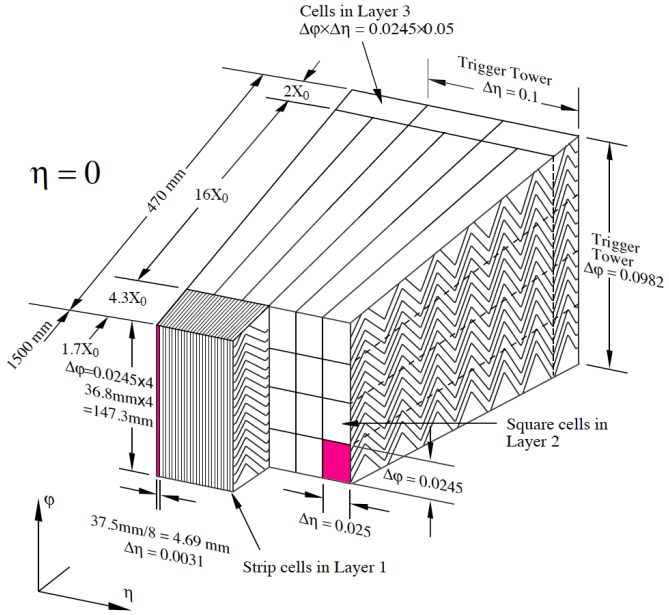

Figure 2.4: Sketch of a barrel EM calorimeter module showing its three layers and their granularity (taken from Ref. [48]).

end-cap components of the EM calorimeter and covers the region $1.5 < |\eta| < 3.2$.

The tile calorimeter is a sampling calorimeter using steel as absorber material and a scintillator as active medium. It is longitudinally divided into three layers with the inner two layers having a granularity of $\Delta\eta \times \Delta\phi = 0.1 \times 0.1$ and the outer one of $\Delta\eta \times \Delta\phi = 0.2 \times 0.1$. As the tile calorimeter, the hadronic end-cap is a sampling calorimeter, but uses liquid argon like the EM calorimeter as active medium and copper as the absorber material. The intrinsic energy resolution of the hadronic calorimeters for jets is $\sigma_E/E = 50\ \%/\sqrt{E/\mathrm{GeV}} \oplus 3\ \%$ [48].

LAr Forward Calorimeter

The *Forward Calorimeter* (FCal) is located in the region surrounded by the HEC calorimeter and covers the region $3.1 < |\eta| < 4.9$ and due to limited space uses a high-density design. Each end-cap module consists of three layers, with the first layer, using copper as active medium, being optimized for electromagnetic measurements, while the second and the third layer are made of tungsten and are optimized for the measurement of hadronic interactions. The intrinsic energy resolution of the FCal for jets is $\sigma_E/E = 100\ \%/\sqrt{E/\mathrm{GeV}} \oplus 30\ \%$ [48].

2.2.3. Muon System

The *Muon System* (MS) is the outermost subcomponent of the ATLAS detector (see Figure 2.1) and has been designed to provide efficient and precise muon identification and momentum measurements over a momentum range of approximately 3 GeV $\leq p_{\mathrm{T}} \leq 1$ TeV and a geometric coverage of $|\eta| < 2.7$. It uses three large superconducting air-core toroid magnets to deflect muon tracks, which are then measured by separate trigger and high-precision tracking chambers. A cut-away view of the MS is presented in Figure 2.5.

A large barrel toroid magnet provides magnetic bending in the region $|\eta| < 1.4$, whereas two smaller end-cap magnets, which are inserted at both ends of the barrel toroid, provide magnetic bending for muon tracks in the region $1.6 < |\eta| < 2.7$. Each toroid magnet is

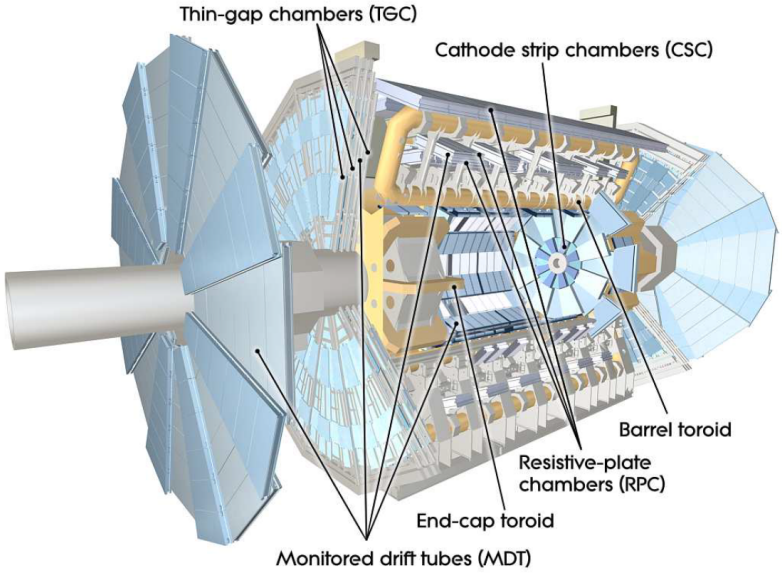

Figure 2.5: Cut-away view of the Muon System (MS) of the ATLAS detector (taken from Ref. [48]).

built from eight coils assembled radially and symmetrically around the beam axis. In the transition region $1.4 < |\eta| < 1.6$ magnetic bending is accomplished by a combination of the magnet fields of the barrel and the end-cap magnets. In order to optimize the bending power in this region, the two end-cap toroids are rotated by 22.5° with respect to the barrel toroid system.

Muon tracks are measured using four different types of detectors, which are installed in three cylindrical layers in the barrel region and two times three wheels in the end-cap regions. A precise measurement of the η coordinate is provided by *Monitored Drift Tubes* (MDTs), except for the innermost end-cap wheel, where for $2 < |\eta| < 2.7$ *Cathode Strip Chambers* (CSCs) are used. CSCs have a higher granularity than MDTs and additionally provide a rough measurement of the ϕ coordinate. Triggering as well as a further measurement of the ϕ coordinate of muon tracks is performed by *Resistive Plate Chambers* (RPCs) and *Thin Gap Chambers* (TGCs). RPCs are used in the region $|\eta| < 1.05$, whereas TGCs are used in the region $1.05 < |\eta| < 2.7$. However, the coverage of the muon trigger system only reaches up to $|\eta| < 2.4$. The intrinsic momentum resolution of the MS is $\sigma_{p_\mathrm{T}}/p_\mathrm{T} = 10\ \%$ at $p_\mathrm{T} = 1$ TeV [48].

2.2.4. Trigger

At the LHC an enormous event rate of approximately 40 MHz is expected for operation at design parameters. The offline computing resources are designed to achieve an event storage rate of approximately 200 Hz. In order to reduce the initial event rate to values compatible with the storage capabilities, while still capturing the physics of interest with high efficiency, the ATLAS trigger and data acquisition system consists of three subsequent trigger levels, which each apply selection criteria with increasing strictness and accuracy.

The first layer of the ATLAS trigger system is referred to as *Level 1* (L1) and is implemented in dedicated hardware components to enable 40 million trigger decisions per second, each within 2.5 μs at most. The L1 trigger has dedicated access to calorimeter and muon detector data and its decision is based on multiplicity and energy thresholds of objects like jets, muons, missing transverse energy and total transverse energy. It thereby achieves a reduction of the

event rate to 75 kHz.

Both the second and the third layer, referred to as *Level 2* (L2) and *Event Filter* (EF), respectively, use selection algorithms which are running on a farm of commodity computing hardware. Based on information provided by the L1 trigger, the L2 trigger identifies *Regions-of-Interest* (RoI) and performs a refined analysis of associated detector data to reduce the event rate to approximately 2 kHz. The final trigger decision is made by the EF, employing algorithms very similar to the offline identification and reconstruction algorithms (see also Section 2.3). The event rate accepted by the EF is of the order of 200 Hz and the corresponding event data is written to persistent data storage systems.

2.3. Reconstruction and Identification of Physical Objects

The ATLAS detector is built from numerous sub-detector systems and these subsystems in turn are built from many different modules, with each module usually featuring a large number of single detection channels that are sensitive to the passage of charged particles or the deposition of energy. Provoked by a positive trigger decision, the digitized information representing the response of the individual sub-channels is read out and stored on appropriate persistent storage media for future processing. This raw event data represents a snapshot of the detector activity without an explicit specification of the physical objects that induced the detector response. Since a physics analysis relies on the final state physics objects like electrons[4], photons, muons and jets as well as indirect objects like interaction vertices and missing transverse energy, these objects have to be reconstructed and identified from the raw event data using dedicated algorithms. These identification and reconstruction algorithms are implemented and bundled in the ATLAS software framework ATHENA [50], a tool for simulation, data processing and data analysis related to the ATLAS experiment.

The following sections outline the most important identification and reconstruction algorithms for primary interaction vertices, particle tracks, electrons, muons, jets and missing transverse energy.

2.3.1. Track and Vertex Reconstruction

Seeding the reconstruction of other physical objects the identification and reconstruction of tracks induced by charged particles [49, 51] is a crucial ingredient for further data processing and physics analyses. The track reconstruction is based on information provided by the two independent tracking devices of the ATLAS detector, the IDand the MS. It is initiated by *space points* inferred from hits in the pixel detector and the first layer of the SCT, which are subsequently used to build track candidates. A dedicated track finding algorithm is employed, which, going from the inner layers of the detector to the outer ones, extends the initial track candidates throughout the outer SCT layers, adding further hits associated to the track. Before being extrapolated to the TRT, the tracks are fitted using a refined detector model, ambiguities are resolved using a scoring system and fake tracks are removed by applying quality cuts. Finally, the tracks are refitted including pixel, SCT and TRT hits.

Dedicated algorithms are used to identify primary interaction vertices and to determine their position with respect to the beam spot [52]. The reconstruction of primary interaction vertices is based on tracks reconstructed as described in the previous paragraph and fulfilling

[4]The term *electron* will be used for both negatively charged electrons as well as for positively charged positrons throughout this thesis.

certain quality requirements to ensure the compatibility of the track to originate from the interaction region. In a first step, a vertex seed is created from the maximum in the distribution of z coordinates, which correspond to the closest approach of the tracks to the beam spot center. The second step is an iterative process fitting the position of a vertex seed including a refit of associated tracks with a constraint to originate from the vertex and creating new vertex seeds from tracks that are highly incompatible with the previous vertex. After no unassociated track is left or no new vertex seed can be created, the identified vertices are ordered according to the sum of squared transverse momenta of associated tracks, $\sum p_{\mathrm{T}}^2$, and the vertex with the maximum is considered as the primary vertex of the hard scattering [49].

The track impact parameters of a track quantify the distance between the track and the primary vertex at the point of closest approach, either in the plane transverse to the beam axis (*transverse impact parameter* d_0) or along the beam direction (*longitudinal impact parameter* z_0).

2.3.2. Electron Reconstruction and Identification

The main procedure used for the reconstruction of electrons in the range $|\eta| < 2.47$ is an algorithm starting from energy depositions (*clusters*) in the EM calorimeter [53], which are identified using a *sliding-window* approach [54]. A rectangular window in $\eta \times \phi$ space with a size of 3×5 in units of 0.025×0.025 corresponding to the granularity of the calorimeter middle layer is slided scanning for longitudinal calorimeter towers with a total transverse energy exceeding 2.5 GeV. Reconstructed tracks from the IDare extrapolated to the middle layer of the calorimeter and matched to energy clusters as identified in the previous step, if the distance in η and ϕ space between the track impact point and the cluster position is below a certain threshold. An electron candidate is reconstructed if at least one track can be associated to the initial energy cluster. Track association ambiguities are resolved by preferring tracks with silicon hits and small $\Delta R = \sqrt{\Delta\eta^2 + \Delta\phi^2}$ between the track impact point and the cluster position. The energy of the electron candidate is determined by rebuilding the calorimeter clusters consisting of 3×7 and 5×5 cells in the barrel and the end-cap, respectively, and summing over several contributions including longitudinal and lateral energy leakage. The four-momentum is computed from this energy and the parameters of the matched track.

These electron candidates are still very likely to be of a different origin than true electrons. This in particular includes jets and electrons arising from photon conversions. The purity of electron candidates to really correspond to genuine high-p_{T} electrons is enhanced by three successive sets of identification criteria with increasing strictness, referred to as "loose++", "medium++" and "tight++"[5], respectively, each implemented as a cut-based selection using calorimeter, tracking and combined variables. The "loose++" selection is based on variables describing the particle shower properties in the middle layer of the EM calorimeter as well as hadronic leakage variables, whereas the "medium++" selection adds requirements on variables related to the strip layer of the EM calorimeter, the track quality and the track-cluster matching. The "tight++" finally adds criteria based on E/p, the TRT, hits in the innermost pixel layer and reconstructed conversion vertices to suppress electrons arising from photon conversions. Going from "loose++" to "tight++" the three identification criteria feature an increasing background rejection power.

The criteria used by electron triggers are very similar to the ones described above [55].

[5]The suffix "++" is to allow for a distinction from the identification criteria used for data analyses in the year 2010.

However, in order to cope with the limitations imposed by the availability of detector information and the admissible decision latency, the employed algorithms may be slightly modified with respect to the offline version.

The *electron calorimeter isolation* is defined as the sum of transverse energies in the EM calorimeter in a cone around the electron candidate, whereas the *electron track isolation* is defined as the sum of transverse momenta of tracks in a cone around the track associated to the electron candidate.

Electron Energy Scale and Resolution

In order to achieve an accurate measurement of the electron energy, the response of the EM calorimeter has to be calibrated. This is done in three steps [53]. An electronic calibration converting the raw calorimeter signal into deposited energy is followed by a Monte Carlo (MC) simulation based correction mainly accounting for energy loss due to absorption in the passive material and leakage outside the calorimeter cluster. The residual mis-calibration is then parametrized by

$$E_{\text{meas}} = E_{\text{true}} \cdot (1 + \alpha_i)\,,$$

where E_{true} is the true electron energy, E_{meas} is the energy measured after the previous two calibration steps and α_i is a correction for a given region i, which is derived using $Z \to e^+e^-$ and $J/\Psi \to e^+e^-$ events. The determination of the correction factors α_i is taking advantage of the well-known masses of the Z and J/Ψ particles and is based on a likelihood maximization of the shape of the corresponding invariant di-electron mass distribution.

Apart from the electron energy scale the energy resolution is an important parameter of the electron measurement. Several effects, e.g. electronic noise in the calorimeter, with different energy dependencies impair the resolution and a parametrization is available with the corresponding coefficients being determined from MC simulation or from data.

Both the calibration of the electron energy scale as well as the parametrization of the electron energy resolution is outlined in detail in Ref. [53].

2.3.3. Muon Reconstruction

As charged particles muons will produce tracks in the ID, but their peculiarity is an entire passage through the calorimeter system with a minimal energy deposition. As the outermost component of the ATLAS detector the MS (see Section 2.2.3) is designed to record the passage of muons covering a wide range in transverse momentum (p_{T}) and η. Within the ATLAS experiment several strategies for the reconstruction and identification of muons are employed [53, 56], where the resulting collection of reconstructed muons is labeled according to the underlying strategy.

Standalone muons are reconstructed from hits in the MS and their trajectory is extrapolated towards the interaction point, taking into account the energy loss in the calorimeter. Standalone muons suffer from a significant contamination of muons not being produced in nominal proton-proton collisions but in the decay of hadrons in the calorimeter. However, since this reconstruction approach does not rely on the tracking capability of the ID, the coverage reaches up to $|\eta| < 2.7$.

The reconstruction of *segment tagged* muons is seeded by tracks in the IDexceeding a certain p_{T} threshold. These tracks are extrapolated to the innermost station of the MS and matched to muon track segments, if the latter are sufficiently close to the predicted track position. In case of an successful match, the corresponding track in the IDis flagged as a muon track. Per default, the muon kinematics are exclusively deduced from the IDtrack.

Combined muons are built from pairs of independent tracks in the IDand the MS that allow a justifiable match, which is assessed using a dedicated quality measure based on several track parameters. The kinematic properties of the muon are obtained from a weighted combination of both measurements in the IDand the MS (Staco muons), or, using an alternative implementation, by partially refitting the combined muon track (Muid muons). In either case, the momentum measurement is dominated by the IDfor $p_{\mathrm{T}} \lesssim 100$ GeV and by the MS for $p_{\mathrm{T}} \gtrsim 100$ GeV.

Both, muon calorimeter as well as muon track isolation, are defined in the same manner as for electrons (see Section 2.3.2).

Muon Momentum Scale and Resolution

The scale and the resolution of the muon momentum measurement as a function of the muon p_{T} and η has been studied using $Z \to \mu^+\mu^-$ and $W \to \mu\nu_\mu$ decays [57]. The width and the position of the Z invariant mass peak is sensitive to the momentum resolution and to the momentum scale, respectively, whereas single muons from $W \to \mu\nu_\mu$ decays are used to probe the convoluted momentum resolution of combined measurements in the IDand the MS. The analysis shows a worse performance in data compared to the MC simulation. The disagreement is mainly attributed to an imperfect knowledge of the detector alignment and a *smearing procedure* is applied to simulated muons to match the performance in data.

2.3.4. Jet Reconstruction and Quality

Quarks and gluons are objects carrying color charge and undergo a complex parton showering and hadronization process into colorless states before being observable (see also Section 1.3.3). The experimental signature of a final state quark or gluon is characterized by a collimated spray of energetic hadrons of different type and charge (called *jet*) [58,59] mainly depositing energy in the hadronic calorimeter, while tracks in the IDare produced from charged hadrons only. In order to deduce the kinematic properties of the original quark or gluon, the observed hadrons have to be clustered and track momenta as well as energy depositions have to be summed[6]. The clustering is performed by dedicated *jet algorithms* merging proximate objects based on an algorithm-specific metric. Several jet algorithms with different characteristics are available [59] and the choice is usually motivated by experimental or theoretical demands.

Jet Reconstruction

The jet algorithm commonly used within the ATLAS experiment is the *anti-k_t algorithm* [60] sequentially clustering objects (*entities*) based on a distance measure $d_{i,j}$ defined between two entities i, j and $d_{i,B}$ defined between one entity i and the beam axis. These are given by

$$d_{i,j} = \min\left(k_{t,i}^{-2}, k_{t,j}^{-2}\right) \cdot \frac{\Delta_{i,j}^2}{R^2} \quad \text{and} \quad d_{i,B} = k_{t,i}^{-2},$$

[6] This assumes that the kinematics of the cluster of particles provides a useful measure of the kinematics of the original quark or gluon.

respectively, where $\Delta_{i,j}^2 = (y_i - y_j)^2 + (\phi_i - \phi_j)^2$ and k_t, y and ϕ are the transverse momentum, the rapidity and the azimuthal angle of the corresponding entity, respectively. The clustering starts from a list of entities and proceeds by combining the two entities i and j with the smallest distance $d_{i,j}$, or, in case $d_{i,B}$ is the smallest distance, by calling entity i a jet and removing it from the list. The procedure is repeated until no entity is left, implicitly resolving jets up to a distance given by the *radius parameter* R. Typical values are $R = 0.4$ or $R = 0.6$. The choice of R is guided by an appropriate balance of including an adequate fraction of genuine objects related to the jet (preferring large values of R) and minimizing the sensitivity to contributions from extrinsic objects (preferring small values of R).

In the typical[7] case of *calorimeter jets*, the entities passed to the jet algorithm are *topological calorimeter clusters* [54], which are seeded by calorimeter cells with an energy deposition significantly larger than the expected noise and successively grown by adding neighboring cells exceeding a lower energy threshold. In order to allow for an appropriate separation between close-by particles, the building process of topological calorimeter clusters is finalized by splitting clusters featuring more than one local maximum above a certain threshold.

Apart from the hadronization of quarks and gluons from collision events, there is a list of processes and effects that can result in the reconstruction of a jet which has to be considered as background (*fake jet*). Electronic noise in the calorimeter or beam gas events, where one proton of the beam collided with the residual gas within the beam pipe, are two examples for such processes. Several jet quality selection criteria have been devised in order to reject fake jets, while keeping a high selection efficiency for jets produced in nominal proton-proton collisions [61, 62]. These jet quality criteria are referred to as "Looser", "Loose", "Medium" and "Tight" and provide increasing fake jet rejection capability with each of them being based on calorimeter pulse quality and timing information.

Another source of jets to be excluded in most analyses is given by pile-up events that are unrelated to the hard scattering interaction. With increasing instantaneous luminosity provided by the LHC, the number of such additional pile-up interactions increases as well, making the identification of pile-up related jets more important. The *jet vertex fraction* (JVF) algorithm is designed to quantify the compatibility of a particular jet to emerge from a particular primary vertex by measuring the fraction of the p_{T} of tracks associated to the jet as well as to the primary vertex with respect to the p_{T} of all tracks associated to the jet [63]

$$\mathrm{JVF}(\text{jet } i, \text{vertex } j) = \frac{\sum\limits_{\text{track} \in i \cap j} p_{\mathrm{T}}^{\text{track}}}{\sum\limits_{\text{track} \in i} p_{\mathrm{T}}^{\text{track}}}.$$

The value of JVF is bound by $0 \leq \mathrm{JVF} \leq 1$, with 0 representing a full incompatibility and 1 representing a full compatibility of jet i with primary vertex j. Since the track reconstruction relies on the ID, which has a geometrical coverage of $|\eta| < 2.5$, the JVF algorithm can only be used for jets reconstructed within the tracking acceptance. By convention, $\mathrm{JVF} = -1$ is assigned to jets outside the tracking acceptance.

[7] Within the ATLAS experiment also *track jets* are used, where the entities seeding the jet reconstruction are given by reconstructed tracks [61]. However, track jets are not used in the analysis presented in this thesis.

Jet Energy Scale and Resolution

Jets are complex objects containing numerous hadrons and the jet energy and momentum measurement is affected by several detector effects [61]. Due to different physical processes governing the energy deposition, the calorimeter response to hadronic showers usually differs from the one to electromagnetic showers (*non-compensation*) and only part of the energy of hadrons entering the calorimeter can be measured. Additional energy losses can arise from energy depositions in inactive detector regions or outside the jet reconstruction cone. Jets are reconstructed from energy depositions in the calorimeter calibrated for electromagnetic showers (*EM scale*) and the measurement has to be corrected to match the energy of the corresponding jet of stable particles entering the ATLAS detector.

Several *jet energy scale* (JES) calibration schemes have been developed within the ATLAS experiment [61] and the one used for the $H \to WW^{(*)} \to \ell\nu\ell\nu$ analysis is referred to as the "EM+JES" scheme. Starting from jets reconstructed at the EM scale, this scheme applies corrections based on the number of reconstructed primary vertices accounting for unrelated energy depositions arising from pile-up events. In a second step, the jet origin is adjusted to match the position of the primary vertex rather than the geometric center of the detector. Finally, the jet energy calibration is performed as a function of the uncalibrated jet energy and jet η before the origin correction. Here, constants that are derived from MC simulation relating the energy of particle jets to the corresponding reconstructed calorimeter jets are used. The calibrated jet energy $E^{\text{jet}}_{\text{EM+JES}}$ is given by

$$E^{\text{jet}}_{\text{EM+JES}} = \frac{E^{\text{jet}}_{\text{EM}}}{\mathcal{F}_{\text{calib}}(E^{\text{jet}}_{\text{EM}})|_{\eta_{\text{det}}}},$$

where $E^{\text{jet}}_{\text{EM}}$ is the uncalibrated jet energy and $\mathcal{F}_{\text{calib}}$ is the jet response calibration function (see Ref. [61] for details).

The *jet energy resolution* (JER) has been determined using both data and MC simulation and has been found to be in good agreement [64].

2.3.5. Identification of b-jets

Usually the type of parton initiating a jet cannot be determined reliably. However, jets stemming from b-quarks[8] (referred to as *b-jets*) allow an effective identification by exploiting the characteristics of b-hadron decays (referred to as *b-tagging*). Several distinctive properties contribute to the separation of b-jets and jets stemming from light quarks or gluons, but the most important one is the relatively long lifetime of hadrons containing a b-quark, which is of the order of 1.5 ps, resulting in a flight path length of the order of millimeter. [49].

The most commonly used b-tagging algorithms within the ATLAS experiment are based on the measurement of track impact parameters with respect to the primary vertex, the reconstruction of secondary and tertiary vertices or on a combination of both [65]. An example for the first is the IP3D algorithm, which uses a likelihood ratio technique based on the signed transverse impact parameter significance d_0/σ_{d_0} and the longitudinal impact parameter significance z_0/σ_{z_0} of corresponding tracks. JetFitter [66] is a secondary vertex algorithm exploiting the topological structure of weak b- and c-hadron decays inside a jet. A third example is a neural network driven combination of the latter two algorithms, referred to as JetFitterCombNN. Finally, MV1 is a b-tagging algorithm likewise using a neural network, but receiving input from the output of IP3D, JetFitterCombNN and SV1, which is another secondary vertex based algorithm.

[8] and to some extent c-quarks

The *working point* of a b-tagging algorithm is defined based on the inclusive b-tagging efficiency in a simulated sample of $t\bar{t}$ events and several selected values for each algorithm are calibrated from data using different methods [67]. Typical working points are in the range of 60 % to 85 % b-tagging efficiency with increasing misidentification rate of jets originating from light quarks or gluons.

2.3.6. Reconstruction of Missing Transverse Energy ($\mathbf{E_T^{miss}}$)

The initial state of a pp collision event in the ATLAS detector is given by two incoming proton beams, with each parton inside the proton having a negligible p_{T}. Given the conservation of momentum, the vectorial sum of the transverse momenta of all objects produced in a collision is expected to be zero. The presence of undetectable particles like neutrinos will produce an apparent momentum imbalance in the event called *missing transverse energy* or *momentum* and is denoted by $\vec{\mathbf{E}}_{\mathbf{T}}^{\mathbf{miss}}$ or $\vec{\mathbf{p}}_{\mathbf{T}}^{\mathbf{miss}}$. It is given by the transverse vector restoring the momentum conservation in the sum of all detected transverse energies or momenta. Its magnitude is given by $E_{\mathrm{T}}^{\mathrm{miss}} = |\vec{\mathbf{E}}_{\mathbf{T}}^{\mathbf{miss}}|$ and $p_{\mathrm{T}}^{\mathrm{miss}} = |\vec{\mathbf{p}}_{\mathbf{T}}^{\mathbf{miss}}|$, respectively.

The reconstruction of $\vec{\mathbf{E}}_{\mathbf{T}}^{\mathbf{miss}}$ includes contributions from energy depositions in the calorimeters as well as from muons reconstructed in the MS [68]. The magnitude of the missing transverse energy and the individual vector components are given by

$$E_{\mathrm{T}}^{\mathrm{miss}} = \sqrt{\left(E_{\mathrm{T},x}^{\mathrm{miss}}\right)^2 + \left(E_{\mathrm{T},y}^{\mathrm{miss}}\right)^2} \quad \text{and} \quad E_{\mathrm{T},x(y)}^{\mathrm{miss}} = E_{\mathrm{T},x(y)}^{\mathrm{miss,calo}} + E_{\mathrm{T},x(y)}^{\mathrm{miss,muon}},$$

respectively. The calorimeter term $E_{\mathrm{T},x(y)}^{\mathrm{miss,calo}}$ is calculated from calorimeter cells calibrated according to the associated reconstructed physics object and from cells not associated with any physics object

$$\begin{aligned} E_{\mathrm{T},x(y)}^{\mathrm{miss,calo}} = {} & E_{\mathrm{T},x(y)}^{\mathrm{miss,e}} + E_{\mathrm{T},x(y)}^{\mathrm{miss},\gamma} + E_{\mathrm{T},x(y)}^{\mathrm{miss},\tau} + E_{\mathrm{T},x(y)}^{\mathrm{miss,jets}} \\ & + E_{\mathrm{T},x(y)}^{\mathrm{miss,SoftJets}} + E_{\mathrm{T},x(y)}^{\mathrm{miss,CellOut}} + \left(E_{\mathrm{T},x(y)}^{\mathrm{miss,calo,muon}}\right). \end{aligned}$$

The terms $E_{\mathrm{T},x(y)}^{\mathrm{miss,e}}$, $E_{\mathrm{T},x(y)}^{\mathrm{miss},\gamma}$, $E_{\mathrm{T},x(y)}^{\mathrm{miss},\tau}$, $E_{\mathrm{T},x(y)}^{\mathrm{miss,jets}}$, $E_{\mathrm{T},x(y)}^{\mathrm{miss,SoftJets}}$ and $E_{\mathrm{T},x(y)}^{\mathrm{miss,CellOut}}$ correspond to electrons, photons, τ-jets from hadronically decaying τ-leptons, jets with calibrated $p_{\mathrm{T}} > 20$ GeV, jets with 7 GeV $< p_{\mathrm{T}} <$ 20 GeV and cells in topological clusters, which are not associated to reconstructed objects, respectively. $E_{\mathrm{T},x(y)}^{\mathrm{miss,calo,muon}}$ is an optional term for non-isolated muons that have undergone a considerable energy loss in the calorimeter. Each individual term is calculated from the negative sum of calibrated cell energies inside the corresponding objects

$$E_{\mathrm{T},x}^{\mathrm{miss,term}} = -\sum_{i \in \mathrm{cells}} E_i \sin\theta_i \cos\phi_i \quad \text{and} \quad E_{\mathrm{T},y}^{\mathrm{miss,term}} = -\sum_{i \in \mathrm{cells}} E_i \sin\theta_i \sin\phi_i,$$

where E_i, θ_i and ϕ_i are the energy, the polar angle and the azimuthal angle, respectively.

The direct muon term $E_{\mathrm{T},x(y)}^{\mathrm{miss,muon}}$ is calculated from the momenta of tracks associated to selected muons reconstructed within $|\eta| < 2.7$

$$E_{\mathrm{T},x(y)}^{\mathrm{miss,muon}} = -\sum_{i \in \mathrm{muons}} p_{x(y)}^{i}.$$

Within the coverage of the ID, contributing muons are required to have a matched track in the ID, whereas outside this region the momentum measurement is purely obtained from the MS.

3 Phenomenology of the Standard Model Higgs Boson at ATLAS

The Higgs mechanism and the Higgs boson are introduced in Section 1.2. The objective of this chapter is to provide an overview of the phenomenology of the SM Higgs boson at hadron colliders, placing emphasis on the LHC and the ATLAS experiment in particular. Section 3.1 summarizes the important Higgs boson production mechanisms at the LHC as well as the Higgs boson decay modes, whereas the major Higgs boson search channels analyzed within the ATLAS experiment are briefly discussed in Section 3.2.

3.1. Higgs Boson Production and Decay at the LHC

In the context of the SM, the Higgs mechanism introduces its only free parameter, the mass of the Higgs boson m_H. Once the mass parameter is fixed, all couplings of the Higgs boson to other particles can be determined from theoretical calculations. Since the Higgs boson is closely related to the generation of the masses of fermions and gauge bosons, its couplings to other particles is proportional to their mass. Thus, the production of the Higgs boson as well as its decay is dominated by processes involving couplings to particles with the largest possible masses.

At the LHC, the Higgs boson production mainly proceeds through four different production mechanisms. These are the *gluon fusion* mode ($pp \to H$, referred to as ggF[1]), the *vector-boson fusion* mode ($pp \to qqH$, referred to as VBF), the radiation off massive vector bosons ($pp \to WH, ZH$, referred to as *Higgs-strahlung* or WH/ZH) and the production in association with a pair of top quarks ($pp \to ttH$, referred to as *associated production* or ttH). The corresponding leading order Feynman diagrams are displayed in Figure 3.1. The total SM Higgs boson production cross sections at the LHC for different center-of-mass energies as a function of the Higgs boson mass m_H are illustrated in Figure 3.2(a). The cross sections of individual production mechanisms as a function of m_H at a center-of-mass energy of $\sqrt{s} = 8$ TeV are shown in Figure 3.2(b). The total production cross section decreases with increasing Higgs boson mass m_H. The gluon fusion production mode is the dominant production mechanism over the full interesting Higgs boson mass range of 100 GeV $\leq m_H \leq$ 1 TeV. It proceeds through heavy quarks running in a triangular loop. The vector-boson fusion production mode features the second largest cross section with an increasing relative contribution to the total production cross section with increasing Higgs boson mass m_H. The two outgoing quarks in the VBF process induce a distinctive event topology, which is characterized by two jets in the forward regions of the detector. Due to the low cross sections, both the Higgs-strahlung process as well as the associated production are of minor importance at the LHC.

[1] Using "ggF" as an abbreviation for the term "gluon fusion" appears to be inconsistent. However, since it is commonly used in the literature this abbreviation is adopted and used throughout this thesis.

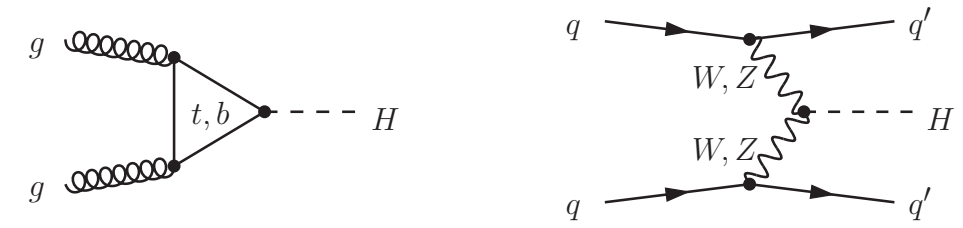

(a) Gluon fusion (ggF)

(b) Vector-boson fusion (VBF)

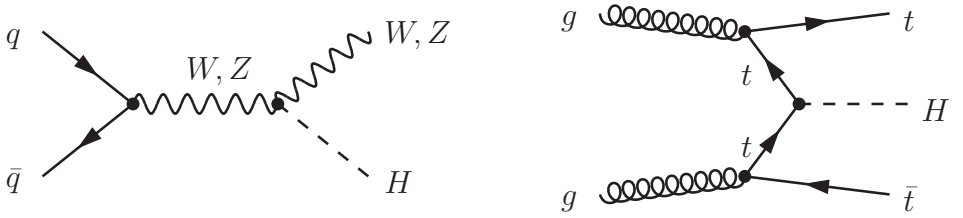

(c) Higgs-strahlung (WH/ZH)

(d) Associated production (ttH)

Figure 3.1: Leading order Feynman diagrams of the four main production mechanisms of a SM Higgs boson at the LHC.

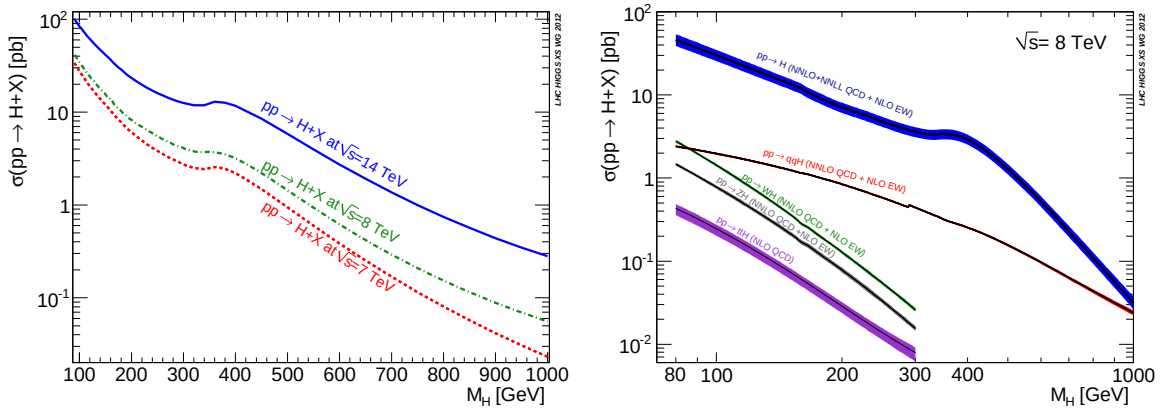

(a)

(b)

Figure 3.2: (a) Total SM Higgs boson production cross sections for center-of-mass energies of $\sqrt{s} = 7, 8$ and 14 TeV at the LHC. (b) SM Higgs boson production cross sections at the LHC at a center-of-mass energy of $\sqrt{s} = 8$ TeV, broken down into the gluon fusion ($pp \to H$), the vector-boson fusion ($pp \to qqH$), the Higgs-strahlung ($pp \to WH, ZH$) and the associated production with top quarks ($pp \to ttH$). The discontinuity for the VBF cross section at $m_H = 300$ GeV is due to the change from the zero-width-approximation to the complex-pole-scheme. Both plots are taken from Ref. [69].

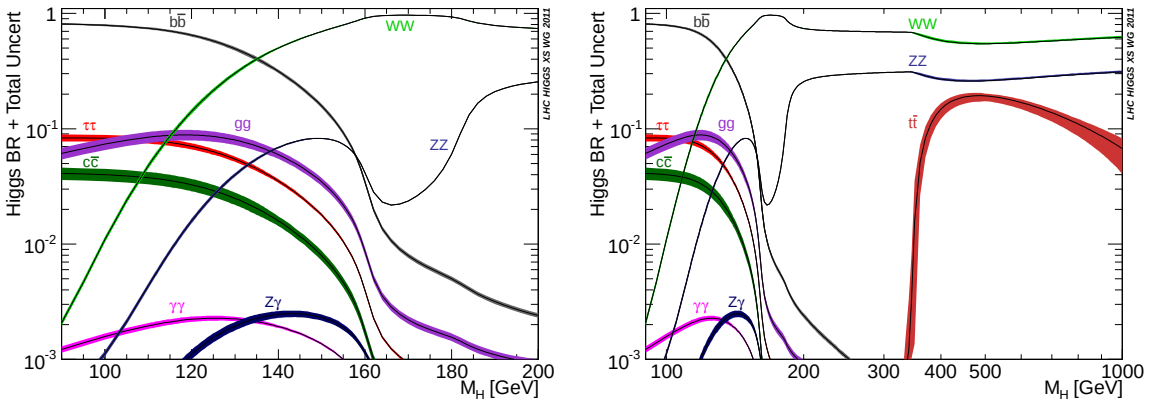

(a) 90 GeV $\leq m_H \leq$ 200 GeV

(b) 90 GeV $\leq m_H \leq$ 1 TeV

Figure 3.3: Decay branching ratios of the SM Higgs boson as a function of the Higgs boson mass m_H (taken from Ref. [69]).

The branching ratios of the SM Higgs boson into descendant particles strongly depends on its hypothesized mass m_H. Figure 3.3 shows the corresponding branching ratios into different types of fermions and gauge bosons. For low Higgs boson masses $m_H \lesssim 135$ GeV the decay into a pair of b-quarks dominates, whereas for $m_H \gtrsim 135$ GeV the decay into two W bosons is the predominant mode. Like in the case of the gluon fusion, the decay into two massless photons proceeds through heavy particles in a loop. It features a branching ratio which is at least between two and three orders of magnitude below the dominant decay mode.

3.2. Higgs Boson Search Channels at ATLAS

Within the ATLAS experiment, various Higgs boson decay channels are subject to a search and feature sensitivity to a SM Higgs boson over a broad range in m_H [70, 71]. However, due to the environment of hadronic collisions, some decay modes feature an inappropriate signal-to-background ratio and thereby are completely invisible at the LHC or at least only accessible in conjunction with a production mechanism featuring a distinctive topology.

Figure 3.4 illustrates the cross sections of the SM Higgs boson production at the LHC, multiplied by the branching ratios into various decay modes. Apart from the expected signal event rates, the sensitivity is strongly affected by the type and strength of the contributing background processes. Generally, the highest sensitivity is expected from the $H \to \gamma\gamma$, $H \to ZZ^{(*)} \to 4\ell$ and $H \to WW^{(*)} \to \ell\nu\ell\nu$ decay modes, where $H \to \gamma\gamma$ is mainly sensitive in the low mass range 110 GeV $\leq m_H \leq$ 140 GeV. In this mass region, also the $H \to \tau\tau$ and the $H \to b\bar{b}$ decay modes constitute interesting search channels, which, however, are not accessible in the gluon fusion production mode. For $m_H > 200$ GeV, further search channels like $H \to WW^{(*)} \to \ell\nu qq$, $H \to ZZ^{(*)} \to \ell\ell\nu\nu$ and $H \to ZZ^{(*)} \to \ell\ell b\bar{b}$ become available.

Due to a large cross section times branching ratio and a distinctive final state featuring two isolated leptons with large transverse momenta (see Section 4.1), the $H \to WW^{(*)} \to \ell\nu\ell\nu$ channel is the most sensitive search channel over a wide Higgs boson mass range.

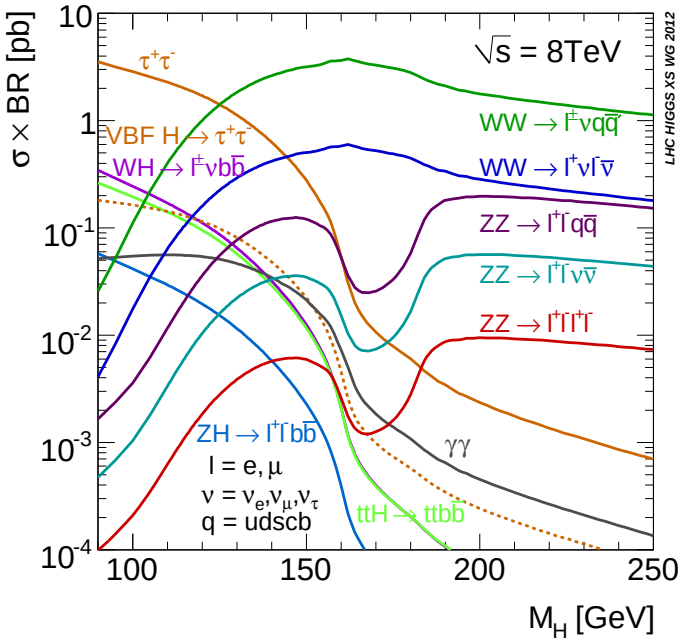

Figure 3.4: SM Higgs boson production cross sections times branching ratios at the LHC at a center-of-mass energy of $\sqrt{s} = 8$ TeV (taken from Ref. [69]). For $H \to \tau\tau$, both the inclusive (solid line) and the vector-boson fusion (dashed line) modes are plotted.

4 Signal and Background Processes

This chapter presents a general overview of the relevant physics processes involved in the search for the SM Higgs boson in the $H \to WW^{(*)} \to \ell\nu\ell\nu$ decay channel using pp collision data recorded with the ATLAS detector. After a discussion of the Higgs boson signal process and the characteristics of its final state for different benchmark Higgs boson mass hypotheses m_H, the processes posing potential backgrounds to the search in this channel are summarized. This chapter does neither cover details of the analysis nor of the techniques employed to estimate and suppress the individual backgrounds (see Chapters 7 and 8).

For the sake of illustration, plots of representative distributions of the signal as well as of background processes are displayed in this chapter. These plots are based on MC simulation of pp collisions at a center-of-mass energy of $\sqrt{s} = 8$ TeV including a detailed simulation of the ATLAS detector and the reconstruction of physical objects using the default algorithms. In the case of the $W+$jets background, a data-driven estimation technique is used. In either case, the events making up these distributions are taken from the 2012 dataset as it is used for the final results (see Chapter 5). The event selection includes the default object selection criteria described in Section 7.1 and the event preselection described in Section 7.2.1, up to the requirement of two oppositely charged leptons.

4.1. $H \to WW^{(*)} \to \ell\nu\ell\nu$ Signal Process

The SM Higgs boson is a short-lived particle, which, once produced in a high-energy particle collision, will decay into one of various possible pairs of descendants. The branching ratio of a given decay mode is a function of the Higgs boson mass m_H (see Section 3.1). For Higgs boson masses larger than $m_H \gtrsim 135$ GeV the decay into a pair of W bosons is the predominant decay mode, while still being the second dominant decay mode down to $m_H \gtrsim 115$ GeV [69]. For Higgs boson masses considerably off twice the W boson mass of approximately 160 GeV, at least one W boson in the $H \to WW^{(*)}$ decay tends to be off-shell (see also Ref. [34]).

With approximately 90 %, the majority of W boson pairs emanating from the Higgs boson will decay involving either two or even four quarks, resulting in a *single-leptonic* or a *full-hadronic* final state, respectively. Only approximately one tenth of WW pair decays proceed into *double-leptonic* (*dilepton*) final states. At the LHC, the full-hadronic final state, corresponding to $H \to WW^{(*)} \to qqqq$, is desperately concealed by QCD parton-parton scattering processes (in the following referred to as QCD *multijet* background). However, the single-leptonic final state, corresponding to $H \to WW^{(*)} \to \ell\nu qq$, still features sensitivity at larger Higgs boson masses [72] (see also Section 3.2).

4.1.1. Signature of the $H \to WW^{(*)} \to \ell\nu\ell\nu$ Final State

The $H \to WW^{(*)} \to \ell\nu\ell\nu$ analysis considers contributions from the decay of the Higgs boson into a pair of oppositely[1] charged W bosons ($H \to W^+W^-$), which both subsequently decay leptonically into either an electron or a muon plus the associated neutrinos ($W \to e\nu_e$ or

[1] Throughout this thesis WW refers to W^+W^-, a pair of oppositely charged W bosons, where one or even both are allowed to be off-shell.

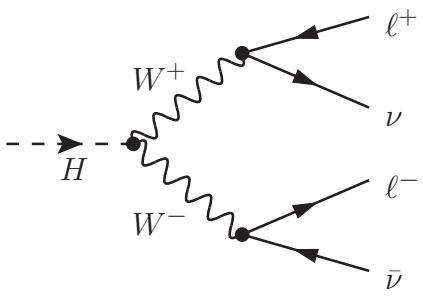

Figure 4.1: Leading order Feynman diagram of the $H \to WW^{(*)} \to \ell\nu\ell\nu$ decay mode. The final state is characterized by a pair of oppositely charged leptons and a neutrino/anti-neutrino pair.

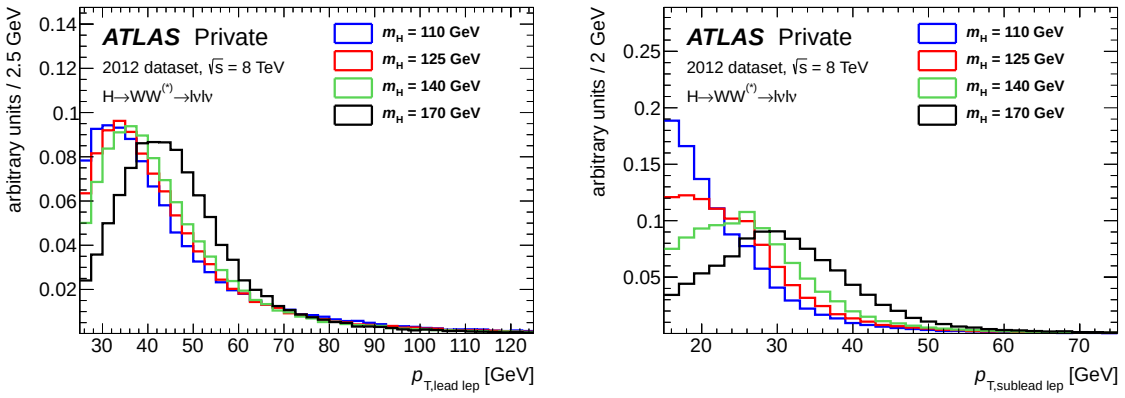

(a) Leading lepton p_{T}

(b) Sub-leading lepton p_{T}

Figure 4.2: Distributions of the transverse momenta p_{T} of the leading (highest p_{T}) charged lepton (a) and the sub-leading (second highest p_{T}) charged lepton (b) in simulated $H \to WW^{(*)} \to \ell\nu\ell\nu$ events for different Higgs boson mass hypotheses m_H. The distributions are normalized to unit area individually.

$W \to \mu\nu_\mu$), covering approximately 4.7 % of all possible WW decay modes. Figure 4.1 shows the leading order Feynman diagram of the $H \to WW^{(*)} \to \ell\nu\ell\nu$ decay mode. Contributions from the decay of the W bosons into τ-leptons are not explicitly taken into account in the analysis, since they decay inside the detector volume and would have to be reconstructed from their decay products. However, $H \to WW^{(*)}$ events with leptonically decaying τ-leptons still feature a small contribution through $H \to WW^{(*)} \to \ell\nu\tau\nu_\tau \to \ell\nu\ell\nu + X$, though being suppressed due to the softer transverse momentum spectrum of electrons and muons arising from decays of τ-leptons.

The signature of the $\ell\nu\ell\nu$ final state corresponding to the $H \to WW^{(*)} \to \ell\nu\ell\nu$ signal process is characterized by two isolated, oppositely charged leptons (electron or muon) with large transverse momenta p_{T} and a neutrino/anti-neutrino pair, each arising from the leptonic decay of the two W bosons. For all Higgs boson masses the two charged leptons are primarily emitted in the central region of the detector, but the p_{T}-spectrum becomes harder with increasing Higgs boson mass (see Figure 4.2).

Table 4.1 summarizes the total Higgs boson production cross sections in pp collisions at the LHC at center-of-mass energies of $\sqrt{s} = 7$ TeV and $\sqrt{s} = 8$ TeV as well as the corresponding production cross sections multiplied by the $H \to WW^{(*)} \to \ell\nu\ell\nu$ branching ratios for different

m_H [GeV]	BR($H \to WW^{(*)}$)	$\sigma(pp \to H)$ [pb]		$\sigma \cdot$ BR($H \to WW \to \ell\nu\ell\nu$) [pb]	
		$\sqrt{s} = 7$ TeV	$\sqrt{s} = 8$ TeV	$\sqrt{s} = 7$ TeV	$\sqrt{s} = 8$ TeV
110	4.82 %	22.71	28.67	0.05	0.06
125	21.6 %	17.51	22.30	0.18	0.22
140	50.4 %	13.90	17.83	0.33	0.42
170	96.5 %	8.93	11.61	0.40	0.52
200	74.1 %	6.20	8.21	0.21	0.28
240	70.4 %	4.41	5.93	0.15	0.20

Table 4.1: Summary of the total inclusive production cross sections of a SM Higgs boson in pp collisions at the LHC at center-of-mass energies of $\sqrt{s} = 7$ TeV and $\sqrt{s} = 8$ TeV for different Higgs boson mass hypotheses m_H as well as the branching ratios (BRs) of the $H \to WW^{(*)}$ decay mode and the corresponding $\sigma \cdot$ BR for the $H \to WW^{(*)} \to \ell\nu\ell\nu$ ($\ell = e, \mu$) decay mode. The numbers are taken from Ref. [69]. The branching ratio of $WW \to \ell\nu\ell\nu$ is given by BR($WW \to \ell\nu\ell\nu$) $= (2 \cdot 10.8\ \%)^2 \simeq 4.67\ \%$ derived from BR($W \to \ell\nu$) $= 10.8\ \%$ for $\ell = e$ or μ [29].

Final state	Referred to as
Same flavor leptons	Same flavor (SF)
$e^+e^- + X$ jets	ee
$\mu^+\mu^- + X$ jets	$\mu\mu$
Opposite flavor leptons	Opposite flavor (OF)
$e^\pm\mu^\mp(p_{\mathrm{T}}^{\mathrm{e}} > p_{\mathrm{T}}^{\mu}) + X$ jets	$e\mu$
$e^\pm\mu^\mp(p_{\mathrm{T}}^{\mathrm{e}} < p_{\mathrm{T}}^{\mu}) + X$ jets	μe

Table 4.2: Overview of the distinct final states of the $H \to WW^{(*)} \to \ell\nu\ell\nu$ analysis distinguished according to the flavors of the charged leptons and their p_{T}-hierarchy. The expected momentum imbalance ($E_{\mathrm{T}}^{\mathrm{miss}}$) is not listed explicitly.

Higgs boson mass hypotheses m_H. Even though the total production cross section of the Higgs boson decreases with increasing Higgs boson mass, its branching ratio into two W bosons behaves conversely for low masses. This results in an increase of the $pp \to H \to WW^{(*)} \to \ell\nu\ell\nu$ cross section with increasing Higgs boson mass up to its maximum at twice the W boson mass (see also Figure 3.4).

4.1.2. Lepton Flavor Channels

Motivated by a significant difference of the composition of backgrounds, four different final states are distinguished according to the combination of the flavors of the charged leptons and the hierarchy of their transverse momenta p_{T} (see Table 4.2). Final states with either two electrons or two muons are referred to as ee and $\mu\mu$ final states, respectively, and as *same flavor* final states collectively. Final states featuring both one electron and one muon are referred to as $e\mu$ and μe final states, depending on whether the electron or the muon has a larger[2] p_{T}. Even though a collective term for the latter two would more correctly be given by *different flavor* final states, these are commonly referred to as *opposite flavor* final states.

4.1.3. Transverse Mass

The presence of two neutrinos in the final state of the $H \to WW^{(*)} \to \ell\nu\ell\nu$ signal generates a significant amount of missing transverse energy ($E_{\mathrm{T}}^{\mathrm{miss}}$) in the event as the neutrinos escape detection (see Figure 4.3(a)). Neither the z-component of the neutrino momenta nor their angular separation can be measured, inhibiting a full reconstruction of the decaying Higgs boson system. Thus, no mass peak of the Higgs boson resonance can be extracted. Compared to other Higgs boson decay channels allowing a full reconstruction of the final state like $H \to \gamma\gamma$ and $H \to ZZ^{(*)} \to 4\ell$, the $H \to WW^{(*)} \to \ell\nu\ell\nu$ channel has a significantly degraded mass resolution. However, this disadvantage is countervailed by a large cross section times branching ratio, resulting in a comparatively large number of expected signal events (see also Figure 3.4).

One quantity accounting for the lack of the full final state information, which is still sensitive to the Higgs boson mass m_H, is the *transverse mass* m_{T} defined as [73]

$$m_{\mathrm{T}} = \sqrt{\left(E_{\mathrm{T}}^{\ell\ell} + E_{\mathrm{T}}^{\mathrm{miss}}\right)^2 - \left|\vec{p}_{\mathrm{T}}^{\,\ell\ell} + \vec{p}_{\mathrm{T}}^{\,\mathrm{miss}}\right|^2} \quad \text{with} \quad E_{\mathrm{T}}^{\ell\ell} = \sqrt{\left|\vec{p}_{\mathrm{T}}^{\,\ell\ell}\right|^2 + m_{\ell\ell}^2}. \tag{4.1}$$

[2] The object with the largest transverse momentum p_{T} is commonly referred to as the *leading* object, whereas the second largest p_{T} defines the *sub-leading* object.

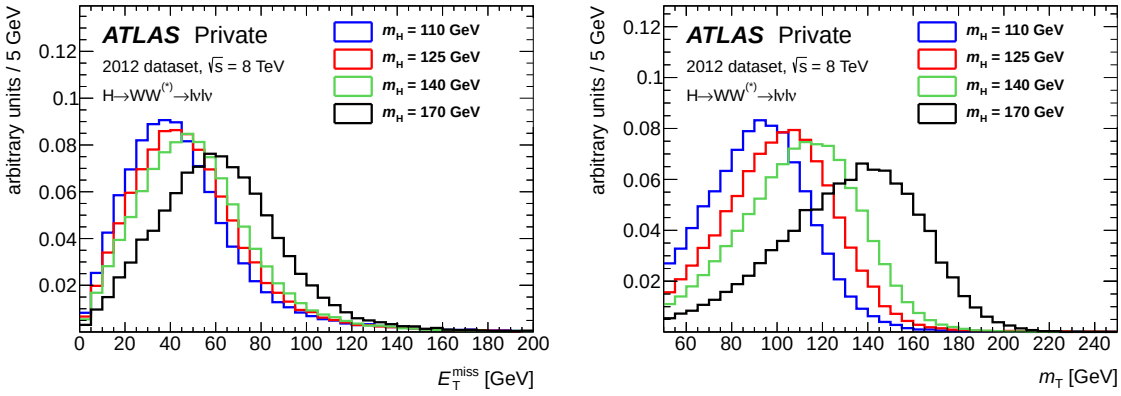

(a) $E_{\mathrm{T}}^{\mathrm{miss}}$ (b) m_{T}

Figure 4.3: Distributions of the missing transverse energy $E_{\mathrm{T}}^{\mathrm{miss}}$ (a) and the transverse mass m_{T} (b) in simulated $H \to WW^{(*)} \to \ell\nu\ell\nu$ events for different Higgs boson mass hypotheses. The distributions are normalized to unit area individually.

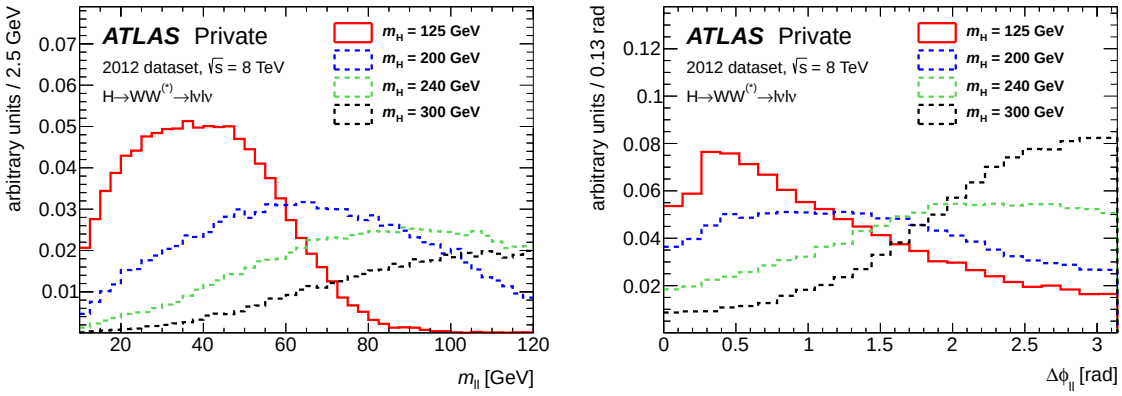

(a) $m_{\ell\ell}$ (b) $\Delta\phi_{\ell\ell}$

Figure 4.4: Distributions of the invariant mass $m_{\ell\ell}$ of the two charged leptons (a) and their azimuthal separation angle $\Delta\phi_{\ell\ell}$ (b) in simulated $H \to WW^{(*)} \to \ell\nu\ell\nu$ events for different Higgs boson mass hypotheses m_H. The distributions are normalized to unit area individually.

The distribution of m_{T} in simulated $H \to WW^{(*)} \to \ell\nu\ell\nu$ events for different Higgs boson mass hypotheses is shown in Figure 4.3(b).

4.1.4. Signal Event Topology

A distinctive kinematic feature of the $H \to WW^{(*)} \to \ell\nu\ell\nu$ signal is induced by the scalar (spin-0) nature of the SM Higgs boson. In the rest frame of the Higgs boson the two oppositely charged W bosons from the Higgs boson decay emerge in opposite directions with an opposite relative spin orientation due to the conservation of angular momentum. Because of the $V-A$ structure of the electroweak coupling (see Section 1.1.4), the charged leptons stemming from the W decays tend to be emitted in the same spatial direction oppositely to the two neutrinos. For low and intermediate Higgs boson masses ($m_H \lesssim 200$ GeV), this topology results in a low invariant mass $m_{\ell\ell}$ of the two charged leptons and a small azimuthal separation angle

$\Delta\phi_{\ell\ell}$ as well as large missing transverse energy $E_{\mathrm{T}}^{\mathrm{miss}}$ balancing the transverse momentum $p_{\mathrm{T}}^{\ell\ell}$ of the dilepton system. Figure 4.4 displays the distributions of $m_{\ell\ell}$ and $\Delta\phi_{\ell\ell}$ in simulated $H \to WW^{(*)} \to \ell\nu\ell\nu$ events for different Higgs boson mass hypotheses.

4.1.5. Accompanying Jets

For any Higgs boson mass m_H the predominant Higgs boson production mechanism in pp collisions at the LHC is the gluon fusion mode (see also Section 3.1), which does not involve final state objects in addition to the Higgs boson decay objects. However, due to initial state radiation or multiple pp collisions (pile-up events), a $H \to WW^{(*)} \to \ell\nu\ell\nu$ event may be accompanied by additional hard jets. If the Higgs boson is produced in the vector-boson fusion mode additional hard jets are expected from the quarks that radiated off the vector bosons, which finally produce the Higgs boson. Figure 4.5 shows the distributions of the number of accompanying jets in simulated $H \to WW^{(*)} \to \ell\nu\ell\nu$ events for $m_H = 125$ GeV in the gluon fusion and the vector-boson fusion production modes. According to the number n of reconstructed jets accompanying the event, the corresponding final state category is referred to as "$H + n$ jets" (see Table 4.3).

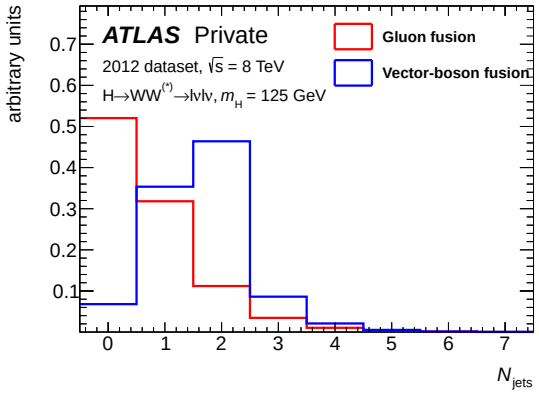

Figure 4.5: Distributions of the number of accompanying jets in simulated $H \to WW^{(*)} \to \ell\nu\ell\nu$ events for $m_H = 125$ GeV in different Higgs boson production mechanism. Jets are selected according to the jet selection criteria described in Section 7.1.3. The distributions are normalized to unit area individually.

Final state	Referred to as
$\ell^{\pm}\ell'^{\mp} + 0$ jets	$H + 0$ jets
$\ell^{\pm}\ell'^{\mp} + 1$ jets	$H + 1$ jet
$\ell^{\pm}\ell'^{\mp} + \geq 2$ jets	$H + 2$ jets

Table 4.3: Overview of the distinct final states of the $H \to WW^{(*)} \to \ell\nu\ell\nu$ analysis distinguished according to the number of reconstructed jets. The expected momentum imbalance ($E_{\mathrm{T}}^{\mathrm{miss}}$) is not listed explicitly.

4.2. Backgrounds to $H \to WW^{(*)} \to \ell\nu\ell\nu$ Searches

Several well-established SM processes can either mimic the signature of or even have exactly the same final state as the $H \to WW^{(*)} \to \ell\nu\ell\nu$ signal process, which contains two isolated,

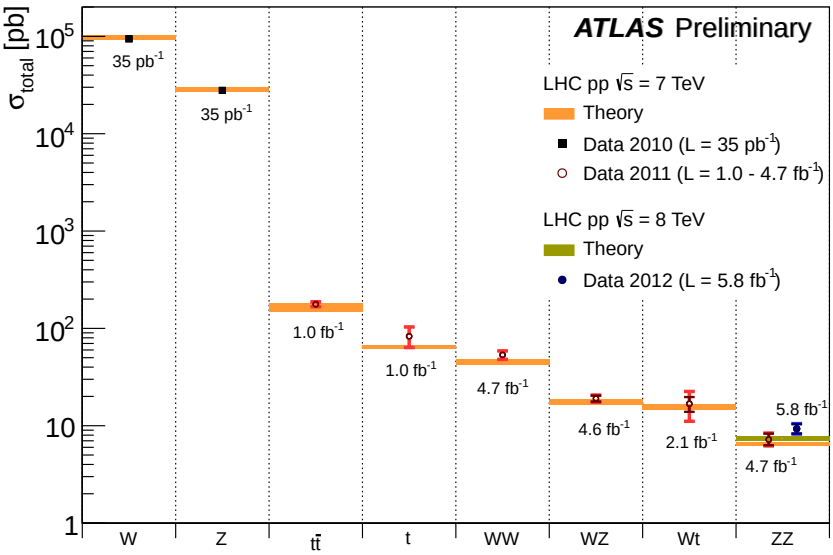

Figure 4.6: Summary of total production cross section measurements and corresponding theoretical predictions at the LHC for several SM processes that contribute as backgrounds to the $H \to WW^{(*)} \to \ell\nu\ell\nu$ analysis (taken from Ref. [74]).

oppositely charged leptons with large transverse momenta and a neutrino/anti-neutrino pair leading to missing transverse energy. Processes other than the signal but having the same final state are referred to as *irreducible backgrounds*. Furthermore, detector effects like a finite resolution of the measurement of important quantities or the limited geometric coverage of the device as well as additional activity arising from pile-up events may flaw an accurate reconstruction of objects associated to the interaction of interest, possibly resulting in a misinterpretation of the true final state. In this way, a process with a signature being different from the one of the signal still can look similar to the latter. In the context of the analysis, processes of these kind are referred to as *reducible backgrounds*. By all means, both types of processes give rise to backgrounds to the Higgs boson search in the $H \to WW^{(*)} \to \ell\nu\ell\nu$ channel and their contributions need to be understood with sufficient accuracy.

Figure 4.6 presents a summary of the total production cross sections of several SM processes at the LHC that contribute as backgrounds to the $H \to WW^{(*)} \to \ell\nu\ell\nu$ analysis. The largest cross sections are featured by the inclusive W and Z boson production which can contribute through the mis-measurement of the missing transverse energy or the misidentification of an accompanying jet as an additional lepton, respectively. Top quark related processes and the pair production of vector bosons, in particular the production of a WW pair, contribute through genuine isolated high-p_{T} leptons and missing transverse energy.

The following sections provide a summary of the individual processes, their properties and the mechanisms responsible for a contribution to the $H \to WW^{(*)} \to \ell\nu\ell\nu$ background. The MC generators used to model the backgrounds are outlined in Chapter 5 and the techniques employed to estimate and suppress their contribution are detailed in Chapters 7 and 8.

4.2.1. Standard Model WW Production

One of the most important background processes to Higgs boson searches in the $H \to WW^{(*)} \to \ell\nu\ell\nu$ channel is the SM production of an oppositely charged WW pair, which at the LHC predominantly proceeds through the annihilation of quark/anti-quark pairs ($q\bar{q} \to WW$)

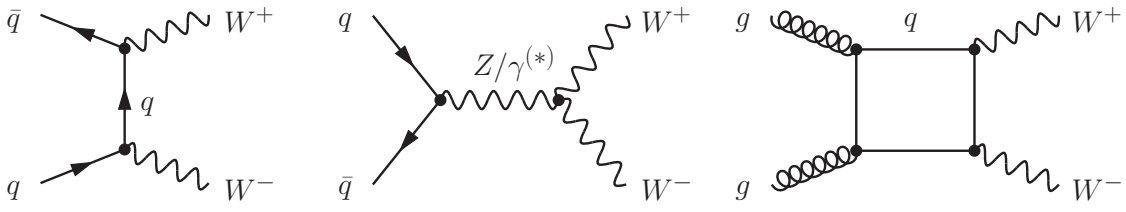

Figure 4.7: Representative Feynman diagrams illustrating the SM production of WW pairs in pp collisions at the LHC.

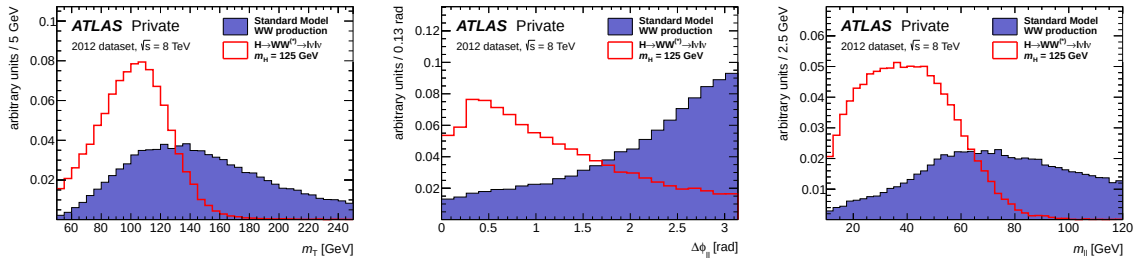

(a) m_{T} (b) $\Delta\phi_{\ell\ell}$ (c) $m_{\ell\ell}$

Figure 4.8: Distributions of the transverse mass m_{T} (a), the azimuthal separation angle $\Delta\phi_{\ell\ell}$ between the two charged leptons (b) and their invariant mass $m_{\ell\ell}$ (c) of the SM WW background. The expected distributions of the $H \to WW^{(*)} \to \ell\nu\ell\nu$ signal for $m_H = 125$ GeV are superimposed as red histograms. The distributions are normalized such that the SM WW background as well as the $H \to WW^{(*)} \to \ell\nu\ell\nu$ signal contributions correspond to unit area.

or through gluon-induced processes ($gg \to WW$). Both the quark and the gluon-initiated production have resonant as well as non-resonant contributions. Figure 4.7 shows several representative Feynman diagrams contributing to the SM WW production at the LHC.

The total inclusive production cross section of a WW pair at the LHC at a center-of-mass energy of $\sqrt{s} = 7$ TeV has been measured[3] to be $\sigma^{\mathrm{tot}}_{WW} = 54.4 \pm 4.0(\mathrm{stat.}) \pm 3.9(\mathrm{syst.}) \pm 2.0(\mathrm{lumi.})$ pb [75]. Applying the $WW \to \ell\nu\ell\nu$ branching ratio of 4.67 % (see Table 4.1) results in an expected cross section of the order of $\sigma^{\mathrm{tot}}_{WW} \cdot \mathrm{BR}(WW \to \ell\nu\ell\nu) \simeq 2.5$ pb contributing to the $H \to WW^{(*)} \to \ell\nu\ell\nu$ channel. Theoretical calculations at next-to-leading order (NLO) yield an expected increase of the total SM WW production cross section of approximately 22 % by going from a center-of-mass energy of $\sqrt{s} = 7$ TeV to $\sqrt{s} = 8$ TeV.

While the SM WW production is an irreducible background, the kinematic properties of the final state objects are different compared to the ones arising from Higgs boson decays which have imprinted the characteristics of the resonant WW production through a scalar particle. Figure 4.8 shows the distributions of the transverse mass m_{T}, the opening angle $\Delta\phi_{\ell\ell}$ between the two charged leptons and their invariant mass $m_{\ell\ell}$ for the SM WW background as well as for the $H \to WW^{(*)} \to \ell\nu\ell\nu$ signal process with $m_H = 125$ GeV. The $\Delta\phi_{\ell\ell}$ and the $m_{\ell\ell}$ distributions clearly exhibit the features of the different production mechanisms.

In principle one has to consider interference effects between the SM WW production and the one through a Higgs boson. In the case of gluon-initiated WW production the effect has been shown to affect the number of expected Higgs boson signal events of the order of

[3] The influence of a potential contribution from a SM Higgs boson has been shown to be small (see Ref. [75]).

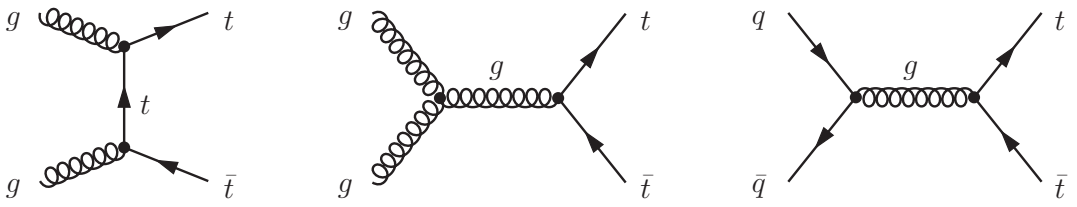

(a) Top quark pair production

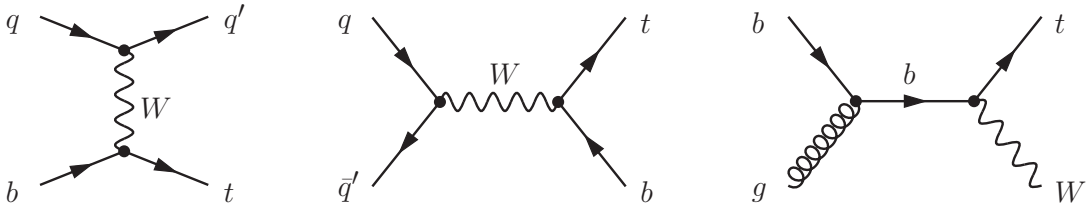

(b) Single top quark production

Figure 4.9: Representative leading order Feynman diagrams of the major top quark production mechanisms in pp collisions at the LHC. (a) Production of top quark pairs ($t\bar{t}$). (b) Production of single top quarks in association with other quarks or a W boson ($tq'/tb/Wt$).

10 % for Higgs boson masses below 500 GeV [76]. However, this effect is not included in the simulation of the $H \to WW^{(*)} \to \ell\nu\ell\nu$ signal process and is neglected in the following since it has been found to have a marginal impact on the final result [25].

4.2.2. Top Quark Production

Top quarks may either be produced in pairs ($t\bar{t}$ production) or singly in association with a W boson or other quarks (single top production). Figure 4.9 displays representative Feynman diagrams of the most important production mechanisms of top quarks in pp collisions at the LHC. The top quark pair production proceeds through the annihilation of a quark/anti-quark pair or through gluon-initiated processes with the latter dominating by far. Single top quarks can be produced by three different mechanisms with a W boson either in the t-channel, the s-channel or produced in association with the top quark.

A top quark decays into a W boson and a b-quark ($t \to Wb$) with a branching ratio of approximately 0.99 [29]. Thus, the combination of production and decay modes related to top quarks prevalently involves two W bosons similarly to the $H \to WW^{(*)}$ signal process. The background contribution arising from top quark related processes is collectively referred to as *top background*.

The total top quark pair production cross section at the LHC at a center-of-mass energy of $\sqrt{s} = 7$ TeV has been measured to be $\sigma_{t\bar{t}}^{\text{tot}} = 176 \pm 5(\text{stat.})\,^{+14}_{-11}(\text{syst.}) \pm 8(\text{lumi.})$ pb [77], whereas the single top quark production cross sections have been measured to be $\sigma_t^{\text{tot}}(t\text{−channel}) = 83 \pm 4(\text{stat.})\,^{+20}_{-19}(\text{syst.})$ pb for the t-channel production [78], $\sigma_{Wt}^{\text{tot}} = 16.8 \pm 2.9(\text{stat.}) \pm 4.9(\text{syst.})$ pb for the associated Wt production [79] and $\sigma_t^{\text{tot}}(s\text{−channel}) < 26.5$ pb at 95 % CL for the s-channel production [80], respectively.

The QCD nature of the top quark production as well as the accompanying b-quarks pro-

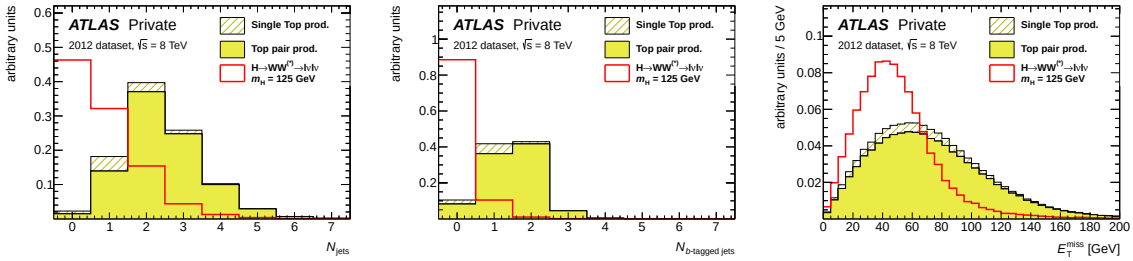

(a) N_{jets} (b) $N_{\text{jets}}^{b-\text{tagged}}$ (c) $E_{\text{T}}^{\text{miss}}$

Figure 4.10: Distributions of the number of reconstructed jets N_{jets} (a), the number of b-tagged jets $N_{\text{jets}}^{b-\text{tagged}}$ (b), and the missing transverse energy $E_{\text{T}}^{\text{miss}}$ (c) of the top quark related background. Jets are reconstructed and b-tagged according to the criteria outlined in Sections 7.1.3 and 7.1.4, respectively. The relative contributions from single top quark and top quark pair production are drawn to their true scale. The expected distributions for the $H \to WW^{(*)} \to \ell\nu\ell\nu$ signal for $m_H = 125$ GeV are superimposed as red histograms. The distributions are normalized such that the total top background as well as the $H \to WW^{(*)} \to \ell\nu\ell\nu$ signal contributions correspond to unit area.

duced in the top quark decay lead to a significant hadronic jet activity in the event. Figure 4.10 shows the distributions of the number of reconstructed jets N_{jets}, the number of b-tagged jets $N_{\text{jets}}^{b-\text{tagged}}$ and the missing transverse energy $E_{\text{T}}^{\text{miss}}$ for the top background and the $H \to WW^{(*)} \to \ell\nu\ell\nu$ signal with $m_H = 125$ GeV. Jets are reconstructed and b-tagged according to the criteria outlined in Sections 7.1.3 and 7.1.4, respectively.

4.2.3. Z /γ^*+ jets Production

Two isolated, oppositely charged leptons with large transverse momenta naturally arise from the SM *Drell-Yan* process as well as from the leptonic decay of a Z boson produced in association with jets (referred to as Z + jets production). Figure 4.11 shows representative Feynman diagrams of the main production mechanisms at the LHC. Being measured to be of the order of one nanobarn for each lepton flavor at the LHC at a center-of-mass energy of $\sqrt{s} = 7$ TeV, the total leptonic production cross section $\sigma_{Z/\gamma^*}^{\text{tot}} \cdot \text{BR}(\text{Z}/\gamma^* \to \ell\ell)$ [81] is very large compared to the signal process and even to other backgrounds.

One of the most prominent features of the Z + jets production process is the peak in the spectrum of the invariant mass $m_{\ell\ell}$ of the two charged leptons, which is located at the mass of the Z boson (see Figure 4.12(a)).

The Z + jets processes with the Z boson decaying into electrons or muons have no intrinsic missing transverse energy and consequently should not fulfill the selection criteria of the $H \to WW^{(*)} \to \ell\nu\ell\nu$ final state. However, they can still contribute to $H \to WW^{(*)} \to \ell\nu\ell\nu$ backgrounds if the event is accompanied by a false signature of a transverse momentum imbalance. Such a signature can be induced by the mis-measurement of the transverse energies of real final state objects originating from the hard interaction or by spuriously including energy depositions originating from pile-up events or other sources not related to the hard interaction. The overall effect is a deterioration of the resolution of the missing transverse energy measurement. Figures 4.12(b) and (c) show the distributions of the missing transverse energy $E_{\text{T},x}^{\text{miss}}$ along the x-axis of the ATLAS detector and the magnitude $E_{\text{T}}^{\text{miss}}$ of the total missing transverse energy, respectively, for the $(Z/\gamma^* \to ee, \mu\mu)$+jets processes. While $E_{\text{T},x}^{\text{miss}}$

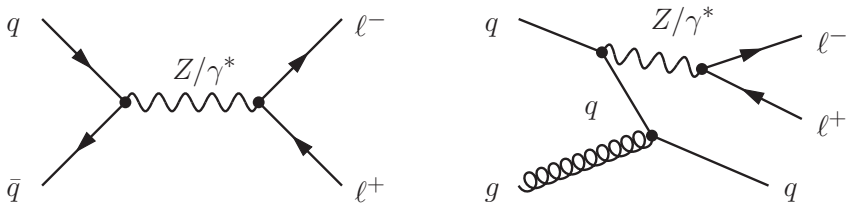

Figure 4.11: Representative Feynman diagrams of Drell-Yan charged lepton pair and $Z/\gamma^* +$ jets production in pp collisions at the LHC.

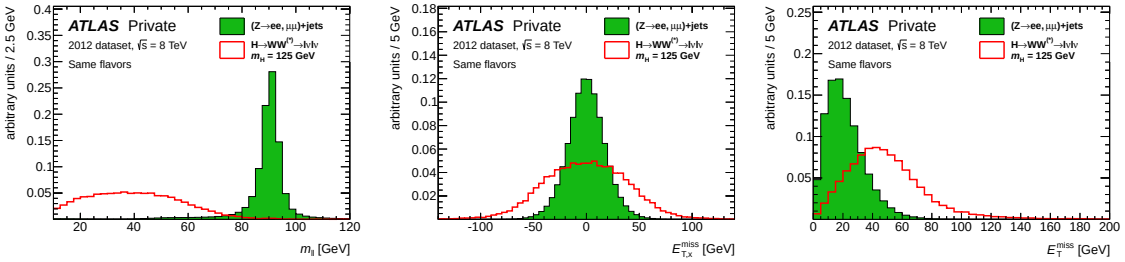

(a) $m_{\ell\ell}$ (b) $E_{\mathrm{T},x}^{\mathrm{miss}}$ (c) $E_{\mathrm{T}}^{\mathrm{miss}}$

Figure 4.12: Distributions of the invariant mass $m_{\ell\ell}$ of the two charged leptons (a), the missing transverse energy $E_{\mathrm{T},x}^{\mathrm{miss}}$ along the x-axis of the ATLAS detector (b), and the magnitude $E_{\mathrm{T}}^{\mathrm{miss}}$ of the total missing transverse energy (c) of the $(Z/\gamma^* \to ee, \mu\mu)$+jets background. The expected distributions for the $H \to WW^{(*)} \to \ell\nu\ell\nu$ signal for $m_H = 125$ GeV are superimposed as red histograms. The distributions are normalized such that the $(Z/\gamma^* \to ee, \mu\mu)$+jets background as well as the $H \to WW^{(*)} \to \ell\nu\ell\nu$ signal contributions correspond to unit area.

is centered around zero GeV with a width of approximately 20 GeV caused by the finite resolution, $E_{\mathrm{T}}^{\mathrm{miss}}$ has its maximum shifted towards a value around 15 to 20 GeV.

The $Z/\gamma^* +$ jets background mainly affects the same lepton flavor final states ($ee\nu\nu$ and $\mu\nu\mu\nu$) but can also lead to opposite lepton flavor final states through the decay of two τ-leptons originating from the Z decay ($Z \to \tau\tau \to ee\nu\nu\mu\nu\nu$). Since the decay of τ-leptons involves final state neutrinos it gives rise to true missing transverse energy, which, however, is small because the neutrinos from the τ-lepton decays tend to be back-to-back.

4.2.4. W+jets Production

At the LHC, W bosons are copiously produced in association with jets (in the following referred to as $W +$ jets production). Figure 4.13 shows representative Feynman diagrams of this process. Unlike other backgrounds, the $W +$ jets process does not feature two isolated high-p_{T} leptons. However, $W +$ jets events can still contribute to the $\ell\nu\ell\nu$ final state if the W boson decays leptonically and an accompanying jet is misidentified as the second lepton. The misidentification rate strongly depends on the isolation[4] requirement imposed on the reconstructed lepton. Even though it is rather small[5], the large production cross section, which has been measured to be of the order of $\sigma_{W^\pm}^{\mathrm{tot}} \cdot \mathrm{BR}(\mathrm{W} \to \ell\nu) \simeq 10$ nb for each lepton flavor at the LHC at a center-of-mass energy of $\sqrt{s} = 7$ TeV [81], can result in a significant

[4]The isolation quantifies additional energy depositions in a cone around the reconstructed object (see also Section 2.3.2).

[5]It has been estimated to be on average of the order of 10^{-4} for electrons [49].

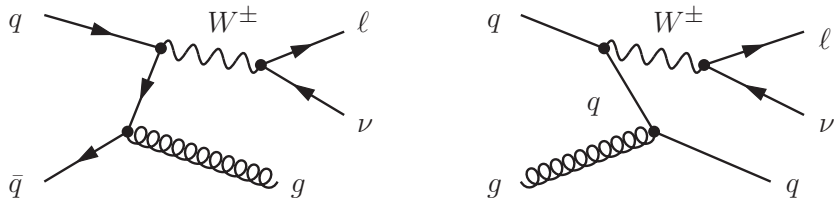

Figure 4.13: Representative Feynman diagrams of the production of a W boson in association with a quark or a gluon inducing a jet in pp collisions at the LHC.

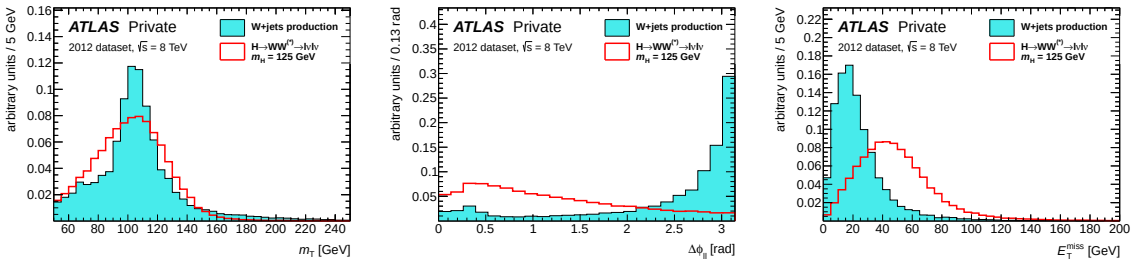

(a) m_{T} (b) $\Delta\phi_{\ell\ell}$ (c) $E_{\mathrm{T}}^{\mathrm{miss}}$

Figure 4.14: Distributions of the transverse mass m_{T} (a), the azimuthal separation angle $\Delta\phi_{\ell\ell}$ between the two reconstructed leptons (b), and the missing transverse energy $E_{\mathrm{T}}^{\mathrm{miss}}$ (c) of the $W+$jets background. The expected distributions for the $H \to WW^{(*)} \to \ell\nu\ell\nu$ signal for $m_H = 125$ GeV are superimposed as red histograms. The distributions are normalized such that the $W+$jets background as well as the $H \to WW^{(*)} \to \ell\nu\ell\nu$ signal contributions correspond to unit area.

number of $W+$jets events passing the final $H \to WW^{(*)} \to \ell\nu\ell\nu$ selection.

Figure 4.14 shows the distributions of the transverse mass m_{T}, the azimuthal separation angle $\Delta\phi_{\ell\ell}$ between the two reconstructed leptons and the missing transverse energy $E_{\mathrm{T}}^{\mathrm{miss}}$ of the $W+$jets background. The transverse mass in $W+$jets events shows a distribution very similar in shape to that of the expected signal from a $m_H = 125$ GeV Higgs boson. Since the $W+$jets background is subject to large systematic uncertainties, its contribution has to be suppressed as much as possible in order to retain a sensible low mass Higgs boson sensitivity.

4.2.5. Standard Model WZ/ZZ/Wγ Production

Apart from WW pairs, boson pair production involves WZ, ZZ and $W\gamma^{(*)}$ processes (referred to as *diboson* processes). The total WZ production cross section $\sigma_{WZ}^{\mathrm{tot}}$ at the LHC at a center-of-mass energy of $\sqrt{s} = 7$ TeV has been measured to be of the order of $\sigma_{WZ}^{\mathrm{tot}} = 19.0^{+1.4}_{-1.3}(\mathrm{stat.}) \pm 0.9(\mathrm{syst.}) \pm 0.4(\mathrm{lumi.})$ pb [82], whereas under the same conditions the total cross section of on-shell ZZ production has been measured to be $\sigma_{ZZ}^{\mathrm{tot}} = 8.5^{+2.7}_{-2.3}(\mathrm{stat.})^{+0.4}_{-0.3}(\mathrm{syst.}) \pm 0.3(\mathrm{lumi.})$ pb [83]. Furthermore, the $W\gamma$ cross section defined in a fiducial region in the $\ell\nu\gamma$ final state with certain kinematic requirements has been measured to be of the order of $\sigma_{W\gamma}^{\mathrm{fid}} \simeq 3.3$ pb for each lepton flavor [84].

The WZ and ZZ processes potentially feature the signature of the $\ell\nu\ell\nu$ final state through the leptonic decay of the W and Z bosons. The $W\gamma^{(*)}$ can contribute to $H \to WW^{(*)} \to \ell\nu\ell\nu$ backgrounds if the photon converts into an electron-positron pair. Like the $W+$jets process, the $W\gamma^{(*)}$ process has a transverse mass shape which is very similar to the one of the $H \to WW^{(*)} \to \ell\nu\ell\nu$ signal after the final event selection.

5 Data and Monte Carlo Samples

The search for the SM Higgs boson in the $H \to WW^{(*)} \to \ell\nu\ell\nu$ channel as it is presented in this thesis is using experimental input from the ATLAS detector at the LHC to take its share in the answer to the question of the existence or non-existence of the Higgs boson. In order to compare the observations with the expectations from hypotheses either including or excluding the SM Higgs boson detailed Monte Carlo (MC) simulations of the relevant physics processes as well as the corresponding detector response have to be performed. Furthermore, the determination and definition of effective selection criteria to extract the hypothetical $H \to WW^{(*)} \to \ell\nu\ell\nu$ signal events is based on MC simulations.

Sections 5.1 and 5.2 of this chapter provide a summary of the experimental as well as the corresponding simulated data the analysis is based on. The section about the simulation also covers corrections applied by means of dynamically reweighting MC events to attain agreement of certain important distributions with an appropriate predefined reference.

In the following, the abstract term *data* denotes real physics events recorded with the ATLAS detector, whereas *dataset* denotes a conceptional set of events including both real data and the corresponding MC events generated in dedicated simulations. *Data sample* and *Monte Carlo sample* are used to denominate a certain subset of real data events or MC events, respectively.

5.1. Data Samples

The analysis is based on proton-proton (pp) collision data recorded in the years 2011 and 2012 with the ATLAS detector at the LHC. The machine has been operated at a center-of-mass energy of $\sqrt{s} = 7$ TeV and $\sqrt{s} = 8$ TeV in 2011 and 2012, respectively. Figure 5.1 shows the cumulative luminosity delivered to and recorded by the ATLAS experiment during this period of time. In 2011, between March and October, the ATLAS experiment recorded 5.25 fb^{-1} of pp collision data, corresponding to 93.6 % of the total integrated luminosity delivered by the LHC. In 2012, the ATLAS experiment achieved to record 6.3 fb^{-1} between April and June, corresponding to a data taking efficiency of 94.7 %. The analysis presented in this thesis is based on both the full data taken in 2011 and the data taken in 2012 between April and June.

The data taking is split into several *periods* which reflect different LHC and ATLAS detector operation conditions. The 2011 data is split into eleven periods (B to M), whereas the 2012 data considered in this thesis is split into two periods (A and B).

The search in the $H \to WW^{(*)} \to \ell\nu\ell\nu$ decay mode directly relies on electrons, muons, jets, and missing transverse energy, requiring virtually every subcomponent of the ATLAS detector to operate properly during data taking. Data runs impaired by an unacceptable malfunction of the detector have to be excluded in physics analyses in order to ensure the reliability of the reconstructed physical objects. The data quality, affected by detector defects, is monitored by a dedicated sub-group within the ATLAS experiment providing results by means of a list of *good runs* [86]. Certainly, the exclusion of data runs on the basis of quality

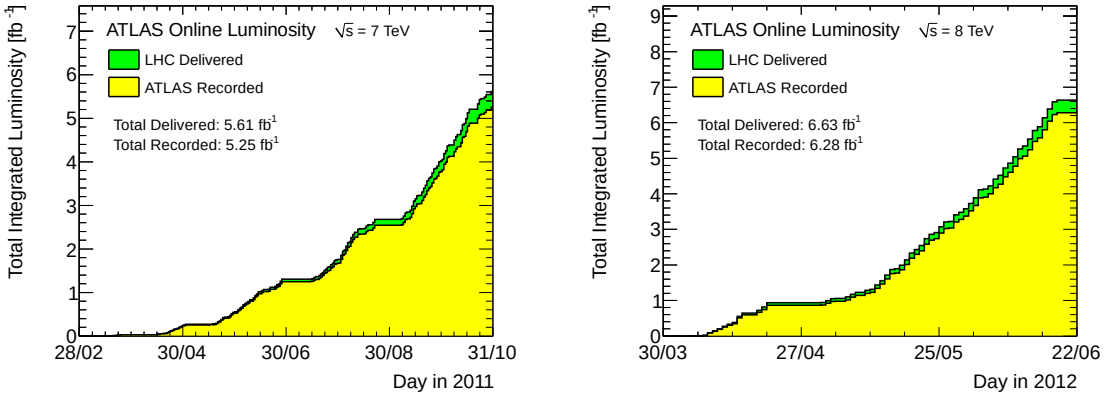

(a) 2011, $\sqrt{s} = 7$ TeV (b) 2012, $\sqrt{s} = 8$ TeV

Figure 5.1: Cumulative luminosity versus day delivered to (green), and recorded by (yellow) the ATLAS experiment during stable beams and for pp collisions at a center-of-mass energy of $\sqrt{s} = 7$ TeV in 2011 (a) and at a center-of-mass energy of $\sqrt{s} = 8$ TeV in 2012 (b). The analysis presented in this thesis is based on both the full data taken in 2011 and the data taken in 2012 between April and June. The plots are taken from the public luminosity web page of the ATLAS experiment [85].

requirements results in a reduction of the total integrated luminosity available for analysis compared to the one initially recorded.

After the application of data quality requirements the 2011 data used in the $H \to WW^{(*)} \to \ell\nu\ell\nu$ analysis is equivalent to the one published in Ref. [24] corresponding to an integrated luminosity of $\mathcal{L} = 4.7$ fb^{-1}. The 2012 data used is equivalent to the one published in Ref. [25] and corresponds to an integrated luminosity of $\mathcal{L} = 5.8$ fb^{-1}. Table 5.1 summarizes the data samples recorded with the ATLAS detector and used in the analysis.

Data year / period	Peak Instantaneous Luminosity [cm^{-2}s^{-1}]	Integrated Luminosity
2011 ($\sqrt{s} = 7$ TeV)		**Total $\mathcal{L} = 4.7$ fb^{-1}**
B to K	$\mathcal{O}(1 \cdot 10^{33})$	$\mathcal{L} = 2.1$ fb^{-1}
L, M	$\mathcal{O}(4 \cdot 10^{33})$	$\mathcal{L} = 2.6$ fb^{-1}
2012 ($\sqrt{s} = 8$ TeV)		
A, B	$\mathcal{O}(7 \cdot 10^{33})$	$\mathcal{L} = 5.8$ fb^{-1}

Table 5.1: Summary of the data samples recorded with the ATLAS detector and used in the analysis after the application of data quality requirements.

Apart from the moderate increase of the center-of-mass energy from 7 TeV to 8 TeV, the LHC delivered a significantly higher instantaneous luminosity in 2012 compared to 2011. This fact is reflected in a higher number of interactions simultaneously taking place during one bunch crossing, which in turn yields a higher number of reconstructed primary interaction vertices N_{vxp} in a single event. Figure 5.2 shows the distributions of both the mean number of interactions per crossing as well as the number of reconstructed vertices N_{vxp} in events of the 2011 and the 2012 data. Vertices are reconstructed and selected as described in Section 2.3.1 and the corresponding distributions comprise events which have passed the object selection

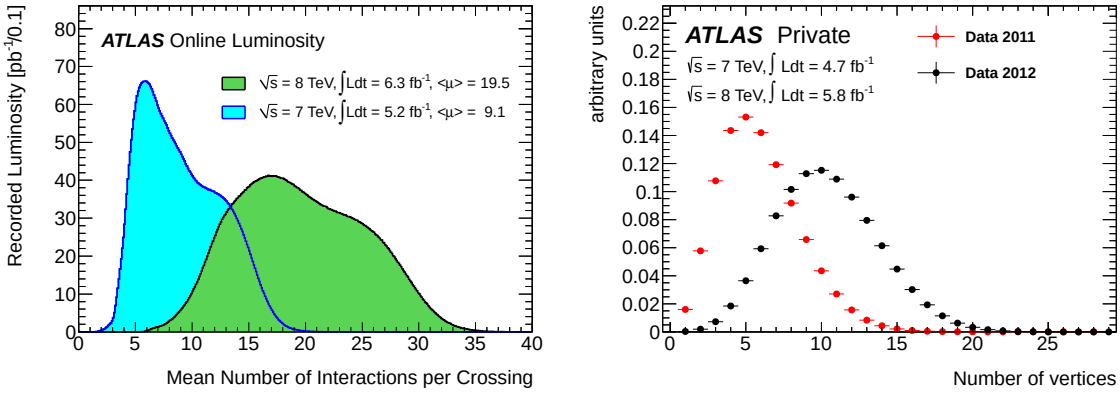

(a) $\langle\mu\rangle$ (b) N_{vxp}

Figure 5.2: (a) Luminosity weighted distributions of the mean number $\langle\mu\rangle$ of interactions per crossing for the full set of 2011 data and the 2012 data accumulated between April and June (taken from Ref. [85]). (b) Normalized distribution of the number of reconstructed primary interaction vertices N_{vxp} in events of the 2011 (red markers) and the 2012 (black markers) data. Vertices are reconstructed and selected as described in Section 2.3.1 and the events making up these distributions have passed the object selection criteria as described in Section 7.1 and the event preselection as described in Section 7.2.1 up to the requirement of two oppositely charged leptons.

criteria as described in Section 7.1 and the event preselection as described in Section 7.2.1 up to the requirement of two oppositely charged leptons.

5.2. Monte Carlo Samples

The determination of the properties and relative yields of signal and background events is based on MC simulation which involves a detector simulation and the default reconstruction and identification algorithms. Depending on the physics process different MC event generators are employed and interfaced to dedicated showering and hadronization programs. The overall normalization is calculated from theoretical cross sections which are given as external parameters. A comprehensive summary of the MC generators and the corresponding cross sections is given in Table 5.2. In some cases simulated MC events are weighted (*reweighted*) in order to force certain distributions to agree with an appropriate reference. A reweighting is not supposed to change the estimated event yield unless the event acceptance depends either on the quantity subject to the reweighting or on a quantity correlated with the latter. An important example for a reweighting applied to every MC sample is the *pile-up reweighting* which is explained in Section 5.2.3.

5.2.1. $H \to WW^{(*)} \to \ell\nu\ell\nu$ Signal Samples

In the event simulation the $H \to WW^{(*)} \to \ell\nu\ell\nu$ signal process is split into the four major SM Higgs boson production mechanisms at the LHC. The ggF process $gg \to H$ as well as the VBF process $qq' \to qq'H$ are modeled using Powheg [87, 88] interfaced to Pythia [42] (Pythia8 [43]) for showering and hadronization, where Pythia is used for the 2011 dataset and Pythia8 for the 2012 dataset. The Higgs-strahlung processes $qq' \to WH, ZH$ (denoted as WH/ZH) are modeled entirely using Pythia or Pythia8 for event generation, showering and hadronization. In the case of the ggF process the spectrum of the transverse momentum

of the Higgs boson is reweighted to agree with the prediction from HqT [89]. The theoretical cross sections used to normalize the expected signal event yields are taken from Ref. [90] and subsequent updates.

The calculation of the signal cross sections include higher-order corrections up to next-to-next-leading order (NNLO) in QCD [91–96], QCD soft-gluon resummations up to next-to-next-to-leading logarithm (NNLL) [97] and next-to-leading order (NLO) electroweak radiative corrections [98, 99] for the ggF process. These calculations, assuming factorization between the QCD and the electroweak corrections, are detailed in Refs. [100–102] and updated in Refs. [103, 104] for a center-of-mass energy of $\sqrt{s} = 8$ TeV. For the 2012 dataset, the effects of finite quark masses [105] in the loop of the ggF production mode are taken into account as well. For the VBF process approximate NNLO QCD corrections [106] as well as full NLO QCD and electroweak corrections [107–109] enter the calculation of the cross section. The cross sections of the WH/ZH processes are calculated including corrections up to NNLO in QCD [110, 111] as well as NLO electroweak corrections [112]. The Higgs boson branching ratios are calculated using Hdecay [113]. Uncertainties on the Higgs boson production cross sections are assessed following the recommendations described in Ref. [90] and are treated as systematic uncertainties as described in Sections 7.4 and 7.5.1.

5.2.2. Background Samples

Depending on the physics process the modeling of backgrounds is performed by different event generators. The production of leptonically decaying single gauge bosons in association with jets ($W+$jets and Z/γ^*+jets) is simulated using Alpgen [114] interfaced for hadronization to Pythia for the 2011 dataset and to Herwig [115] for the 2012 dataset. Here and in the following Jimmy [116] is used for the simulation of the underlying event whenever Herwig is used for hadronization. The MLM matching scheme [117] is used to combine samples with different final state parton multiplicities. The Z/γ^*+jets samples are generated for invariant dilepton masses exceeding 10 GeV. Since the estimation of the $W+$jets contribution to the $H \to WW^{(*)} \to \ell\nu\ell\nu$ analysis is performed using a data-driven technique (see Section 7.3.1), the $W+$jets MC samples are only used for cross checking purposes.

The top quark pair production ($t\bar{t}$) as well as the quark-induced SM WW production ($q\bar{q}/qg \to WW$) are modeled using MC@NLO [44] interfaced to Herwig for hadronization. The gluon-induced SM WW production ($gg \to WW$) is modeled using GG2WW [118], likewise interfaced to Herwig. For the 2011 dataset, the single top quark production is simulated with AcerMC [119] and Pythia for hadronization. For the 2012 dataset, the s-channel and the single top quark production in association with a W boson are modeled using MC@NLO interfaced to Herwig, while the t-channel single top quark production is still modeled using AcerMC, but interfaced to Pythia8.

The $W(\to \ell\nu)\gamma$ background is modeled using Alpgen interfaced to Herwig and kinematic criteria are applied in the generation of this process. The photon must have a transverse momentum p_{T} exceeding 10 GeV (8 GeV) and must be separated from the charged lepton by $\Delta R = \sqrt{(\Delta\eta)^2 + (\Delta\phi)^2} > 0.1$ (0.25) for the 2011 (2012) dataset. The $W(\to \ell\nu)\gamma^*(\to \ell'\ell')$ background is modeled with MadGraph [120, 121] interfaced to Pythia for hadronization. This background is generated with kinematic and geometrical requirements on the leptons as well. The $WZ^{(*)}$ process is generated with MC@NLO interfaced to Herwig for the 2011 dataset and with MadGraph interfaced to Pythia for the 2012 dataset. In the latter case MadGraph includes interference terms between $W\gamma^*$ and $WZ^{(*)}$. For the 2011 dataset the SM ZZ production is modeled with Sherpa and for the 2012 dataset with Powheg interfaced to Pythia8 for hadronization. Here, the invariant mass of the charged leptons stemming

from one Z boson is required to exceed 4 GeV in the event generation with Powheg.

The Alpgen, Sherpa, Pythia8 and MadGraph samples are generated using the CTEQ 6L1 [122] parton distribution functions (PDFs). However, the $Z/\gamma^* + \text{jets}$ samples, which are generated with Alpgen, are reweighted using the MRSTMCal PDF set [123] to improve the agreement of the lepton η distributions with the observation in data. The MRSTMCal PDF set is also used for Pythia and AcerMC samples. The CT10 PDF set [124] is used for the generation of Powheg and MC@NLO samples.

The production cross sections of single gauge bosons are calculated at NNLO using FEWZ [125] and DYNNLO [126]. The top quark pair production cross section is evaluated at approximate NNLO in QCD using Hathor [127]. The single top quark production cross sections include NNLO collinear and soft gluon corrections for the t-channel production [128], NNLL resummation of collinear and soft gluon corrections for the s-channel production [129] and approximate NNLO accuracy for the associated production of a single top quark with a W boson [130]. The diboson production cross sections are calculated at NLO using MCFM [131].

The simulation of any physics process incorporates a model of the expected pile-up conditions present during data taking (see next section). Acceptances as well as reconstruction and identification efficiencies are obtained from a full simulation of the ATLAS detector using Geant4 [45], a toolkit for the simulation of the passage of particles through matter. In the $H \to WW^{(*)} \to \ell\nu\ell\nu$ analysis corrections are applied to rectify discrepancies of reconstruction and identification efficiencies between simulation and data (see Section 7.1).

5.2.3. Pile-Up Reweighting

Given the high instantaneous luminosities at the LHC, every hard scattering event is usually overlaid by several additional pile-up events (see also Sections 1.3.4 and 5.1). A reasonable simulation of interactions in this environment has to include a proper modeling of these additional events and the resulting effect on the measurement and reconstruction of the interaction of interest. In the MC simulation pile-up events are subjoined to the hard scattering event before the detector simulation using predefined parameters. Since these pile-up parameters (mainly given by the mean number of interactions per crossing) may differ from the ones observed in data, a *pile-up reweighting* procedure is employed on MC samples to attain agreement of the pile-up description between data and simulation.

5.3. Blind Analysis

The conclusion of a scientific experiment should neither be sensitive to the individual objectives of the performing experimentalist nor to the ones of other subjects eagerly awaiting *any* result or even *one specific* outcome satisfying personal preference, confirming expectations driven by past experience or maximizing the experimentalist's fame. However, a real experiment will hardly ever comply entirely with this ideal situation. Hence, committed to scientific ideas, an experimentalist must conscientiously avoid hazarding the experiment's impartiality. Adhering to this demand becomes the more challenging the more people have an interest in the result or the more significant its impact is.

The search for the Higgs boson is an experimental effort of particular scientific importance as well as great public attention, naturally making it vulnerable to the aforesaid. Furthermore, the ATLAS experiment [3, 132] as well as the CMS experiment [4] reported first hints

of a Higgs boson-like resonance around a mass of 126 GeV in the data collected in the year 2011. In order to burke any bias in the analysis of the 2012 data, it was decided to perform the $H \to WW^{(*)} \to \ell\nu\ell\nu$ analysis in a *blind* way, such that the parameters of the analysis potentially affecting the conclusion are fixed before exploring data regions where a significant contribution from a low mass Higgs boson signal is expected [25] ("*blind analysis*"). This in particular applies to the adaptation of the event selection criteria towards an optimal signal sensitivity (*optimization*, see also Chapter 9), which has to rely entirely on MC simulation and data with a verifiably negligible signal expectation.

In practice events passing the event preselection of the $H \to WW^{(*)} \to \ell\nu\ell\nu$ analysis as described in Section 7.2.1 and additionally satisfying the following conditions are marked as *blinded*:

- Either no jet or no b-tagged jet in the event
- $m_{\ell\ell} < 50$ GeV
- $\Delta\phi_{\ell\ell} < 1.8$ rad
- 82.5 GeV $< m_{\mathrm{T}} <$ 140 GeV

Applying these blinding criteria, the residual contribution of a $H \to WW^{(*)} \to \ell\nu\ell\nu$ signal with a Higgs boson mass of $m_H = 125$ GeV to the total expected event yields has been found to be below 2 % at every stage of the event selection.

To prevent deliberate or undeliberate premature analysis of the signal enhanced regions in data, data events passing these blinding criteria are removed from the data processing chain at an early stage, whereas MC events passing the blinding criteria are marked accordingly without being removed. This allows both unconfined studies on MC simulation as well as equitable comparisons between simulation and data. Following its policy the decision to lift the restrictions of the blind analysis ("*unblinding*") is approved officially and legitimized by confirming that the data in control samples with a negligible signal contribution is described by the MC simulation to a sufficient degree. Changes to the parameters of the analysis after unblinding have to be documented in detail and must not be motivated by referring to observations potentially affected by the signal process sought after.

At the end of June 2012 the ATLAS Collaboration approved the unblinding of the opposite flavor channels of the 2012 dataset based on a good agreement of the MC simulation with the data in important control samples (see also Section 7.3). The same flavor channels receive a significantly increased Drell-Yan background in 2012 compared to 2011 which is a result of the worse resolution of the missing transverse energy measurement (see also Section 7.2.1). Since the procedures to estimate and suppress this background were not yet finished at that time and the opposite flavor channels feature the major part of the sensitivity of the $H \to WW^{(*)} \to \ell\nu\ell\nu$ search anyway, the same flavor channels were still kept blinded [25].

Process	Event generator		$\sigma \cdot$ BR [pb]	
	2011 dataset	2012 dataset	2011 dataset	2012 dataset
Signal ($\to WW \to \ell\nu\ell\nu$)			($m_H = 125$ GeV)	($m_H = 125$ GeV)
ggF	Powheg + Pythia(8)		0.347	0.442
VBF	Powheg + Pythia(8)		0.027	0.035
WH/ZH	Pythia(8)		0.020	0.025
Backgrounds				
$q\bar{q}/qg \to WW \to \ell\nu\ell\nu$	MC@NLO + Herwig		4.68	5.68
$gg \to WW \to \ell\nu\ell\nu$	GG2WW + Herwig		0.14	0.16
Top pairs ($t\bar{t}$)	MC@NLO + Herwig		167	238.1
Single top			85	116
t-channel	AcerMC + Pythia(8)			
Wt, s-channel	AcerMC + Pythia	MC@NLO + Herwig		
inclusive $W \to \ell\nu$	Alpgen + Pythia	Alpgen + Herwig	$3.2 \cdot 10^4$	$3.7 \cdot 10^4$
inclusive $Z/\gamma^* \to \ell\ell$	Alpgen + Pythia	Alpgen + Herwig	$1.5 \cdot 10^4$	$1.6 \cdot 10^4$
ZZ [$\to \ell\ell\nu\nu, \ell\ell\ell\ell$]	Sherpa	Powheg + Pythia	5.6	0.73
$WZ^{(*)}$ [$\to \ell\nu\ell\ell$]	MC@NLO + Herwig	MadGraph + Pythia	18	1.54
$W(\to \ell\nu)\gamma^*(\to \ell'\ell')$	MadGraph + Pythia		6.5	9.26
$W(\to \ell\nu)\gamma$	Alpgen + Herwig		345	369

Table 5.2: Summary of the MC generators used to model the signal and background processes and the corresponding cross sections used to normalize the event yields. The signal cross sections are quoted for $m_H = 125$ GeV and include the $H \to WW^{(*)} \to \ell\nu\ell\nu$ branching ratios but no branching ratios for the W and Z boson in the WH/ZH production. For the background processes, leptonic decays of W and Z bosons are always assumed, the quoted numbers include the branching ratios and are summed over lepton flavors. The exceptions are top quark production as well as WZ and ZZ production in 2011 for which inclusive cross sections are quoted. For several processes kinematic criteria are applied. The table is created from corresponding tables in Refs. [24] and [25]. For the 2012 dataset Pythia has been replaced by Pythia8 for several processes (in these cases Pythia(8) is quoted). Appropriate references for the different generators are given in the text.

6 Common Analysis Framework

This chapter presents a brief overview of the *Common Analysis Framework* (CAF), a software package developed by several members of the Higgs-to-WW sub-group of the ATLAS Collaboration. The CAF is intended to provide an official analysis tool to all analyzers involved in the $H \to WW^{(*)} \to \ell\nu\ell\nu$ analysis. It comprises several daisy-chained sub-packages, one of which, the `HWWAnalysisCode` sub-package, has been designed and developed in the scope of this thesis. The CAF has become the default analysis tool for official results and publications and thereby has to be considered as a key tool of the $H \to WW^{(*)} \to \ell\nu\ell\nu$ analysis. Preceded by a general motivation for the deployment of a common analysis software in Section 6.1, the general structure of the CAF is outlined in Section 6.2. Finally, Section 6.3 outlines design considerations and technical details of the `HWWAnalysisCode` sub-package.

6.1. Technical Aspects of Physics Analyses

Modern high-energy physics experiments tend to produce a tremendous amount of data as their detectors record the signatures of billions of fundamental physical objects produced in an even larger number of high-energy particle collisions. The efficient operation of such experiments as well as the prosperous analysis of the recorded data cannot abstain from the use of powerful computing resources and appropriate software. Apart from other developments, `ROOT` [133], an object oriented data analysis framework based on `C++`, has been developed to meet the requirements imposed by physics data analyses. It provides a comprehensive set of tools for the analysis, management and visualization of data and became the basis of data analysis software for LHC experiments as well as for other scientific data analysis purposes.

The simulation and reconstruction software used within the ATLAS experiment (see also Section 2.3) is bundled in the ATHENA framework [50]. It implements commonly used algorithms and procedures, which are to some extent specific to the ATLAS detector, and serves as a data preprocessing tool. Based on these common tools, the groups in charge of a specific analysis usually employ a redundant software setup, where each contributing institute or even every individual analyzer is working with an independent implementation of the specifics of the analysis. This approach inherently features plural cross-checks of the obtained analysis results. However, it also constitutes a vast multiplication of work and waste of manpower. Furthermore, it complicates the compilation and retraceability of the analysis documentation as well as its official presentation.

6.2. The $\mathrm{H} \to \mathrm{WW}^{(*)} \to \ell\nu\ell\nu$ Common Analysis Framework

Motivated by considerations mentioned in the previous paragraph, the Higgs-to-WW subgroup of the ATLAS Collaboration decided to centrally develop and introduce a common software setup, the *Common Analysis Framework* (CAF), providing services and tools to process the default analysis chain up to the final visualization of the results. This brings about a long list of significant benefits like an immanent consistency of the results and a

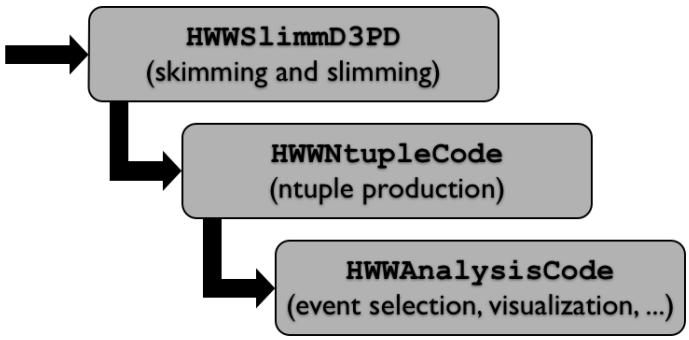

Figure 6.1: Diagram of the basic structure and processing stages of the $H \to WW^{(*)} \to \ell\nu\ell\nu$ Common Analysis Framework (see text for a detailed explanation).

welcome coherence of their presentation. Additionally, it conveniently enables newcomers to join the group and quickly contribute to the analysis. Doubtlessly, it does not abrogate the necessity of an independent setup for cross-checking purposes.

The CAF is based on the `ROOT` framework and built up of three levels consecutively processing and condensing the data. Figure 6.1 depicts the basic structure and processing stages of the CAF.

The input to the first processing stage (*skimming and slimming*, `HWWSlimmD3PD`) are the ATLAS detector physics data as well as the corresponding MC samples including the detector simulation and the reconstruction of physical objects. Since these inputs amount to bulky datasets, the purpose of this stage is a dedicated removal of dispensable information by rejecting events not conforming to basic event selection requirements and by only keeping event information essential for the subsequent analysis.

The second processing stage (*ntuple production*, `HWWNtupleCode`) performs the selection of physical objects and determines corresponding efficiency and acceptance corrections. Furthermore, it calculates quantities derived from fundamental properties associated to physical objects or events (e.g. kinematic variables like the invariant mass of a group of objects in an event). The resulting event data is stored in a matrix-like data structure (referred to as *ntuple*), where individual events correspond to the rows and event and object quantities correspond to the columns. The ntuple data storage is based on the concept of `TTree` objects introduced by the `ROOT` framework.

Based on these *common ntuples*, the third processing stage (`HWWAnalysisCode`) allows to comprehensively investigate the properties of event samples passing certain selection requirements by performing the candidate event selection, incorporating data-driven background estimates, and providing easy-to-use functionality to plot distributions of event quantities (*plots*) as well as to print out observed and expected event yields after various event selection stages (*cutflows*).

The CAF turned out to be a great success and it has been used to produce the official results for all recent publications of the ATLAS Collaboration related to the $H \to WW^{(*)} \to \ell\nu\ell\nu$ analysis (e.g. Refs. [24] and [25]) as well as for numerous internal reports and presentations within the ATLAS Collaboration.

6.3. The HWWAnalysisCode Sub-Package

The HWWAnalysisCode sub-package (referred to as the HWWAnalysisCode in the following) initially has been a private effort devised and pursued in view of the present and anticipated requirements related to this thesis. The initial demands were defined by the need for a flexible analysis software which operates on a set of event samples given by means of ROOT ntuples and which allows for almost any kind of data analysis. An integral part of this is the capability to determine expected and observed event yields for certain event selection requirements from MC and data samples, respectively, as well as to use corresponding event samples to generate histograms of quantities associated to physical objects or individual events.

A first version of the HWWAnalysisCode ready for operation has been deployed shortly before the official CAF effort emerged. During the early planning phase it has been decided to adopt this private analysis code as part of the CAF owing to its coherent and flexible design. Since its official release, the HWWAnalysisCode experienced major technical advancements. In the following, no distinction will be drawn between the private and the official development phase.

6.3.1. Design Considerations

The development of the HWWAnalysisCode was preceded by the employment of an existing analysis software with components and corresponding tasks similar to the CAF. However, it had been designed very closely following specific details of the $H \to WW^{(*)} \to \ell\nu\ell\nu$ analysis and thereby was not well suited to deal with upcoming aspects of the analysis. Based on advantages and drawbacks related to this setup, the design of the HWWAnalysisCode has been guided by several general considerations, which are summarized in the following. Given the widespread use of the ROOT analysis framework as well as its extensive scope of supply and services, it was beyond all question to build the HWWAnalysisCode on top of ROOT.

- Private analysis software is typically written in view of urgent demands and hence is not based on long-term considerations. This usually inhibits the incorporation of highly desirable software-structural properties like *flexibility*, *modularity* or a *decoupling* of general and analysis specific components. While featuring such properties is not absolutely mandatory, it certainly enhances convenience and ease of operation for the user and simultaneously allows for an efficient maintenance by developers. The latter has to be considered as a prerequisite for a long lifetime of a software project.

- Many computational challenges one faces in the context of the $H \to WW^{(*)} \to \ell\nu\ell\nu$ analysis are shared among a wide class of physics analyses. In fact, this commonality is reflected in the ROOT framework, which, however, leaves some fundamental desires unsatisfied. Even though targeting at the $H \to WW^{(*)} \to \ell\nu\ell\nu$ analysis, the HWWAnalysisCode should try to extract general concepts and implement them in an abstract way.

- Performing a physics analysis brings about numerous technical challenges the analyzer has to deal with. The HWWAnalysisCode should try to hide these issues from the user as far as possible.

- The $H \to WW^{(*)} \to \ell\nu\ell\nu$ analysis has to account for numerous different MC and data event samples, which correspond to different background and signal processes or to real data collected with the ATLAS detector. The software implementation should be independent of any detail related to the actual choice of samples for the analysis. It should instead provide configurable services to manage samples and allow for a hierarchical categorization which is reflected in the structural organization of the data storage.

- The majority of physics data analyses can be broken down into the need for event counting as well as histograms of certain properties associated to physical objects or events (*analysis objects*). Therefore, event counters and histograms constitute fundamental objects that play a central role. It is within the field of responsibility of the `HWWAnalysisCode` to master the creating of these objects, which should be organized and stored in a coherent and flexible way. Having defined a categorization of event samples (see previous item), it appears to be straightforward to adopt this categorization for the organization of associated analysis objects.
- Many parameters affecting the results of an analysis have to be specified in advance and one might be unable to infer their values from the results of the analysis alone. Since an analysis usually is iterated many times with different parameter settings, it seems highly desirable to be able to efficiently keep track of such analysis parameters. This in particular applies to results which have been or are going to be subject to a publication. In other words, the `HWWAnalysisCode` should provide an easy way to handle detailed analysis parameters in close association to the analysis results.
- In the course of an analysis one frequently has to apply temporary changes to the software, e.g. to meet the requirements related to current questions. The design of the `HWWAnalysisCode` should allow for an easy implementation of such changes without the need of an extensive re-engineering. The most favorable scenario certainly is that the majority of these changes can be covered by adapting the configuration of the software rather than the software itself. Thus, a highly configurable design is pursued.
- The analysis objects generated by the `HWWAnalysisCode` should be stored in a way avoiding limitations of flexibility which go beyond the conceptual minimum. That is, operations on analysis objects, that are computationally inexpensive but significantly confine the flexibility, should be performed as far down downstream the data processing chain as possible.

6.3.2. Implementation

Condensing the abstract considerations listed above results in the need for an efficient hierarchical data structure as well as a flexible software machinery to operate on it. The fundamental functionality of the `HWWAnalysisCode` is implemented in a `C++` *shared library*, which provides abstract services and general analysis tools. Based on this library, the actual $H \to WW^{(*)} \to \ell\nu\ell\nu$ analysis is implemented in an additional subsidiary `C++` component, which could easily be replaced to implement any other analysis.

The centerpiece of the `HWWAnalysisCode` library is a `C++` class, which recursively allows for a hierarchical organization of data in *folders*, adopting a tree-like structure. Each folder can be assigned properties (*tags*) of basic data types. Event samples are represented by specialized *sample folders*, which thereby affords to reflect an arbitrary sample categorization. Analysis objects like histograms and event counters are stored as sub-elements of these sample folders. A dedicated `C++` class provides services to read analysis objects from this data structure and perform a summation of contributions from individual samples, if requested. The presentation of histograms and tables of event counts (*cutflows*) are accomplished by flexibly configurable *plotting* and *printing* classes.

Specific analysis tasks like the generation of histograms or the counting of events are represented by *analysis jobs*, which are centrally managed and executed on a given sample folder hierarchy. Event selection requirements are represented by a dedicated `C++` class, whose instances are created from a simple definition syntax.

7 $\mathrm{H} \to \mathrm{WW}^{(*)} \to \ell\nu\ell\nu$ Analysis in the $\mathrm{H}+0$ and $\mathrm{H}+1$ Jets Channels

This chapter outlines the fundamental framework of the $H \to WW^{(*)} \to \ell\nu\ell\nu$ analysis in the $H+0$ and $H+1$ jet channels using the 2011 dataset and the 2012 dataset as defined in Chapter 5. In order to emphasize its specific characteristics, the analysis in the $H+2$ jets channel, which is geared towards Higgs boson production via vector-boson fusion rather than via gluon fusion, is covered in Chapter 8.

The first $H \to WW^{(*)} \to \ell\nu\ell\nu$ analysis undertaken with the ATLAS experiment is based on proton-proton collision data corresponding to an integrated luminosity of $\mathcal{L} = 35$ pb^{-1} collected at a center-of-mass energy of $\sqrt{s} = 7$ TeV with the ATLAS detector in the year 2010. It has been published in Ref. [134] and quotes an observed 95 % CL upper limit on the Higgs boson production cross section of 1.2 times the SM expectation at $m_H = 160$ GeV and 12.2 times the SM expectation at $m_H = 130$ GeV, being compatible with the cross section limits that are expected under the assumption of the absence of a Higgs boson signal.

The analysis presented in this thesis constitutes a follow-up of the 2010 analysis and is equivalent to the one published by the ATLAS Collaboration in Refs. [24] and [25] for the 2011 dataset and the 2012 dataset, respectively. It is based on data corresponding to an integrated luminosity of $\mathcal{L} = 4.7$ fb^{-1} and 5.8 fb^{-1} recorded at center-of-mass energies of $\sqrt{s} = 7$ TeV and 8 TeV, respectively. Apart from the considerably increased amount of data, the analysis has significantly evolved compared to the 2010 version, and major improvements related to the object and event selection as well as to the statistical methods have been incorporated. The 2011 and 2012 versions of the $H \to WW^{(*)} \to \ell\nu\ell\nu$ analysis eventually were an essential ingredient to the observation of a new particle in the search for the SM Higgs boson announced by the ATLAS Collaboration in July 2012 [8].

The $H \to WW^{(*)} \to \ell\nu\ell\nu$ analysis relies on several different physical objects like electrons, muons and jets. Their object definitions used in the context of this analysis are described in Section 7.1. Based on these object definitions, Section 7.2 describes the $H \to WW^{(*)} \to \ell\nu\ell\nu$ candidate event selection. Section 7.3 details the procedures which are used to estimate the contributions of several background processes from data. The sources and evaluation of systematic uncertainties is described in Section 7.4, which is finally followed by the presentation of the results in Section 7.5.

7.1. Trigger, Object Selection, and Efficiency Corrections

This section provides an overview of the triggers relevant for the $H \to WW^{(*)} \to \ell\nu\ell\nu$ analysis as well as the identification procedures and selection criteria applied to reconstructed physical objects before being used in the event selection. These procedures and criteria are equally applied to both the data as well as the MC simulation, which provides a detailed description of the interactions between particles and the detector. Thus, the efficiency of an object to pass the corresponding selection is expected to agree to a great extent between data and the

MC simulation. However, due to numerous influences affecting the trigger decision as well as the reconstruction and identification of physical objects, small differences may be present and appropriate *scale factors* (SFs) have to be applied to simulated MC events in order to compensate for such discrepancies. An efficiency scale factor is generally defined as the ratio of the corresponding efficiency $\varepsilon_{\text{data}}$ determined from data over the one determined using the MC simulation ε_{MC},

$$\text{SF} = \frac{\varepsilon_{\text{data}}}{\varepsilon_{\text{MC}}}.$$

An event acceptance efficiency scale factor is applied as an additional multiplicative event weight to MC events, effectively correcting the efficiency in the simulation to match the one measured in data. An object-related scale factor usually numerically depends on the kinematic properties of the object it corresponds to. Hence, the application of a correction by means of a scale factor does in most cases not only affect the overall normalization of the expected event yield but also the shape of the distributions of quantities which affect the efficiency or which are correlated with such quantities. Several scale factors have to be applied in the context of the $H \to WW^{(*)} \to \ell\nu\ell\nu$ analysis, and these are introduced in the sections covering the corresponding selections.

As already mentioned, the analysis presented in this and the following chapters is based on two different datasets corresponding to data taken in the years 2011 and 2012, respectively. With respect to the 2011 data taking period, several data processing, reconstruction and identification algorithms common to the whole ATLAS experiment have been subject to substantial changes for the 2012 data taking period. These changes are motivated by general improvements and in particular by the need to cope with the challenges posed by the altered data taking conditions in 2012. Similarly, several $H \to WW^{(*)} \to \ell\nu\ell\nu$ analysis specific object selection criteria have been changed for the analysis of the 2012 dataset with respect to the 2011 dataset. In the following, the focus will be on the joint aspects and differences will be highlighted and motivated adequately.

7.1.1. Trigger

The trigger system of the ATLAS experiment provides an comprehensive set of trigger items[1], which are based on various decision criteria (see also Section 2.2.4). The distinctive observable final state objects, which highlight the $H \to WW^{(*)} \to \ell\nu\ell\nu$ signal process out of an overwhelming number of background events in hadron collisions, are given by electrons and muons with large transverse momenta (p_{T}). Consequently, the $H \to WW^{(*)} \to \ell\nu\ell\nu$ analysis is seeded by unprescaled single-electron and single-muon triggers which are stimulated by the presence of an electron or a muon candidate that passes the *event filter*. The exact criteria triggering the recording of an event depend on the individual trigger items. The changing LHC operating conditions during 2011 and towards 2012 necessitated a gradual readjustment of the trigger criteria in order to keep the trigger rate at an acceptable level without the need of prescaling[2] the trigger. Table 7.1 summarizes the trigger items used in the $H \to WW^{(*)} \to \ell\nu\ell\nu$ analysis, broken down into the associated data taking periods.

Data taken early in the year 2011 use the "EF_e20_medium" and the "EF_mu18_MG" trigger items for electrons and muons, respectively. The trigger terminology allows to deduce the primary object triggering criteria, which are in the case of the "EF_e20_medium" trigger item

[1] In the following "trigger item" refers to one specific element of the *trigger menu*, whereas "trigger" refers to the whole trigger system of the ATLAS experiment.

[2] A trigger prescale factor of n randomly accepts events, on average every n^{th} event passing the trigger selection criteria only.

Data year / period	Electron trigger	Muon trigger
2011		
B to I	EF_e20_medium	EF_mu18_MG
J	EF_e20_medium	EF_mu18_MG_medium
K	EF_e22_medium	EF_mu18_MG_medium
L to M	EF_e22vh_medium1	EF_mu18_MG_medium
2012		
A to B	EF_e24vhi_medium1	EF_mu24i_tight
	$\vee$ EF_e60_medium1	$\vee$ EF_mu36_tight

Table 7.1: Summary of the event trigger items seeding the $H \to WW^{(*)} \to \ell\nu\ell\nu$ analysis. The analysis is based on single-electron and single-muon triggers, which have been adjusted gradually to cope with the increasing instantaneous luminosity delivered by the LHC in the course of the data taking in the years 2011 and 2012. In 2011, electrons and muons are triggered by one trigger item each, whereas in 2012 each is triggered by a logical OR of two individual trigger items. The trigger terminology allows to deduce the primary object triggering criteria. The number after "EF_e" or "EF_mu" indicates the lepton transverse momentum threshold at the event filter level. Other elements of the denotation encode additional specific trigger requirements (see text).

an electron candidate passing the "medium" electron identification criteria and having a p_{T} exceeding 20 GeV [55]. The "EF_mu18_MG" trigger item requires a muon candidate with a p_{T} exceeding 18 GeV [135].

For subsequent data taking periods in the year 2011 the trigger items "EF_e22_medium" and "EF_e22vh_medium1" are used for electrons and "EF_mu18_MG_medium" for muons. Here, the insertion "vh" in the trigger denotation indicates $|\eta|$-dependent p_{T} thresholds and a *hadronic leakage*[3] requirement at the first trigger level (L1), whereas the suffix "medium1" indicates a tightness of the electron identification criteria which is different with respect to "medium". For the muon trigger items, the suffix "medium" indicates a tightened muon p_{T} trigger threshold at L1 while the muon p_{T} threshold at the event filter has been kept constant.

Data taken in the year 2012 use a disjunction of two different trigger items with low and high p_{T} thresholds, respectively, to recover the efficiency loss at high p_{T}. Electrons are triggered by either of the two trigger items "EF_e24vhi_medium1" and "EF_e60_medium1", while muons are triggered by either of the items "EF_mu24i_tight" and "EF_mu36_tight". The insertion "i" indicates an additional requirement on the muon *track isolation* at trigger level (see also Section 2.3.3). For muons, the suffix "tight" indicates a further increased muon p_{T} trigger threshold at L1.

The trigger efficiencies of electrons [53] and muons have been determined in both data and the MC simulation using *tag-and-probe* methods, and are used to determine an event-based trigger efficiency scale factor $\mathrm{SF}_{\mathrm{Trig}}$. Since the $H \to WW^{(*)} \to \ell\nu\ell\nu$ analysis requires exactly two leptons based on single-lepton triggers either of the two leptons can provoke a trigger. The efficiency of at least one lepton triggering is given by one minus the probability that neither of the two leptons stimulates the trigger. This in turn is given by the product of $(1 - \varepsilon_i)$ for each lepton, where ε_i denotes the trigger efficiency for lepton i. Finally, one

[3] The hadronic leakage is a measure of the energy percolating the electromagnetic calorimeter and being deposited in the hadronic calorimeter.

obtains the event-based scale factor $\mathrm{SF}_{\mathrm{Trig}}$ which is calculated from leptons i selected in the analysis,

$$\mathrm{SF}_{\mathrm{Trig}} = \frac{1 - \prod_i (1 - \varepsilon_{i,\mathrm{data}})}{1 - \prod_i (1 - \varepsilon_{i,\mathrm{MC}})}. \tag{7.1}$$

7.1.2. Lepton Selection

Electrons and muons are essential physical objects for the $H \to WW^{(*)} \to \ell\nu\ell\nu$ analysis and have to be selected in a way that minimizes the spurious acceptance of false signatures while retaining a maximum efficiency for genuine signal leptons. The following sub-sections summarize the selection of muons and electrons for the $H \to WW^{(*)} \to \ell\nu\ell\nu$ analysis including the correction of the acceptance efficiencies from MC simulation by means of applying corresponding scale factors. A detailed summary of the lepton selection requirements is given in Table 7.2.

Muon Selection

Muons are reconstructed using the "Staco combined" reconstruction algorithm, which performs a combination of measurements of the Inner Detector (ID) and the Muon Spectrometer (see Section 2.3.3). For the 2011 dataset, a muon candidate is required to be reconstructed within the geometrical acceptance of the muon trigger given by $|\eta| < 2.4$, whereas the muon acceptance is extended to $|\eta| < 2.5$ for the analysis of the 2012 dataset since it has been shown to still allow reliable reconstruction. In either case, the muon candidate must have a p_{T} exceeding 15 GeV.

Further quality requirements based on the track impact parameters with respect to the primary vertex (see Section 2.3.1) as well as on the track and calorimeter isolation are imposed to suppress backgrounds, in particular the contribution arising from W + jets events. The muon isolation is calculated from objects within a cone of $\Delta R = \sqrt{(\Delta\phi)^2 + (\Delta\eta)^2} = 0.3$ around the muon (see Section 2.3.3). Based on the number of reconstructed vertices, both the track and the calorimeter isolation are corrected for contributions from pile-up interactions. The isolation requirement is further strengthened by rejecting a muon candidate if a jet candidate passing the selection described in Section 7.1.3 is present within a cone of $\Delta R = 0.3$ around the muon candidate.

The muon reconstruction and identification efficiencies are corrected for a potential mismodeling in the MC simulation by applying corresponding identification scale factors $\mathrm{SF}_{\mu}^{\mathrm{Id}}$, which are determined using a tag-and-probe method in $Z \to \mu^+\mu^-$ decays [56]. The acceptance efficiency of the supplementary isolation and track impact parameter criteria is corrected using an additional scale factor $\mathrm{SF}_{\mu}^{\mathrm{Iso}}$. The final scale factor SF_{μ} related to one individual muon candidate is given by

$$\mathrm{SF}_{\mu} = \mathrm{SF}_{\mu}^{\mathrm{Id}} \cdot \mathrm{SF}_{\mu}^{\mathrm{Iso}}.$$

Electron Selection

The $H \to WW^{(*)} \to \ell\nu\ell\nu$ analysis relies on electron candidates that are reconstructed by the default algorithms (see Section 2.3.2) using the standard track fitting for the 2011 dataset and a *Gaussian Sum Filter* (GSF) algorithm[4] [136] for the 2012 dataset, in either case within the

[4]The GSF algorithm improves the performance of the track reconstruction in the case of electron bremsstrahlung.

geometrical acceptance of $|\eta| < 2.47$ but excluding the transition region between the barrel and the end-cap parts of the calorimeter ($1.37 < |\eta| < 1.52$). In addition, electron candidates are excluded if they are reconstructed in detector regions where the LAr calorimeter was affected by read-out problems or noise bursts during the corresponding data run.

The electron identification is based on the "tight++" identification criteria and the candidate's p_{T} is required to exceed 15 GeV. Like for muons, background events, mainly from W + jets, are suppressed by additional impact parameter and electron isolation criteria requirements (see Table 7.2 for details).

Muons traversing the calorimeter may deposit a significant amount of energy in the latter, inducing the reconstruction of an electron candidate. Such cases are eliminated by rejecting an electron candidate if a muon is identified within a narrow cone of $\Delta R = 0.1$ around it. Finally, in order to avoid multiple reconstruction of one single electron, an electron candidate is rejected if another electron candidate with a larger p_{T} is reconstructed and identified within a cone of $\Delta R = 0.1$ around the first candidate.

Efficiency scale factors $\mathrm{SF}_e^{\mathrm{Reco}}$ and $\mathrm{SF}_e^{\mathrm{Id}}$ are applied to correct for discrepancies between data and the MC simulation of reconstruction and identification efficiencies, respectively. These scale factors are based on efficiency measurements in data as well as in the MC simulation using tag-and-probe methods in $Z \to e^+e^-$, $W \to e\nu$ and $J/\Psi \to e^+e^-$ decays [53]. An additional scale factor $\mathrm{SF}_e^{\mathrm{Iso}}$ corresponds to the $H \to WW^{(*)} \to \ell\nu\ell\nu$ analysis specific impact parameter and isolation requirements. The final scale factor SF_e related to one individual electron candidate is given by

$$\mathrm{SF}_e = \mathrm{SF}_e^{\mathrm{Reco}} \cdot \mathrm{SF}_e^{\mathrm{Id}} \cdot \mathrm{SF}_e^{\mathrm{Iso}}.$$

7.1.3. Jet Selection

The $H \to WW^{(*)} \to \ell\nu\ell\nu$ analysis uses jets that are reconstructed within the geometrical acceptance of $|\eta| < 4.5$ using the anti-k_t algorithm with a radius parameter of $R = 0.4$ and the EM+JES calibration scheme (see Section 2.3.4). The baseline requirement imposed on the p_{T} of a jet candidate is to exceed 25 GeV. However, in order to ensure the selection of a clean sample of jets associated with the hard-scattering interaction additional criteria have to be fulfilled by a jet candidate.

The absolute value[5] of the *jet vertex fraction* (JVF, see Section 2.3.4) has to exceed 0.75 for the 2011 dataset and 0.5 for the 2012 dataset. The threshold has been changed from 0.75 to 0.5 to retain a stable acceptance efficiency with respect to the JVF requirement as a function of the number of reconstructed primary vertices.

In both the 2011 dataset and the 2012 dataset the minimal jet p_{T} threshold has to be raised above the baseline of $p_{\mathrm{T}} > 25$ GeV in certain regions of the detector. In the region around $|\eta| \simeq 3$, corresponding to the transition region between the electromagnetic end-cap calorimeter and the forward calorimeter, a significant excess of jets has been observed in the 2011 data which is not properly modeled by the MC simulation. The excess is likely to be caused by a coarser calorimeter granularity and hence worse resolution, making this region more sensitive to jets arising from pile-up events. Since these jets tend to have a low p_{T}, the effect can be suppressed by raising the jet candidate p_{T} threshold to $p_{\mathrm{T}} > 30$ GeV in the region $2.75 < |\eta| < 3.25$ [137].

[5] The use of the absolute value is motivated by the intent to include jets without a well defined jet vertex fraction, in which case JVF = −1.

Object / Requirement	2011 dataset	2012 dataset
Muons		
Reconstruction algorithm	Staco combined	
Transverse momentum	$p_{\mathrm{T}} > 15$ GeV	
Geometrical acceptance	$\lvert\eta\rvert < 2.4$	$\lvert\eta\rvert < 2.5$
Impact parameters		
Transverse	$\lvert d_0/\sigma(d_0)\rvert < 3$	$\lvert d_0/\sigma(d_0)\rvert < 3$
Longitudinal	$\lvert z_0\rvert < 1$ mm	$\lvert z_0 \cdot \sin\theta\rvert < 1$ mm
Isolation ($\Delta R < 0.3$)		
Track	$\left(\sum p_{\mathrm{T}}^{\mathrm{trk}}\right)_{\mathrm{C}} / p_{\mathrm{T}} < 0.13$	$\left(\sum p_{\mathrm{T}}^{\mathrm{trk}}\right)_{\mathrm{C}} / p_{\mathrm{T}} < 0.15$ and $\left(\sum p_{\mathrm{T}}^{\mathrm{trk}}\right)_{\mathrm{C}} / p_{\mathrm{T}} < \frac{0.01 \cdot p_{\mathrm{T}}}{\mathrm{GeV}} - 0.105$
Calorimeter	$\left(\sum E_{\mathrm{T}}^{\mathrm{cell}}\right)_{\mathrm{C}} / p_{\mathrm{T}} < 0.14$	$\left(\sum E_{\mathrm{T}}^{\mathrm{cell}}\right)_{\mathrm{C}} / p_{\mathrm{T}} < 0.2$ and $\left(\sum E_{\mathrm{T}}^{\mathrm{cell}}\right)_{\mathrm{C}} / p_{\mathrm{T}} < \frac{0.014 \cdot p_{\mathrm{T}}}{\mathrm{GeV}} - 0.15$
Overlap removal (μ/j)	–	$\Delta R(\mathrm{muon}, \mathrm{jet}) < 0.3$
Electrons		
Identification criteria	tight++	
Geometrical acceptance	$\lvert\eta\rvert < 2.47$, except $1.37 < \lvert\eta\rvert < 1.52$	
Transverse momentum	$p_{\mathrm{T}} > 15$ GeV	
Overlap removal (e/μ)	$\Delta R(\mathrm{electron}, \mathrm{muon}) < 0.1$	
Track reconstruction	Default	Gaussian Sum Filter
Overlap removal (e/e)	–	$\Delta R(\mathrm{electron}, \mathrm{electron}_{p_{\mathrm{T}}>}) < 0.1$
Impact parameters		
Transverse	$\lvert d_0/\sigma(d_0)\rvert < 10$	$\lvert d_0/\sigma(d_0)\rvert < 3$
Longitudinal	$\lvert z_0\rvert < 1$ mm	$\lvert z_0 \cdot \sin\theta\rvert < 0.4$ mm
Isolation ($\Delta R < 0.3$)		
Track	$\left(\sum p_{\mathrm{T}}^{\mathrm{trk}}\right)_{\mathrm{C}} / p_{\mathrm{T}} < 0.13$	$\left(\sum p_{\mathrm{T}}^{\mathrm{trk}}\right)_{\mathrm{C}} / p_{\mathrm{T}} < 0.12$ (0.16) for $p_{\mathrm{T}} < 25$ GeV ($p_{\mathrm{T}} \geq 25$ GeV)
Calorimeter	$\left(\sum E_{\mathrm{T}}^{\mathrm{cell}}\right)_{\mathrm{C}} / p_{\mathrm{T}} < 0.14$	$\left(\sum E_{\mathrm{T}}^{\mathrm{cell}}\right)_{\mathrm{C}} / p_{\mathrm{T}} < 0.16$

Table 7.2: Summary of the reconstruction and identification parameters of leptons as well as the selection criteria applied to lepton candidates in the 2011 and the 2012 datasets in the context of the $H \to WW^{(*)} \to \ell\nu\ell\nu$ analysis. Both the track and the calorimeter isolation are corrected for contributions from pile-up interactions based on the number of reconstructed vertices, and corresponding quantities are marked with the index "C".

In the 2012 dataset, the contamination from pile-up jets is significantly increased compared to the 2011 dataset. Even though the JVF requirement provides an effective handle to identify such jets, it can only be applied in detector regions covered by the ID. In order to extend the suppression of pile-up jets to the full jet acceptance region, the jet p_{T} threshold is raised to $p_{\mathrm{T}} > 30$ GeV not only in the transition region $2.75 < \lvert\eta\rvert < 3.25$ but in the full region not covered by the ID ($\lvert\eta\rvert > 2.5$) [138].

Object / Requirement	2011 dataset	2012 dataset
Jets		
Reconstruction algorithm	anti-k_t, $R = 0.4$	
Geometrical acceptance	$\|\eta\| < 4.5$	
Overlap removal (j, e)	$\Delta R(\text{jet}, \text{electron}) < 0.3$	
Calibration scheme	EM+JES	
Quality criteria	Looser	
Transverse momentum	$p_{\text{T}} > 25$ GeV ($p_{\text{T}} > 30$ GeV for $2.75 < \|\eta\| < 3.25$)	$p_{\text{T}} > 25$ (30) GeV for $\|\eta\| \leq 2.5$ ($\|\eta\| > 2.5$)
Jet Vertex Fraction	$\|\text{JVF}\| > 0.75$	$\|\text{JVF}\| > 0.5$
b**-tagging**		
Jet selection	Default (see above)	
Tagging algorithm	JetFitterCombNN	MV1
Working point	80 %	85 %

Table 7.3: Summary of the reconstruction and identification parameters of jets and of b-jets as well as the selection criteria applied to jet candidates from the 2011 and the 2012 dataset in the context of the $H \to WW^{(*)} \to \ell\nu\ell\nu$ analysis.

One characteristic of the jet definition is an ambiguity with respect to the electron reconstruction. An electron is usually not only reconstructed as an electron candidate but also as a jet candidate. This feature calls for a dedicated *overlap removal* procedure discarding jet candidates that are likely to originate from single electrons. The identification of electron-induced jet candidates is based on checking for the presence of an electron candidate passing the selection criteria as described in Section 7.1.2 within a cone of $\Delta R = 0.3$ around the jet candidate. In case of an overlap between an electron and a jet candidate the jet candidate is rejected.

7.1.4. Identification of b-Jets

Processes involving top quarks in the final state constitute a major background for the Higgs boson search in the $H \to WW^{(*)} \to \ell\nu\ell\nu$ decay channel. However, these processes can efficiently suppressed by exploiting the characteristic decay topology of b-hadrons which usually accompany top quark decays. In the $H \to WW^{(*)} \to \ell\nu\ell\nu$ analysis, both the JetFitterCombNN as well as the MV1 b-tagging algorithms are used to identify b-hadron jets (see also Section 2.3.5), in either case based on jet candidates selected according to the criteria described in the previous section. For the analysis of the 2011 dataset, the JetFitterCombNN algorithm is employed operating at an 80 % efficiency working point, and in the 2012 dataset b-jet identification is performed by the MV1 algorithm operating at an 85 % efficiency working point.

The identification of jets originating from b-hadrons involves three important efficiencies, one being the efficiency of correctly identifying a true b-jet (*b-tagging efficiency*), one being the efficiency of identifying a jet originating from a c-quark as a b-jet (*c-tagging efficiency*), and the last one being the inefficiency of not identifying a jet stemming from light quarks

(u, d, s) or gluons as a b-jet (*mistag rate*). All three efficiencies have been measured for several b-tagging algorithms at several working points in the MC simulation as well as in data and corresponding jet-based scale factors have been derived [67,139]. The type of scale factor SF_i associated to a jet depends on the true[6] type of parton the jet originates from as well as on the tagging result. The final event-based b-tagging scale factor $\mathrm{SF}_{b-\mathrm{tag}}$ is the product of the individual jet-based scale factors SF_i for all selected jets in the event,

$$\mathrm{SF}_{b-\mathrm{tag}} = \prod_{\text{jets } i} \mathrm{SF}_i.$$

It is applied to MC events if the acceptance of the event depends on the b-tagging result.

7.2. Event Selection

The interaction corresponding to a data event that has been recorded by the experiment by reason of an incentive of the trigger system is a priori unknown. The physics process that took place during the particle collision to form the interaction vertex and the outgoing particles has to be inferred from the measurement of event and particle properties. The isolation of events corresponding to a certain process is typically accomplished by imposing a set of requirements (commonly referred to as *cuts*) on those event properties that feature a suitable discrimination between the process of interest (*signal*) and other processes (*background*). According to the principles of quantum mechanics, the process through which the hard interaction proceeded may not be well defined. Motivated not only by this but also by the presence of irreducible backgrounds (see also Section 4.2) events passing the requirements towards the isolation of the signal process are referred to as signal *candidate events*.

Like many other analyses, the search for the SM Higgs boson in the $H \to WW^{(*)} \to \ell\nu\ell\nu$ decay mode separates the rare signal events from the overwhelming number of background events by rejecting events that are more likely to originate from a background process than from the signal process. The corresponding figure of merit may for example be the output of a *multivariate algorithm* (MVA) operating on a set of discriminating event and object quantities. For the $H \to WW^{(*)} \to \ell\nu\ell\nu$ analysis this has been done and published in Ref. [140]. Another well-established approach is to reject an event if a certain event or object quantity is not within a predefined acceptance interval. This approach is commonly referred to as the *cut-based* approach. The fundamental difference to the MVA approach is that the acceptance interval for one quantity does not depend on the value of other quantities as it is indirectly done in the MVA approach.

Following the cut-based approach for this analysis, an event must pass a sequence of event selection requirements in order to be considered as a $H \to WW^{(*)} \to \ell\nu\ell\nu$ candidate event. These requirements are conceptually classified according to their purpose, and the corresponding categories are referred to as the *event preselection*, the *jet multiplicity specific selection* and the *topological event selection*. Even though logically the full sequence of requirements is a conjunction of individual conditions and hence eventually independent of the order of their application, their sequential arrangement is considered as fixed mainly following historical habits.

The following sections explain and motivate the selection criteria used in the $H + 0$ and $H + 1$ jet channels of the $H \to WW^{(*)} \to \ell\nu\ell\nu$ analysis. Table 7.8 provides a summary of the

[6] Since the scale factor is applied to simulated events, the true origin of the jet is known.

Process	2011 dataset [fb]		2012 dataset [fb]		2011 → 2012	
	SF	OF	SF	OF	SF	OF
Signal						
$m_H = 110$ GeV	3.1	2.9	3.7	3.6	+20 %	+22 %
$m_H = 125$ GeV	19	18	24	23	+25 %	+26 %
$m_H = 140$ GeV	50	48	61	60	+21 %	+24 %
$m_H = 170$ GeV	87	84	98	95	+13 %	+13 %
$m_H = 200$ GeV	50	49	64	64	+29 %	+31 %
$m_H = 240$ GeV	36	35	49	50	+37 %	+41 %
Backgrounds						
SM WW	414	404	491	482	+19 %	+19 %
$WZ/ZZ/W\gamma$	524	54	397	97	-24 %	+80 %
Single top	184	184	251	246	+36 %	+33 %
Top pairs	$1.73 \cdot 10^3$	$1.72 \cdot 10^3$	$2.46 \cdot 10^3$	$2.46 \cdot 10^3$	+42 %	+43 %
$Z/\gamma^* + \text{jets}$						
$Z/\gamma^* \to ee, \mu\mu$	$590 \cdot 10^3$	44	$684 \cdot 10^3$	73	+16 %	+66 %
$Z/\gamma^* \to \tau\tau$	$1.51 \cdot 10^3$	$1.46 \cdot 10^3$	$1.40 \cdot 10^3$	$1.37 \cdot 10^3$	-7 %	-7 %
$W + \text{jets}$	347	156	697	137	+101 %	-12 %

Table 7.4: Summary of cross sections (in femtobarn) of the $H \to WW^{(*)} \to \ell\nu\ell\nu$ signal for different Higgs boson mass hypotheses m_H as well as of the main background processes accepted by the analysis after applying the default object selection criteria (see Section 7.1) and the event preselection (see Section 7.2.1) up to the cuts on the transverse momenta of the charged leptons. "SF" refers to the sums of the same flavor channels and "OF" refers to the sums of the opposite flavor channels. The numbers are obtained from MC simulation and include the default corrections of acceptance efficiencies. The numbers for the $W+\text{jets}$ process are determined using a data-driven technique outlined in Section 7.3.1. The statistical uncertainties on the quoted absolute numbers are less than 5 % in all cases.

full candidate event selection. Even though the object selection criteria have changed for the 2012 dataset compared to the 2011 dataset, the event selection in the $H + 0$ and $H + 1$ jet channels is retained unmodified.

7.2.1. Event Preselection

Leptons provoking a trigger may not necessarily arise from a proton-proton collision but also from cosmic rays traversing the detector or from beam-related backgrounds. In order to suppress the contamination of these undesirable events, the primary interaction vertex of an event is required to be consistent with the beam spot position and has to have at least three associated tracks with a p_{T} exceeding 400 MeV. Additionally, an event is rejected if a jet candidate failing the "Looser" quality criteria is present (see also Section 2.3.4).

An event is required to have exactly two leptons (electron or muon) of opposite charge, reconstructed and selected according to the procedures explained in Section 7.1.2. Events with additional leptons are rejected to suppress backgrounds arising from diboson backgrounds other than the production of a WW pair. The object that provoked the trigger is required to match one of the two selected leptons to minimize the impact of triggering false leptons

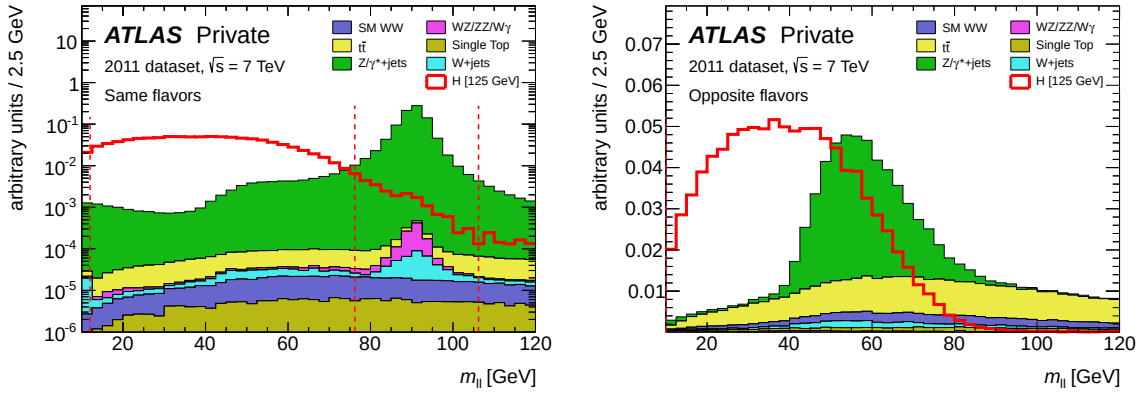

(a) Same flavor (b) Opposite flavor

Figure 7.1: Distributions of the invariant mass $m_{\ell\ell}$ of the two charged leptons after imposing the transverse lepton momentum requirements on the preselected sample of opposite charge dilepton events. The distributions are shown for the same flavor channels (a) and the opposite flavor channels (b). The solid histograms correspond to the total background, while the expected contributions from a $H \to WW^{(*)} \to \ell\nu\ell\nu$ signal for $m_H = 125$ GeV are superimposed as red hisograms. The distributions are obtained from MC simulation corresponding to the 2011 dataset and are normalized such that the total background as well as the $H \to WW^{(*)} \to \ell\nu\ell\nu$ signal correspond to unit area. In the same flavor channels the Z veto cuts and the lower bound on $m_{\ell\ell}$ are indicated as vertical red dashed lines, whereas the lower bound on $m_{\ell\ell}$ in the opposite flavor channels is barely visible.

and to ensure the validity of Equation (7.1). In order to operate in a region where the lepton trigger efficiency only marginally depends on the lepton p_{T} (*trigger plateau*), at least one lepton is required to have a p_{T} exceeding 25 GeV. Due to the lepton selection criteria the second lepton is implicitly required to have $p_{\mathrm{T}} > 15$ GeV.

Table 7.4 summarizes the cross sections of the $H \to WW^{(*)} \to \ell\nu\ell\nu$ signal for different Higgs boson mass hypotheses m_H as well as of the main background processes accepted by the analysis after applying the default object selection criteria (see Section 7.1) and the event preselection (see Section 7.2.1) up to the cuts on the transverse momenta of the charged leptons. Except for the $W+$jets process, the cross sections are obtained from MC simulation including the acceptance efficiency corrections outlined in Section 7.1. The contribution from $W+$ jets is estimated using a data-driven technique summarized in Section 7.3.1. At this event selection stage, the same flavor sample is strongly dominated by $(Z/\gamma^* \to ee, \mu\mu)$+jets events, whereas the opposite flavor sample receives its most important contributions from both the top background as well as $(Z/\gamma^* \to \tau\tau)$+jets events.

Figure 7.1 shows the distributions of the invariant mass $m_{\ell\ell}$ of the two charged leptons at the same selection stage. Contributions from low mass Drell-Yan processes and J/Ψ or Υ resonances are suppressed by placing a lower bound on $m_{\ell\ell}$ of 12 (10) GeV in the same (opposite) flavor channel. Additionally, a large fraction of the contributions from $Z+$jets events is rejected by requiring $m_{\ell\ell}$ to differ from the Z boson mass m_Z by more than 15 GeV in the same flavor channels (referred to as Z *veto*).

Apart from the two leptons, one essential characteristic of the $H \to WW^{(*)} \to \ell\nu\ell\nu$ signal process is the transverse momentum imbalance induced by the neutrinos stemming from the leptonic W decays. It would be straightforward to require the missing transverse energy

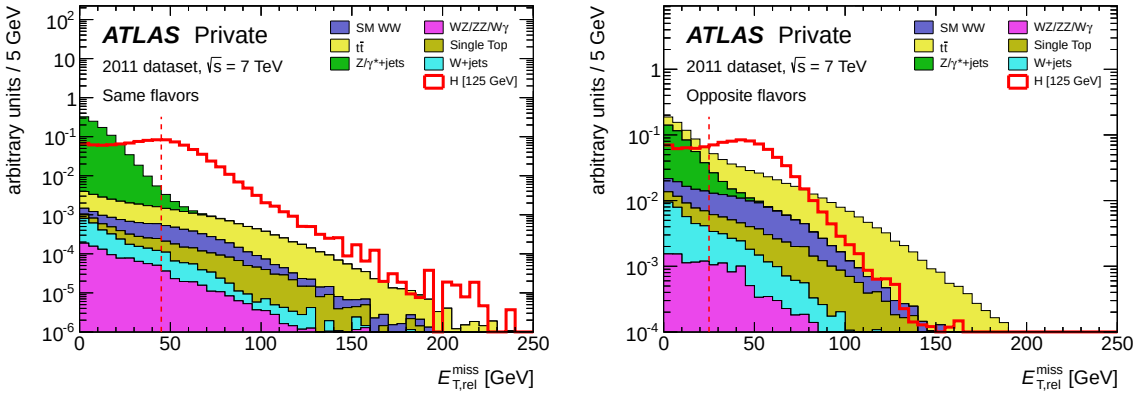

(a) Same flavor (b) Opposite flavor

Figure 7.2: Distributions of the projected missing transverse energy $E_{\mathrm{T,rel}}^{\mathrm{miss}}$ after applying the cuts on the invariant mass $m_{\ell\ell}$. The distributions are shown for the same flavor channels (a) and the opposite flavor channels (b). The solid histograms correspond to the total background, while the expected contributions from a $H \to WW^{(*)} \to \ell\nu\ell\nu$ signal for $m_H = 125$ GeV are superimposed as red hisograms. The distributions are obtained from MC simulation corresponding to the 2011 dataset and are normalized such that the total background as well as the $H \to WW^{(*)} \to \ell\nu\ell\nu$ signal correspond to unit area. The cut thresholds of $E_{\mathrm{T,rel}}^{\mathrm{miss}} > 45$ (25) GeV in the same (opposite) flavor channels are indicated as vertical red dashed lines. See Figure A.1 for a version corresponding to the 2012 dataset.

($E_{\mathrm{T}}^{\mathrm{miss}}$) to exceed a certain threshold to enhance the relative contribution from the signal process. However, as explained in Section 4.2.3, energy and momentum mismeasurements have a non-negligible share in reputed signatures of missing transverse energy (referred to as *fake* $E_{\mathrm{T}}^{\mathrm{miss}}$). In order to reduce the effect of fake $E_{\mathrm{T}}^{\mathrm{miss}}$ arising from mismeasurements, a new quantity, the *projected*[7] *missing transverse energy* $E_{\mathrm{T,rel}}^{\mathrm{miss}}$ is introduced,

$$E_{\mathrm{T,rel}}^{\mathrm{miss}} = \begin{cases} E_{\mathrm{T}}^{\mathrm{miss}} & \text{if } \Delta\phi \geq \pi/2 \\ E_{\mathrm{T}}^{\mathrm{miss}} \cdot \sin(\Delta\phi) & \text{if } \Delta\phi < \pi/2. \end{cases} \tag{7.2}$$

Here, $\Delta\phi$ is the azimuthal angle between the $E_{\mathrm{T}}^{\mathrm{miss}}$ direction and the closest lepton or jet passing the object selection criteria. If the missing transverse energy is accompanied by such an object within its azimuthal hemisphere, $E_{\mathrm{T,rel}}^{\mathrm{miss}}$ corresponds to the component of the $E_{\mathrm{T}}^{\mathrm{miss}}$ vector perpendicular to the axis defined by the closest object. The definition of $E_{\mathrm{T,rel}}^{\mathrm{miss}}$ effectively diminishes[8] the magnitude of $E_{\mathrm{T}}^{\mathrm{miss}}$ if the mismeasurement of a close-by object is likely to be the source of the momentum imbalance.

Figure 7.2 shows the distributions of $E_{\mathrm{T,rel}}^{\mathrm{miss}}$ after applying the cuts on the invariant mass $m_{\ell\ell}$. The $Z/\gamma^* + \mathrm{jets}$ events passing the Z veto peak around low values of $E_{\mathrm{T,rel}}^{\mathrm{miss}}$, whereas the signal has a significant tail towards large values of $E_{\mathrm{T,rel}}^{\mathrm{miss}}$. Even though the $(Z/\gamma^* \to \tau\tau)$+jets process involves neutrinos that elude a momentum measurement, these events still tend to have low values of $E_{\mathrm{T,rel}}^{\mathrm{miss}}$. This fact has to be attributed to the boost of the τ-leptons resulting in a small opening angle of the τ decay products with the neutrinos from different τ-leptons balancing each other and having a large momentum component along the axes of visible τ decay products.

[7] To follow the convention and retain consistency, the symbol $E_{\mathrm{T,rel}}^{\mathrm{miss}}$ derived from the term *relative* $E_{\mathrm{T}}^{\mathrm{miss}}$ is used in this thesis, even though it appears to be more adequat to use the term *projected* $E_{\mathrm{T}}^{\mathrm{miss}}$.

[8] It is always 0 GeV $\leq E_{\mathrm{T,rel}}^{\mathrm{miss}} \leq E_{\mathrm{T}}^{\mathrm{miss}}$.

Process	2011 dataset		2012 dataset	
	SF	OF	SF	OF
Signal				
$m_H = 125$ GeV	36 %	67 %	35 %	64 %
$m_H = 170$ GeV	58 %	80 %	58 %	80 %
$m_H = 240$ GeV	36 %	72 %	36 %	71 %
Backgrounds				
$Z/\gamma^* + \text{jets}$	0.03 %	7.5 %	0.14 %	15 %
Other backgrounds	22 %	57 %	23 %	58 %

Table 7.5: The efficiencies of events from different processes to pass the $m_{\ell\ell}$ and $E_{\text{T,rel}}^{\text{miss}}$ cuts of the preselection. "SF" refers to the sum of the same flavor channels and "OF" refers to the sum of the opposite flavor channels. The relative statistical uncertainties on the quoted numbers are less than 0.4 % in all cases.

The event preselection is completed by requiring $E_{\text{T,rel}}^{\text{miss}}$ to exceed a threshold of 45 GeV in the same flavor channels and a loosened threshold of 25 GeV in the opposite flavor channels.

Table 7.5 summarizes the efficiencies of $H \to WW^{(*)} \to \ell\nu\ell\nu$ signal events for several Higgs boson mass hypotheses m_H as well as of background events to pass the $m_{\ell\ell}$ and $E_{\text{T,rel}}^{\text{miss}}$ criteria applied in the context of the event preselection. While the efficiency of the $H \to WW^{(*)} \to \ell\nu\ell\nu$ signal as well as of the background other than $Z/\gamma^* + \text{jets}$ to pass the event preselection is almost unchanged between the 2011 and the 2012 datasets, the corresponding efficiencies of the $Z/\gamma^* + \text{jets}$ process are increased by a factor of approximately 4.5 (2) in the same (opposite) flavor channels. This is a result of the worse resolution of the missing transverse energy measurement in the 2012 dataset and, since this background involves large systematic uncertainties, has driven the decision to refrain from including the same flavor channels in the analysis of the 2012 data (see also Section 5.3).

7.2.2. Jet Multiplicity Specific Selection

The event preselection ensures that accepted events comply with the fundamental signature of the $H \to WW^{(*)} \to \ell\nu\ell\nu$ signal process and thereby accomplishes a considerable rejection of backgrounds, in particular events from $Z/\gamma^* + \text{jets}$ processes. After the event preselection the largest contributions to the background arise from the top background, residual $Z/\gamma^* + \text{jets}$ events featuring a significant momentum imbalance, and the SM WW production. However, as can be seen from Figure 7.3, which illustrates the distributions of the number of reconstructed jets in events passing the event preselection, the relative contributions from different background processes depend strongly on the *jet multiplicity*. While events without any reconstructed jets are likely to originate from SM WW production or $Z/\gamma^* + \text{jets}$, the top background bears an increasing ascendancy with an increasing number of reconstructed jets. Simultaneously, the fraction of events of the inclusive $H \to WW^{(*)} \to \ell\nu\ell\nu$ signal process with a certain number of reconstructed jets very rapidly approaches zero.

Table 7.6 summarizes the fractions of events with zero, one or at least two jets (*event fractions*) as well as the signal and background composition of event samples with zero, one or at least two jets (*sample compositions*) using the sum of the same and opposite flavor channels of the 2011 dataset. As expected, the relative contributions from the vector-boson fusion

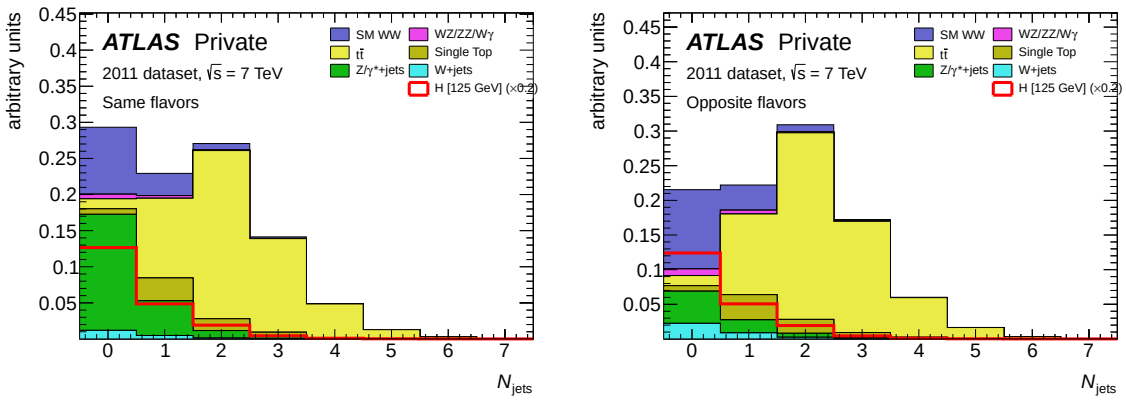

(a) Same flavor

(b) Opposite flavor

Figure 7.3: Distributions of the number of reconstructed jets N_{jets} according to the acceptance criteria described in Section 7.1.3 in events passing the event preselection as described in Section 7.2.1. The distributions are shown for the same flavor channels (a) and the opposite flavor channels (b). The solid histograms correspond to the total background, while the expected contributions from a $H \to WW^{(*)} \to \ell\nu\ell\nu$ signal for $m_H = 125$ GeV are superimposed as red hisograms. The distributions are obtained from MC simulation corresponding to the 2011 dataset and are normalized such that the total background corresponds to unit area and the $H \to WW^{(*)} \to \ell\nu\ell\nu$ signal corresponds to one fifth unit area. See Figure A.2 for a version corresponding to the 2012 dataset.

Higgs boson production mode to the inclusive $H \to WW^{(*)} \to \ell\nu\ell\nu$ signal are enhanced for higher multiplicities of jets in an event. A detailed breakdown into datasets as well as same and opposite flavor final states is presented in Tables A.2-A.5 in the appendix.

In order to fully exploit the variable background and signal compositions of event samples corresponding to specific jet multiplicities, events are allocated to three different event categories (*jet bins*) according to the numbers of reconstructed and selected jets in the event (see also Section 4.1.5). Events with no jet being reconstructed or passing the jet selection are classified as $H + 0$ jets (*zero jet bin*), events with exactly one jet are classified as $H + 1$ jet (*one jet bin*), and events with at least two jets are classified as $H + 2$ jets (*two jet bin*). Additional selection requirements are imposed depending on the jet category.

$\mathbf{H + 0}$ jets Selection

The $H + 0$ jets channel is characterized by a jet veto imposed after the event preselection, rejecting a large fraction of the top background while retaining a signal efficiency of the order of two third for the gluon fusion production mode for $m_H = 125$ GeV. The largest background contribution is given by $Z/\gamma^* +$ jets and the SM WW production, with the first dominating the same flavor channels and the latter dominating the opposite flavor channels. Given the increased efficiencies of $Z/\gamma^* +$ jets events in the 2012 dataset to pass the preselection, also the relative contribution of these events after the jet veto is increased in both the same and the opposite flavor channels.

In order to further suppress the contributions of the $Z/\gamma^* +$ jets background, an additional requirement on the magnitude of the transverse momentum

$$p_{\text{T}}^{\ell\ell} = \left| \vec{p}_{\text{T}}^{\,\ell_1} + \vec{p}_{\text{T}}^{\,\ell_2} \right| \tag{7.3}$$

Process	Event fractions, $\sum(\ \cdots\ ) = 1$			Sample Compositions, $\sum(\ \vdots\ ) = 1$		
	$N_{\text{jets}} = 0$	$N_{\text{jets}} = 1$	$N_{\text{jets}} \geq 2$	$N_{\text{jets}} = 0$	$N_{\text{jets}} = 1$	$N_{\text{jets}} \geq 2$
Signal						
$m_H = 125$ GeV						
ggF	69 %	24 %	8 %	97 %	83 %	55 %
VBF	8 %	38 %	54 %	1 %	10 %	28 %
WH/ZH	29 %	32 %	39 %	3 %	7 %	17 %
Backgrounds						
SM WW	70 %	22 %	8 %	44 %	15 %	2 %
$WZ/ZZ/W\gamma$	55 %	32 %	12 %	3 %	2 %	0 %
Single top	11 %	50 %	39 %	3 %	15 %	5 %
Top pairs	2 %	19 %	79 %	6 %	51 %	90 %
$Z/\gamma^* + \text{jets}$	69 %	23 %	8 %	36 %	13 %	2 %
$W + \text{jets}$	63 %	25 %	12 %	8 %	3 %	1 %

Table 7.6: Fractions of events with zero, one or at least two jets as well as the signal and background compositions of event samples with zero, one or at least two jets. The numbers are determined from MC simulation corresponding to the 2011 dataset using events in the same and opposite flavor channels passing the event preselection (see Section 7.2.1). Jets are selected according to the criteria described in Section 7.1.3. The rounding of the quoted numbers may induce sums deviating from 100 %. The statistical uncertainties on the quoted numbers are less than 4 % in all cases.

of the dilepton system is imposed. Since a jet veto has been applied, $Z/\gamma^* + \text{jets}$ events feature no hard object the Z boson could recoil against. Consequently, the Z boson is expected to have only a small momentum transverse to the beam axis, translating into a small $p_{\text{T}}^{\ell\ell}$ of the dilepton system. In opposition to that, the two charged leptons produced in the $H \to WW^{(*)} \to \ell\nu\ell\nu$ signal process recoil against the two neutrinos, which are forced by the $E_{\text{T,rel}}^{\text{miss}}$ cut to have a large transverse momentum $p_{\text{T}}^{\nu\nu} \simeq E_{\text{T}}^{\text{miss}}$, resulting in a large $p_{\text{T}}^{\ell\ell}$.

In the same flavor channels $p_{\text{T}}^{\ell\ell}$ has to exceed 45 GeV, whereas the threshold in the opposite flavor channels is given by 30 GeV. Figure 7.4 shows the distributions of $p_{\text{T}}^{\ell\ell}$ after the jet veto for the same and the opposite flavor channels separately. The distributions clearly illustrate the motivation for the cuts on $p_{\text{T}}^{\ell\ell}$.

H + 1 jets Selection

Events in the $H + 1$ jet channel feature exactly one reconstructed and selected jet in addition to the two selected leptons and the missing transverse energy. Approximately one fourth of the $H \to WW^{(*)} \to \ell\nu\ell\nu$ signal events with $m_H = 125$ GeV produced in the gluon fusion mode and passing the event preselection are attributed to this category. Thereby, the gluon fusion production mode still dominates the inclusive $H \to WW^{(*)} \to \ell\nu\ell\nu$ signal in the $H + 1$ jet channel. In contrast to the $H + 0$ jets channel, the predominant background contribution arises from top quark related processes, with the notable exception being the same flavor channels in the 2012 dataset, which receive a contribution from $Z/\gamma^* + \text{jets}$ events at approximately the same order of magnitude as from top backgrounds.

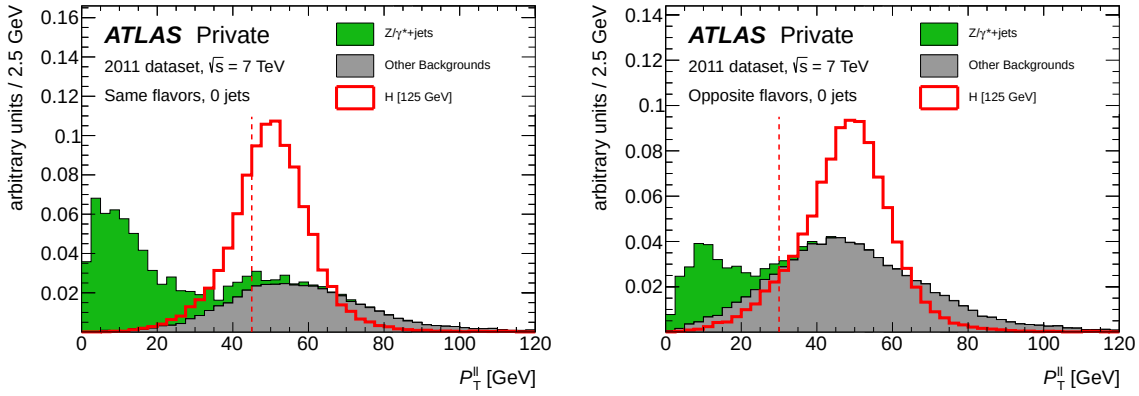

(a) Same flavor (b) Opposite flavor

Figure 7.4: Distributions of the magnitude of the transverse momentum $p_{\mathrm{T}}^{\ell\ell}$ of the dilepton system after applying the jet veto in the $H+0$ jets channel. The distributions are shown for the same flavor channels (a) and the opposite flavor channels (b). The solid histograms, split into the Z/γ^*+jets contribution (green) and the remaining backgrounds (gray), correspond to the total background, while the expected contributions from a $H \to WW^{(*)} \to \ell\nu\ell\nu$ signal for $m_H = 125$ GeV are superimposed as red hisograms. The distributions are obtained from MC simulation corresponding to the 2011 dataset and are normalized such that the total background as well as the $H \to WW^{(*)} \to \ell\nu\ell\nu$ signal correspond to unit area. The vertical red dashed lines indicate the threshold at 45 (30) GeV for the same (opposite) flavor channels below which events are rejected.

Process	2011 dataset	2012 dataset
Signal		
$m_H = 125$ GeV	92 %	85 %
Backgrounds		
Single top	32 %	24 %
Top pairs	29 %	21 %
Other Backgrounds	93 %	83 %

Table 7.7: Overview of the b-jet veto efficiencies in the $H+1$ jet channel for the $H \to WW^{(*)} \to \ell\nu\ell\nu$ signal with $m_H = 125$ GeV, for top backgrounds as well as for the sum of all other backgrounds. The numbers are calculated from events passing the event preselection and being categorized as $H+1$ jet. The statistical uncertainties on the quoted numbers are less than 1 % in all cases.

A significant reduction of the top background is achieved by imposing a veto on events containing at least one b-jet identified using corresponding tagging algorithms (*b-jet veto*). Table 7.7 summarizes the b-jet veto efficiencies for the $H \to WW^{(*)} \to \ell\nu\ell\nu$ signal with $m_H = 125$ GeV, for top backgrounds as well as for the sum of all other backgrounds (*non-top* backgrounds). Both the non-top backgrounds and the $H \to WW^{(*)} \to \ell\nu\ell\nu$ signal are accepted by the b-jet veto with efficiencies higher than 80 %, whereas the top background on average is accepted to approximately 25 %. Since the b-tagging working point has been shifted towards a higher b-tagging efficiency, the veto efficiencies are reduced in the 2012 dataset for any process.

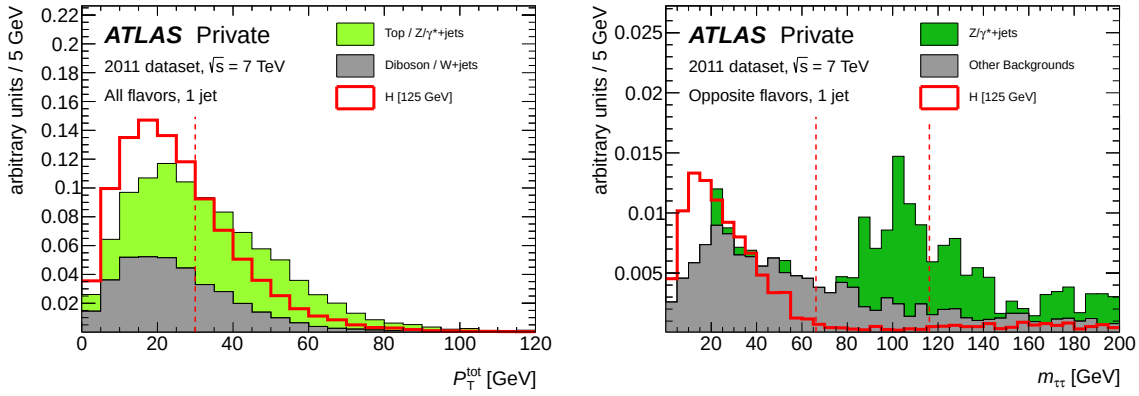

(a) $p_{\mathrm{T}}^{\mathrm{tot}}$ (b) $m_{\tau\tau}$

Figure 7.5: (a) Distributions of the total transverse momentum $p_{\mathrm{T}}^{\mathrm{tot}}$ for events passing the b-jet veto in the $H + 1$ jet channel. The total background, represented by the solid histogram, is split into the top and $Z/\gamma^* +$ jets components (light green) and the sum of the remaining backgrounds (gray). The vertical red dashed line indicates the $p_{\mathrm{T}}^{\mathrm{tot}} < 30$ GeV threshold. (b) The reconstructed invariant $\tau\tau$-mass $m_{\tau\tau}$ for events in the opposite flavor channels passing the $p_{\mathrm{T}}^{\mathrm{tot}} < 30$ GeV cut. The total background, represented by the solid histogram, is split into the Z/γ^*+jets component (dark green) and the sum of the remaining backgrounds (gray). The vertical red dashed lines indicate the interval in $m_{\tau\tau}$ which is cut away. For both figures, the expected contributions from a $H \to WW^{(*)} \to \ell\nu\ell\nu$ signal for $m_H = 125$ GeV are superimposed as red histograms. The distributions are obtained from MC simulation corresponding to the 2011 dataset and are normalized such that the total background as well as the $H \to WW^{(*)} \to \ell\nu\ell\nu$ signal correspond to unit area.

Hadronic activity arising from soft radiation is likely to fail the reconstruction and selection of a jet. However, the presence of soft radiation should be indicated by a non-zero total transverse momentum of all reconstructed and selected objects defined as

$$p_{\mathrm{T}}^{\mathrm{tot}} = \left| \vec{p}_{\mathrm{T}}^{\,\ell_1} + \vec{p}_{\mathrm{T}}^{\,\ell_2} + \vec{p}_{\mathrm{T}}^{\,\mathrm{jet}} + \vec{p}_{\mathrm{T}}^{\,\mathrm{miss}} \right| . \tag{7.4}$$

Placing a cut on $p_{\mathrm{T}}^{\mathrm{tot}}$ is motivated by the expectation of a more frequent occurrence of soft radiation in background processes like top quark production and Z/γ^*+jets events compared to the signal process. Figure 7.5 displays the distributions of $p_{\mathrm{T}}^{\mathrm{tot}}$ after imposing the b-jet veto. While the diboson backgrounds (SM WW, WZ, ZZ and $W\gamma$ production) and the $W +$ jets process show a distribution of $p_{\mathrm{T}}^{\mathrm{tot}}$ similar to the one of the signal for $m_H = 125$ GeV, the top background and the $Z/\gamma^* +$ jets production indeed tend to have a larger $p_{\mathrm{T}}^{\mathrm{tot}}$. Taking advantage of this, $p_{\mathrm{T}}^{\mathrm{tot}}$ is required to be below 30 GeV to accept an event.

The remaining $(Z/\gamma^* \to \tau\tau)$+jets contributions, which are most prominent in the opposite flavor channels, can partially be suppressed by trying to reconstruct the invariant $\tau\tau$-mass $m_{\tau\tau}$ using the *collinear approximation* [141] and rejecting an event if one obtains a physical solution with $|m_{\tau\tau} - m_Z| \leq 25$ GeV. Figure 7.5 shows the distributions of the reconstructed $\tau\tau$-mass $m_{\tau\tau}$ for opposite flavor events yielding a physical solution for $m_{\tau\tau}$.

7.2.3. Topological Selection

Based on events passing the event preselection and the jet multiplicity specific selection, the topological selection is designed to exploit the event topology specific to the decay of a

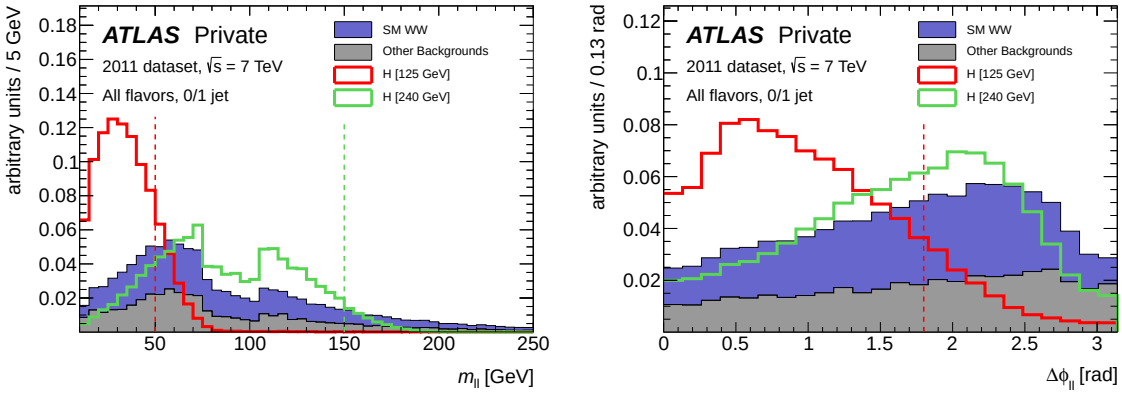

(a) $m_{\ell\ell}$ (b) $\Delta\phi_{\ell\ell}$

Figure 7.6: Distributions of variables subject to cuts in the context of the topological selection. The distributions correspond to events passing the event preselection and the jet multiplicity specific selection. The solid histograms, split into the SM WW contributions (blue) and the sums of the remaining backgrounds (gray), correspond to the total background, while the expected contributions from a $H \to WW^{(*)} \to \ell\nu\ell\nu$ signal with $m_H = 125$ GeV are superimposed as red histograms. The distributions reflect the sum of the same and opposite flavor channels as well as the $H + 0$ and the $H + 1$ jet channels. The distributions are obtained from MC simulation corresponding to the 2011 dataset and are normalized such that the total background as well as the $H \to WW^{(*)} \to \ell\nu\ell\nu$ signals correspond to unit area. The dashed vertical lines indicate the thresholds of the cuts imposed in the context of the topological selection for the Higgs boson mass hypothesis colored accordingly. (a) Invariant mass $m_{\ell\ell}$ of the two charged leptons. The drop in the $m_{\ell\ell}$ distributions around 90 GeV is induced by the Z veto in the same flavor channels. (b) Azimuthal separation angle $\Delta\phi_{\ell\ell}$ between the two charged leptons.

scalar particle like the SM Higgs boson into a pair of W bosons which both subsequently decay leptonically. The kinematic variables carrying the most prominent characteristics of a spin-0 resonance are the invariant mass $m_{\ell\ell}$ of the two charged leptons and their azimuthal separation angle $\Delta\phi_{\ell\ell}$ (see Section 4.1.4).

Based on the 2011 dataset, the topological selection has been optimized as a function of the Higgs boson mass hypothesis m_H (see Section 9.2) in order to achieve a maximum sensitivity while taking into account the strong dependence of the $m_{\ell\ell}$ and $\Delta\phi_{\ell\ell}$ distributions of $H \to WW^{(*)} \to \ell\nu\ell\nu$ signal events on the hypothesized Higgs boson mass m_H. For the benefit of a simple analysis not more than three successive categories in m_H have been defined, which appoint parameters of the topological selection that are specific to the corresponding mass range.

For $m_H < 200$ GeV, the topological selection requires $m_{\ell\ell} < 50$ GeV and $\Delta\phi_{\ell\ell} < 1.8$ rad, whereas for 200 GeV $\leq m_H <$ 300 GeV the $\Delta\phi_{\ell\ell}$ requirement is dropped and the $m_{\ell\ell}$ threshold is raised to 150 GeV. Finally, for $m_H \geq 300$ GeV also the $m_{\ell\ell}$ requirement is omitted. Figure 7.6 illustrates the cuts of the topological selection by means of the $m_{\ell\ell}$ and $\Delta\phi_{\ell\ell}$ distributions for the total background as well as for the $H \to WW^{(*)} \to \ell\nu\ell\nu$ signal with $m_H = 125$ GeV and 240 GeV after the jet multiplicity specific selection.

7.2.4. Final Signal Selection

The final $H \to WW^{(*)} \to \ell\nu\ell\nu$ *signal selection* (*signal region*, SR) for the $H+0$ and $H+1$ jet channels is defined by the conjunction of the event preselection described in Section 7.2.1,

the jet multiplicity specific selection described in Section 7.2.2 and the topological selection described in Section 7.2.3. Depending on the jet multiplicity bin and the lepton flavor channel, the full signal selection accomplishes a signal-to-background ratio which is of the order of 1 to 10 for $m_H = 125$ GeV. Since the $H \to WW^{(*)} \to \ell\nu\ell\nu$ channel does not allow a full mass reconstruction (see Section 4.1.3) the presence of a signal is indicated by an excess of events over the expected background. The quantity featuring a reasonably localized signal contribution is the transverse mass m_{T}, whose distribution for events passing the final signal selection is shown in Figure 7.7 for a Higgs boson mass of $m_H = 125$ GeV.

A further enhancement of the signal-to-background ratio could be achieved by placing an additional cut on m_{T}. In fact, previous versions of the $H \to WW^{(*)} \to \ell\nu\ell\nu$ analysis required $0.75 \cdot m_H < m_{\mathrm{T}} < m_H$ and performed a counting of events passing the cut on m_{T}. However, in the context of the statistical analysis (see Section 7.5) this procedure has been improved to incorporate a simultaneous fit of the m_{T} distributions in the signal regions and the event yields in control regions of the individual channels.

7.3. Background Estimation and Control Samples

Having passed the final signal selection, an event is considered as a $H \to WW^{(*)} \to \ell\nu\ell\nu$ *candidate* event. This terminology reflects the fact that not only signal events are expected to pass the final selection but also events from background processes (see also Section 4.2). As a matter of fact, in the $H + 0/1$ jets channels of the $H \to WW^{(*)} \to \ell\nu\ell\nu$ analysis the expected numbers of background events over the ones of signal events (see also previous section). Since the manifestation of the $H \to WW^{(*)} \to \ell\nu\ell\nu$ signal process is a broad excess of events in the m_{T} distribution, the interpretation of the observed events passing the final selection considerably relies on a precise estimate of background contributions.

The share of individual background processes to the final event yield is typically estimated using MC simulation comprising a full simulation of the detector and its response to the passage of corresponding final state particles. Even though the agreement of the simulation with the observation is usually very impressive, there are several reasons that advise against an unlimited reliance on the former. The physics governing the high-energy interaction are implemented in the MC event generators only to a finite order in perturbation theory, resulting in inherent uncertainties on the prediction. Furthermore, the simulation of the interplay between the final state particles and the detector material is very complex and, even if emulated in great detail, holds potential to a significant deficiency in the modeling of the data.

Innately, the observed data is the best reflection of reality. However, it is clear that from an observed event it is impossible to deduce its true origin with infinite certainty. A general approach towards an observation based (*data-driven*) evaluation of the background contributions after the final event selection is to use *control samples* (*control regions*, CR) which are obtained by applying selection criteria designed to enhance the contribution of one particular background process while suppressing the contamination from signal events. Based on these control samples, one can derive data-driven corrections to be applied to the simulation-based expectations after the final signal selection. The extrapolation of observations from the control sample to the signal region usually relies on MC simulation, but may in turn use data-driven techniques as well. In any case, to minimize systematic uncertainties on the final estimate induced by the extrapolation the selection criteria defining the control sample should be as similar to the final signal selection as possible.

Since the purity of a control sample with respect to the background process one is targeting at is typically below 100% the residual contamination from other background processes has

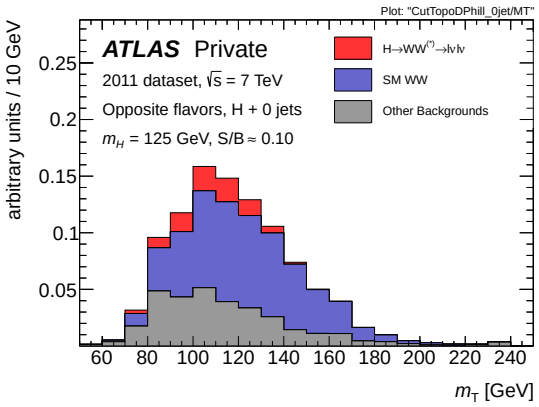

(a) 2011 dataset, OF, $H + 0$ jets

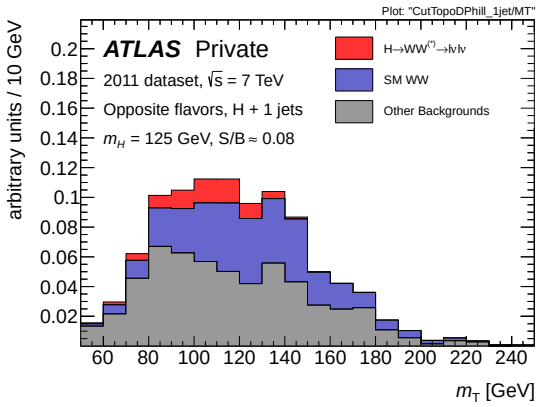

(b) 2011 dataset, OF, $H + 1$ jet

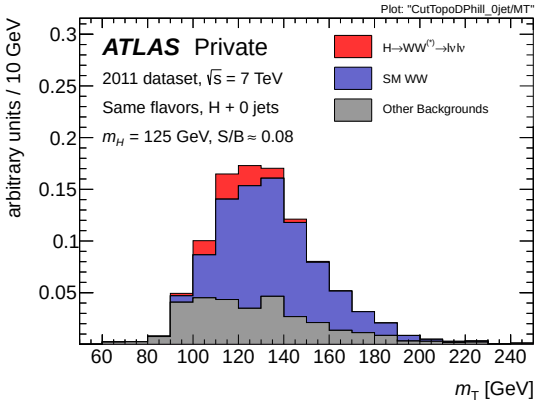

(c) 2011 dataset, SF, $H + 0$ jets

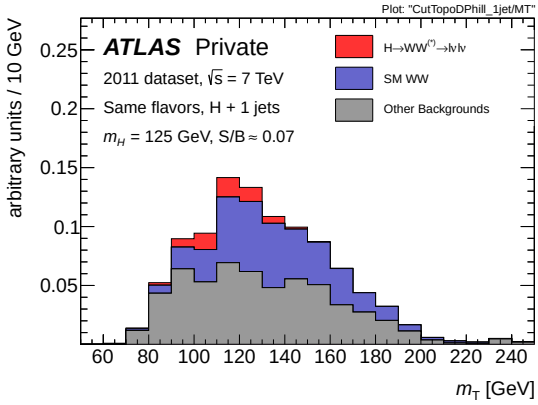

(d) 2011 dataset, SF, $H + 1$ jet

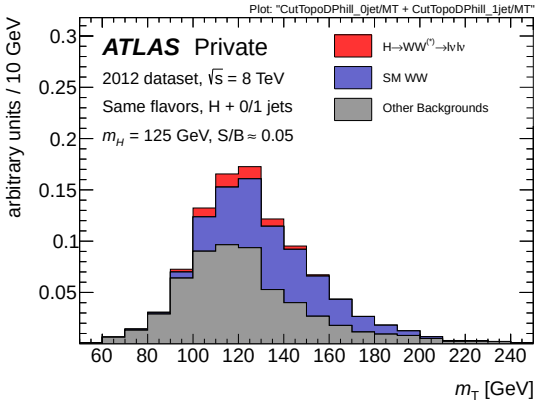

(e) 2012 dataset, SF, $H + 0/1$ jets

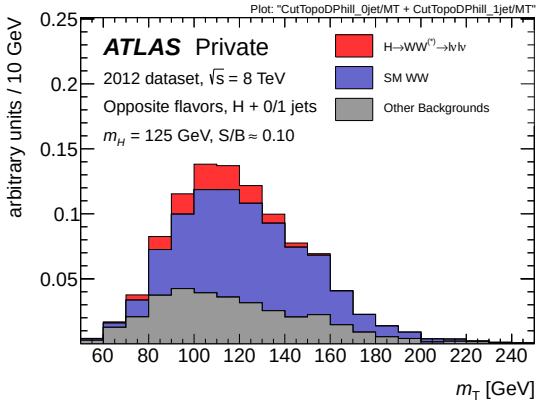

(f) 2012 dataset, OF, $H + 0/1$ jets

Figure 7.7: Distributions of the transverse mass m_{T} of the SM WW background (solid blue histograms), the sums of the remaining backgrounds (solid gray histograms), and the $H \to WW^{(*)} \to \ell\nu\ell\nu$ signal for $m_H = 125$ GeV (solid red histograms) passing the final $H \to WW^{(*)} \to \ell\nu\ell\nu$ signal selections of the $H + 0$ jets channel (left) and the $H + 1$ jet channel (right). The distributions are shown for the same and the opposite flavor channels as well as for the 2011 dataset and the 2012 dataset. The distributions are obtained from MC simulation, except for the W+jets background which is determined using a data-driven technique outlined in Section 7.3.1. The distributions are normalized such that the sums of the total background and the $H \to WW^{(*)} \to \ell\nu\ell\nu$ signal correspond to unit area. The relative sizes of the signal contributions with respect to the total background are drawn to their theoretical scale.

Selection reference	Requirement
Event preselection	
good vertex	$N_{\text{tracks}}(p_{\text{T}} > 400 \text{ MeV}) \geq 3$
two leptons (e, μ)	$N_e + N_\mu = 2$
leading lepton p_{T}	$\max(p_{\text{T}}^{\ell_1}, p_{\text{T}}^{\ell_2}) > 25$ GeV
opposite charge	$Q_{\ell_1} \neq Q_{\ell_2}$
lower $m_{\ell\ell}$ bound	$m_{\ell\ell} > 12$ (10) GeV for same (opposite) flavor channels
Z veto	$\lvert m_{\ell\ell} - m_Z \rvert > 15$ GeV for same flavor channels only
$E_{\text{T,rel}}^{\text{miss}}$	$E_{\text{T,rel}}^{\text{miss}} > 45$ (25) GeV for same (opposite) flavor channels
H + 0 jets selection	
jet veto	$N_{\text{jets}} = 0$
$p_{\text{T}}^{\ell\ell}$	$p_{\text{T}}^{\ell\ell} > 45$ (30) GeV for same (opposite) flavor channels
H + 1 jet selection	
exactly one jet	$N_{\text{jets}} = 1$
b-jet veto	$N_{b-\text{jets}} = 0$ **2011:** `JetFitterCombNN` (80 %) **2012:** `MV1` (85 %)
total p_{T}	$p_{\text{T}}^{\text{tot}} < 30$ GeV
$Z \to \tau\tau$ veto	$m_{\tau\tau}$ unphysical or $\lvert m_{\tau\tau} - m_Z \rvert > 25$ GeV
Topological selection	
$m_H < 200$ GeV	
$\Delta\phi_{\ell\ell}$	$\Delta\phi_{\ell\ell} < 1.8$ rad
$m_{\ell\ell}$	$m_{\ell\ell} < 50$ GeV
200 GeV $\leq m_H < 300$ GeV	
$m_{\ell\ell}$	$m_{\ell\ell} < 150$ GeV
$m_H \geq 300$ GeV	
–	

Table 7.8: Summary of the full event selection of the $H \to WW^{(*)} \to \ell\nu\ell\nu$ analysis in the $H + 0$ and $H + 1$ jet channels. The selection is based on physical objects selected according to Section 7.1 and comprises three successive categories. The event preselection (see Section 7.2.1) ensures that accepted events comply with the basic characteristics of the signal process. The jet multiplicity specific selection (see Section 7.2.2) is geared towards the compositions of backgrounds induced by requiring exactly zero or one reconstructed jet. The topological selection (see Section 7.2.3) exploits the event topology specific to the spin-0 nature of the SM Higgs boson. The b-jet veto is based on jets that are selected according to the default criteria (see Section 7.1.3) and b-tagged as outlined in Section 7.1.4.

to be subtracted using the best estimate of these components. Here, data-driven corrections corresponding to these processes derived from other control samples may be applied.

In the following, the data-driven corrections related to the $W+\text{jets}$ and $Z/\gamma^*+\text{jets}$ backgrounds as well as to the SM WW and the top background are outlined in detail. According to the interplay between different control samples mentioned in the previous paragraph, the order will follow the one induced by hierarchical interdependence of the corresponding control samples.

7.3.1. Estimation of Contributions from W+jets

Even though the lepton reconstruction and identification algorithms employed by the $H \to WW^{(*)} \to \ell\nu\ell\nu$ analysis feature a low misidentification rate, the large inclusive cross section of the $W+\text{jets}$ process results in a non-negligible number of events passing the dilepton selection (see also Section 4.2.4). As a result of the hierarchy between these two quantities, the number of $W+\text{jets}$ events passing the selection is very sensitive to the exact value of the lepton misidentification rate. Since the lepton reconstruction and identification is closely related to complex calorimeter based variables which are difficult to simulate properly, the contribution of $W+\text{jets}$ events to backgrounds of the $H \to WW^{(*)} \to \ell\nu\ell\nu$ analysis is determined using a data-driven approach.

A $W+\text{jets}$ control sample is constructed by relaxing the lepton identification criteria on one lepton while retaining the full identification criteria on the second lepton as well as all other object and event selection criteria. The lepton identification criteria that are relaxed mainly concern calorimeter isolation and track impact parameter requirements. In this way, one obtains an event sample which features kinematic properties similar to the nominal signal selection but with an enhanced $W+\text{jets}$ contribution. Residual contributions from processes other than $W+\text{jets}$ are subtracted using MC simulation. Since it is likely to correspond to a jet misidentified as a lepton, the lepton which passes the alternative identification criteria is referred to as the *fakeable object*.

The observation in the $W+\text{jets}$ control sample is extrapolated to the signal region by means of a *fake factor*, which reflects the probability of a fakeable object to pass the full nominal lepton identification criteria. The fake factor is defined by

$$f_\ell = \frac{N_\ell^{\text{ID}}}{N_\ell^{\text{loose ID}}}$$

and is determined as a function of the p_{T} of the fakeable object using an inclusive di-jet sample after subtracting the contributions from real leptons arising from W and Z decays as well as $W\gamma$ and $W\gamma^*$ events. Here, N_ℓ^{ID} and $N_\ell^{\text{loose ID}}$ denote the numbers of objects passing the full or the alternative lepton identification, respectively. The final $W+\text{jets}$ contribution $N^{\text{SR}}_{\text{d-d},W+\text{jets}}$ in the signal region is then calculated acoording to

$$N^{\text{SR}}_{\text{d-d},W+\text{jets}} = f_\ell(p_{\text{T}}) \otimes \left(N^{\text{CR}}_{\text{data}} - N^{\text{CR}}_{\text{MC,bkg}}\right).$$

Here, $N^{\text{CR}}_{\text{data}}$ denotes the number of events observed in the $W+\text{jets}$ control sample and $N^{\text{CR}}_{\text{MC,bkg}}$ refers to the expected number of events in the $W+\text{jets}$ control sample originating from processes other than $W+\text{jets}$, where each event contributing to $N^{\text{CR}}_{\text{data}}$ and $N^{\text{CR}}_{\text{MC,bkg}}$ is weighted with the corresponding p_{T}-dependent fake factor $f_\ell(p_{\text{T}})$.

	$12\ \text{GeV} < m_{\ell\ell} < 50\ \text{GeV}$	$\lvert m_Z - m_{\ell\ell}\rvert < 15\ \text{GeV}$
$E_{\text{T,rel}}^{\text{miss}} > 45\ \text{GeV}$	Region A	Region C
$20\ \text{GeV} < E_{\text{T,rel}}^{\text{miss}} < 45\ \text{GeV}$	Region B	Region D

Table 7.9: The four different regions in the plane of the invariant mass $m_{\ell\ell}$ of the two charged leptons versus the projected missing transverse energy $E_{\text{T,rel}}^{\text{miss}}$ as defined in the context of the ABCD method. Region A corresponds to the signal region of the same flavor channels.

The W+jets estimation described above also accounts for contributions from QCD multijet backgrounds to the $H \to WW^{(*)} \to \ell\nu\ell\nu$ analysis, where both identified lepton candidates are caused by jets rather than true leptons. However, due to the fact that in QCD di-jet events either of the two jets can be misidentified as a lepton, these events consequently contribute with twice the correct misidentification rate to the W+jets control sample and the QCD contributions in the signal region are eventually double-counted. The estimated QCD contributions in the signal region are less than 5 % of the W + jets contributions, justifying the decision not to employ a dedicated treatment of the double-counting [142].

7.3.2. Estimation of the Z /γ^*+ jets background

$(Z/\gamma^* \to ee, \mu\mu)$+jets events accompanied by a false signature of missing transverse energy constitute a delicate background to the $H \to WW^{(*)} \to \ell\nu\ell\nu$ analysis. Since the inclusive Z boson production cross section is large its contribution to the final signal region is very sensitive to the efficiency of these events to pass the missing transverse energy requirement. As the MC simulation is not expected to model this efficiency sufficiently correct, data in control samples is used to obtain an improved estimation of the Z/γ^*+jets background in the signal region. Two different methods are employed for the Z/γ^*+jets background estimation, the *ABCD method* and the *scale factor method*.

The ABCD method defines four different regions (denoted as A to D) in the two-dimensional plane of the invariant mass $m_{\ell\ell}$ of the two charged leptons versus the projected missing transverse energy $E_{\text{T,rel}}^{\text{miss}}$ as shown in Table 7.9. The estimated contribution N_{est}^{A} from $Z/\gamma^* +$ jets events to region A, which corresponds to the signal region, is determined based on the numbers of observed events N_{data}^{B}, N_{data}^{C}, and N_{data}^{D} in the regions B, C, and D, respectively, where the contributions from other backgrounds are subtracted using estimations based on the MC simulation,

$$N_{\text{est}}^{A} = N_{\text{data}}^{B} \cdot \frac{N_{\text{data}}^{C}}{N_{\text{data}}^{D}} \cdot \alpha \quad \text{with} \quad \alpha = \frac{N_{\text{MC}}^{A}/N_{\text{MC}}^{B}}{N_{\text{MC}}^{C}/N_{\text{MC}}^{D}}.$$

The correction factor α is determined using the expected yields of $Z/\gamma^* +$ jets events from MC simulation and is supposed to correct for potential differences of the corresponding ratios in $Z/\gamma^* +$ jets events. The ABCD method can be employed to estimate the $Z/\gamma^* +$ jets contributions at any selection stage unless requirements that are correlated with $m_{\ell\ell}$ or $E_{\text{T,rel}}^{\text{miss}}$ are imposed. For the final signal selection stage, which includes the $\Delta\phi_{\ell\ell}$ requirement regions C and D are evaluated without this cut and additionally without the $Z \to \tau\tau$ veto in the $H + 1$ jet channel.

The $H \to WW^{(*)} \to \ell\nu\ell\nu$ analysis also employs a control sample targeted at the SM WW process (see Section 7.3.4), where contributions from Z/γ^*+jets events have to be subtracted. Here, the $Z/\gamma^* +$ jets estimation is likewise based on the ABCD method. However, in this

context, the regions A and B are defined by $m_{\ell\ell} > m_Z + 15$ GeV and are referred to as region E and F, respectively.

The scale factor method in contrast determines the efficiencies $\varepsilon_{\text{data}}$ and ε_{MC} of events with an invariant dilepton mass $m_{\ell\ell}$ close to the Z boson mass ($|m_Z - m_{\ell\ell}| < 15$ GeV) to pass the $E_{\text{T,rel}}^{\text{miss}} > 45$ GeV requirement in data and the MC simulation, respectively. The ratio of these efficiencies is used as a *normalization factor* (NF) $\text{NF}_{Z+\text{jets}}$ to correct the normalization of the expected $Z/\gamma^* + \text{jets}$ event yields in the signal region obtained from MC simulation including the $E_{\text{T,rel}}^{\text{miss}} > 45$ GeV requirement,

$$\text{NF}_{Z+\text{jets}} = \frac{\varepsilon_{\text{data}}}{\varepsilon_{\text{MC}}}. \tag{7.5}$$

7.3.3. Top Background Estimation and Control Samples

Depending on the jet multiplicity bin the background arising from top quark production and decays constitutes a major contribution to the expected event yields. Since these processes typically involve final state jets (see Section 4.2.2), the jet veto in the $H + 0$ jets channel accomplishes an efficient rejection of these events (see also Table 7.6). However, these jets may elude a proper reconstruction by being very forward in the detector or below the jet p_{T} threshold. The *jet veto survival probability* (JVSP) obtained from MC simulation is corrected using a dedicated control sample and the estimated number of top background events $N_{\text{data,top}}^{0-\text{jets}}$ passing the jet veto is given by [143]

$$N_{\text{data,top}}^{0-\text{jets}} = N_{\text{data,top}}^{\text{Pres}} \cdot P_2^{\text{est}}.$$

Here, $N_{\text{data,top}}^{\text{Pres}}$ denotes the number of top background events observed in data passing the event preselection and P_2^{est} denotes the estimated JVSP. $N_{\text{data,top}}^{\text{Pres}}$ is determined by subtracting from the number of evens in data passing the preselection the corresponding expected event yields from other backgrounds using MC simulation, or – only in the case of the $W+\text{jets}$ contributions – a data-driven estimation. The calculation of P_2^{est} involves the determination of a corrected JVSP in a control sample which is enriched of top background events (details of this procedure can be found in Ref. [143]). The expected event yields from top backgrounds in the signal region is scaled with a NF, denoted as $\text{NF}_{\text{top}}^{0-\text{jets}}$, determined as the ratio of the data-driven and the MC simulation based estimation after the jet veto,

$$\text{NF}_{\text{top}}^{0-\text{jets}} = \frac{N_{\text{data,top}}^{0-\text{jets}}}{N_{\text{MC,top}}^{0-\text{jets}}}.$$

This NF has been evaluated in both the 2011 and the 2012 datasets individually to

$$\text{NF}_{\text{top}}^{0-\text{jets}} = \begin{cases} 1.04 \pm 0.07 & \text{(2011 dataset)} \\ 1.11 \pm 0.06 & \text{(2012 dataset)}, \end{cases}$$

where the quoted uncertainties reflect the statistical component only.

In the $H + 1$ jet channel, the top background features an efficient handle for suppression which can be exploited by imposing a veto on events containing at least one b-tagged jet. A top background control sample (*top control sample*) is constructed by reversing the b-jet veto and removing the topological selection of the final signal selection. Figure 7.8 displays the distributions of the transverse mass m_{T} of events in the top control sample of the $H + 1$ jet

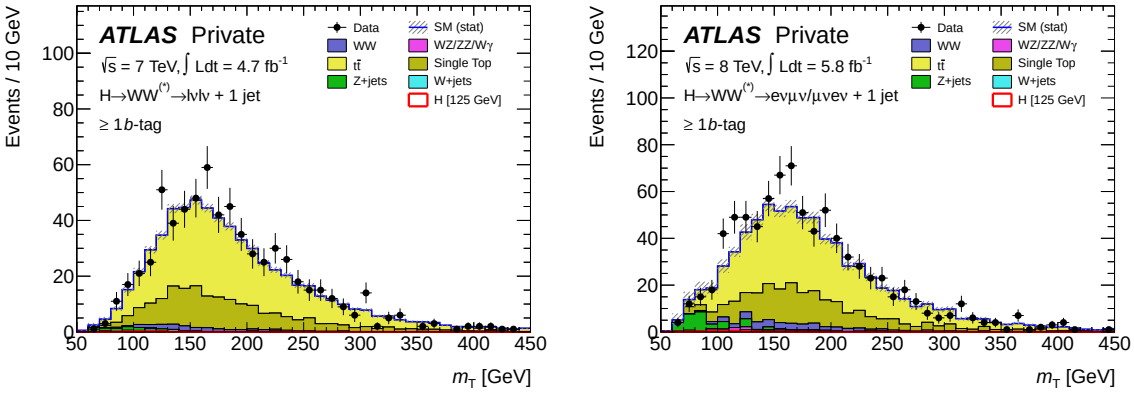

(a) 2011 dataset (b) 2012 dataset

Figure 7.8: Distributions of the transverse mass m_{T} in the top control samples of the $H+1$ jet channel in the 2011 dataset (a) and the 2012 dataset (b). For the 2011 dataset the distributions corresponds to the sum over all lepton flavors, whereas for the 2012 dataset only the sum of the opposite flavor channels is shown. The control sample is constructed by reversing the b-jet veto and removing the topological selection cuts of the final signal selection. The contributions from $W+$jets are determined using a data-driven technique described in Section 7.3.1 and for the 2011 dataset the contributions from $Z/\gamma^{*}+$jets in the same flavor channels are corrected using the scale factor method described in Section 7.3.2.

channel in the 2011 and 2012 datasets. The purity of this control samples, estimated using MC simulation, is of the order of 95 % and 90 % in the 2011 dataset and the 2012 dataset, respectively.

The top control sample is used to determine the number of top background events $N^{\mathrm{SR}}_{\mathrm{data,top}}$ in the final signal region by scaling the observed number of top background events $N^{\mathrm{CR}}_{\mathrm{data,top}}$ in the corresponding control sample,

$$N^{\mathrm{SR}}_{\mathrm{data,top}} = \alpha_{\mathrm{top}} \cdot N^{\mathrm{CR}}_{\mathrm{data,top}}. \tag{7.6}$$

$N^{\mathrm{CR}}_{\mathrm{data,top}}$ is determined by subtracting from the observed number of events $N^{\mathrm{CR}}_{\mathrm{data}}$ in the control sample the expected contributions $N^{\mathrm{CR}}_{\mathrm{MC,non-top}}$ from other backgrounds. The latter is determined using a data-driven estimation for the $W+$jets contribution and MC simulation for the remaining backgrounds, but with a normalization factor $\mathrm{NF}_{Z+\mathrm{jets}}$ determined with the scale factor method according to Equation (7.5) correcting the $Z/\gamma^{*}+$jets contributions in the same flavor channels of the 2011 dataset. The *extrapolation factor* α_{top} is determined using MC simulation and is given by the ratio of the corresponding expected event yields in the signal and the control region,

$$N^{\mathrm{CR}}_{\mathrm{data,top}} = N^{\mathrm{CR}}_{\mathrm{data}} - N^{\mathrm{CR}}_{\mathrm{MC,non-top}} \quad \text{and} \quad \alpha_{\mathrm{top}} = \frac{N^{\mathrm{SR}}_{\mathrm{MC,top}}}{N^{\mathrm{CR}}_{\mathrm{MC,top}}}. \tag{7.7}$$

An alternative interpretation of this data-driven estimation yields a normalization factor $\mathrm{NF}_{\mathrm{top}}$ which is used to scale the theoretical normalization of the expected top background event yields in the signal region based on the observations in the control sample. Rearranging

Process / Quantity	2011 dataset	2012 dataset
Single top	168.5 ± 3.5	195.5 ± 7.2
Top pairs	434.2 ± 4.5	488.5 ± 6.2
Other Backgrounds	32.5 ± 2.1	84.3 ± 7.0
Signal ($m_H = 125$ GeV)	1.2 ± 0.03	2.2 ± 0.10
Observed	676	840
Normalization factor	1.07 ± 0.04	1.10 ± 0.05

Table 7.10: Expected and observed numbers of events in the top background control samples of the $H + 1$ jet channels for the 2011 as well as the 2012 dataset. The control samples are defined by reversing the b-jet veto and removing the topological selection cuts from the final signal selection. For the 2011 dataset the numbers correspond to the sums over all lepton flavors, whereas for the 2012 dataset only the sums of the opposite flavor channels are quoted. The uncertainties reflect the statistical component only. The contribution from W + jets is determined using the data-driven technique described in Section 7.3.1 and for the 2011 dataset the contribution of Z/γ^* + jets in the same flavor channels is corrected using the scale factor method as described in Section 7.3.2.

Equations (7.6) and (7.7),

$$\begin{aligned} N^{\mathrm{SR}}_{\mathrm{data,top}} &= \frac{N^{\mathrm{SR}}_{\mathrm{MC,top}}}{N^{\mathrm{CR}}_{\mathrm{MC,top}}} \cdot \left(N^{\mathrm{CR}}_{\mathrm{data}} - N^{\mathrm{CR}}_{\mathrm{MC,non-top}}\right) \\ &= \frac{N^{\mathrm{CR}}_{\mathrm{data}} - N^{\mathrm{CR}}_{\mathrm{MC,non-top}}}{N^{\mathrm{CR}}_{\mathrm{MC,top}}} \cdot N^{\mathrm{SR}}_{\mathrm{MC,top}} \end{aligned}$$

reveals the normalization factor

$$\mathrm{NF}_{\mathrm{top}} = \frac{N^{\mathrm{CR}}_{\mathrm{data}} - N^{\mathrm{CR}}_{\mathrm{MC,non-top}}}{N^{\mathrm{CR}}_{\mathrm{MC,top}}}. \tag{7.8}$$

Table 7.10 summarizes the expected and observed numbers of events in the top control samples of the $H + 1$ jet analysis for the 2011 and the 2012 datasets. For the 2011 dataset the numbers correspond to the sums over all lepton flavors, whereas for the 2012 dataset only the sums of the opposite flavor channels are quoted. The NFs applied to the expected top background event yields in the final signal region are given by

$$\mathrm{NF}^{1-\mathrm{jet}}_{\mathrm{top}} = \begin{cases} 1.07 \pm 0.04 & \text{(2011 dataset)} \\ 1.10 \pm 0.05 & \text{(2012 dataset).} \end{cases}$$

Here, the quoted uncertainties reflect the statistical component only.

7.3.4. Standard Model WW Estimation and Control Samples

The SM WW process is an irreducible background to the $H \to WW^{(*)} \to \ell\nu\ell\nu$ analysis and depending on the Higgs boson mass hypothesis m_H its contribution after the final signal selection is a multiple of the signal expectation. However, for low Higgs boson masses $m_H <$ 200 GeV it is possible to define a corresponding control sample with a negligible signal contamination which can be used to constrain the contribution of the SM WW process to the event yields after the final signal selection. The definition of this control sample

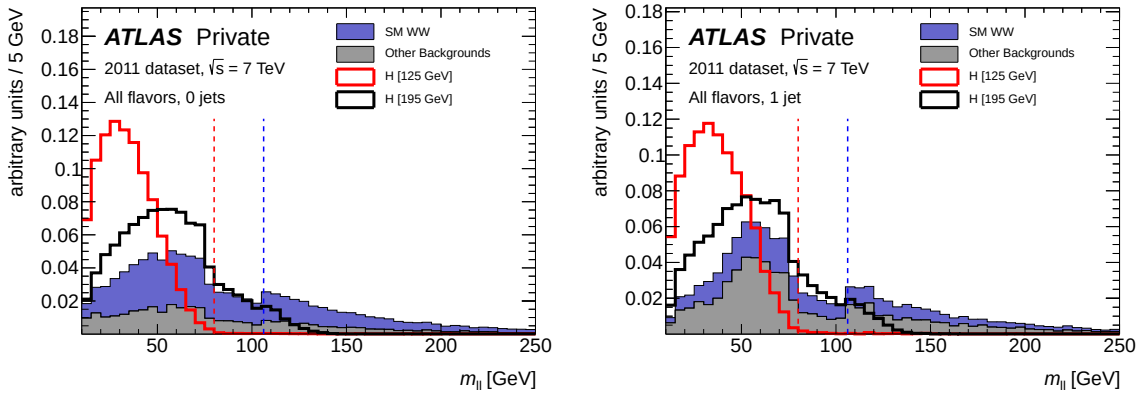

(a) $H + 0$ jets channel

(b) $H + 1$ jet channel

Figure 7.9: Distributions of the invariant mass $m_{\ell\ell}$ of the two charged leptons for the total background, split into the SM WW contributions (solid blue histograms) and the remaining backgrounds (solid gray histograms), and the $H \to WW^{(*)} \to \ell\nu\ell\nu$ signals for $m_H = 125$ GeV and 195 GeV after the jet multiplicity specific selection of the $H + 0$ jets channel (a) or the $H + 1$ jet channel (b) in the 2011 dataset. Same and opposite flavor channels have been summed. The contributions are normalized such that the distributions of the total background as well as the individual signal contributions correspond to unit area. The SM WW control samples correspond to the regions $m_{\ell\ell} > 80$ GeV or $m_{\ell\ell} > m_Z + 15$ GeV for the opposite flavor and same flavor channels, respectively (the lower bounds on $m_{\ell\ell}$ are indicated as red and blue dashed lines).

exploits the kinematic differences between the $H \to WW^{(*)} \to \ell\nu\ell\nu$ signal and the SM WW process induced by the scalar SM Higgs boson. It is constructed by removing the topological requirements of the final signal selection and requiring the invariant mass $m_{\ell\ell}$ of the two charged leptons to exceed 80 GeV. Since a Z veto is applied in the same flavor channels the threshold is effectively given by $m_Z + 15$ GeV in the ee and $\mu\mu$ channels. Two independent instances of the SM WW control sample, one corresponding to the $H + 0$ jets channel and another corresponding to the $H + 1$ jet channel, exist. Evaluated using MC simulation corresponding to the 2011 dataset, the purity of these control samples is of the order of 70 % and 45 % in the $H + 0$ jets channel and the $H + 1$ jet channel, respectively.

Figure 7.9 displays the $m_{\ell\ell}$ distribution of the total background and the $H \to WW^{(*)} \to \ell\nu\ell\nu$ signal for $m_H = 125$ GeV and 195 GeV before placing the cut on it.

As for the top background, the SM WW control samples are used to obtain corresponding normalization factors NF_{WW}, which are used to scale the theoretical normalization of the expected SM WW event yields in the signal region. The calculation follows the concept outlined in Equation (7.8) an implicitly involves corresponding extrapolation factors $\alpha_{WW}^{0-\mathrm{jets}}$ and $\alpha_{WW}^{1-\mathrm{jet}}$. The contributions from top backgrounds to the SM WW control samples are scaled using the corresponding normalization factors $\mathrm{NF}_{\mathrm{top}}$, the contributions from $W +$ jets are determined using a data-driven technique described in Section 7.3.1, and in the same flavor channels of the 2011 dataset the contributions from $Z/\gamma^* +$ jets events are determined using the modified ABCD method as described in Section 7.3.2.

Table 7.11 summarizes the expected and observed numbers of events in the SM WW control samples of the $H + 0/1$ jets channels for the 2011 and the 2012 dataset. For the 2011 dataset the numbers correspond to the sums over all lepton flavors, whereas for the 2012 dataset only the sums of the opposite flavor channels are quoted. The quoted uncertainties reflect the

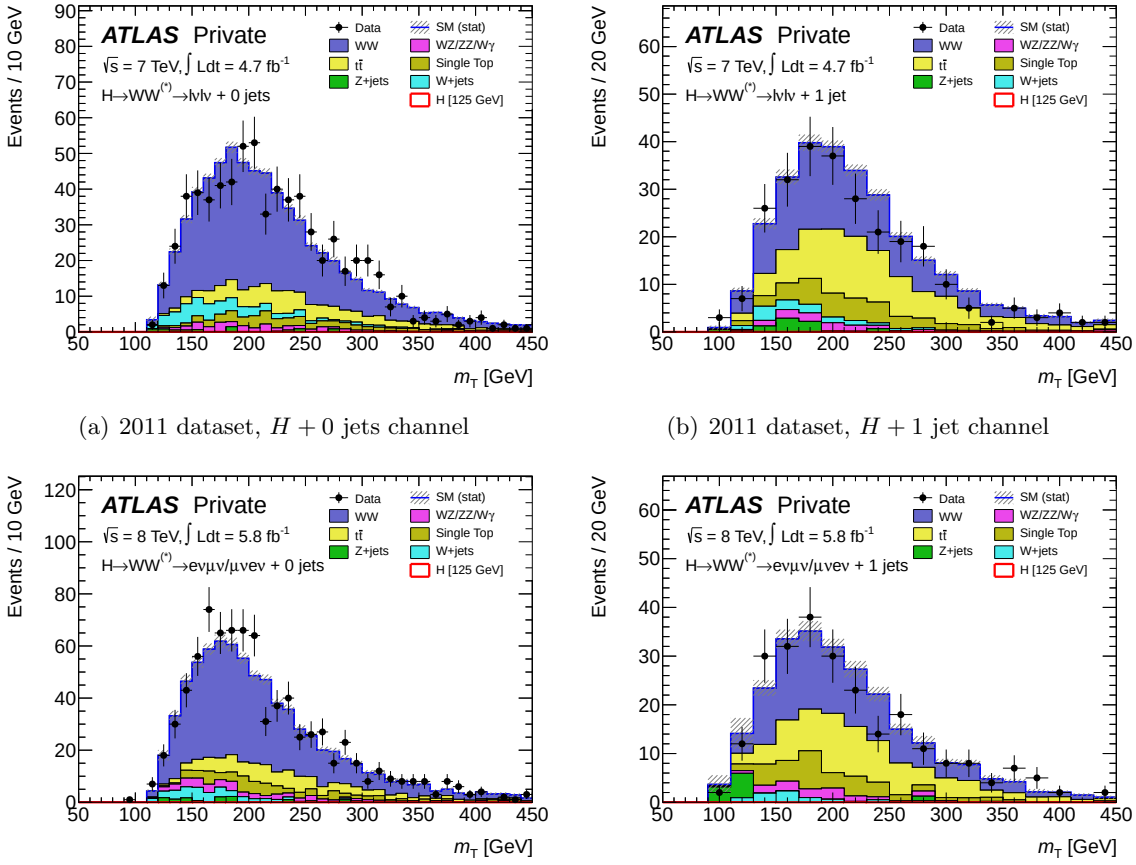

(a) 2011 dataset, $H + 0$ jets channel

(b) 2011 dataset, $H + 1$ jet channel

(c) 2012 dataset, $H + 0$ jets channel

(d) 2012 dataset, $H + 1$ jet channel

Figure 7.10: Distributions of the transverse mass m_{T} of events in the SM WW control samples of the $H + 0$ channel (left) and the $H + 1$ jet channel (right) in the 2011 dataset (top) and the 2012 dataset (bottom). For the 2011 dataset the distributions correspond to the sum over all lepton flavors, whereas for the 2012 dataset only the sum of the opposite flavor channels is shown. The control samples are constructed by removing the topological requirements of the final signal selection and requiring the invariant mass $m_{\ell\ell}$ of the two charged leptons to exceed 80 GeV in the opposite flavor channels and $m_Z + 15$ GeV in the same flavor channels.

statistical component only. The resulting SM WW normalization factors are given by

$$\mathrm{NF}_{WW}^{0-\mathrm{jets}} = \begin{cases} 1.02 \pm 0.06 & \text{(2011 dataset)} \\ 1.06 \pm 0.06 & \text{(2012 dataset)} \end{cases}$$

for the $H + 0$ jets channel and

$$\mathrm{NF}_{WW}^{1-\mathrm{jet}} = \begin{cases} 0.82 \pm 0.13 & \text{(2011 dataset)} \\ 0.99 \pm 0.15 & \text{(2012 dataset)} \end{cases}$$

for the $H + 1$ jet channel.

Process / Quantity	2011 dataset		2012 dataset	
	$H + 0$ jets	$H + 1$ jet	$H + 0$ jets	$H + 1$ jet
Standard Model WW	470.7 ± 3.3	127.7 ± 1.7	531.0 ± 5.4	112.2 ± 2.5
Single top / top pairs	134.6 ± 2.7	133.1 ± 2.8	165.7 ± 5.0	114.1 ± 4.2
Other Backgrounds	81.8 ± 3.0	31.6 ± 2.4	91.8 ± 4.5	29.9 ± 3.9
Signal ($m_H = 125$ GeV)	0.3 ± 0.03	0.1 ± 0.02	0.3 ± 0.04	0.1 ± 0.03
Observed	697	270	820	255
Normalization factor	1.02 ± 0.06	0.82 ± 0.13	1.06 ± 0.06	0.99 ± 0.15

Table 7.11: Expected and observed numbers of events in the SM WW control samples of the $H + 0/1$ jets analysis for the 2011 and the 2012 datasets. For the 2011 dataset the numbers correspond to the sums over all lepton flavors, whereas for the 2012 dataset only the sums of the opposite flavor channels are quoted. The quoted uncertainties reflect the statistical component only. The contributions from $W +$ jets are determined using a data-driven technique described in Section 7.3.1, the top backgrounds are normalized using the corresponding normalization factors as described in Section 7.3.3, and for the 2011 dataset the contributions of $Z/\gamma^* +$ jets in the same flavor channels are corrected using the modified ABCD method as described in Section 7.3.2.

7.4. Systematic Uncertainties

Measurements and predictions in high-energy physics generally involve two fundamentally different types of uncertainties. *Statistical uncertainties* arise from a finite number of events a measurement or prediction is based on. Usually, the number of events is either limited by the extent of the simulated MC samples or by the amount of recorded collision data. In principle, any of the two cases allows a reduction of the *relative* statistical uncertainties down to an arbitrary level, since it scales with the number of involved events N like $\mathcal{O}(1/\sqrt{N})$. However, one is usually bound to practical constraints and has to accept and deal with a finite or even non-negligible statistical uncertainty.

In contrast to that, *systematic uncertainties* are typically induced by an imperfect knowledge of parameters entering the measurement or prediction and do not allow a reduction by scaling the extent of the considered data. An example for a source of a systematic uncertainty in the $H \to WW^{(*)} \to \ell\nu\ell\nu$ analysis is the jet energy calibration (see Section 2.3.4), which affects the jet energy measurement and thereby may cause uncertainties on the jet multiplicity categorization of events.

The following sections outline the theoretical and experimental sources of systematic uncertainties in the context of the $H \to WW^{(*)} \to \ell\nu\ell\nu$ analysis. The description of experimental systematic uncertainties places emphasis on the assessment for the purpose of a visualization in MC distributions. Though the sources are common, the treatment of systematic uncertainties in the scope of the statistical analysis (see Section 7.5.1) is unrelated to the aforesaid.

7.4.1. Theoretical Uncertainties

Theoretical systematic uncertainties mainly arise from theoretical cross section calculations and their dependence related to he choice of energy scales and to parton distribution functions (PDFs). The description of theoretical systematic uncertainties follows Refs. [24] and [25] for the 2011 dataset and the 2012 dataset, respectively.

Uncertainties on the $H \to WW^{(*)} \to \ell\nu\ell\nu$ signal production cross section are determined following the procedures explained in Refs. [90, 144]. By independently varying the QCD renormalization and factorization scales up and down by a factor of two, the uncertainties on the inclusive cross sections of the gluon fusion process as well as the production in association with at least one or at least two jets are determined. These are used to derive uncertainties in exclusive jet multiplicity bins including anti-correlations induced by migrations between different jet multiplicities. For a Higgs boson mass hypothesis of $m_H = 125$ GeV, these uncertainties amount to ± 21 %(± 17 %) for the $H+0$ jets channel and ± 31 %(± 36 %) for the $H+1$ jet channel in the 2011 (2012) dataset. For large Higgs boson masses m_H an additional uncertainty related to the Higgs boson lineshape description in the Powheg MC generator is added in quadrature for both the gluon fusion and the vector-boson fusion signal process and amounts to $\pm 150\ \% \cdot (m_H/1\ \text{TeV})^3$ [144–147].

Following Refs. [39, 124, 148, 149], uncertainties related to PDFs are estimated using the envelopes of error sets as well as different PDF sets, applied separately to quark-quark, quark-gluon, and gluon-gluon initiated processes. The relative PDF uncertainty on the accepted cross section of the gluon fusion signal process is approximately ± 8 % at $m_H = 125$ GeV.

The uncertainties related to the underlying event and parton showering are taken into account but turn out to be negligible compared to the scale uncertainties on the cross sections in exclusive jet multiplicity bins. Uncertainties on the modeling of signal and background processes are estimated by using alternative MC generators for individual processes.

The theoretical uncertainties on the extrapolation factors $\alpha_{WW}^{0-\text{jets}}$ and $\alpha_{WW}^{1-\text{jet}}$ (see Section 7.3.4) from scale variations, PDFs, and the MC modeling amount to ± 5.7 % and ± 6.1 %, respectively [150].

7.4.2. Experimental Uncertainties

The acceptance of a data event is affected by numerous experimental parameters λ_k which are only known up to an uncertainty σ_k corresponding to one standard deviation. These parameters are for instance related to the energy calibration of physical objects. MC simulation, normalized to theoretical cross sections and to some extent corrected for an imperfect modeling using data-driven techniques, is used to obtain an estimation of the expected event yield N for a certain physics process after a certain event selection. N is a function of the experimental parameters λ_k

$$N(\lambda_1, \ldots, \lambda_n).$$

Since the calculation of $N(\lambda_1, \ldots, \lambda_n)$ is a complex computational task and by no means related to a simple analytical expression, the determination of the systematic uncertainty σ_N^{sys} on the expected event yield N induced by the uncertainties σ_k on the parameters λ_k is not straightforward. One approach towards an assessment of σ_N^{sys} is driven by an evaluation of $N(\lambda_1, \ldots, \lambda_n)$ with the central values of the input parameters as well as after systematically varying individual input parameters by one associated standard deviation. This results in a central value $N_0 = N(\lambda_1, \ldots, \lambda_n)$ of the expected event yield as well as in systematically shifted event yields

$$N_{\pm k} = N(\lambda_1, \ldots, \lambda_k \pm \sigma_k, \ldots, \lambda_n).$$

This can be translated into an approximate systematic uncertainty $(\Delta N)_k$ of the expected event yield N induced by the uncertainty on the input parameter λ_k,

$$\Delta_k N = \frac{|N_{+k} - N_{-k}|}{2}.$$

Selection	Signal ($m_H = 125$ GeV)		Total Background	
	2011 dataset	2012 dataset	2011 dataset	2012 dataset
H + 0 jets channel				
Trigger efficiency	–	±1.2 %	–	±0.6 %
W + jets fake factor	–	–	±4.9 %	±1.2 %
Electron energy scale/res.	±0.7 %	±0.5 %	±0.3 %	±0.4 %
Muon momentum sc./res.	±0.4 %	negl.	±0.3 %	±0.1 %
Lepton efficiency	±4.0 %	±3.4 %	±1.5 %	±0.6 %
Jet energy scale/resolution	±5.4 %	±6.5 %	±2.8 %	±1.0 %
Pile-up	±0.9 %	±0.9 %	±1.0 %	±0.5 %
$E_{\mathrm{T}}^{\mathrm{miss}}$ terms	±1.5 %	±0.4 %	±1.1 %	±0.2 %
H + 1 jets channel				
Trigger efficiency	–	±1.0 %	–	±0.5 %
W + jets fake factor	–	–	±8.4 %	±2.0 %
Electron energy scale/res.	±0.6 %	±0.7 %	negl.	±0.9 %
Muon momentum sc./res.	±0.3 %	negl.	±0.1 %	negl.
Lepton efficiency	±3.9 %	±3.3 %	±0.5 %	±0.6 %
Jet energy scale/resolution	±4.2 %	±3.4 %	±8.1 %	±1.9 %
b-tagging	±0.7 %	±1.1 %	±5.8 %	±0.7 %
Pile-up	±4.8 %	±4.1 %	±2.4 %	±0.6 %
$E_{\mathrm{T}}^{\mathrm{miss}}$ terms	±7.5 %	±3.1 %	±3.8 %	±0.7 %

Table 7.12: Impact of the main experimental systematic uncertainties on the expected event yields after the final signal selection in the $H + 0$ and $H + 1$ jet channels. The numbers correspond to the sums of the same and opposite flavor channels for the 2011 dataset and to the sums of the opposite flavor channels for the 2012 dataset and are determined by systematically varying corresponding input parameters of the analysis within their uncertainties. Numbers less than 0.1 % are quoted as "negl." For the 2011 dataset, the uncertainties related to the trigger efficiencies have not been evaluated.

Assuming the uncertainties σ_k on the input parameters λ_k are uncorrelated, the approximate total systematic uncertainty σ_N^{sys} is given by

$$\sigma_N^{\mathrm{sys}} = \sqrt{\sum_k (\Delta_k N)^2}.$$

This approach of determining the impact of the uncertainties σ_k on the final expected event yield N implicitly accounts for constraints imposed by the observed data in control regions if the computation of $N(\lambda_1, \ldots, \lambda_n)$ involves data-driven corrections. However, it does neither account for potential correlations present in the uncertainties on the input parameters nor does it allow for asymmetric effects. Furthermore, in case the prediction of the expected event yield N possesses large statistical uncertainties, the obtained systematic uncertainty may overestimate the true systematic uncertainty due to single simulated MC events with large individual weights satisfying and failing acceptance upon a systematic variation.

Uncertainties related to the trigger, lepton as well as the b-tagging efficiencies are assessed by varying the corresponding efficiency scale factors within their uncertainties. Uncertainties related to the energy and momentum scales and resolutions of the electron, muon and jet reconstruction are determined by varying the corresponding calibration parameters within their uncertainties. The uncertainties on the data-driven W + jets estimation are obtained from a variation of the fake factor (see Section 7.3.1) within its uncertainty. The pile-up related uncertainties are estimated by varying a parameter affecting the pile-up reweighting (see also Section 5.2.3). Finally, the $E_{\mathrm{T}}^{\mathrm{miss}}$ related uncertainties are estimated by varying the calibration of contributing terms in the calculation of $E_{\mathrm{T}}^{\mathrm{miss}}$.

Table 7.12 summarizes the impact of several sources of experimental systematic uncertainties on the expected event yields of the $H \to WW^{(*)} \to \ell\nu\ell\nu$ signal with $m_H = 125$ GeV and the total background after the final signal selection. The numbers correspond to the sums of the same and opposite flavor channels for the 2011 dataset and to the sums of the opposite flavor channels for the 2012 dataset. The dominant uncertainties are related to the jet energy calibration (see Section 2.3.4), the determination of the W + jets fake factor in the 2011 dataset (see Section 7.3.1), pile-up, and the calculation of the missing transverse energy in the $H + 1$ jet channel.

The difference in corresponding numbers in the 2011 and the 2012 dataset reflect on the one hand different sample compositions mainly due to the omitting the same flavor channels in the 2012 dataset. On the other hand, differences arise from altered object selection criteria and the split of the $e\mu$ and the μe channels in the 2012 dataset, which results in a significant reduction of the systematic uncertainties related to the W + jets estimation.

The uncertainties on the total integrated luminosity amount to ± 3.9 % in the 2011 dataset [151, 152], and preliminarily to ± 3.6 % in the 2012 dataset based on the same calibration. However, due to the employment of control samples this uncertainty mainly affects the signal prediction.

7.5. Results

Tables 7.13 and 7.14 present the expected and observed numbers of events after the application of successive selection requirements in the 2011 dataset and the 2012 dataset, respectively. For the 2011 dataset the numbers correspond to the sums of same and opposite flavor channels, whereas for the 2012 dataset only the opposite flavor channels are summed. The expected event yields are determined using MC simulation and are normalized to the integrated luminosity in data. Starting from jet multiplicity specific selection stages, the numbers for the SM WW and top backgrounds are corrected using the NF derived from the corresponding control samples. In the same flavor channels of the 2011 dataset, the Z/γ^* + jets contributions are corrected using the ABCD method, or – for selection stages including topological cuts on $\Delta\phi_{\ell\ell}$ or $m_{\ell\ell}$ – the scale factor method (see Section 7.3.2). The W + jets contributions are determined using a data-driven technique described in Section 7.3.1.

Figure 7.11 displays the distributions of the transverse mass m_{T} of events observed in data as well as the expectations from the total background split into individual processes in the $H + 0$ and $H + 1$ jet channels of the 2011 and 2012 datasets. The expected contributions from a $H \to WW^{(*)} \to \ell\nu\ell\nu$ signal for $m_H = 125$ GeV are overlaid as red histograms. The expected event yields are normalized to the total integrated luminosity of the data and the background contributions are corrected or estimated using control samples in data where applicable as described in Section 7.3. The corresponding expected and observed event yields

	H [125 GeV]	WW	$WZ/ZZ/W\gamma$	Top	Z/γ^*+jets	$W+$jets	Total Bkg.	Observed
Lepton p_{T}	181 ± 0.40	3871 ± 9.55	3214 ± 20.7	18086 ± 29.9	2800788 ± 1309	3160 ± 37.1	2829118 ± 1310	2823123
Opposite Charge	178 ± 0.39	3856 ± 9.53	2734 ± 15.8	17975 ± 29.8	2793618 ± 1308	2374 ± 36.2	2820557 ± 1309	2816240
$m_{\ell\ell} > 10$ (12) GeV	175 ± 0.39	3848 ± 9.52	2716 ± 15.7	17944 ± 29.8	2790757 ± 1307	2194 ± 35.9	2817460 ± 1308	2806551
Z veto (for $ee, \mu\mu$)	173 ± 0.39	3421 ± 8.97	560 ± 8.00	15999 ± 28.1	278757 ± 404	1403 ± 20.7	300140 ± 406	298691
$E_{\mathrm{T,rel}}^{\mathrm{miss}} > 25$ (45) GeV	90.8 ± 0.28	1829 ± 6.62	178 ± 4.82	8162 ± 20.5	1523 ± 27.9	342 ± 5.92	12033 ± 36.1	12231
0j: Jet veto	56.7 ± 0.23	1273 ± 5.58	96.6 ± 3.71	269 ± 3.96	1039 ± 23.7	217 ± 3.63	2894 ± 25.2	2849
0j: $m_{\ell\ell} < 50$ GeV	45.2 ± 0.21	312 ± 2.79	40.8 ± 2.77	48.2 ± 1.76	168 ± 8.81	69.5 ± 2.00	639 ± 10.0	645
0j: $p_{\mathrm{T}}^{\ell\ell} > 30$ (45) GeV	40.1 ± 0.19	282 ± 2.65	34.8 ± 2.51	45.0 ± 1.70	28.0 ± 3.77	49.2 ± 1.52	439 ± 5.72	443
0j: $\Delta\phi_{\ell\ell} < 1.8$ rad	39.0 ± 0.19	276 ± 2.62	33.3 ± 2.43	44.5 ± 1.69	27.7 ± 3.76	44.1 ± 1.42	425 ± 5.64	429
0j: $0.75 \cdot m_H < m_{\mathrm{T}} < m_H$	25.9 ± 0.15	108 ± 1.66	11.7 ± 1.29	11.2 ± 0.85	14.1 ± 2.54	27.4 ± 1.11	172 ± 3.58	174
1j: $N_{\mathrm{jets}} = 1$	22.7 ± 0.13	343 ± 2.58	55.8 ± 2.66	1874 ± 10.3	357 ± 12.7	85.4 ± 2.90	2716 ± 17.0	2706
1j: b-jet veto	20.9 ± 0.13	319 ± 2.48	52.0 ± 2.55	550 ± 5.68	332 ± 12.2	75.9 ± 2.47	1330 ± 14.2	1369
1j: $p_{\mathrm{T}}^{\mathrm{tot}} < 30$ GeV	14.0 ± 0.10	226 ± 2.10	34.1 ± 2.16	261 ± 3.96	108 ± 6.23	37.4 ± 1.69	666 ± 8.15	684
1j: $Z \to \tau\tau$ veto	14.0 ± 0.10	220 ± 2.07	33.6 ± 2.16	250 ± 3.88	84.6 ± 5.70	37.7 ± 1.66	627 ± 7.70	644
1j: $m_{\ell\ell} < 50$ GeV	10.9 ± 0.09	48.8 ± 0.97	13.5 ± 1.57	50.4 ± 1.82	23.6 ± 2.73	12.0 ± 0.96	148 ± 3.88	170
1j: $\Delta\phi_{\ell\ell} < 1.8$ rad	10.1 ± 0.09	44.5 ± 0.92	13.1 ± 1.57	48.2 ± 1.78	10.0 ± 1.73	9.9 ± 0.82	126 ± 3.19	145
1j: $0.75 \cdot m_H < m_{\mathrm{T}} < m_H$	6.3 ± 0.07	16.0 ± 0.55	4.6 ± 0.97	12.1 ± 0.90	4.6 ± 1.19	5.0 ± 0.54	42.4 ± 1.94	56

Table 7.13: Expected and observed numbers of events in the 2011 dataset after applying successive cuts of the $H+0$ and $H+1$ jet channels. The numbers correspond to the sums of the same and opposite flavor channels. Cut thresholds differing between the same and opposite flavor channels are quoted for the opposite (same) flavor channels. The column "H [125 GeV]" refers to the $H \to WW^{(*)} \to \ell\nu\ell\nu$ signal for $m_H = 125$ GeV taking into account the ggF, VBF and WH/ZH production modes. The column "Top" refers to the sums of the contributions from single top and top quark pair production. The expected event yields are determined using MC simulation and are normalized to the integrated luminosity in data. The quoted uncertainties reflect the statistical component only. Starting from jet multiplicity specific selection stages, the numbers for the SM WW and top background are corrected using the NFs derived from the corresponding control samples. In the same flavor channels, the Z/γ^*+jets contributions are corrected using the ABCD method, or – for selection stages including topological cuts on $\Delta\phi_{\ell\ell}$ or $m_{\ell\ell}$– the scale factor method (see Section 7.3.2). The $W+$jets contributions are determined using a data-driven technique described in Section 7.3.1. For the cut on m_{T} a mass of $m_H = 125$ GeV is assumed.

	H [125 GeV]	WW	$WZ/ZZ/W\gamma$	Top	$Z/\gamma^* + \text{jets}$	$W + \text{jets}$	Total Bkg.	Observed
Lepton p_{T}	138 ± 0.74	2820 ± 12.7	1141 ± 10.8	15821 ± 39.4	8557 ± 107	1255 ± 13.8	29594 ± 116	30510
Opposite Charge	136 ± 0.73	2813 ± 12.7	566 ± 7.58	15773 ± 39.1	8396 ± 106	799 ± 12.3	28348 ± 114	29368
$m_{\ell\ell} > 10$ GeV	135 ± 0.73	2810 ± 12.7	559 ± 7.51	15761 ± 39.1	8393 ± 106	797 ± 12.3	28320 ± 114	29339
$E_{\mathrm{T,rel}}^{\mathrm{miss}} > 25$ GeV	86.9 ± 0.59	1879 ± 10.7	230 ± 5.02	9752 ± 31.8	1237 ± 39.4	277 ± 6.27	13376 ± 52.4	13410
0j: Jet veto	47.5 ± 0.44	1308 ± 8.98	125 ± 3.94	293 ± 6.85	850 ± 32.0	138 ± 4.00	2714 ± 34.4	2691
0j: $p_{\mathrm{T}}^{\ell\ell} > 30$ GeV	43.4 ± 0.42	1077 ± 8.14	99.2 ± 3.53	264 ± 6.52	46.9 ± 7.69	102 ± 2.29	1589 ± 13.6	1664
0j: $m_{\ell\ell} < 50$ GeV	34.9 ± 0.38	244 ± 3.96	32.6 ± 2.05	45.1 ± 2.84	5.3 ± 2.27	29.0 ± 1.13	356 ± 5.86	421
0j: $\Delta\phi_{\ell\ell} < 1.8$ rad	33.6 ± 0.37	234 ± 3.87	31.6 ± 2.02	44.3 ± 2.82	4.0 ± 1.87	25.0 ± 1.05	339 ± 5.62	407
0j: $0.75 \cdot m_H < m_{\mathrm{T}} < m_H$	20.2 ± 0.29	101 ± 2.56	11.5 ± 1.19	11.4 ± 1.18	1.9 ± 1.31	15.4 ± 0.80	142 ± 3.42	185
1j: $N_{\mathrm{jets}} = 1$	24.9 ± 0.31	396 ± 4.64	74.2 ± 2.70	2131 ± 16.8	283 ± 19.8	68.4 ± 3.05	2953 ± 26.7	2874
1j: b-jet veto	21.1 ± 0.28	334 ± 4.23	56.2 ± 2.34	464 ± 8.31	236 ± 18.1	53.0 ± 2.49	1144 ± 20.6	1115
1j: $p_{\mathrm{T}}^{\mathrm{tot}} < 30$ GeV	12.2 ± 0.22	210 ± 3.42	30.5 ± 1.79	203 ± 5.83	124 ± 13.6	23.3 ± 1.61	590 ± 15.4	611
1j: $Z \to \tau\tau$ veto	12.2 ± 0.22	204 ± 3.37	28.8 ± 1.73	193 ± 5.73	97.8 ± 11.7	22.7 ± 1.56	547 ± 13.6	580
1j: $m_{\ell\ell} < 50$ GeV	9.2 ± 0.19	37.3 ± 1.45	10.0 ± 1.10	32.8 ± 2.45	16.1 ± 4.56	8.0 ± 0.91	104 ± 5.56	122
1j: $\Delta\phi_{\ell\ell} < 1.8$ rad	8.6 ± 0.18	33.7 ± 1.37	9.2 ± 1.05	31.2 ± 2.39	3.2 ± 2.28	6.4 ± 0.72	83.6 ± 3.80	106
1j: $0.75 \cdot m_H < m_{\mathrm{T}} < m_H$	4.8 ± 0.14	11.8 ± 0.82	1.9 ± 0.40	9.7 ± 1.31	0.1 ± 0.06	2.3 ± 0.40	25.9 ± 1.64	38

Table 7.14: Expected and observed numbers of events in the 2012 dataset after applying successive cuts of the $H+0$ and $H+1$ jet channels. The numbers correspond to the sums of the opposite flavor channels. The column "H [125 GeV]" refers to the $H \to WW^{(*)} \to \ell\nu\ell\nu$ signal for $m_H = 125$ GeV taking into account the ggF, VBF and WH/ZH production modes. The column "Top" refers to the sums of the contributions from single top and top quark pair production. The expected event yields are determined using MC simulation and are normalized to the integrated luminosity in data. The quoted uncertainties reflect the statistical component only. Starting from jet multiplicity specific selection stages, the numbers for the SM WW and top background are corrected using the NFs derived from the corresponding control samples. The $W+\text{jets}$ contributions are determined using a data-driven technique described in Section 7.3.1. For the cut on m_{T} a mass of $m_H = 125$ GeV is assumed.

are listed in Table 7.15.

In the $H + 1$ jet channel as well as the $H + 0$ jets same flavor channel of the 2011 dataset the number of observed events is higher than the expectation from background processes alone. The corresponding m_{T} distributions do not feature a clear indication of the source of these excess events. In the $H + 0$ jets opposite flavor channel the observed number of events is below the background-only expectation, though compatible with the latter within uncertainties.

In the 2012 dataset, an excess of events over the expected background is observed in the opposite flavor channels of both the $H + 0$ jets as well as the $H + 1$ jet channels. Here, it is most prominent in the $H + 0$ jets channel and the excess events are distributed in m_{T} as expected from a $m_H = 125$ GeV Higgs boson signal, though with a signal strength larger than one. Since the same flavor channels of the 2012 dataset have been kept blinded (see also Section 5.3), no results are available for these channels.

The interpretation of these results with respect to different Higgs boson hypotheses requires a dedicated statistical analysis as it is outlined in the following section.

7.5.1. Statistical Analysis

A proper assessment of the implications of an observation has to involve an appropriate statistical analysis by means of testing corresponding hypotheses with respect to the observed data [153]. Aiming for the discovery of a new physics process, one usually goes for the exclusion of the background-only hypothesis H_0 by revealing that its incompatibility with the observed data exceeds a certain threshold. This incompatibility can be quantified through the probability p_0 to observe data which is less compatible with H_0 than the actual observation assuming H_0 is true. The particle physics community has agreed to claim a discovery if $p_0 < 2.87 \cdot 10^{-7}$, which corresponds to the probability to find a Gaussian distributed variable five standard deviations above its mean (referred to as "5σ"). That is, H_0 is rejected only if this is about to happen falsely less than one time out of at least approximately 3.5 million times where H_0 is true.

Not observing any statistically significant deviation of the data from the background-only hypothesis, one can try to exclude a set of alternative (signal) hypotheses $H_1(\vec{\theta})$ to a given level of confidence. The set of signal hypotheses may be parametrized by $\vec{\theta}$, which in the case of the $H \to WW^{(*)} \to \ell\nu\ell\nu$ analysis includes the Higgs boson mass hypothesis m_H. In this context one usually introduces an artificial *signal strength parameter* μ, which multiplies the theoretical signal cross section. Consequently, the level of confidence of the exclusion of a certain signal hypothesis becomes a function of μ and one can in turn set upper limits on μ corresponding to a minimal predefined level of confidence. A commonly employed procedure is based on the *modified frequentist method* known as CL_s [154]. It defines a quantity CL_s as

$$\mathrm{CL}_s = \frac{p_\mu}{1 - p_b},$$

where p_μ (p_b) is the probability to observe data which is more (less) background-like than the actual observation under the assumption of H_1 (H_0). Here, one typically regards $H_1(\vec{\theta})$ as excluded if CL_s is less than 0.05. At any point in the $\vec{\theta}$-space with $\mathrm{CL}_s < 0.05$ the probability of having falsely excluded a true signal with these parameters is less than 5 %.

Profile Likelihood Ratio

In order to obtain the p-values mentioned in the previous paragraph, the $H \to WW^{(*)} \to \ell\nu\ell\nu$ analysis employs several slightly different *test statistics* depending on the hypothesis to test.

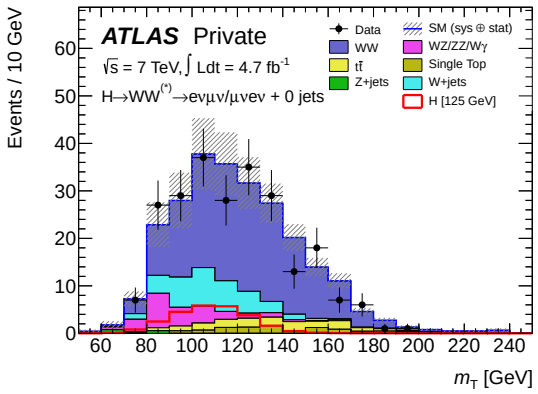

(a) 2011 dataset, $e\mu + \mu e$, $H + 0$ jets

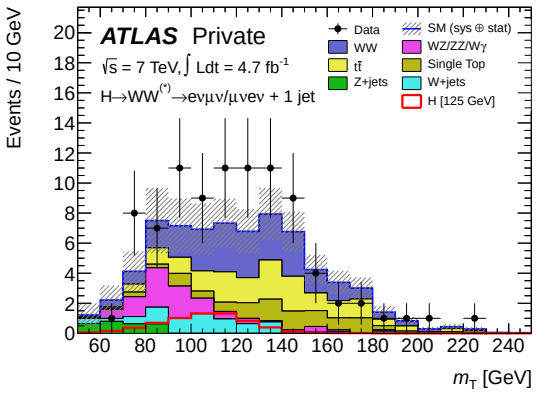

(b) 2011 dataset, $e\mu + \mu e$, $H + 1$ jet

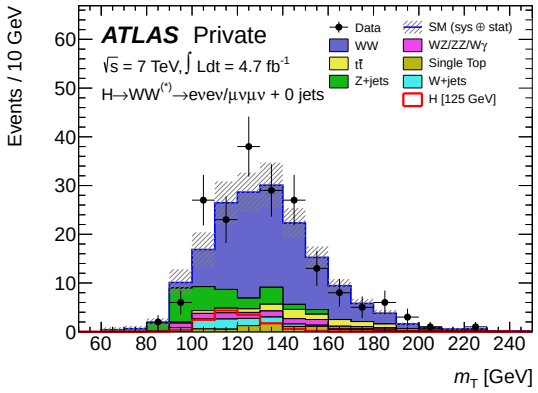

(c) 2011 dataset, $ee + \mu\mu$, $H + 0$ jets

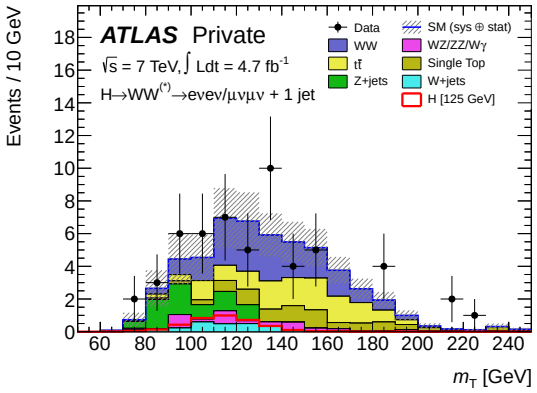

(d) 2011 dataset, $ee + \mu\mu$, $H + 1$ jet

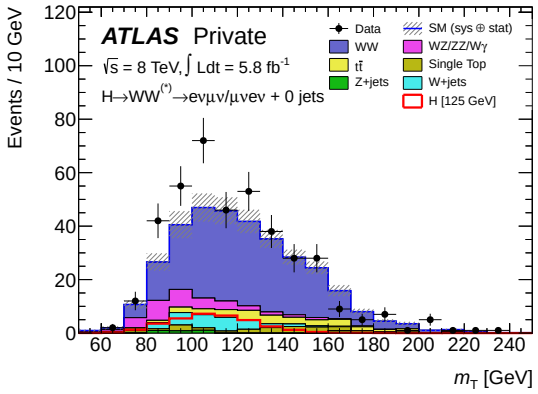

(e) 2012 dataset, $e\mu + \mu e$, $H + 0$ jets

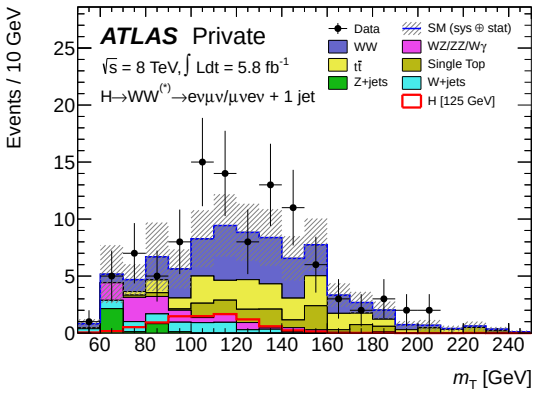

(f) 2012 dataset, $e\mu + \mu e$, $H + 1$ jet

Figure 7.11: Distributions of the transverse mass m_{T} in the final signal region of the $H+0$ and $H + 1$ jet channels. The black markers indicate the observations in data. The solid colored histograms reflect the background expectations normalized to the total integrated luminosity in data and corrected or estimated using control samples where applicable as described in Section 7.3. The expected contributions from a $H \to WW^{(*)} \to \ell\nu\ell\nu$ signal for $m_H = 125$ GeV are indicated as red histograms. The hatched areas indicate the total uncertainties on the background predictions.

(a) $H + 0$ jets channel

Process	2011 dataset		2012 dataset
	Opposite flavor	Same flavor	Opposite flavor
Backgrounds			
SM WW	164.1 ± 2.0	111.4 ± 1.7	233.8 ± 3.9
$WZ/ZZ/W\gamma$	23.0 ± 2.3	10.3 ± 0.9	31.6 ± 2.0
Single top	9.6 ± 0.9	8.0 ± 0.8	17.2 ± 2.3
Top pairs	15.8 ± 0.9	11.1 ± 0.8	27.1 ± 1.6
$Z/\gamma^* + \text{jets}$	1.6 ± 0.8	26.1 ± 3.7	4.0 ± 1.9
$W + \text{jets}$	35.0 ± 1.3	9.0 ± 0.7	25.0 ± 1.1
Total	249.2 ± 3.6	175.9 ± 4.3	338.8 ± 5.6
Signal			
$m_H = 125$ GeV	25.7 ± 0.2	13.3 ± 0.1	33.6 ± 0.4
Observed	239	190	407

(b) $H + 1$ jet channel

Process	2011 dataset		2012 dataset
	Opposite flavor	Same flavor	Opposite flavor
Backgrounds			
SM WW	25.2 ± 0.7	19.3 ± 0.6	33.7 ± 1.4
$WZ/ZZ/W\gamma$	9.6 ± 1.4	3.5 ± 0.7	9.2 ± 1.1
Single top	9.8 ± 0.9	7.3 ± 0.8	11.0 ± 1.9
Top pairs	17.7 ± 1.0	13.4 ± 0.9	20.1 ± 1.4
$Z/\gamma^* + \text{jets}$	2.9 ± 1.0	7.1 ± 1.4	3.2 ± 2.3
$W + \text{jets}$	7.3 ± 0.7	2.6 ± 0.5	6.4 ± 0.7
Total	72.4 ± 2.4	53.2 ± 2.1	83.6 ± 3.8
Signal			
$m_H = 125$ GeV	6.4 ± 0.1	3.7 ± 0.1	8.6 ± 0.2
Observed	90	55	106

Table 7.15: Expected and observed numbers of events passing the final signal selection of the $H+0$ jets channel (a) and the $H+1$ jet channel (b) in the 2011 dataset as well as the 2012 dataset. The signal and background contributions are determined from MC simulation and are normalized to the total integrated luminosity of the data. The background contributions are corrected or estimated using control samples in data where applicable (see Section 7.3). The quoted uncertainties reflect the statistical component only.

These test statistics are calculated from a *profile likelihood ratio* based on a binned *likelihood function* $\mathcal{L}(\mu, \vec{\theta}, m_H)$. Here, μ is the signal strength parameter, m_H is the hypothesized Higgs boson mass, and $\vec{\theta}$ is a set of *nuisance parameters*[9] which are used to let the normalizations of backgrounds with corresponding control samples float and to parametrize systematic uncertainties.

For each channel of the analysis, given by the combinations of the lepton flavor channels and the jet multiplicity channels, an individual likelihood function is constructed from Poisson probability terms of expected and observed event yields in the signal and the control regions as well as from additional terms representing external constraints on the nuisance parameters. These individual likelihood functions are then combined to one global likelihood function by multiplication. For the analysis of the 2011 dataset, the individual channels are given by $(ee, \mu\mu, e\mu + \mu e) \times (H + 0 \text{ jets}, H + 1 \text{ jet}, H + 2 \text{ jets})$, whereas for the 2012 dataset the two opposite flavor channels $e\mu$ and μe are split to take advantage of an reduced systematic uncertainty on the W + jets background estimation. The $H + 2$ jets channel is included in the statistical results presented in the following, even though details of this channel are given in Chapter 8. In the $H + 0$, $H + 1$ and $H + 2$ jets channel the final signal region considered in the likelihood function is given by five, three and one bin in m_{T}, respectively. The bins are chosen such that the expected total backgrounds are equally distributed among them.

In case of testing the hypothesis H_0, the test statistic q_0 is constructed as

$$q_0 = \begin{cases} -2 \ln \dfrac{\mathcal{L}(0, \hat{\vec{\theta}}_\mu)}{\mathcal{L}(\hat{\mu}, \hat{\vec{\theta}})} & \hat{\mu} \geq 0 \\ 0 & \hat{\mu} < 0. \end{cases}$$

Here, $\mathcal{L}(\mu, \vec{\theta})$ denotes the global likelihood function. $\hat{\mu}$ and $\hat{\vec{\theta}}$ denote the values of μ and $\vec{\theta}$, respectively, that simultaneously maximize the likelihood function, whereas $\hat{\vec{\theta}}_\mu$ denotes the value of $\vec{\theta}$ that maximizes the likelihood function for a given value of μ.

The p-values corresponding to a certain observation are obtained from asymptotic approximations of the sampling distributions of the corresponding test statistics [153].

It is worthwhile to emphasize that the statistical analysis performed in the $H \to WW^{(*)} \to \ell\nu\ell\nu$ analysis is independent of the numerical values of the NFs and the systematic uncertainties quoted in Sections 7.3 and 7.4, respectively.

Results of the Statistical Analysis

Based on the 2011 dataset [24], Figure 7.12 shows the expected and observed 95 % CL upper limits on the inclusive Higgs boson production cross section divided by the SM prediction as a function of the Higgs boson mass hypothesis m_H. Generally, a SM Higgs boson with a mass m_H can be excluded at better than 95 % CL if the corresponding upper limit on the cross section ratio is below one. In the 2011 dataset the observed 95 % CL exclusion interval in m_H is given by 133 GeV $\leq m_H \leq$ 261 GeV, whereas the expected exclusion interval assuming the absence of a signal is given by 127 GeV $\leq m_H \leq$ 233 GeV. That is, driven by the excess observed in the 2011 data, which corresponds to a minimal observed p_0 of 0.15, the observed signal exclusion is weaker than the expected one.

[9] Nuisance parameters are parameters of the model which are not of primary interest but which affect the predictions of the model. See e.g. Ref. [153] for details.

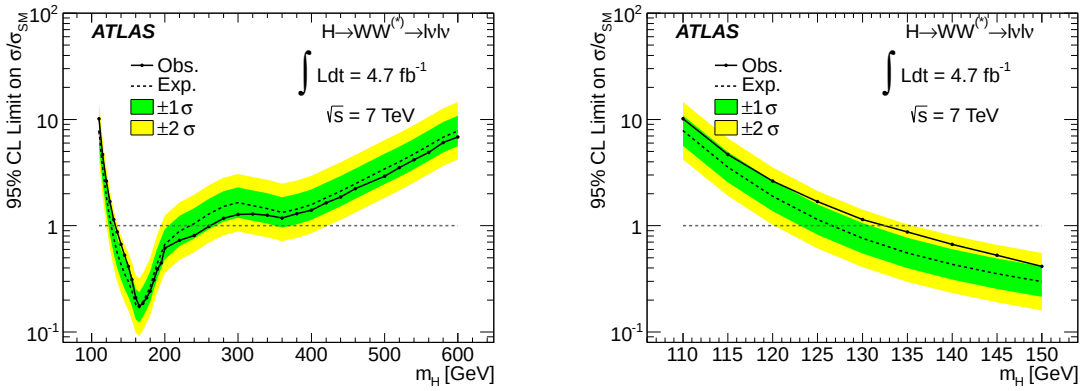

(a) 110 GeV $\leq m_H \leq$ 600 GeV

(b) 110 GeV $\leq m_H \leq$ 150 GeV

Figure 7.12: Expected (dashed) and observed (solid) 95 % CL upper limits on the Higgs boson production cross section, normalized to the SM cross section, as a function of the Higgs boson mass hypothesis m_H. The green and yellow regions indicate the $\pm 1\sigma$ and $\pm 2\sigma$ uncertainty bands on the expected limit, respectively. The results for nearby masses are highly correlated due to the limited mass resolution (5 to 8 GeV, as inferred from a study of the effect of a hypothetical $m_H = 125$ GeV signal on the behavior of $q_\mu(\mu = 1)$ as a function of m_H) in this final state. The plots correspond to the 2011 dataset and are taken from Ref. [24].

In the 2012 dataset [25], an excess of events is observed for low Higgs boson mass hypotheses m_H, which is reflected by a low value of the observed probability p_0 for a fluctuation of the background and a fitted signal strength parameter $\hat{\mu}$ which deviates from zero. Figures 7.13(a) and (b) display the expected and observed p_0 as well as the fitted signal strength parameter $\hat{\mu}$ as a function of m_H using the 2012 dataset. The expected p_0 is determined assuming the signal plus background hypothesis at the given value of m_H and the nominal signal strength $\mu = 1$. The lowest observed value of p_0 is $6 \cdot 10^{-4}$ at a mass of $m_H = 120$ GeV and is equivalent to 3.2 standard deviations. For $m_H = 125$ GeV the observed value of p_0 is given by $8 \cdot 10^{-4}$, which is equivalent to 3.1 standard deviations, while the expected value of p_0 is 0.05, which is equivalent to 1.6 standard deviations. The fitted signal strength parameter $\hat{\mu}$ exceeds a value of one for $m_H < 135$ GeV and increases for decreasing hypothesized m_H. This behaviour is a result of the low mass resolution of the $H \to WW^{(*)} \to \ell\nu\ell\nu$ analysis and a decreasing signal expectation for decreasing Higgs boson masses. At $m_H = 125$ GeV, the best fit value of μ is given by $\hat{\mu} = 2.1^{+0.8}_{-0.7}$.

Finally, the results of the combination of the 2011 and the 2012 datasets are illustrated in Figures 7.13(c) and (d). With respect to the 2012 dataset alone, the inclusion of the 2011 dataset shifts the position of the minimum of the observed p_0 to $m_H = 125$ GeV and reduces its value to $p_0 = 3 \cdot 10^{-3}$, equivalent to 2.8 standard deviations. At this mass, the best fit of the signal strength parameter μ is given by $\hat{\mu} = 1.4 \pm 0.5$.

7.5.2. Visualization of the Excess around 125 GeV

The analyses searching for a SM Higgs boson in the $H \to \gamma\gamma$ [155] and the $H \to ZZ^{(*)} \to 4\ell$ [156] channels using data collected in the years 2011 and 2012 with the ATLAS detector have observed an excess of events compatible with a SM Higgs boson with a mass close to $m_H \simeq 126$ GeV. The results of the $H \to WW^{(*)} \to \ell\nu\ell\nu$ analysis are consistent with these

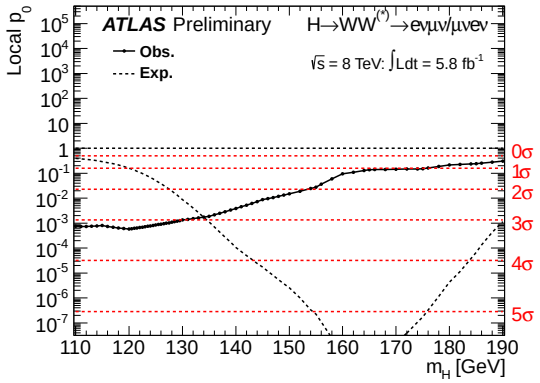

(a) $p_0(m_H)$, 2012 dataset

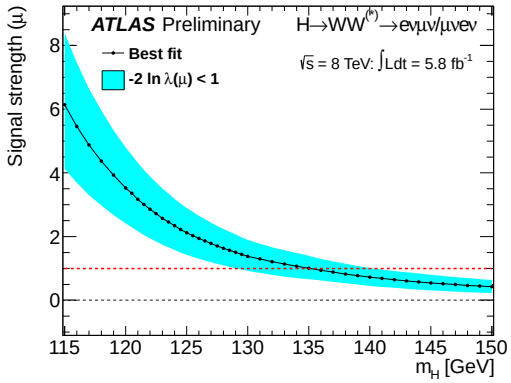

(b) $\hat{\mu}(m_H)$, 2012 dataset

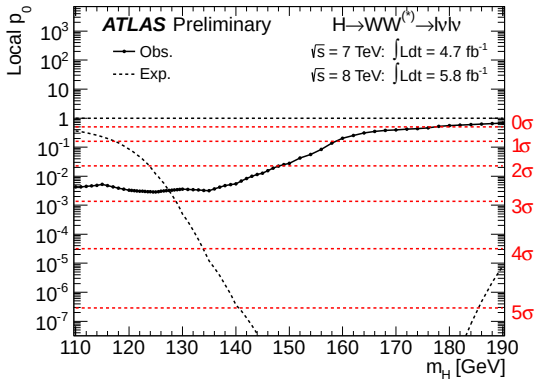

(c) $p_0(m_H)$, 2011+2012 dataset

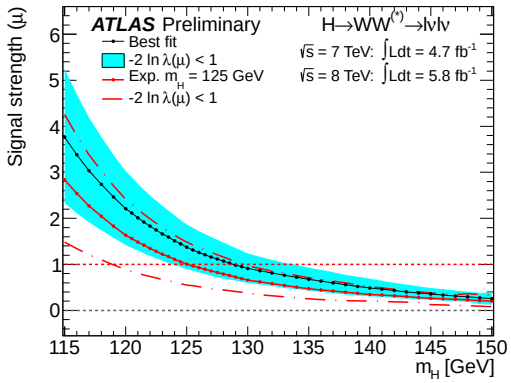

(d) $\hat{\mu}(m_H)$, 2011+2012 dataset

Figure 7.13: Probability for a fluctuation of the background p_0 and fitted signal strength parameter $\hat{\mu}$ as a function of the Higgs boson mass hypothesis m_H. The plots are taken from Ref. [25]. (a) Observed (solid line) p_0 using the 2012 dataset. The dashed line shows the corresponding expectation for the signal-plus-background hypothesis at the given value of m_H. At $m_H = 125$ GeV the observed p_0 is $8 \cdot 10^{-4}$ whereas the expected p_0 is 0.05. (b) $\hat{\mu}$ for the low mass range using the 2012 dataset. (c) Same as (a) but using the combination of the 2011 and the 2012 datasets. At $m_H = 125$ GeV the observed p_0 is $3 \cdot 10^{-3}$ whereas the expected p_0 is 0.01. (d) Same as (b) but using the combination of the 2011 and the 2012 datasets. The expected result for a signal hypothesis of $m_H = 125$ GeV (red line) is included for comparison.

observations and motivate a dedicated visualization of the signal hypothesis[10] $m_H = 125$ GeV.

Figure 7.14(a) shows the distribution of m_{T} for events passing the final signal selection of the $H + 0$ or the $H + 1$ jet channels in the 2012 data with the estimated backgrounds subtracted. The backgrounds are normalized to the total integrated luminosity in data and corrected or estimated using control samples where applicable as described in Section 7.3. The expected contribution from a $H \to WW^{(*)} \to \ell\nu\ell\nu$ signal with $m_H = 125$ GeV is overlaid as a red histogram. The m_{T} distribution of the excess events in data is compatible with a $H \to WW^{(*)} \to \ell\nu\ell\nu$ signal with $m_H = 125$ GeV and a signal strength greater than one.

Several parameters of the data taking as well as the analysis itself are different for the 2012

[10] The value $m_H = 125$ GeV has to be chosen since no MC samples for $m_H = 126$ GeV have been available at the time of writing.

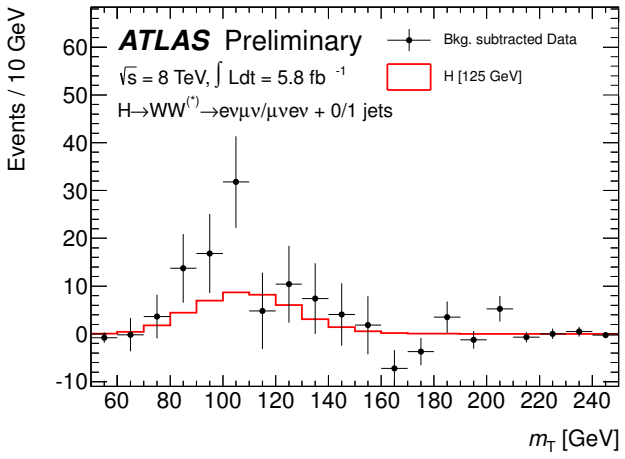

(a) 2012 dataset

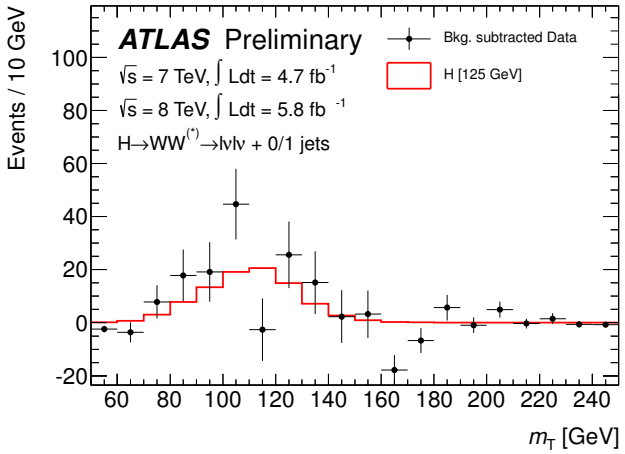

(b) 2011+2012 datasets

Figure 7.14: Distributions of the transverse mass m_{T} for data events passing the final signal selection of the $H + 0$ or $H + 1$ jet channel with the corresponding estimated background contribution subtracted. The background is normalized to the total integrated luminosity in data and corrected or estimated using control samples where applicable as described in Section 7.3. The expected contributions from a $H \to WW^{(*)} \to \ell\nu\ell\nu$ signal for $m_H = 125$ GeV are overlaid as red histograms. The distributions correspond to the sum of the $H + 0$ and $H + 1$ jet channels. The statistical uncertainties of both the data and the subtracted background are reflected in the error bars of the data markers. The systematic uncertainty on the background estimate is not included. These plots have been published in Ref. [25]. (a) Sum of opposite flavor channels in the 2012 dataset. (b) Sum of same and opposite flavor channels in the 2011 dataset and opposite flavor channels in the 2012 datasets.

dataset compared to the 2011 dataset. The expected distributions of the transverse mass for $H \to WW^{(*)} \to \ell\nu\ell\nu$ signal events with $m_H = 125$ GeV are still very similar between the two datasets (see Figure A.3 in the appendix). This fact justifies to sum the m_{T} distributions in both datasets and visualize the excess events in the same way as done in Figure 7.14(a) for the 2012 dataset alone. The corresponding distributions are displayed in Figure 7.14(b), reflecting the full data and the best estimate of the backgrounds available.

8 $\mathrm{H} \rightarrow \mathrm{WW}^{(*)} \rightarrow \ell\nu\ell\nu$ Analysis in the $\mathrm{H} + 2$ Jets Channel

The search for the SM Higgs boson in the $H \rightarrow WW^{(*)} \rightarrow \ell\nu\ell\nu$ decay channel implements a categorization of candidate events into different *jet multiplicity channels*, which are distinguished according to the number of selected jets accompanying the event. The previous chapter covers the $H + 0$ jets and $H + 1$ jet channels, which are characterized by the requirement of zero or one reconstructed jet, respectively. The motivation for this categorization is mainly driven by substantially different background compositions in these two event samples (see also Section 7.2.2). Following this argument, the $H + 2$ jets channel appears to be an obvious extension. However, apart from the fact that a sample of events featuring more than one jet is by far dominated by top background events, the motivation for an additional $H + 2$ jets category is somewhat out of the scope of the original argument.

Assuming a SM Higgs boson an unique opportunity to select a clean and pure sample of $H \rightarrow WW^{(*)} \rightarrow \ell\nu\ell\nu$ signal events opens up if one explicitly considers the second largest Higgs boson production mechanism at the LHC. The *vector-boson fusion* (VBF) Higgs boson production proceeds through the fusion of two massive vector bosons (W or Z) that are emitted from two incoming quarks. The leading order Feynman diagram illustrating this process is presented in Figure 3.1(b). For low Higgs boson masses m_H the cross section of the VBF process is approximately one order of magnitude lower than the one of the dominating gluon fusion process but approaches the value of the latter with increasing m_H (see also Section 3.1). The reduced signal event rate is countervailed by a distinctive event topology induced by the two outgoing quarks which are expected to be observable as jets with large transverse momenta in the forward regions of the detector. Additional jet activity is expected to be suppressed due to the lack of color exchange between the two quarks.

Apart from the powerful handles provided by the VBF process to achieve an experimental detection, it is from a theoretical point of view very interesting on its own. As opposed to the gluon fusion mode, the VBF production mode does not involve the coupling of the Higgs boson to fermions. Hence, considering the decays $H \rightarrow WW$ and $H \rightarrow ZZ$, one is able to purely probe Higgs boson couplings to massive vector bosons. Furthermore, separating the gluon fusion and VBF production modes bears potential for a measurement of the ratio of the corresponding production cross sections, which may support the determination of Higgs boson properties [157–160].

The $H+2$ jets channel of the $H \rightarrow WW^{(*)} \rightarrow \ell\nu\ell\nu$ analysis, in opposition to its naming also comprising events with more than two jets, is dedicated to exclusively isolate signal events where the Higgs boson is produced via vector-boson fusion (VBF *signal*). The feasibility and prospects of a VBF analyses at the LHC have been studied extensively in the context of the $H \rightarrow WW^{(*)} \rightarrow \ell\nu\ell\nu$ channel in Refs. [161–167]. Given the observation of a new Higgs boson-like particle at a mass of $m_H \simeq 126$ GeV, the objective of the VBF analysis has somewhat shifted from a discovery of the Higgs boson to supporting the SM Higgs boson hypothesis by establishing the VBF process. This chapter provides a summary of the analysis

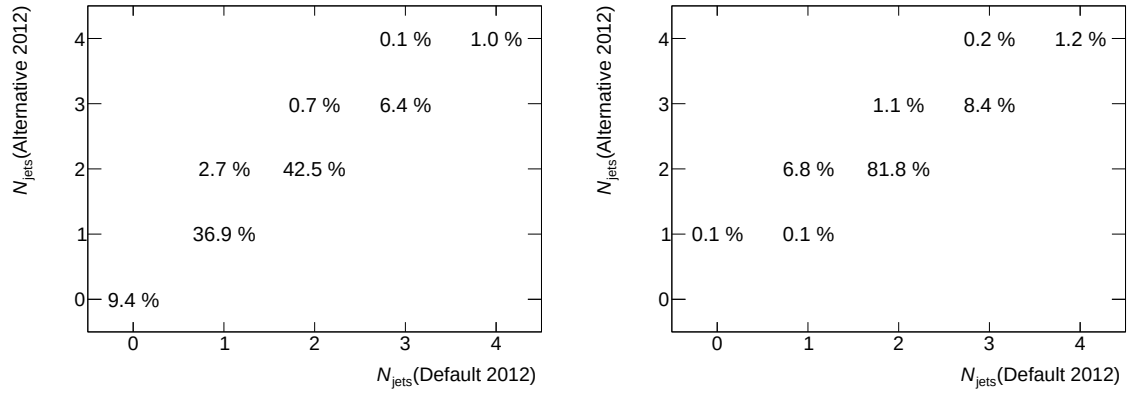

(a) After event preselection

(b) $N_{\text{jets}} \geq 2$, $\Delta\eta_{\text{jj}} > 3.8$, $m_{\text{jj}} > 500$ GeV

Figure 8.1: Fraction of events from a VBF $H \to WW^{(*)} \to \ell\nu\ell\nu$ signal with $m_H = 125$ GeV to be assigned certain numbers of jets counted with two different jet p_{T} thresholds. The baseline is given by the jet selection criteria used for the analysis of the 2011 dataset (see Section 7.1.3). N_{jets}(Default 2012) reflects the number of jets exceeding a p_{T} threshold which is raised to 30 GeV in the region $|\eta| > 2.5$ for any jet, whereas for N_{jets}(Alternative 2012) the jet p_{T} threshold is raised to 30 GeV only for the jet of highest p_{T}. The numbers are obtained from MC simulation corresponding to the 2011 dataset. (a) Events have passed the event preselection as described in Section 7.2.1. (b) Events additionally feature two jets selected according to the default jet selection criteria in 2011 (see Section 7.1.3) and pass the cuts $\Delta\eta_{\text{jj}} > 3.8$ and $m_{\text{jj}} > 500$ GeV (see Section 8.2.2). Here, $\Delta\eta_{\text{jj}}$ and m_{jj} are calculated with respect to the two jets of highest p_{T}.

in the $H + 2$ jets channel using the 2011 and 2012 datasets. The performance of the jet selection in the context of the VBF analysis is investigated in Section 8.1, followed by a discussion of the VBF event selection in Section 8.2. Data-driven background estimations and systematic uncertainties are summarized in Sections 8.3 and 8.4, respectively. Finally, results are presented in Section 8.5.

8.1. Object Selection

The $H \to WW^{(*)} \to \ell\nu\ell\nu$ analysis in the $H + 2$ jets channel uses the same trigger and object definitions as the analysis in the $H + 0$ and $H + 1$ jet channels (see Section 7.1). This in particular applies to the definition of jets which constitute primary physical objects of the VBF process. In preparation of the analysis of the 2012 dataset, the p_{T} threshold of the jet selection has been raised from $p_{\text{T}} > 25$ GeV to $p_{\text{T}} > 30$ GeV in the forward regions of the detector given by $|\eta| > 2.5$ (see also Section 7.1.3). Since this region coincides with the detector region where the VBF jets are expected, the impact of the raised jet p_{T} threshold on the acceptance of the VBF signal has been checked.

Figure 8.1 compares the impact of two different jet selections using different jet p_{T} thresholds for jets with $|\eta| > 2.5$ on a sample of VBF $H \to WW^{(*)} \to \ell\nu\ell\nu$ signal events with $m_H = 125$ GeV obtained from MC simulation corresponding to the 2011 dataset. The baseline is given by the jet selection used for the analysis of the 2011 dataset (see Section 7.1.3). N_{jets}(Default 2012) reflects the number of jets imposing the default jet p_{T} thresholds of the 2012 analysis for any jets, whereas N_{jets}(Alternative 2012) reflects an alternative jet selection where the default jet p_{T} thresholds of the 2012 analysis are used only for the jet of highest

p_{T} (*leading jet*). In order to obtain realistic results, the jet counting is performed and presented not only for events passing the event preselection (Figure 8.1(a)), but also for events additionally passing cuts enhancing the VBF topology (Figure 8.1(b)).

Using the default jet selection of the 2012 analysis approximately half of those VBF signal events that pass the event preselection are categorized as $H + 2$ jets events, while using the alternative jet selection less than three percent of these events could additionally be assigned to $H + 2$ jets category. However, enhancing the VBF topology the difference between these two jet counting procedures becomes more prominent. Here, approximately seven percent of those VBF signal events that are categorized as $H + 2$ jets using the default selection criteria of the 2011 analysis fail this category using the default jet selection criteria of the 2012 analysis. Most of these events can be recovered using the alternative jet p_{T} thresholds. However, adopting the alternative jet selection for the $H+2$ jets channel only would introduce a non-trivial overlap with the $H + 0$ and $H + 1$ jet channels, which would have to be dealt with explicitly. Thus, retaining consistency between all jet multiplicity channels, it has been decided to use the default jet selection criteria for the analysis of the $H + 2$ jets channel in the 2012 dataset as well.

8.2. Event Selection

The selection of candidate events in the $H + 2$ jets channel is seeded by events passing the default event preselection of the $H + 0$ and $H + 1$ jet channels (see Section 7.2.1). Events featuring *at least* two jets selected according to the default jet selection (see Section 7.1.3) are categorized as $H + 2$ jets events. However, since a veto on additional central jet activity (see Section 8.2.2) is imposed in the context of the VBF specific selection, the contribution from events with more than two jets eventually is small. Table 8.1 summarizes the accepted cross sections of the $H \to WW^{(*)} \to \ell\nu\ell\nu$ signal in the gluon fusion and the VBF production modes for several Higgs boson mass hypothesis m_H as well as of important background processes for an event selection comprising the preselection and the requirement of at least two jets.

In contrast to the candidate event selection of the $H + 0$ and $H + 1$ jet channels, the selection in the $H + 2$ jets channels has been subject to changes between the analysis of the 2011 and the 2012 dataset. In the following sections summarizing the event selection these changes are highlighted adequately.

8.2.1. Forward Jet Tagging

An essential constituent of the selection of VBF events is the identification (*tagging*) of those two jets that correspond to the two outgoing quarks in the VBF process. These jets are referred to as *tagging jets* and establish handles and a reference for further event selection criteria.

In the VBF process the incoming quarks are expected to have relatively high energy and undergo an emission of W or Z bosons which typically only carry over a small fraction of the original energy of the quarks [162]. Since the p_{T} of the emitted vector bosons is of the order of m_W and therefore likewise the p_{T} of the quarks, their large remaining energy results in a small scattering angle with respect to the beam-line. Thus, the tagging jets are expected to be reconstructed in the forward regions of the detector. Figure 8.2 shows the distribution of the p_{T} and the pseudo-rapidity η of the leading jet for events passing the event preselection and featuring at least two jets. The distributions are shown separately for the total background, the $H \to WW^{(*)} \to \ell\nu\ell\nu$ signal with $m_H = 125$ GeV produced via vector-boson

Process	2011 dataset [fb]		2012 dataset [fb]		2011 → 2012	
	SF	OF	SF	OF	SF	OF
Signal (VBF)						
$m_H = 125$ GeV	0.2	0.4	0.3	0.6	+27 %	+25 %
$m_H = 200$ GeV	1.0	2.0	1.3	2.5	+27 %	+24 %
$m_H = 300$ GeV	0.5	1.1	0.7	1.4	+44 %	+34 %
Signal (ggF)						
$m_H = 125$ GeV	0.5	0.9	0.9	1.6	+88 %	+84 %
$m_H = 200$ GeV	1.9	3.7	3.5	6.5	+81 %	+73 %
$m_H = 300$ GeV	1.3	2.7	2.3	4.6	+77 %	+70 %
Backgrounds						
SM WW	10	20	13	24	+27 %	+20 %
$WZ/ZZ/W\gamma$	1.5	3.2	2.2	5.2	+47 %	+63 %
Single top	21	45	34	61	+59 %	+36 %
Top pairs	390	789	576	1,150	+48 %	+46 %
$Z/\gamma^* + \text{jets}$	13	12	60	18	+356 %	+49 %
$W + \text{jets}$	1.8	6.5	5.3	12	+187 %	+86 %

Table 8.1: Summary of cross sections (in femtobarn) of the $H \to WW^{(*)} \to \ell\nu\ell\nu$ signal for different Higgs boson mass hypotheses m_H as well as of the main background processes accepted in the $H+2$ jets channel. The numbers correspond to an event selection comprising the event preselection (see Section 7.2.1) and the requirement of at least two jets selected according to Section 7.1.3. "SF" refers to the sums of the same flavor channels and "OF" refers to the sums of the opposite flavor channels. The numbers are obtained from MC simulation and include the default corrections of acceptance efficiencies. The numbers for the $W+$jets process are determined using a data-driven technique outlined in Section 7.3.1. The statistical uncertainties on the quoted absolute numbers are less than 12 % in all cases, except for $W+$ jets where it amounts to 22 % at most.

fusion and via gluon fusion or WH/ZH.

A tagging procedure which has been found to feature the highest efficiency of correctly identifying the true VBF jets [162] selects in each rapidity hemisphere the jet with the highest p_{T}. This procedure is to be compared to approaches selecting those two jets in the event with the largest separation in pseudo-rapidity or the least momentum imbalance with the Higgs boson system. However, as studied in Ref. [167], the $H \to WW^{(*)} \to \ell\nu\ell\nu$ analysis has adopted an approach which selects those two jets in the event that feature the highest p_{T}, while requiring these two jets to be reconstructed within opposite rapidity hemispheres (*opposite hemispheres requirement*). The primary difference is that in the latter approach an event is reject if it fails the opposite hemispheres requirement, rather than considering another potential pair of tagging jets in the event as it is inherent in the first approach.

While the $H \to WW^{(*)} \to \ell\nu\ell\nu$ VBF analyses of both the 2010 and 2011 datasets have implemented the tagging approach of Ref. [167] including the opposite hemispheres requirement, the analysis of the 2012 dataset is based on a slightly revised version which omits the opposite hemispheres requirement. A detailed investigation of the performance of this requirement in the context of the following VBF specific selection is subject to Section 9.3. It

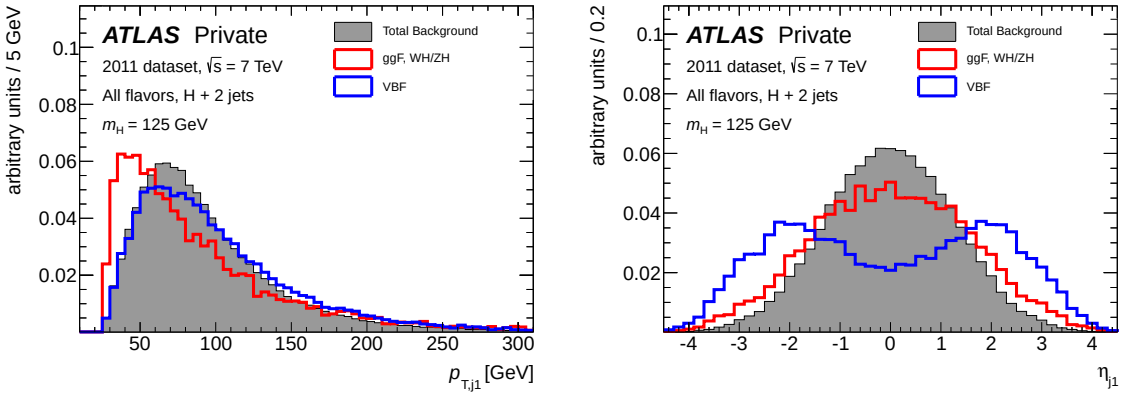

(a) Leading jet p_{T} (b) Leading jet η

Figure 8.2: Distributions of the transverse momentum p_{T} (a) and the pseudo-rapidity η (b) of the leading jet in events passing the event preselection (see Section 7.2.1) and featuring at least two jets selected according to Section 7.1.3. The total background is represented by gray solid histograms, while the $H \to WW^{(*)} \to \ell\nu\ell\nu$ signal for $m_H = 125$ GeV is shown as red (sums of ggF, WH/ZH production modes) and blue (VBF production mode) histograms. The distributions are obtained from MC simulation corresponding to the 2011 dataset and are normalized such that the total background as well as the individual $H \to WW^{(*)} \to \ell\nu\ell\nu$ signal contributions correspond to unit area. Same and opposite flavor channels are summed.

turns out that events rejected by the opposite hemispheres requirement in both background processes as well as in the VBF signal process are to a large extent also rejected by other VBF specific selection requirements, in particular by demanding a large separation of the tagging jets in pseudo-rapidity. Including VBF specific cuts (see next section), the residual rejection efficiency of the opposite hemispheres requirement is of the order of 0.5 % for background events, rendering the opposite hemispheres requirement almost uninfluential.

8.2.2. VBF Specific Selection

Having identified the two tagging jets dedicated VBF selection cuts are applied which exploit the VBF event topology. Since the tagging jets are expected to be reconstructed in the forward and backward regions of the detector at small angles with respect to the beam-line, a large separation in rapidity and pseudo-rapidity between these jets, given by

$$\Delta y_{\mathrm{jj}} = |y_{\mathrm{j1}} - y_{\mathrm{j2}}| \quad \text{and} \quad \Delta\eta_{\mathrm{jj}} = |\eta_{\mathrm{j1}} - \eta_{\mathrm{j2}}|\,, \tag{8.1}$$

respectively, is expected. Figure 8.3(a) displays the distributions of $\Delta\eta_{\mathrm{jj}}$ obtained from MC simulation for an event selection comprising the event preselection and the requirement of at least two jets. The distributions are shown separately for the total background, the $H \to WW^{(*)} \to \ell\nu\ell\nu$ signal with $m_H = 125$ GeV produced via VBF, and via gluon fusion or WH/ZH. Interestingly, but as expected, the $H \to WW^{(*)} \to \ell\nu\ell\nu$ signal in the gluon fusion or the WH/ZH production modes is distributed similarly as the total background and peaks around low values of $\Delta\eta_{\mathrm{jj}}$. In contrast to this, the bulk of VBF signal events is located at larger values of $\Delta\eta_{\mathrm{jj}}$ and thereby is well separated from backgrounds.

For the VBF candidate selection in the 2011 dataset, the separation is required to exceed 3.8 units in pseudo-rapidity, whereas for the analysis of the 2012 dataset the separation is required to exceed 3.8 units in rapidity. The decision to switch from $\Delta\eta_{\mathrm{jj}}$ to Δy_{jj} is mainly

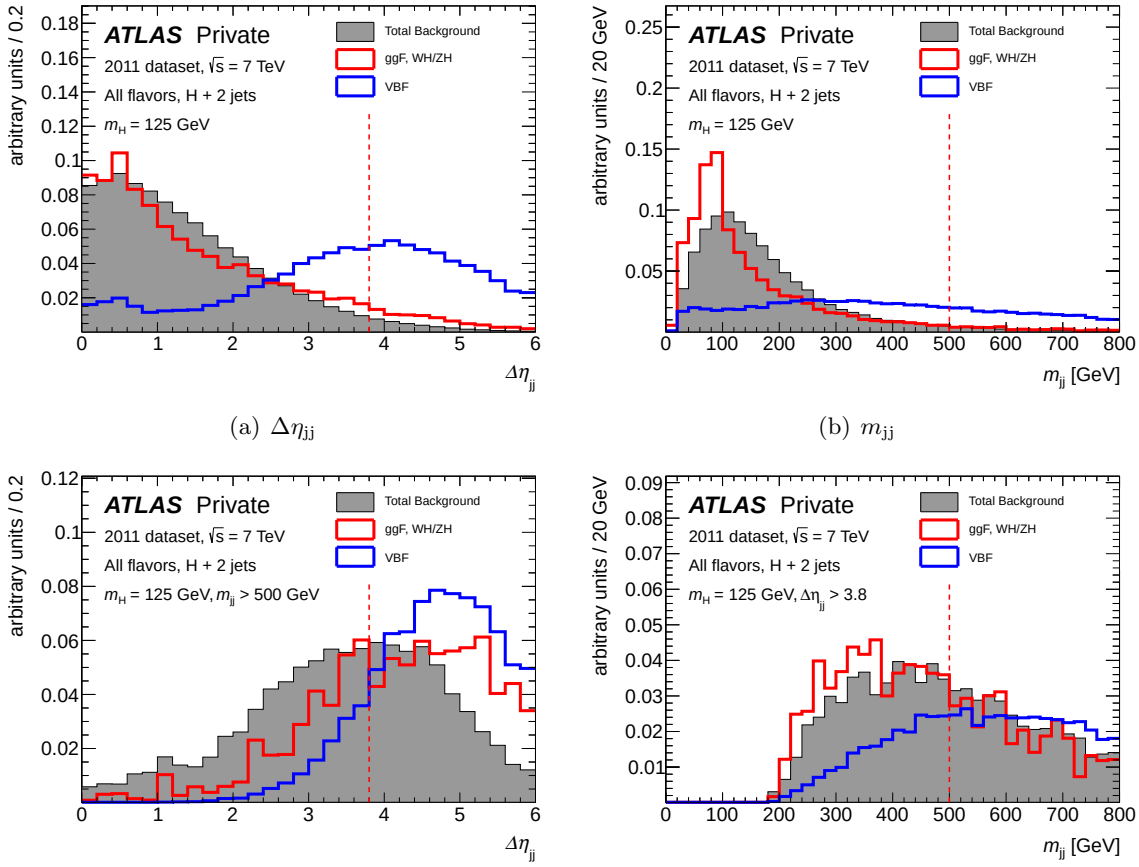

(a) $\Delta\eta_{\mathrm{jj}}$ (b) m_{jj}

(c) $\Delta\eta_{\mathrm{jj}}$ (for $m_{\mathrm{jj}} > 500$ GeV) (d) m_{jj} (for $\Delta\eta_{\mathrm{jj}} > 3.8$)

Figure 8.3: Distributions of the pseudo-rapidity separation between the two tagging jets $\Delta\eta_{\mathrm{jj}}$ (left) and their invariant mass m_{jj} (right). The total background is represented by gray solid histograms, while the $H \to WW^{(*)} \to \ell\nu\ell\nu$ signal for $m_H = 125$ GeV is shown as red (sums of ggF, WH/ZH production modes) and blue (VBF production mode) histograms. The distributions are obtained from MC simulation corresponding to the 2011 dataset and are normalized such that the total background as well as the individual $H \to WW^{(*)} \to \ell\nu\ell\nu$ signal contributions correspond to unit area. Same and opposite flavor channels are summed. (a), (b) Distributions for events passing the event preselection (see Section 7.2.1) and featuring at least two jets selected according to Section 7.1.3. (c) Same as (a) but with an additional $m_{\mathrm{jj}} > 500$ GeV cut. (d) Same as (b) but with an additional $\Delta\eta_{\mathrm{jj}} > 3.8$ cut. Cut thresholds are indicated as vertical red dashed lines.

driven by the intention to match experimental and theoretical definitions. However, practically the difference between these two quantities is negligible.

As the energy of the quarks in the VBF signal process inducing the tagging jets is relatively high and their separation in pseudo-rapidity is large, the invariant mass of the two tagging jets m_{jj} is expected to be large as well. In contrast, for background events this quantity is expected to be comparatively small. Figure 8.3(b) displays the distributions of m_{jj} obtained from MC simulation for an event selection comprising the event preselection and the requirement of at least two jets. The distributions are shown separately for the total background, the $H \to WW^{(*)} \to \ell\nu\ell\nu$ signal with $m_H = 125$ GeV produced via VBF, and via gluon fusion or WH/ZH. Here, background as well as $H \to WW^{(*)} \to \ell\nu\ell\nu$ signal events in production

(a) Efficiency of $\Delta\eta_{jj} > 3.8$ and $m_{jj} > 500$ GeV cuts

Process	2011 dataset		2012 dataset	
	SF	OF	SF	OF
Signal				
$m_H = 125$ GeV				
VBF	41 %	40 %	41 %	41 %
ggF	4.9 %	5.0 %	5.1 %	5.5 %
Backgrounds				
Top	1.8 %	1.9 %	2.0 %	2.0 %
Other backgrounds	2.6 %	2.8 %	3.2 %	2.3 %

(b) Central jet veto efficiency

Process	2011 dataset		2012 dataset	
	SF	OF	SF	OF
Signal				
$m_H = 125$ GeV				
VBF	90 %	91 %	85 %	84 %
ggF	76 %	79 %	67 %	58 %
Backgrounds				
Top	33 %	34 %	28 %	29 %
Other backgrounds	58 %	82 %	47 %	58 %

Table 8.2: Selection efficiencies of VBF specific cuts for different physics processes as determined from MC simulation. (a) Efficiencies of events passing the preselection and featuring at least two jets to pass the cuts $\Delta\eta_{jj} > 3.8$ and $m_{jj} > 500$ GeV. The relative statistical uncertainties on the quoted numbers are less than 0.9 % in all cases. (b) Efficiencies of events passing the cuts in (a) to additionally pass the central jet veto. Here, the relative statistical uncertainties on the quoted numbers are less than 9.4 % in all cases. The efficiencies to pass the cuts $\Delta\eta_{jj} > 3.8$ and $m_{jj} > 500$ GeV as well as the central jet veto are the product of the individual efficiencies.

modes other than VBF are enhanced at low values of m_{jj}, whereas the VBF signal is distributed almost flat over a broad range reaching beyond $m_{jj} > 800$ GeV. The corresponding threshold for the VBF candidate selection is chosen to $m_{jj} > 500$ GeV for the analysis of both the 2011 and 2012 datasets.

The two quantities $\Delta\eta_{jj}$ and m_{jj} are highly correlated and by placing a cut on one variable the distribution of the other variable is significantly affected. In order to provide a fair picture of the performance of cuts on these variables, Figures 8.3(c) and (d) show the corresponding distributions after placing the default cut on the respective other variable. Placing a lower bound on one of these quantities creates an event sample which inherently exhibits a distribution of the other variable shifted to larger values. Thus, the acceptance efficiencies cuts on these two variables do not factorize.

In contrast to many background processes, no color flow between the two partons radiating the vector bosons is present in the VBF signal process and hence additional jet activity is expected to be highly suppressed. Based on this fact, the VBF specific selection is completed by vetoing events with additional jet activity in the central region of the detector, referred to as *central jet veto* (CJV). However, the definition of the central jet veto is different between the analysis of the 2011 dataset and the one of the 2012 dataset.

Adopted from the 2010 version of the $H \to WW^{(*)} \to \ell\nu\ell\nu$ analysis, the analysis of the 2011 dataset vetoes an event if a third jet selected according to the default selection criteria (see Section 7.1.3) is present in the region $|\eta| < 3.2$. For the analysis of the 2012 dataset, events are vetoed if an additional jet with a p_{T} exceeding 20 GeV is present between the two tagging jets in rapidity space.

Table 8.2 lists the selection efficiencies of the VBF specific cuts on m_{jj} and $\Delta\eta_{\mathrm{jj}}$ for different physics processes in the $H + 2$ jets channel as well as the efficiencies for events passing these cuts to additionally pass the CJV. All numbers are obtained from MC simulation. Since the CJV efficiencies are calculated with respect to a selection including the cuts $\Delta\eta_{\mathrm{jj}} > 3.8$ and $m_{\mathrm{jj}} > 500$ GeV, the individual efficiencies can be multiplied to obtain the efficiencies for the combination of these cuts.

Of the order of one third of the VBF signal events for $m_H = 125$ GeV pass the VBF specific selection including the cuts on m_{jj} and $\Delta\eta_{\mathrm{jj}}$ as well as the CJV, whereas only of the order of two percent of events from backgrounds other than the top background and of the order of 0.6 % of events from the top background do. The $H \to WW^{(*)} \to \ell\nu\ell\nu$ signal with the Higgs boson produced via gluon fusion is accepted with an efficiency of the order of three percent. The modified CJV definition for the analysis of the 2012 dataset brings about a marginal improvement of the selection, but achieves a convergence of experimental and theoretical definitions.

8.2.3. Additional Selection Cuts in the VBF Analysis

As shown in the previous section, the VBF specific selection is extremely powerful in enhancing the signal-to-background ratio. In fact, one can further isolate signal events by adopting several selection cuts used in the $H + 1$ jet channel. Since neither the two tagging jets nor other jets in an VBF signal event are expected to originate from b-quarks, a b-jet veto is imposed rejecting an event if a jet selected according to the default criteria (see Section 7.1.3) is tagged as a b-jet (see Section 7.1.4). Furthermore, the $Z \to \tau\tau$ veto and the $p_{\mathrm{T}}^{\mathrm{tot}} < 30$ GeV cut (see Section 7.2.2) are applied in the $H + 2$ jets channel.

The topological selection applied in the $H + 0$ and $H + 1$ jet channels (see Section 7.2.3) is adopted by the $H + 2$ jets channel. Here, the $m_{\ell\ell} < 50$ GeV cut is loosened to $m_{\ell\ell} < 80$ GeV to increase the signal acceptance.

The full event selection applied in the $H + 2$ jets channel is summarized in Table 8.3.

8.3. Background Normalization and Control Samples

Like the analysis in the $H + 0$ and $H + 1$ jet channels (see Section 7.3) the VBF analysis in the $H + 2$ jets channel employs several control samples to perform a data-driven estimation of background contributions. Before the VBF specific selection the top background dominates the expected event yields by far, whereas after the full candidate selection both the SM WW and the top background contribute to the total background to a similar extent. However, while one can easily construct a top background control sample in the $H + 2$ jets channel,

Selection reference	Requirement
Event preselection	
(see Table 7.8)	(same as for $H+0$ and $H+1$ jet channels)
VBF specific selection	
at least two jets	$N_{\text{jets}} \geq 2$
forward jet tagging	select the two jets with highest p_{T}
tagging jet separation	**2011:** $\Delta\eta_{\text{jj}} > 3.8$ **2012:** $\Delta y_{\text{jj}} > 3.8$
m_{jj} cut	$m_{\text{jj}} > 500$ GeV
central jet veto	**2011:** no jet with $p_{\text{T}} > 25$ GeV within $\lvert\eta\rvert < 3.2$, **2012:** no jet with $p_{\text{T}} > 20$ GeV within rapidity gap spanned by tagging jets
Adopted selection	
b-jet veto	$N_{b-\text{jets}} = 0$ **2011:** `JetFitterCombNN` (80 %) **2012:** `MV1` (85 %)
total p_{T}	$p_{\text{T}}^{\text{tot}} < 30$ GeV
$Z \to \tau\tau$ veto	$m_{\tau\tau}$ unphysical or $\lvert m_{\tau\tau} - m_Z\rvert > 25$ GeV
Topological selection	
$m_{\ell\ell}$	$m_{\ell\ell} < 80$ GeV
$\Delta\phi_{\ell\ell}$	$\Delta\phi_{\ell\ell} < 1.8$ rad

Table 8.3: Summary of the event selection in the $H+2$ jets channel. The event preselection is the same as in the $H+0$ and $H+1$ jet channels. The b-jet veto, the $Z \to \tau\tau$ veto as well as the cut on $p_{\text{T}}^{\text{tot}}$ are straightly adopted from the $H+1$ jet channel. The topological selection is adopted from the $H+0/1$ jet channels, but the $m_{\ell\ell} < 50$ GeV cut is loosened to $m_{\ell\ell} < 80$ GeV to increase the signal acceptance. The b-jet veto is based on jets that are selected according to the default criteria (see Section 7.1.3) and b-tagged as outlined in Section 7.1.4.

it is not possible to define a sufficiently pure SM WW control sample due to the large cross section of the top background. Thus, the SM WW contribution has to be taken purely from MC simulation.

8.3.1. Estimation of Contributions from W+jets

The contributions from $W+$jets processes are determined using the same data-driven technique as employed in the $H+0$ and $H+1$ jet channels (see Section 7.3.1). Since the VBF selection requires a quite specific event topology, the $W+$jets control sample gets depleted and, as a result of the subtraction of other backgrounds in the $W+$jets control sample, statistical fluctuations can induce negative expected event yields for the $W+$jets process. In these cases the contributions from $W+$jets processes are assumed to be zero.

8.3.2. Top Control Samples

To validate the MC modeling of the top background in the $H+2$ jets channel a top background *validation region* (VR) is defined by requiring events to pass the event preselection, feature

Process / Quantity	2011 dataset		2012 dataset	
	VR	Default	VR	Default
Single Top	253 ± 4	1.0 ± 0.3	315 ± 10	0.9 ± 0.8
Top pairs	5039 ± 15	10.0 ± 0.7	6371 ± 23	13.3 ± 1.0
Other Backgrounds	57 ± 4	0.3 ± 0.1	154 ± 9	0.5 ± 0.2
Signal ($m_H = 125$ GeV)	2.0 ± 0.05	0.1 ± 0.00	4.9 ± 0.14	0.2 ± 0.01
Observed	5729	10	7178	15
Normalization factor	1.07 ± 0.01	0.88 ± 0.29	1.05 ± 0.01	1.03 ± 0.29

Table 8.4: Expected and observed numbers of events in the top validation regions ("VR") as well as in the top background control samples ("Default") of the $H+2$ jets channel in the 2011 and 2012 datasets. The top validation region is defined by requiring events to pass the event preselection, feature at least two jets, and to contain at least one b-tagged jet. The top control sample is defined by removing from the final signal selection in the $H + 2$ jets channel the topological selection cuts on $m_{\ell\ell}$ and $\Delta\phi_{\ell\ell}$ and reversing the veto on b-tagged jets. For the 2011 dataset the numbers correspond to the sums over all lepton flavors, whereas for the 2012 dataset only the sums of the opposite flavor channels are quoted. The quoted uncertainties reflect the statistical component only. The contributions from $W+$jets processes are determined using a data-driven technique described in Section 7.3.1.

at least two jets, and to contain at least one b-tagged jet. The distributions of the invariant mass m_{jj} of the two tagging jets is of particular interest since a rather stringent requirement of $m_{\mathrm{jj}} > 500$ GeV is imposed in the context of the VBF specific selection. As illustrated in Figures 8.4(a) and (b) a prominent deficiency in the MC modeling of the data can be observed in the VR of the 2011 dataset, whereas this observation is not as significant in the 2012 dataset. At the time of writing the source of the discrepancy in the m_{jj} distributions was still unknown.

In order to correct and constrain the normalization of the top background, a top control sample is defined by removing from the final signal selection in the $H + 2$ jets channel the topological selection cuts on $m_{\ell\ell}$ and $\Delta\phi_{\ell\ell}$ and reversing the veto on b-tagged jets. This explicitly includes the cut on the invariant mass m_{jj} and consequently allows to take into account the deficiency in the MC simulation of the top background mentioned above.

The expected and observed numbers of events in the top VRs as well as in the top control sample are presented in Table 8.4. For comparison, NFs are derived from both the VRs as well as the control samples, though the first are not used in the analysis. Due to numerous additional selection requirements in the control samples compared to the VRs, the numbers of events in the control samples are significantly smaller and result in larger statistical uncertainties on the corresponding NFs. In the 2011 dataset, the NFs derived from the VR and the control sample exhibit a deviation of the central values reflecting the modeling issue in the m_{jj} distribution, though being compatible within the statistical uncertainties. By contrast, in the 2012 dataset the central values of both NFs agree well. For the normalization of the top background the NFs derived from the control samples, given by

$$\mathrm{NF}_{\mathrm{top}}^{2-\mathrm{jet}} = \begin{cases} 0.88 \pm 0.29 & \text{(2011 dataset)} \\ 1.03 \pm 0.29 & \text{(2012 dataset)} \end{cases}$$

are used. These are favored over the ones derived from the VRs since the additional application of default analysis cuts reduces the impact of systematic uncertainties on the normalization and is expected to provide a more realistic estimate.

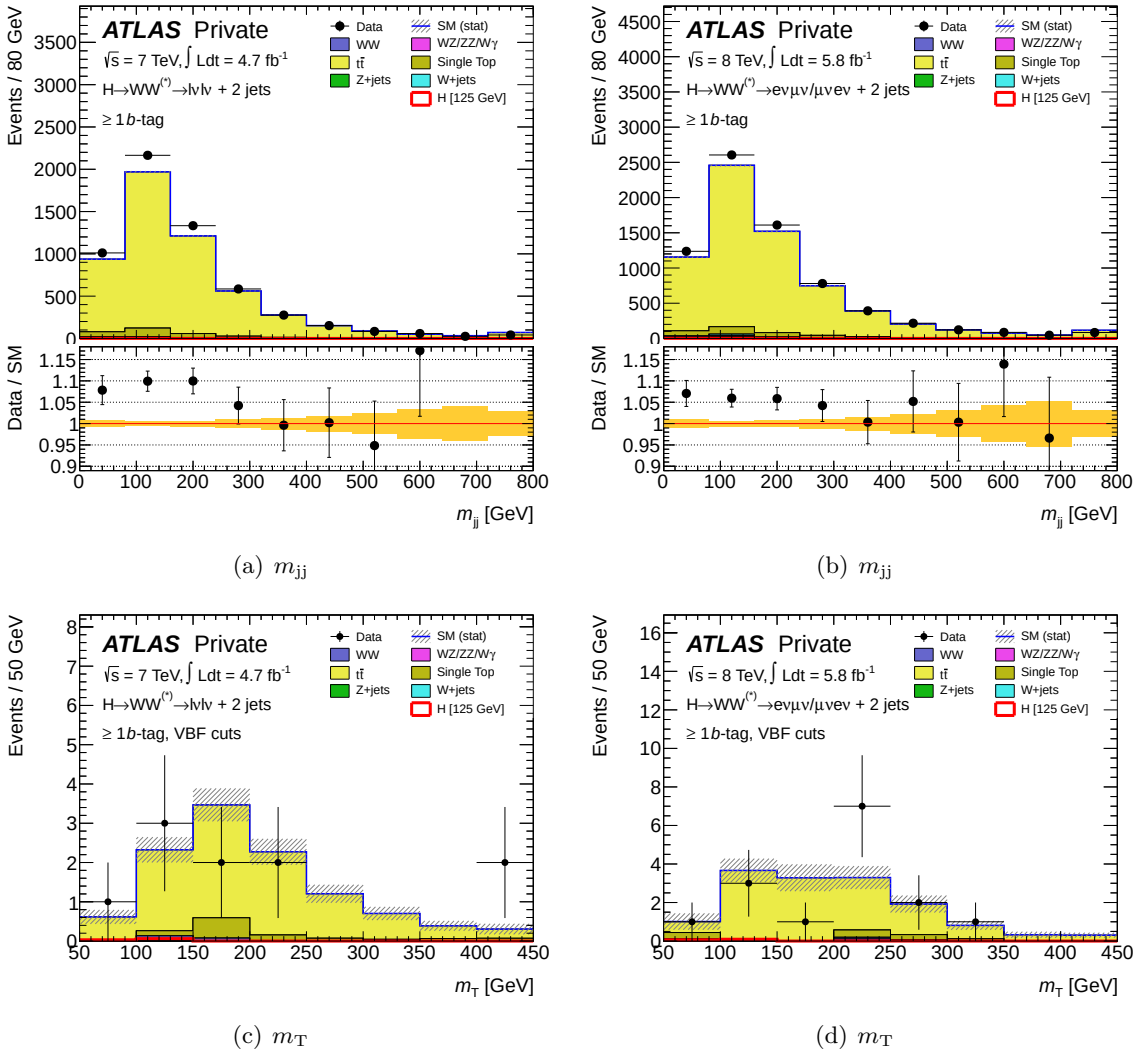

(a) m_{jj} (b) m_{jj}

(c) m_{T} (d) m_{T}

Figure 8.4: Distributions of the invariant mass of the two tagging jets m_{jj} in the top validation region (VR) of the 2011 dataset (a) and the 2012 dataset (b). The top VR is defined as the conjunction of the event preselection and the requirement of at least two jets with at least one of them being b-tagged. The transverse mass m_{T} in the top control samples (CR) of the 2011 dataset (c) and the 2012 dataset (d). The top control sample is defined by removing from the final candidate selection the topological selection cuts on $m_{\ell\ell}$ and $\Delta\phi_{\ell\ell}$ and reversing the b-jet veto. The last bins include the overflow.

8.3.3. Z+jets Control Samples

The contributions from $Z/\gamma^* + \mathrm{jets}$ processes to the $H + 2$ jets channel are determined using MC simulation. Since the VBF candidate selection is highly effective in suppressing the Z/γ^*+jets background, the MC-based Z/γ^*+jets estimation possesses large statistical uncertainties and finally not a single simulated MC event satisfies all selection criteria. Therefore, the analysis of the same flavor channels in the 2011 dataset is backed-up by cross-checking the $Z/\gamma^* + \mathrm{jets}$ contribution using a *cut factorization method* [168], which confirms that the $Z/\gamma^* + \mathrm{jets}$ component features a negligible contribution to the total background after the full signal selection.

8.4. Systematic Uncertainties

Many sources of systematic uncertainties relevant for the $H \to WW^{(*)} \to \ell\nu\ell\nu$ analysis are common to all three jet multiplicity bins ($H+0$, $H+1$, and $H+2$ jets) and these are detailed in Section 7.4. The following section places emphasis on the aspects specific to the $H+2$ jets channel and the VBF process.

8.4.1. Theoretical Uncertainties

The theoretical uncertainties on the VBF signal cross sections and the efficiencies of the VBF signal to pass the VBF selection cuts have been studied extensively in Refs. [90] and [144]. The scale uncertainty on the VBF signal cross section has been evaluated to be of the order of ± 4 % for $m_H = 125$ GeV, while the uncertainty arising from PDFs is of the order of ± 5 %. The scale uncertainty on the VBF cut efficiency has been evaluated to be of the order of ± 3.5 % from scale variations and of the order of ± 1.5 % from PDFs. These numbers explicitly include the veto on central jet activity.

In the $H+2$ jets channel the relative uncertainties on the cross sections of the gluon fusion process, which contributes to approximately 25 % to the total $H \to WW^{(*)} \to \ell\nu\ell\nu$ signal after the final event selection, is of the order of ± 25 %.

The production cross section of $WW + 2$ jets is assigned a large, conservative systematic uncertainty of ± 80 % reflecting large scale uncertainties and discrepancies between predictions using the MC@NLO and the Alpgen MC generators [169].

8.4.2. Experimental Uncertainties

Table 8.5 summarizes the impact of varying experimental parameters within their uncertainties on the expected event yields in the $H + 2$ jets channel before the topological selection. The evaluation is equivalent to the one outlined in Section 7.4.2. The topological selection cuts $m_{\ell\ell} < 80$ GeV and $\Delta\phi_{\ell\ell} < 1.8$ rad are omitted to avoid artificially large fluctuations due to large statistical uncertainties on the determination of expected event yields.

The central role of jets in the VBF analysis is reflected by relative systematic uncertainties on the acceptance of a VBF signal for $m_H = 125$ GeV arising from the jet energy measurement of the order of ± 15 %, which is the dominant experimental systematic uncertainty. The corresponding effect on the background acceptance is evaluated to be of the order of ± 30 %. Furthermore, the prediction of the total background exhibits an uncertainty of the order of ± 15 % from uncertainties on the resolution of the jet energy measurement.

Since the definition of the top control samples, which are used to constrain the normalization of the top backgrounds by means of the data, does include the default VBF specific selection requirement on the invariant mass of the two tagging jets m_{jj} no additional systematic uncertainty to account for the deficiency of the m_{jj}-modeling is assigned.

8.5. Results

In the VBF channel of the $H \to WW^{(*)} \to \ell\nu\ell\nu$ analysis a very high signal-to-background ratio can be achieved, which is of the order of one third without placing a cut on m_{T}. However, this comes only at the expense of a very small number of events from a VBF signal expected to pass the full candidate selection. Furthermore, the low efficiency of background events to pass the VBF specific selection significantly affects the number of simulated MC events the determination of backgrounds can rely on and thereby results in large statistical uncertainties on the MC prediction.

Selection	Signal ($m_H = 125$ GeV)		Total Background	
	2011 dataset	2012 dataset	2011 dataset	2012 dataset
H + 2 jets channel				
Trigger efficiency	–	±0.9 %	–	±0.3 %
W + jets fake factor	–	–	–	±1.5 %
Electron energy scale/res.	±0.5 %	±0.3 %	±0.3 %	±1.6 %
Muon momentum sc./res.	±0.2 %	±0.1 %	±0.3 %	±0.9 %
Lepton efficiency	±3.8 %	±3.2 %	±3.6 %	±1.2 %
Jet energy scale	±15 %	±12 %	±30 %	±22 %
Jet energy resolution	±0.7 %	±0.4 %	±14 %	±12 %
Pile-up	±3.3 %	±7.0 %	±3.9 %	±4.3 %
$E_{\mathrm{T}}^{\mathrm{miss}}$ terms	±5.2 %	±2.5 %	±6.1 %	±4.0 %

Table 8.5: Impact of the main experimental systematic uncertainties on the expected event yields after applying the VBF signal selection in the $H + 2$ jets channel. Here, the topological selection cuts $m_{\ell\ell} < 80$ GeV and $\Delta\phi_{\ell\ell} < 1.8$ rad are omitted to avoid artificially large fluctuations. The numbers correspond to the sums of the same and opposite flavor channels for the 2011 dataset and to the sums of the opposite flavor channels for the 2012 dataset and are determined by systematically varying corresponding input parameters of the analysis within their uncertainties. For the 2011 dataset, the uncertainties related to the trigger efficiencies have not been evaluated.

Tables 8.8 and 8.9 present the expected and observed numbers of events after applying successive selection requirements of the $H + 2$ jets channel in the 2011 and the 2012 dataset, respectively. For the 2011 dataset the numbers correspond to the sums of same and opposite flavor channels, whereas for the 2012 dataset only the sums of the opposite flavor channels are presented. The expected event yields are determined using MC simulation and are normalized to the integrated luminosity in data. For the 2011 dataset, the top background estimation from MC simulation is corrected using a reweighting procedure in m_{jj} which is at the final selection stage equivalent to the NF-based correction using the corresponding control sample. The reweighting function is derived from the top background validation region and is supposed to correct the modeling deficiency of the MC simulation in the m_{jj} distribution (see also Section 8.3.2) [150]. It is important to emphasize that this reweighting procedure is only used for the sake of a reasonable presentation of expected and observed event yields before the final selection stage.

For the 2012 dataset, the top background is corrected using the NF derived from the corresponding control sample.

Figure 8.5 presents the m_{T} distributions in the signal region of the $H + 2$ jets channel but without the topological selection cuts on $m_{\ell\ell}$ and $\Delta\phi_{\ell\ell}$ and without the $Z \to \tau\tau$ veto. The expected contributions from a $H \to WW^{(*)} \to \ell\nu\ell\nu$ signal for $m_H = 125$ GeV split into the gluon fusion and the VBF production modes are shown individually and scaled by a factor of five for the sake of improved visibility. In both the 2011 and the 2012 dataset the observed data agrees well with the background expectation within large statistical uncertainties.

Additionally applying the $Z \to \tau\tau$ veto as well as the $m_{\ell\ell} < 80$ GeV and the $\Delta\phi_{\ell\ell} < 1.8$ rad cuts, the expected and observed numbers of events in the final signal region of the $H + 2$ jets

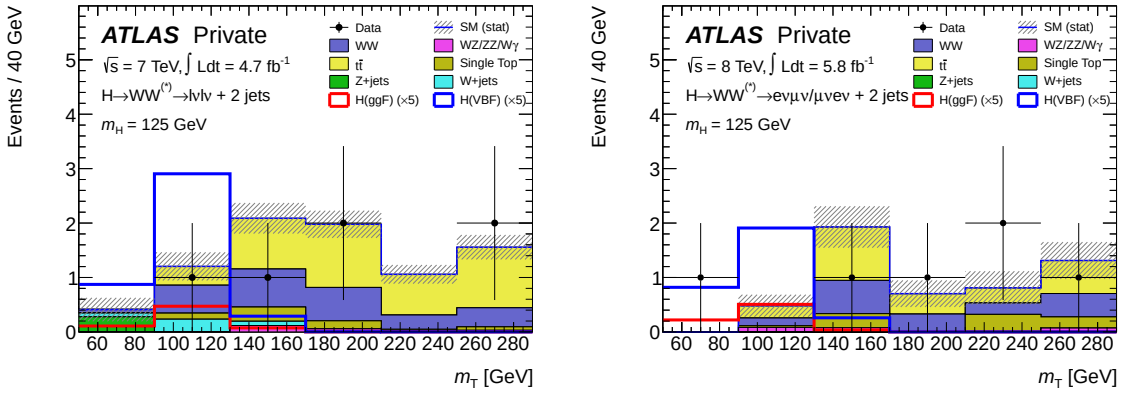

(a) 2011 dataset

(b) 2012 dataset

Figure 8.5: Distributions of the transverse mass m_{T} in the $H + 2$ jets channel of the 2011 dataset (a) and the 2012 dataset (b) after applying the VBF candidate selection except the topological selection cuts on $m_{\ell\ell}$ and $\Delta\phi_{\ell\ell}$ as well as the $Z \to \tau\tau$ veto. The expected contributions from a $H \to WW^{(*)} \to \ell\nu\ell\nu$ signal for $m_H = 125$ GeV split into the gluon fusion and the VBF production modes are shown as red and blue histograms, respectively, and are scaled by a factor of five to improved the visibility. For the 2011 dataset the distributions correspond to the sum over all lepton flavor channels, whereas for the 2012 dataset only the sum of the opposite flavor channels is shown. The last bin includes the overflow. The hatched area indicates the statistical uncertainty on the background prediction induced by the finite number of simulated MC events.

channel are listed for both the 2011 and 2012 datasets in Table 8.6. The expected total background in the individual channels is of the order of one event, while the expected contribution from a Higgs boson with $m_H = 125$ GeV produced in the VBF mode is of the order of half an event. In the 2011 data one event satisfies all selection criteria, while in the 2012 data two events pass the final selection. The observed numbers of events are well compatible with the background-only expectations. The corresponding transverse mass distributions are presented in Figure 8.6 and an overview of the properties of the VBF candidate events is given in Table 8.7.

Featuring four, seven, and ten reconstructed primary interaction vertices, respectively, each of the three observed candidate events is located close to the center of the corresponding N_{vxp} distributions in data (see Figure 5.2(b)). Furthermore, the leading and the second leading jet in these events have a p_{T} exceeding 65 GeV and 40 GeV, respectively. This confirms that the VBF topology is unlikely to be mimicked by jets arising from additional pile-up interactions. The one single candidate event observed in the 2011 data has a transverse mass of the order of $m_{\mathrm{T}} \approx 130$ GeV and thereby is compatible with a VBF Higgs boson event for $m_H = 125$ GeV. In contrast, the two candidate events observed in the 2012 data have a transverse mass of the order of $m_{\mathrm{T}} \approx 170$ GeV and 200 GeV, respectively, and thereby are not well compatible with the Higgs boson hypothesis of $m_H = 125$ GeV.

Since no significant excess of events is found these observations are translated into 95 % CL upper limits on the inclusive Higgs boson production cross section using the $H + 2$ jets channel only. The statistical analysis follows the one outlined in Section 7.5.1, however, without using the shape information in the distributions of the transverse mass in the signal region. The resulting 95 % CL upper limits on the Higgs boson production cross section are displayed in Figure 8.7. Using the 2011 dataset, the observed upper limit is of the order of

Process	2011 dataset		2012 dataset
	Opposite flavor	Same flavor	Opposite flavor
Backgrounds			
SM WW	0.45 ± 0.09	0.30 ± 0.08	0.50 ± 0.15
$WZ/ZZ/W\gamma$	0.08 ± 0.06	0.01 ± 0.01	0.13 ± 0.10
Single top	0.07 ± 0.07	0.07 ± 0.07	0.26 ± 0.21
Top pairs	0.53 ± 0.17	0.32 ± 0.12	0.54 ± 0.26
$Z/\gamma^* + \text{jets}$	0.00 ± 0.00	0.00 ± 0.00	0.00 ± 0.00
$W + \text{jets}$	(-0.02 ± 0.03)	(-0.02 ± 0.01)	(-0.14 ± 0.21)
Total	1.13 ± 0.21	0.70 ± 0.16	1.42 ± 0.38
Signal			
$m_H = 125$ GeV			
ggF	0.08 ± 0.01	0.04 ± 0.00	0.13 ± 0.02
VBF	0.46 ± 0.01	0.25 ± 0.01	0.51 ± 0.02
Observed	1	0	2

Table 8.6: Expected and observed event yields for the final signal selection of the $H+2$ jets channel in the 2011 and the 2012 dataset. The expected event yields are normalized to the luminosity in data. Negative predictions for the $W+$ jets process are an artefact of the corresponding data-driven estimation and are treated as zero in the predictions of the total background. The quoted uncertainties reflect the statistical uncertainties induced by the finite number of MC events.

Dataset	channel	Run	Event	N_{vxp}	$p_{\text{T}}^{\text{jet0}}$ [GeV]	$p_{\text{T}}^{\text{jet1}}$ [GeV]	m_{T} [GeV]
2011	$e\mu$	182796	14768407	4	140	48	131
2012	μe	203027	68604558	7	68	42	199
		205016	44709633	10	123	73	168

Table 8.7: Properties of $H \to WW^{(*)} \to \ell\nu\ell\nu$ VBF candidate events in the 2011 and the 2012 data. The events have passed the full event selection of the $H+2$ jets channel.

four times the SM expectation for $m_H = 125$ GeV, whereas using the 2012 dataset it is of the order of 5.5 times the SM expectation. In either case, the observed value is well compatible with the expected cross section limits under the assumption of the absence of a VBF signal.

Given a moderate number of expected events from a VBF signal for $m_H = 125$ GeV passing the full candidate selection the analysis in combination with the present dataset is not capable of providing a definite conclusion on the existence of the VBF process. As outlined in Section 9.4, the sensitivity of the analysis in the opposite flavor channels might be increased by $\mathcal{O}(10\ \%)$ adopting a moderate modification of the VBF candidate event selection. Furthermore, the amount of pp collision data recorded with the ATLAS detector is rapidly augmenting and subsequent updates of the analysis presented herein may allow to observe the vector-boson fusion process in data.

	H [125 GeV]		WW	$WZ/ZZ/W\gamma$	Top	Z/γ^*+jets	$W+$jets	Total Bkg.	Observed
	VBF	ggF/VH							
$E_{\mathrm{T,rel}}^{\mathrm{miss}} > 25$ (45) GeV	6.0 ± 0.03	84.9 ± 0.28	1829 ± 6.62	178 ± 4.82	8162 ± 20.5	1523 ± 27.9	342 ± 5.92	12033 ± 36.1	12231
$\geq$ 2j: $N_{\mathrm{jets}} \geq 2$	3.2 ± 0.02	8.2 ± 0.09	142 ± 1.73	25.5 ± 1.53	6278 ± 18.0	120 ± 6.68	39.6 ± 3.66	6605 ± 19.7	6676
$\geq$ 2j: CJV	2.8 ± 0.02	6.2 ± 0.08	113 ± 1.55	19.5 ± 1.44	3517 ± 13.4	89.5 ± 5.94	25.5 ± 2.60	3765 ± 15.0	3811
$\geq$ 2j: b-jet veto	2.4 ± 0.02	5.2 ± 0.07	97.8 ± 1.42	17.5 ± 1.38	404 ± 4.70	77.4 ± 5.48	18.9 ± 1.58	615 ± 7.65	667
$\geq$ 2j: $\eta_{\mathrm{j1}} \cdot \eta_{\mathrm{j2}} < 0$	2.0 ± 0.02	2.1 ± 0.04	46.0 ± 0.97	7.3 ± 0.84	170 ± 3.01	31.6 ± 3.39	8.6 ± 1.06	264 ± 4.83	269
$\geq$ 2j: $\Delta\eta_{\mathrm{jj}} > 3.8$	1.3 ± 0.01	0.5 ± 0.02	8.4 ± 0.41	0.9 ± 0.17	25.3 ± 1.05	5.8 ± 1.68	1.7 ± 0.41	42.2 ± 2.07	40
$\geq$ 2j: $m_{\mathrm{jj}} > 500$ GeV	1.0 ± 0.01	0.2 ± 0.01	3.9 ± 0.28	0.4 ± 0.11	11.4 ± 0.66	0.7 ± 0.35	0.9 ± 0.32	17.3 ± 0.87	13
$\geq$ 2j: $p_{\mathrm{T}}^{\mathrm{tot}} < 30$ GeV	0.8 ± 0.01	0.1 ± 0.01	2.5 ± 0.22	0.2 ± 0.08	4.9 ± 0.44	0.3 ± 0.20	0.4 ± 0.22	8.3 ± 0.58	6
$\geq$ 2j: $Z \to \tau\tau$ veto	0.8 ± 0.01	0.1 ± 0.01	2.4 ± 0.21	0.2 ± 0.08	4.9 ± 0.44	0.2 ± 0.16	0.3 ± 0.21	8.0 ± 0.56	6
$\geq$ 2j: $m_{\ell\ell} < 80$ GeV	0.8 ± 0.01	0.1 ± 0.01	1.1 ± 0.15	0.1 ± 0.06	1.7 ± 0.28	0.2 ± 0.16	0.2 ± 0.18	3.2 ± 0.40	2
$\geq$ 2j: $\Delta\phi_{\ell\ell} < 1.8$ rad	0.7 ± 0.01	0.1 ± 0.01	0.8 ± 0.12	0.1 ± 0.06	1.0 ± 0.23	0.0 ± 0.00	(-0.0 ± 0.03)	1.8 ± 0.26	1

Table 8.8: Expected and observed numbers of events in the 2011 dataset after applying successive cuts of the $H+2$ jets channel. The numbers correspond to the sums of the same and opposite flavor channels. Cut thresholds differing between the same and opposite flavor channels are quoted for the opposite (same) flavor channels. The column "H [125 GeV]" refers to the $H \to WW^{(*)} \to \ell\nu\ell\nu$ signal for $m_H = 125$ GeV split into the VBF production mode and the sum of the ggF/WH/ZH production modes (denoted as "ggF/VH"). The column "Top" refers to the sums of the contributions from single top and top quark pair production. The expected event yields are determined using MC simulation and are normalized to the integrated luminosity in data. The quoted uncertainties reflect the statistical component only. Starting from the CJV stage, the numbers for the top background are corrected using a reweighting procedure in the m_{jj} distribution which is at the final selection stage equivalent to the NF-based correction using the corresponding control sample. The $W+$jets contributions are determined using a data-driven technique described in Section 7.3.1. Negative predictions for this background are an artefact of the corresponding estimation technique and are treated as zero in the prediction of the total background.

	H [125 GeV]		WW	$WZ/ZZ/W\gamma$	Top	Z/γ^* + jets	W + jets	Total Bkg.	Observed
	VBF	ggF/VH							
$E_{\mathrm{T,rel}}^{\mathrm{miss}} > 25$ GeV	6.0 ± 0.06	80.9 ± 0.58	1879 ± 10.7	230 ± 5.02	9752 ± 31.8	1237 ± 39.4	277 ± 6.27	13376 ± 52.4	13410
$\geq$ 2j: $N_{\mathrm{jets}} \geq 2$	3.2 ± 0.04	11.2 ± 0.22	139 ± 2.76	30.4 ± 1.54	7415 ± 26.6	104 ± 11.8	70.8 ± 3.74	7759 ± 29.5	7845
$\geq$ 2j: b-jet veto	2.3 ± 0.04	7.3 ± 0.18	94.9 ± 2.25	19.2 ± 1.23	400 ± 6.77	61.7 ± 9.00	21.4 ± 1.79	597 ± 11.7	667
$\geq$ 2j: $\Delta y_{\mathrm{jj}} > 3.8$	1.3 ± 0.03	0.8 ± 0.06	8.3 ± 0.61	2.0 ± 0.40	36.7 ± 2.05	3.6 ± 2.13	1.4 ± 0.51	52.0 ± 3.09	44
$\geq$ 2j: CJV	1.1 ± 0.02	0.5 ± 0.04	6.5 ± 0.53	1.3 ± 0.31	19.7 ± 1.55	1.2 ± 1.16	0.5 ± 0.34	29.2 ± 2.06	22
$\geq$ 2j: $m_{\mathrm{jj}} > 500$ GeV	0.9 ± 0.02	0.2 ± 0.03	3.2 ± 0.37	0.7 ± 0.23	8.0 ± 0.94	0.0 ± 0.00	(-0.2 ± 0.23)	11.9 ± 1.03	13
$\geq$ 2j: $p_{\mathrm{T}}^{\mathrm{tot}} < 30$ GeV	0.6 ± 0.02	0.2 ± 0.03	1.7 ± 0.29	0.3 ± 0.13	3.3 ± 0.60	0.0 ± 0.00	(-0.2 ± 0.21)	5.3 ± 0.68	6
$\geq$ 2j: $Z \to \tau\tau$ veto	0.6 ± 0.02	0.2 ± 0.03	1.8 ± 0.29	0.3 ± 0.13	3.2 ± 0.59	0.0 ± 0.00	(-0.2 ± 0.21)	5.2 ± 0.67	6
$\geq$ 2j: $m_{\ell\ell} < 80$ GeV	0.6 ± 0.02	0.2 ± 0.03	0.6 ± 0.16	0.1 ± 0.10	1.1 ± 0.36	0.0 ± 0.00	(-0.2 ± 0.21)	1.8 ± 0.41	3
$\geq$ 2j: $\Delta\phi_{\ell\ell} < 1.8$ rad	0.5 ± 0.02	0.1 ± 0.02	0.5 ± 0.15	0.1 ± 0.10	0.8 ± 0.33	0.0 ± 0.00	(-0.1 ± 0.21)	1.4 ± 0.38	2

Table 8.9: Expected and observed numbers of events in the 2012 dataset after applying successive cuts of the $H + 2$ jets channel. The numbers correspond to the sums of the opposite flavor channels. The column "H [125 GeV]" refers to the $H \to WW^{(*)} \to \ell\nu\ell\nu$ signal for $m_H = 125$ GeV split into the VBF production mode and the sum of the ggF/WH/ZH production modes (denoted as "ggF/VH"). The column "Top" refers to the sums of the contributions from single top and top quark pair production. The expected event yields are determined using MC simulation and are normalized to the integrated luminosity in data. The quoted uncertainties reflect the statistical component only. Starting from jet multiplicity specific selection stages, the numbers for the top background are corrected using the NF derived from the corresponding control sample. The W + jets contributions are determined using a data-driven technique described in Section 7.3.1. Negative predictions for this background are an artefact of the corresponding estimation technique and are treated as zero in the prediction of the total background.

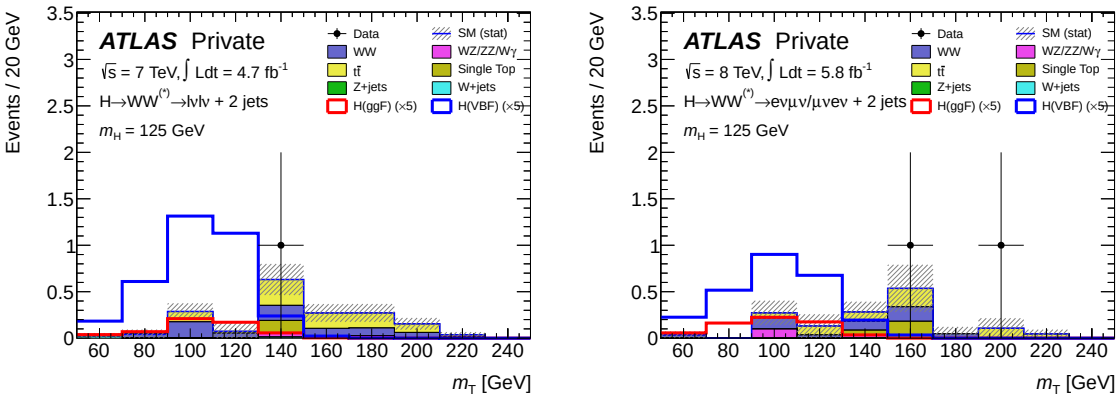

(a) 2011 dataset (b) 2012 dataset

Figure 8.6: Distributions of the transverse mass m_{T} in the final signal region of the $H +$ 2 jets channel in the 2011 dataset (a) and the 2012 dataset (b). The expected contributions from a $H \to WW^{(*)} \to \ell\nu\ell\nu$ signal for $m_H = 125$ GeV split into the gluon fusion and the VBF production modes are shown as red and blue histograms, respectively, and are scaled by a factor of five to improve the visibility. For the 2011 dataset the distributions correspond to the sums over all lepton flavors, whereas for the 2012 dataset only the sums of the opposite flavor channels are shown. The last bins include the overflow. The distributions are obtained from MC simulation and are normalized to the integrated luminosity in data. The top background is corrected using the NFs from the corresponding control samples and the $W +$ jets background is assumed to be zero. The hatched areas indicate the statistical uncertainties on the background predictions.

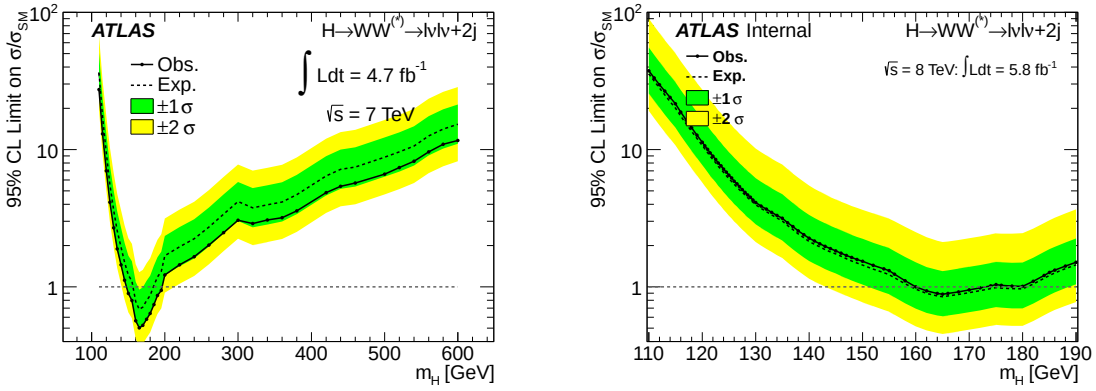

(a) 2011 dataset (b) 2012 dataset

Figure 8.7: Expected (dashed) and observed (solid) 95 % CL upper limits on the Higgs boson production cross section, normalised to the SM cross section, as a function of m_H for the $H + 2$ jets channel only. The green and yellow regions indicate the $\pm 1\sigma$ and $\pm 2\sigma$ uncertainty bands on the expected limit, respectively. (a) Using the same and opposite flavor channels in the 2011 dataset (the plot is taken from public auxiliary material of Ref. [24]). (b) Using the opposite flavor channels in the 2012 dataset (the plot is taken from Ref. [170]).

9 Optimization of the Event Selection

In high-energy physics one usually records detailed properties of particle collision events using an appropriate detection device. Based on the collected data, the search for a hypothetical physics process aims for either establishing (*discovering*) or excluding the presence of the sought-after signal process on the basis of a statistical analysis. As a first step, the analysis typically involves the isolation of the hypothetical signal events from the inevitably present background events by imposing requirements on distinctive event and object quantities. The capability of an analysis to claim the presence of a signal with a certain significance or its exclusion with a given level of confidence is referred to as its *sensitivity* to the physics process of interest and depends, among other things, on the performance of the preceding event selection. In order to achieve the highest possible signal sensitivity on a given dataset, one has to ensure that the event selection is as close to its optimum as possible.

Details of the $H \to WW^{(*)} \to \ell\nu\ell\nu$ analysis are explained in Chapters 7 and 8 for the $H + 0/1$ jet and the $H + 2$ jets channels, respectively. The objective of this chapter is to detail the optimization studies performed in the scope of this thesis. The *topological event selection* of the $H + 0$ and $H + 1$ jet channels as summarized in Section 7.2.3 is the result of an optimization study which is described in Section 9.2. A study of the performance of the opposite hemispheres requirement applied in the context of the VBF selection is summarized in Section 9.3, while a multi-dimensional optimization of the VBF selection is described in Section 9.4.

In general, an *optimization* is the process of identifying the element out of a given set of elements which is optimal with respect to a predefined measure. Mathematically, it corresponds to the maximization of a *quality function* $\mathcal{S} : \Omega \to \mathbb{R}$ which is defined on the set of elements Ω and assigns each element $\omega \in \Omega$ a real number $\mathcal{S}(\omega)$ reflecting the *selection quality*. A solution $\omega_{\mathcal{S}} \in \Omega$ considered as *optimal* with respect to $\mathcal{S}$ fulfills

$$\max_{\omega' \in \Omega} \left[\mathcal{S}(\omega')\right] = \mathcal{S}(\omega_{\mathcal{S}})$$

and is not necessarily unique. In the case of the optimization of an event selection the set of elements Ω is given by the set of different event selection criteria under consideration. The quality function $\mathcal{S}$ is given by an appropriate measure of the analysis' sensitivity to the sought-after signal process. Section 9.1 of this chapter provides an introduction to two commonly used instances of the latter.

It is self-evident that the optimization of the sensitivity to a hypothetical signal process must not refer to real physics data which is potentially affected by this signal. That is, the optimal event selection has to be determined and justified based on MC simulation and by no means on observations in data which might seduce one to design the event selection in a way, such that data and expectation fit best (see also Section 5.3).

9.1. Measures of Sensitivity

This section provides a clipped formal derivation of important measures of sensitivity and follows to a large extent Ref. [153].

Generally, the discovery of a new physics process is based on a statistical analysis which employs a *test statistic* t to quantify the incompatibility of the observed data with the *background-only hypothesis*, which only comprises known physics processes. In the case of the $H \to WW^{(*)} \to \ell\nu\ell\nu$ analysis presented in this thesis, the test statistic is given by q_0 which is calculated from a *profile likelihood ratio* (see also Section 7.5.1)

$$q_0 = \begin{cases} -2 \ln \dfrac{\mathcal{L}(0, \hat{\vec{\theta}}_\mu)}{\mathcal{L}(\hat{\mu}, \hat{\vec{\theta}})} & \hat{\mu} \geq 0 \\ 0 & \hat{\mu} < 0. \end{cases}$$

Here $\mathcal{L}(\mu, \vec{\theta})$ denotes the likelihood function of the observed data with respect to the hypothesized model characterized by a signal strength parameter μ and a set of nuisance parameters $\vec{\theta}$. $\hat{\mu}$ and $\hat{\vec{\theta}}$ denote the value of μ and $\vec{\theta}$ respectively that simultaneously maximize the likelihood function, whereas $\hat{\vec{\theta}}_\mu$ denotes the value of $\vec{\theta}$ that maximizes the likelihood function for a given value of μ.

For a sufficiently large data sample the statistical significance Z_0, with which one would reject the background-only hypothesis given the observed data, is a simple function of the test statistic q_0

$$Z_0 = \sqrt{q_0}. \tag{9.1}$$

The expected sensitivity of an analysis under the assumption of a positive signal contribution can be estimated by considering a simple counting experiment where the expected signal and background event yields s and b are known without uncertainty. In this case, the likelihood function $\mathcal{L}$ contains only one Poisson term and becomes

$$\mathcal{L} = \frac{(\mu s + b)^n}{n!} e^{-(\mu s + b)},$$

where n denotes the observed number of events. Assuming $n > b$ the test statistic q_0 can be written as

$$q_0 = -2 \ln \frac{\mathcal{L}(0)}{\mathcal{L}(1)} = -2 \left[n \ln \left(\frac{b}{s+b} \right) + s \right].$$

Replacing n by its *Asimov value* $s+b$ one obtains the median value $\mathrm{med}[q_0|\mu = 1]$ of the test statistic q_0 given an expected signal contribution s with $\mu = 1$

$$\mathrm{med}[q_0|\mu = 1] = 2 \left[(s+b) \ln \left(1 + \frac{s}{b} \right) - s \right].$$

This can be translated into the corresponding median significance $\mathrm{med}[Z_0|\mu = 1]$ using Equation (9.1)

$$\mathrm{med}[Z_0|\mu = 1] = \sqrt{2 \left[(s+b) \ln \left(1 + \frac{s}{b} \right) - s \right]} \tag{9.2}$$

and is commonly referred to as the *Poisson significance*. Expanding the logarithm in the ratio s over b one finds

$$\mathrm{med}[Z_0|\mu = 1] = \frac{s}{\sqrt{b}} \left[1 + \mathcal{O}\left(\frac{s}{b} \right) \right].$$

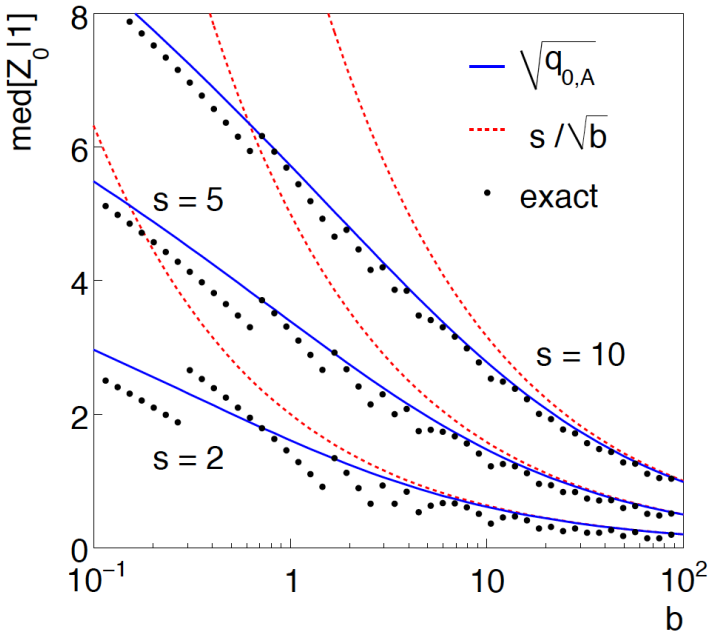

Figure 9.1: The exact median discovery significance Z_0 for different signal event yields s as a function of the expected background event yield b, assuming $\mu = 1$, compared to different approximations. The black markers represent the exact values obtained from MC simulation, whereas the continuous blue line is the Poisson significance according to Equation (9.2) and the red dashed line corresponds to the approximation given in Equation (9.3). The structure seen for the points representing the MC simulation is due to the discrete nature of the data. The plot is taken from Ref. [153].

That is, for expected signal event yields s that are much lower than the expected background b one obtains a well-known and commonly employed simple expression for an estimation of the expected (median) sensitivity

$$\text{med}[Z_0|\mu = 1] \simeq \frac{s}{\sqrt{b}} \quad \text{for} \quad s \ll b. \tag{9.3}$$

Figure 9.1 displays the median discovery significance Z_0 for different expected signal event yields s as a function of the expected background event yield b, assuming $\mu = 1$. The exact values obtained from MC simulation are reflected by black markers, whereas the continuous blue line is the Poisson significance according to Equation (9.2) and the red dashed line corresponds to the approximation given in Equation (9.3). As expected, for a signal contribution s comparable in size to that of the background b, the Poisson significance provides a much better approximation than does Equation (9.3), which tends to overestimate the expected sensitivity in these regions.

9.2. Topological Selection of the $H+0$ and $H+1$ Jet Channel

Aiming for an isolation of $H \to WW^{(*)} \to \ell\nu\ell\nu$ candidate events in data, the event preselection (see Section 7.2.1) and the subsequent jet multiplicity specific selection (see Section 7.2.2) efficiently suppress a large fraction of the contributing backgrounds. This in particular concerns the $(Z/\gamma^* \to \ell\ell)$+jets process and the production and decay of top quarks. The rejection is based on distinctive properties of these backgrounds with respect to the

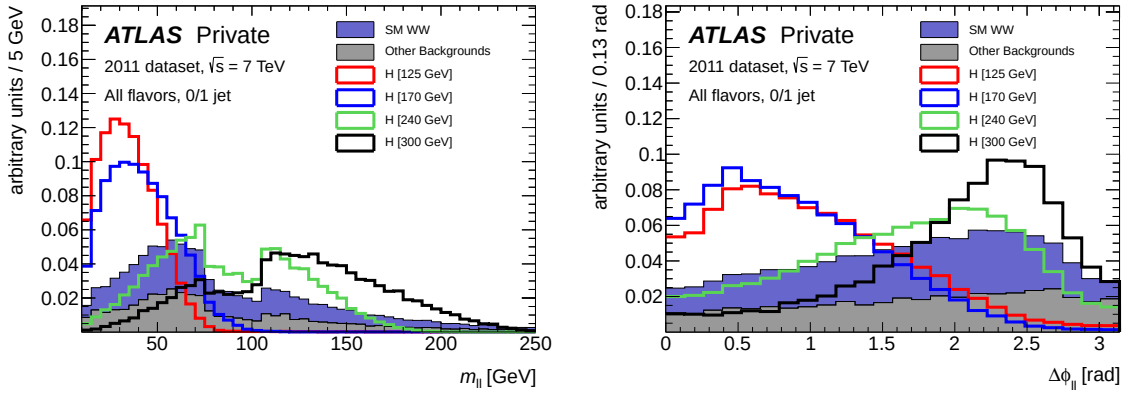

(a) $m_{\ell\ell}$ (b) $\Delta\phi_{\ell\ell}$

Figure 9.2: Distributions of the invariant mass $m_{\ell\ell}$ of the two charged leptons (a) and distributions of the azimuthal separation angle $\Delta\phi_{\ell\ell}$ of the two charged leptons(b). The solid histograms, split into the Standard Model WW contribution (blue) and remaining backgrounds (gray), correspond to the total background. The distributions of the $H \to WW^{(*)} \to \ell\nu\ell\nu$ signal with $m_H = 125$ GeV, 170 GeV, 240 GeV and 300 GeV are superimposed as colored histograms. The distributions correspond to the sum of the same and opposite flavor channels as well as the $H+0$ and $H+1$ jet channels and the events have passed the preselection and the jet multiplicity specific selection. The total background as well as the $H \to WW^{(*)} \to \ell\nu\ell\nu$ signal distributions for different values of m_H are normalized to unit area individually. The drop in the $m_{\ell\ell}$ distribution around 90 GeV is induced by the Z veto in the same flavor channels.

$H \to WW^{(*)} \to \ell\nu\ell\nu$ signal, where the expected momentum imbalance and the absence of b-jets in the signal provide the pivotal separation agains the $(Z/\gamma^* \to \ell\ell)$+jets and the top background, respectively. Even though the magnitude of the missing transverse energy in a $H \to WW^{(*)} \to \ell\nu\ell\nu$ signal event is expected to be larger for larger Higgs boson masses, its presence is a general feature which is independent of the mass hypothesis m_H. Certainly the absence of b-jets in the signal is another feature which is independent of m_H. Thus, the event preselection as well as the jet multiplicity specific selection concentrate on general properties of the $H \to WW^{(*)} \to \ell\nu\ell\nu$ signal and do not exploit features which strongly depend on m_H.

However, there are powerful handles towards an enhancement of the purity of the signal, which are specific to certain values of, or intervals in m_H, though. Figure 9.2 shows the distributions of the invariant mass $m_{\ell\ell}$ of the two charged leptons and their azimuthal separation angle $\Delta\phi_{\ell\ell}$ for $H \to WW^{(*)} \to \ell\nu\ell\nu$ signal and background events passing the preselection and the jet multiplicity specific selection. The distributions correspond to the sum of the same and opposite flavor channels as well as the sum of the $H+0$ and $H+1$ jet channels and are shown for the 2011 dataset. Given the spin-0 nature of the Standard Model Higgs boson, the charged leptons in the $H \to WW^{(*)} \to \ell\nu\ell\nu$ channel tend to have a small azimuthal separation $\Delta\phi_{\ell\ell}$ and a small invariant mass $m_{\ell\ell}$ (see also Section 4.1.4). This topology is most prominent for low and intermediate masses m_H and degenerates for increasing m_H. This is a result of the increase of the transverse momenta of the two W bosons induced by an increase of the Higgs boson mass. Thus, the exploitation of the event topology characteristic for the scalar Standard Model Higgs boson in a $H \to WW^{(*)} \to \ell\nu\ell\nu$ candidate selection evidently has to possess a dependence on the mass hypothesis m_H.

9.2.1. Definition of the Optimization Problem

In order to take advantage of the distinctive signal event topology, the *topological selection* is applied after the jet multiplicity specific selection and is defined by requiring $m_{\ell\ell}$ and $\Delta\phi_{\ell\ell}$ of an event to stay below certain thresholds $m_{\ell\ell}^{\max}(m_H)$ and $\Delta_{\phi_{\ell\ell}}^{\max}(m_H)$ which depend on the Higgs boson mass hypothesis m_H. That is,

$$\begin{aligned} m_{\ell\ell} &< m_{\ell\ell}^{\max}(m_H) \text{ and} \\ \Delta\phi_{\ell\ell} &< \Delta_{\phi_{\ell\ell}}^{\max}(m_H). \end{aligned}$$

Since the range of $\Delta\phi_{\ell\ell}$ is bound by $0 \leq \Delta\phi_{\ell\ell} < \pi$, a threshold of $\Delta_{\phi_{\ell\ell}}^{\max} \geq \pi$ effectively omits a cut on $\Delta\phi_{\ell\ell}$ in the context of the topological selection.

The dependence of the cut thresholds $m_{\ell\ell}^{\max}$ and $\Delta_{\phi_{\ell\ell}}^{\max}$ on m_H is determined by maximizing the expected sensitivity of the analysis with respect to $m_{\ell\ell}^{\max}$ and $\Delta_{\phi_{\ell\ell}}^{\max}$ as a function of m_H. Since the two variables $m_{\ell\ell}$ and $\Delta\phi_{\ell\ell}$ are kinematically strongly correlated, the maximization of the sensitivity has to be performed in both variables simultaneously. The expected sensitivity $\mathcal{S}$ as a function of $m_{\ell\ell}^{\max}$ and $\Delta_{\phi_{\ell\ell}}^{\max}$ is estimated using the Poisson significance according to Equation (9.2)

$$\mathcal{S} = \sqrt{2\left[(s+b)\ln\left(1+\frac{s}{b}\right)-s\right]}, \tag{9.4}$$

where $s = s(m_H, m_{\ell\ell}^{\max}, \Delta_{\phi_{\ell\ell}}^{\max})$ is the number of $H \to WW^{(*)} \to \ell\nu\ell\nu$ signal events with a Higgs boson mass of m_H and $b = b(m_{\ell\ell}^{\max}, \Delta_{\phi_{\ell\ell}}^{\max})$ is the total number of background events, each passing the preselection, the jet multiplicity specific selection and the cuts $m_{\ell\ell} < m_{\ell\ell}^{\max}$ and $\Delta\phi_{\ell\ell} < \Delta_{\phi_{\ell\ell}}^{\max}$. Since this measure of sensitivity does neither account for systematic uncertainties nor involves an appropriate statistical evaluation, it has to be considered as an upper bound on the true sensitivity, but should still enable a reasonable assessment of the relative performance of different values of $m_{\ell\ell}^{\max}$ and $\Delta_{\phi_{\ell\ell}}^{\max}$.

The determination of the expected event yields is based on MC simulation corresponding to the 2011 dataset and takes into account all relevant background processes as well as Higgs boson production mechanisms with their theoretical relative contribution. The contribution from $W+$jets processes is determined using a data-driven estimation technique described in Section 7.3.1. The optimization is performed using the combination of the same and opposite flavor channels as well as the $H+0$ and $H+1$ jets channels. To ensure the validity of the results obtained from the combination of the individual channels, the optimization procedure is also performed for these channels separately and presented in Appendix B. It turns out that the optimal values of $m_{\ell\ell}^{\max}$ and $\Delta_{\phi_{\ell\ell}}^{\max}$ do neither show a significant dependence on the lepton flavor combination nor on the jet multiplicity channel.

The Higgs boson mass hypotheses used in the optimization are given by

$$\begin{aligned} 110 \text{ GeV} &\leq m_H \leq 200 \text{ GeV} \quad \text{in 19 steps of 5 GeV and} \\ 220 \text{ GeV} &\leq m_H \leq 300 \text{ GeV} \quad \text{in 5 steps of 20 GeV,} \end{aligned}$$

in total amounting to 24 different *mass points*. The intervals of $m_{\ell\ell}^{\max}$ and $\Delta_{\phi_{\ell\ell}}^{\max}$ considered in the optimization are given by

$$\begin{aligned} 10 \text{ GeV} &\leq m_{\ell\ell}^{\max} \leq 250 \text{ GeV} \quad \text{and} \\ 0 \text{ rad} &\leq \Delta_{\phi_{\ell\ell}}^{\max} \leq 3.2 \text{ rad} \end{aligned}$$

with the granularity of $m_{\ell\ell}^{\max}$ and $\Delta_{\phi_{\ell\ell}}^{\max}$ being 5 GeV and 0.1 rad, respectively. Figures 9.3 and 9.4 show the corresponding two-dimensional distribution of $m_{\ell\ell}$ versus $\Delta\phi_{\ell\ell}$ for the total background as well as for the $H \to WW^{(*)} \to \ell\nu\ell\nu$ signal for different benchmark mass hypotheses after passing the event preselection and the jet multiplicity specific selection.

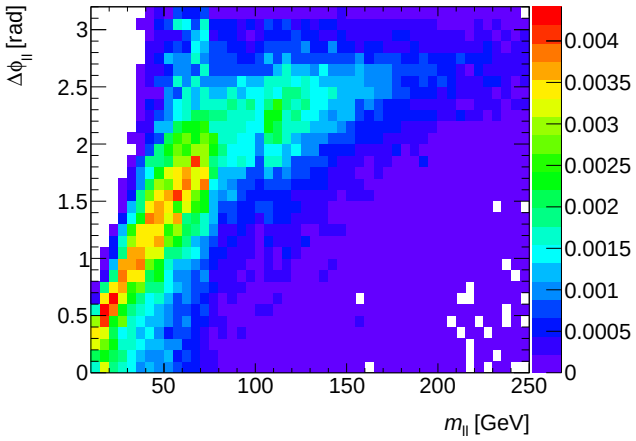

Figure 9.3: Two-dimensional distribution of the invariant mass $m_{\ell\ell}$ of the two charged leptons versus their azimuthal separation angle $\Delta\phi_{\ell\ell}$ for the total background passing the event preselection as described in Section 7.2.1 and the jet multiplicity specific selection as described in Section 7.2.2. The distribution is taken from MC simulation of the 2011 dataset and corresponds to the sum of the same and opposite flavor channels as well as the $H + 0$ and $H + 1$ jet channels. The contribution from $W +$ jets processes is determined using a data-driven estimation technique described in Section 7.3.1. The total background is normalized to unity.

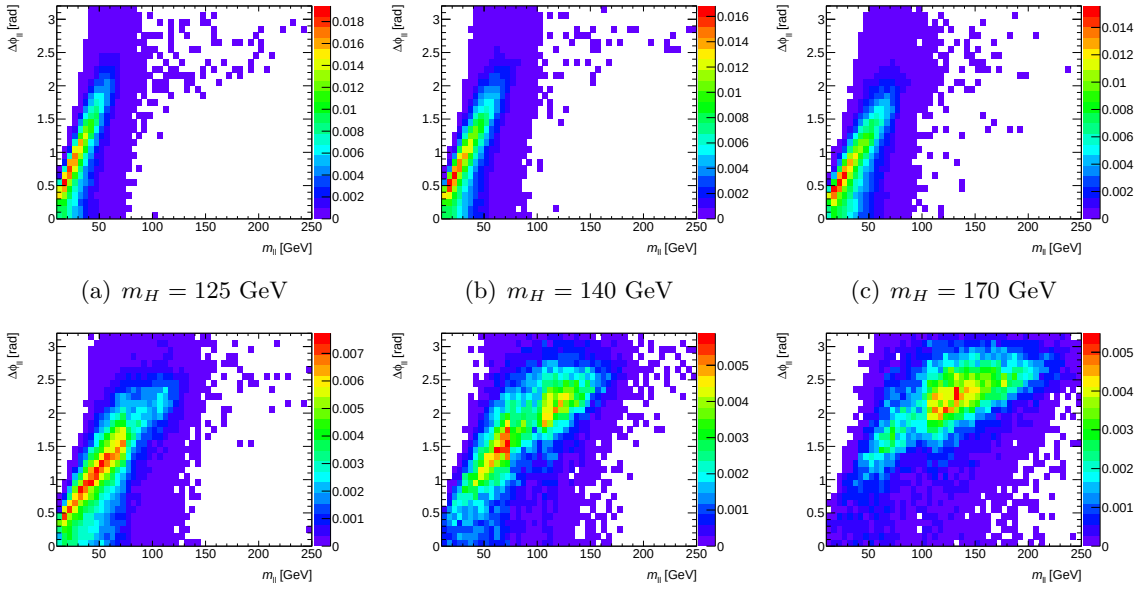

(a) $m_H = 125$ GeV (b) $m_H = 140$ GeV (c) $m_H = 170$ GeV

(d) $m_H = 200$ GeV (e) $m_H = 240$ GeV (f) $m_H = 300$ GeV

Figure 9.4: Two-dimensional distribution of the invariant mass $m_{\ell\ell}$ of the two charged leptons versus their azimuthal separation angle $\Delta\phi_{\ell\ell}$ for the $H \to WW^{(*)} \to \ell\nu\ell\nu$ signal passing the event preselection as described in Section 7.2.1 and the jet multiplicity specific selection as described in Section 7.2.2. The plots correspond to Higgs boson mass hypotheses $m_H = 125$ GeV, 140 GeV, 170 GeV, 200 GeV, 240 GeV and 300 GeV, respectively. With increasing Higgs boson mass m_H the bulk of the events is shifted towards larger values of both $m_{\ell\ell}$ and $\Delta\phi_{\ell\ell}$. The distributions are taken from MC simulation of the 2011 dataset and correspond to the sum of the same and opposite flavor channels as well as the $H + 0$ and $H + 1$ jet channels. Each distribution is normalized to unity individually.

9.2.2. Results of the Optimization

The two-dimensional distributions of the total background and the $H \to WW^{(*)} \to \ell\nu\ell\nu$ signal processes are integrated to obtain Figure 9.5, which displays for several Higgs boson mass hypotheses m_H a two-dimensional map of the estimated sensitivity according to Equation (9.4) as a function of the cut thresholds $m_{\ell\ell}^{\max}$ and $\Delta_{\phi_{\ell\ell}}^{\max}$. As expected, the location of the global maximum as well as the area with a sensitivity close to the global maximum shows a strong dependence on the Higgs boson mass hypothesis m_H. In order to visualize this dependence, four arrows originating from the location of the global maximum point along the axes of $m_{\ell\ell}^{\max}$ and $\Delta_{\phi_{\ell\ell}}^{\max}$ in positive and negative direction each. The length of the arrows matches the interval on the corresponding axis where the sensitivity exceeds 95 % of the global maximum. Thus, short arrows indicate a well defined and narrow maximum of the sensitivity, whereas a wide-stretched region with a sensitivity close to the maximum results in long arrows.

A comprehensive overview summarizing the results of the maximization of the sensitivity as a function of the Higgs boson mass hypothesis m_H is presented in Figure 9.6. The optimal value of $m_{\ell\ell}^{\max}$ is located in the proximity of 50 GeV for Higgs boson masses below $m_H \leq 165$ GeV and increases almost linearly from $m_H = 165$ GeV up to the maximum in both the considered Higgs boson mass m_H of 300 GeV as well as the considered range of $m_{\ell\ell}^{\max}$ at 250 GeV. The spread of the regions along $m_{\ell\ell}^{\max}$ with a sensitivity better than 95 % of its global maximum is at the order of 20 to 30 GeV for $m_H \leq 165$ GeV and increases for larger values of m_H. The optimal value of $\Delta_{\phi_{\ell\ell}}^{\max}$ has its minimum around $m_H \simeq 165$ GeV and increases for Higgs boson masses smaller or larger than that. This reflects the fact that $\Delta\phi_{\ell\ell}$ in $H \to WW^{(*)} \to \ell\nu\ell\nu$ signal events tends to be smallest for $m_H \simeq 165$ GeV. However, over a wide range of m_H and for cut thresholds which are compatible with not imposing any requirement on $\Delta\phi_{\ell\ell}$ at all, the sensitivity is better than 95 % of its global maximum.

The reason for the marginal importance of the exact value of $\Delta_{\phi_{\ell\ell}}^{\max}$ can be inferred from Figure 9.7, which illustrates the $m_{\ell\ell}$ and $\Delta\phi_{\ell\ell}$ distributions for the total background as well as the $H \to WW^{(*)} \to \ell\nu\ell\nu$ signal with $m_H = 125$ GeV, 165 GeV and 240 GeV before and after applying the optimal cut on the respective other variable. In the case of the $m_H = 125$ GeV signal, a cut of $m_{\ell\ell} < 50$ GeV has been determined to be optimal. Due to the correlation of $m_{\ell\ell}$ and $\Delta\phi_{\ell\ell}$, imposing the $m_{\ell\ell} < 50$ GeV requirement enhances a topology in background events which inherently features a small azimuthal separation $\Delta\phi_{\ell\ell}$. The region in $\Delta\phi_{\ell\ell}$ which, if cut at, results in a sensitivity exceeding 95 % of its global maximum is depleted of both signal and background events. Thus, scanning the $\Delta_{\phi_{\ell\ell}}^{\max}$ cut threshold has no significant effect on the expected event yields and likewise not on the estimated sensitivity. In fact, even though this region gets populated with events for larger values of m_H, the $\Delta\phi_{\ell\ell}$ distributions of signal and background events after applying the $m_{\ell\ell}$ cut are very similar in shape up to Higgs boson masses of $m_H \leq 160$ GeV. For masses of $m_H \geq 240$ GeV the cut threshold $\Delta_{\phi_{\ell\ell}}^{\max}$ reaches its maximum driven by the $H \to WW^{(*)} \to \ell\nu\ell\nu$ signal being shifted towards larger values of $\Delta\phi_{\ell\ell}$.

9.2.3. Stability of the Results

In order to assess the stability and validity of the optimization results it is also instructive to investigate the behavior of the local maxima of the estimated sensitivity with respect to the cut threshold on one variable while keeping the cut threshold on the other variable fixed. Figure 9.8 illustrates the dependence of the optimal cut thresholds as a function of the respective other cut threshold. Apparently, a general feature of the analysis is a marginal

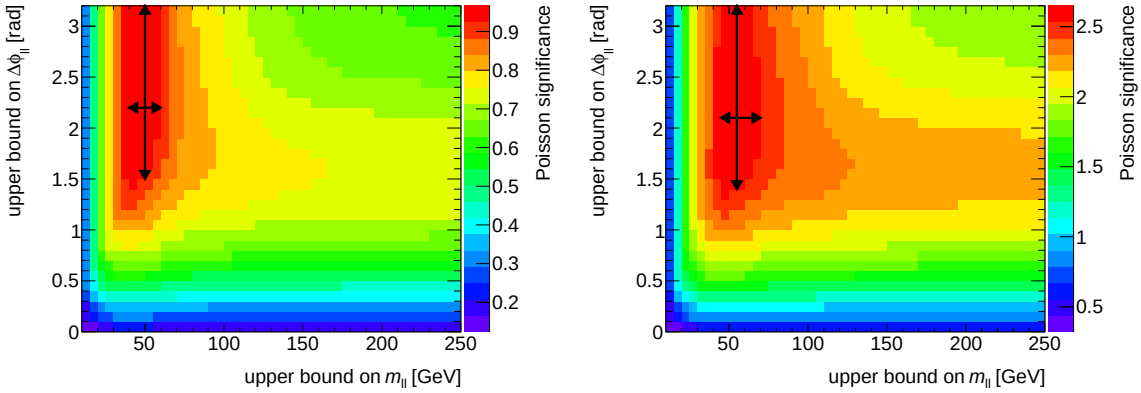

(a) $m_H = 125$ GeV

(b) $m_H = 140$ GeV

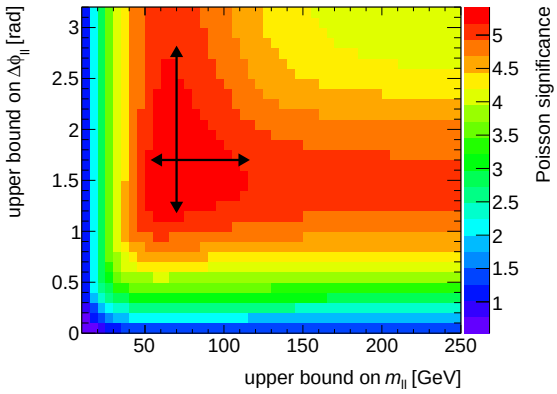

(c) $m_H = 170$ GeV

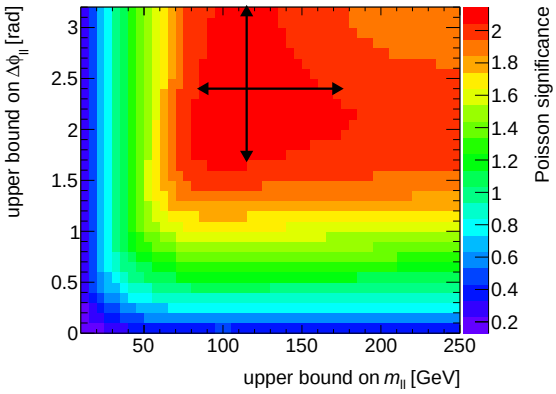

(d) $m_H = 200$ GeV

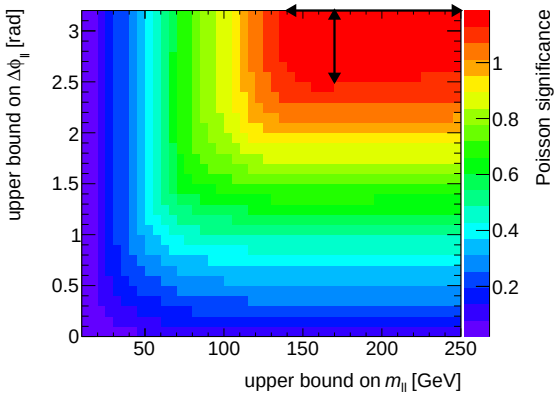

(e) $m_H = 240$ GeV

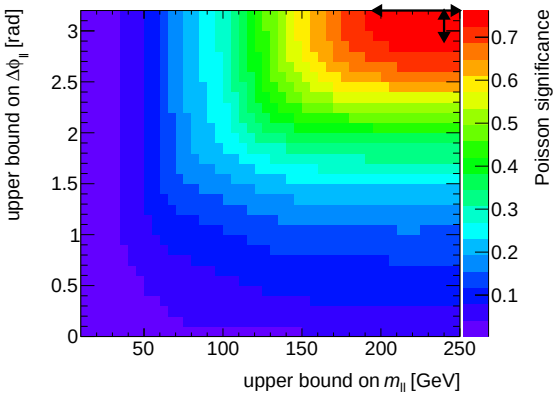

(f) $m_H = 300$ GeV

Figure 9.5: The estimated $H \to WW^{(*)} \to \ell\nu\ell\nu$ signal sensitivity $\mathcal{S}$ (Poisson significance) according to Equation (9.4) for different Higgs boson mass hypotheses m_H as a function of the cut thresholds $m_{\ell\ell}^{\max}$ and $\Delta_{\phi_{\ell\ell}}^{\max}$. The plots correspond to $m_H = 125$ GeV, 140 GeV, 170 GeV, 200 GeV, 240 GeV and 300 GeV, respectively. For each mass hypothesis the highest sensitivity is obtained for cut thresholds located at the point where the vertical and the horizontal arrows cross. The arrows indicate the spread of the region in the ($m_{\ell\ell}^{\max}$-$\Delta_{\phi_{\ell\ell}}^{\max}$)-plane where the sensitivity exceeds 95 % of its global maximum. The expected event yields entering the sensitivity calculation are normalized to an integrated luminosity of $\mathcal{L} = 1$ fb^{-1}.

Mass range	$m_{\ell\ell}^{\max}$	$\Delta_{\phi_{\ell\ell}}^{\max}$
$m_H < 200$ GeV	50 GeV	1.8 rad
200 GeV $\leq m_H < 300$ GeV	150 GeV	–
$m_H \geq 300$ GeV	–	–

Table 9.1: Summary of the three Higgs boson mass categories defined in the context of the topological selection and the corresponding cut thresholds $m_{\ell\ell}^{\max}$ and $\Delta_{\phi_{\ell\ell}}^{\max}$. For $m_H \geq 200$ GeV the requirement on $\Delta\phi_{\ell\ell}$ is removed and for $m_H \geq 300$ GeV also the cut on $m_{\ell\ell}$ is omitted.

dependence of the locally optimal $m_{\ell\ell}^{\max}$ on the value of $\Delta_{\phi_{\ell\ell}}^{\max}$, emphasizing a larger importance of the quantity $m_{\ell\ell}$ relative to the quantity $\Delta\phi_{\ell\ell}$. A somewhat unexpected behavior can be observed for cuts on $m_{\ell\ell}$ that are tighter than the global optimum. In this case, a decrease of $m_{\ell\ell}^{\max}$ induces a decrease of the locally optimal value of $\Delta_{\phi_{\ell\ell}}^{\max}$. However, this can be explained by the fact that by shifting the upper bound on $m_{\ell\ell}$ towards lower values, the distribution of $\Delta\phi_{\ell\ell}$ is forced towards small values as well.

Another very important feature supporting the reliability of the optimization results can likewise be observed in Figure 9.8. The globally optimal values of both $m_{\ell\ell}^{\max}$ and $\Delta_{\phi_{\ell\ell}}^{\max}$ are larger than the locally optimal value of one variable if the cut on the other variable is relaxed. That is, placing a cut on the second variable results in an optimal cut on the first variable which is looser than without the second cut.

9.2.4. Consequences for the Analysis

Certainly, the best for the analysis in terms of the expected sensitivity would be to straightly adopt the values of $m_{\ell\ell}^{\max}(m_H)$ and $\Delta_{\phi_{\ell\ell}}^{\max}(m_H)$ as determined in the optimization for each mass hypothesis m_H. However, in order to retain a simple Higgs boson mass dependence of the topological selection it has been decided to define not more than three mass categories, with each category comprising an event selection common to all associated values of m_H. Table 9.1 summarizes the topological selection eventually employed by the analysis. The three mass categories are given by $m_H < 200$ GeV, 200 GeV $\leq m_H < 300$ GeV and $m_H \geq 300$ GeV. The baseline selection in the low mass category ($m_H < 200$ GeV) is $m_{\ell\ell} < 50$ GeV and $\Delta\phi_{\ell\ell} < 1.8$ rad. For $m_H \geq 200$ GeV the requirement on $\Delta\phi_{\ell\ell}$ is removed and for $m_H \geq 300$ GeV also the cut on $m_{\ell\ell}$ is omitted. Even though these cut thresholds do not exactly correspond to the optimal values, their choice does not diminish the sensitivity by more than $\mathcal{O}(5\ \%)$, as can be confirmed by means of Figures 9.6(a) and (b).

For the analysis of the 2012 dataset the topological selection criteria have not been changed with respect to the 2011 analysis. To confirm that the sensitivity of the 2012 analysis is not impaired by the employment of an event selection whose optimization is based on the 2011 dataset, the optimization procedure as outlined in this section has been repeated on the 2012 dataset. The corresponding results are briefly presented in Appendix B and indicate a – if at all – marginal change in the optimal values of $m_{\ell\ell}^{\max}(m_H)$ and $\Delta_{\phi_{\ell\ell}}^{\max}(m_H)$ with respect to the optimization based on the 2011 dataset.

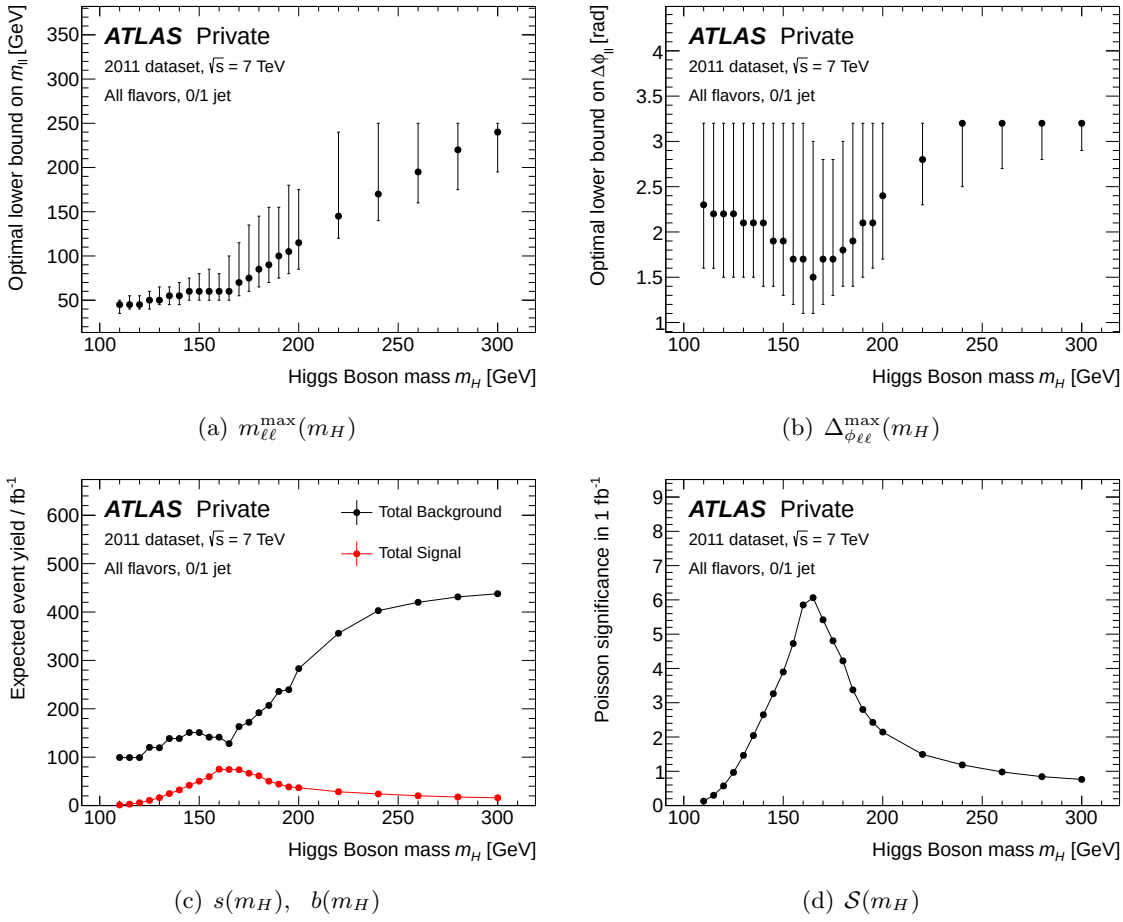

(a) $m_{\ell\ell}^{\max}(m_H)$ (b) $\Delta_{\phi_{\ell\ell}}^{\max}(m_H)$

(c) $s(m_H)$, $b(m_H)$ (d) $\mathcal{S}(m_H)$

Figure 9.6: Results of the maximization of the estimated sensitivity as a function of the Higgs boson mass hypothesis m_H. (a) and (b) illustrate the optimal cut thresholds $m_{\ell\ell}^{\max}(m_H)$ and $\Delta_{\phi_{\ell\ell}}^{\max}(m_H)$ as a function of m_H, respectively. The values are determined by maximizing the estimated sensitivity (Poisson significance) for each value of m_H individually. The vertical error bars indicate the interval which retains a sensitivity better than 95 % of the global maximum. (c) Expected event yields of the total background as well as the $H \to WW^{(*)} \to \ell\nu\ell\nu$ signal with the given value of m_H after applying the optimal cuts on $m_{\ell\ell}$ and $\Delta\phi_{\ell\ell}$. The event yields are normalized to an integrated luminosity of $\mathcal{L} = 1$ fb^{-1} and their statistical uncertainty is below the visibility threshold. (d) Estimated sensitivity $\mathcal{S}$ (Poisson significance) to a $H \to WW^{(*)} \to \ell\nu\ell\nu$ signal with the given value of m_H with data corresponding to an integrated luminosity of $\mathcal{L} = 1$ fb^{-1} after applying the optimal cuts on $m_{\ell\ell}$ and $\Delta\phi_{\ell\ell}$. The conjunctive lines in the bottom plots are present for the sake of an improved visibility.

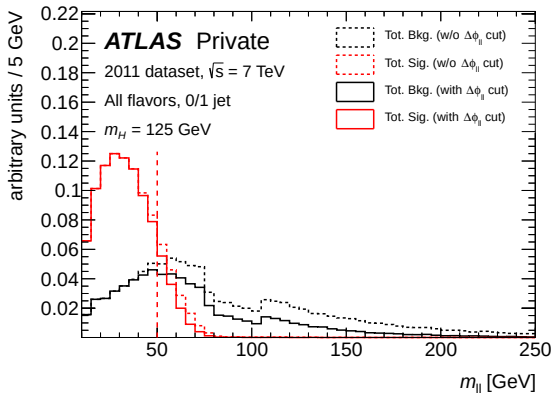

(a) $m_{\ell\ell}$ ($m_H = 125$ GeV)

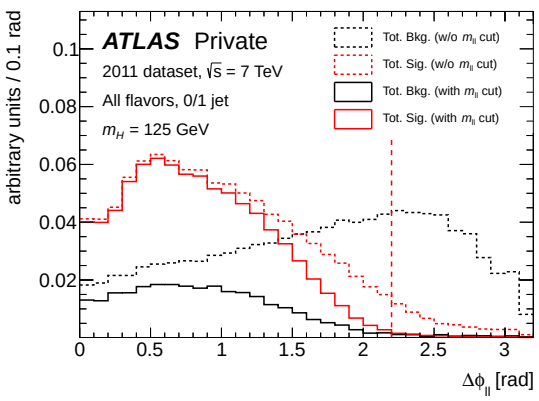

(b) $\Delta\phi_{\ell\ell}$ ($m_H = 125$ GeV)

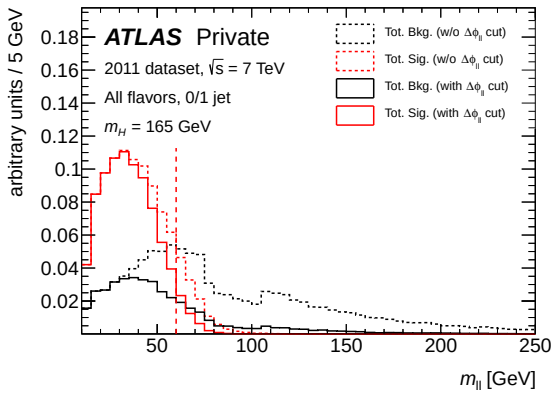

(c) $m_{\ell\ell}$ ($m_H = 165$ GeV)

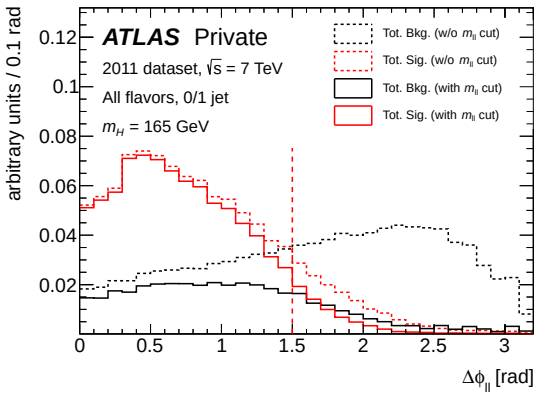

(d) $\Delta\phi_{\ell\ell}$ ($m_H = 165$ GeV)

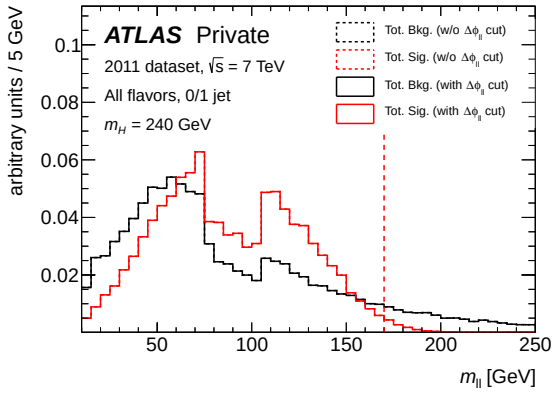

(e) $m_{\ell\ell}$ ($m_H = 240$ GeV)

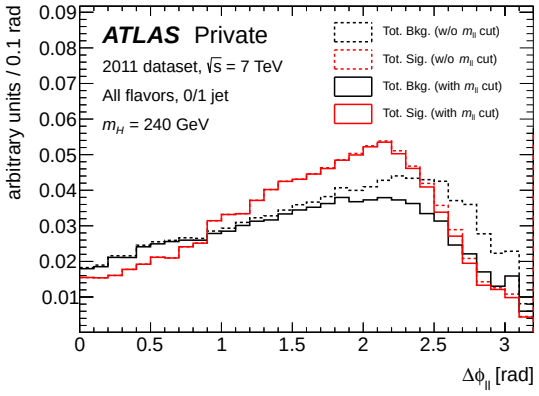

(f) $\Delta\phi_{\ell\ell}$ ($m_H = 240$ GeV)

Figure 9.7: Distributions of the invariant mass $m_{\ell\ell}$ of the two charged leptons and their azimuthal separation angle $\Delta\phi_{\ell\ell}$ after the event preselection and the jet multiplicity specific selection, but before (dashed histogram) and after (continuous histogram) applying the optimal cut on the respective other variable in the context of the topological selection. The plots display the distributions of the total background (black histograms) and the $H \to WW^{(*)} \to \ell\nu\ell\nu$ signal (red histograms) with $m_H = 125$ GeV, 165 GeV and 240 GeV. The red vertical dashed lines indicate the location of the cut threshold on the corresponding variable that maximizes the estimated sensitivity. The distributions are normalized such that both the total background as well as the $H \to WW^{(*)} \to \ell\nu\ell\nu$ signal correspond to unit area before applying the $m_{\ell\ell}$ and $\Delta\phi_{\ell\ell}$ cuts of the topological selection.

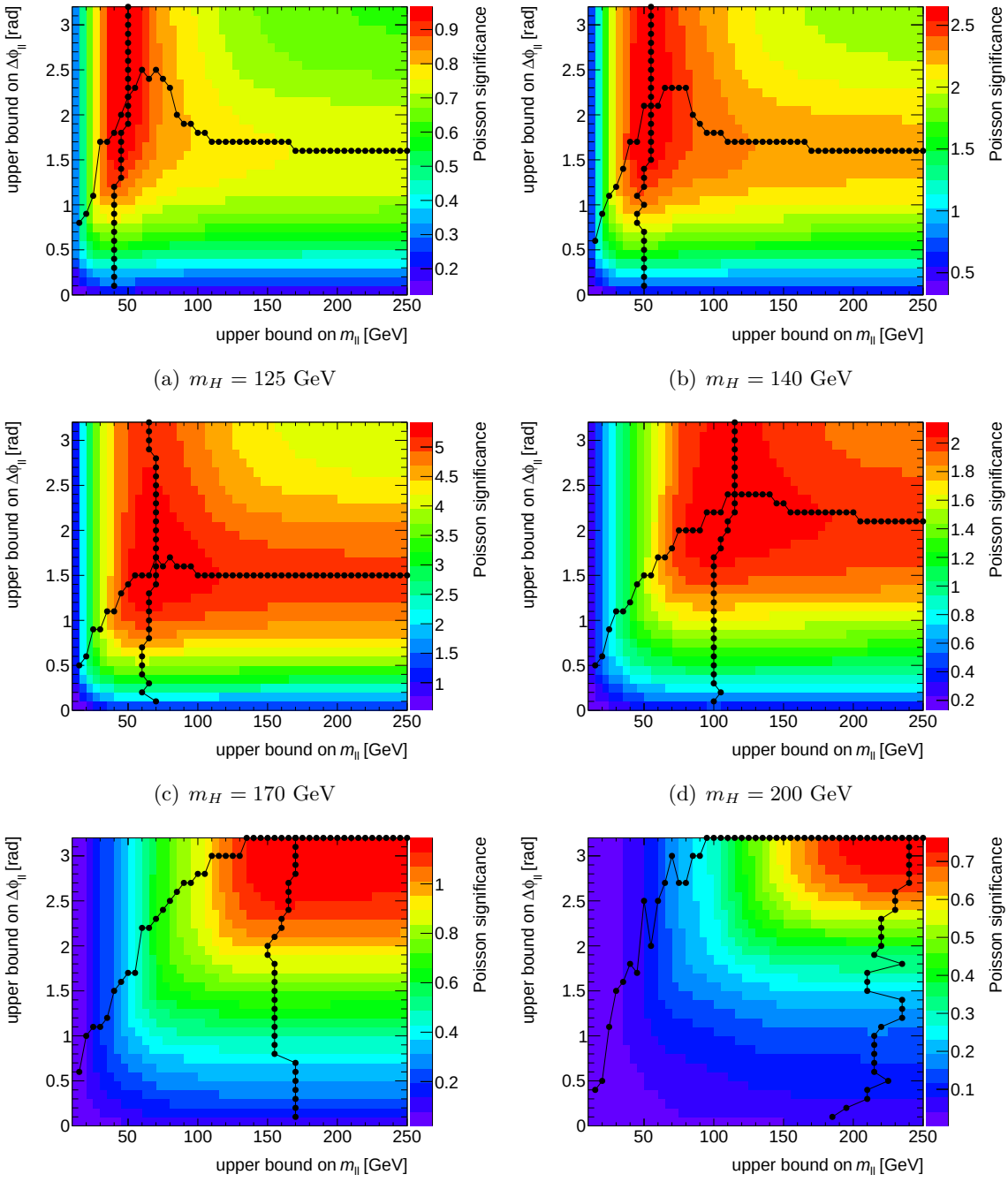

(a) $m_H = 125$ GeV (b) $m_H = 140$ GeV

(c) $m_H = 170$ GeV (d) $m_H = 200$ GeV

(e) $m_H = 240$ GeV (f) $m_H = 300$ GeV

Figure 9.8: The estimated $H \to WW^{(*)} \to \ell\nu\ell\nu$ signal sensitivity $\mathcal{S}$ (Poisson significance) according to Equation (9.4) for different Higgs boson mass hypotheses m_H as a function of the cut thresholds $m_{\ell\ell}^{\max}$ and $\Delta_{\phi_{\ell\ell}}^{\max}$. The plots correspond to $m_H = 125\,\text{GeV}, 140\,\text{GeV}, 170\,\text{GeV}, 200\,\text{GeV}, 240\,\text{GeV}$ and $300\,\text{GeV}$, respectively. For each mass hypothesis the highest sensitivity is obtained for cut thresholds located at the point where the vertical and the horizontal strings, which indicate the local maximum on one axis while scanning the other axis, cross. The expected event yields entering the sensitivity calculation are normalized to an integrated luminosity of $\mathcal{L} = 1\ \text{fb}^{-1}$.

9.3. Opposite Hemispheres Requirement in the $\mathrm{H} + 2$ Jets Channel

The isolation of a signal from the SM Higgs boson produced vie vector-boson fusion (VBF signal) is based on distinctive features in several variables which are related to the two *tagging jets* (see Section 8.2.1). These provide unique handles for an efficient rejection of backgrounds while retaining a reasonable acceptance efficiency for the VBF signal. In the scope of this thesis, several studies have been performed to investigate and optimize the performance of the event selection that is aiming for an isolation of a VBF signal (VBF *selection*). This section discusses the performance of the *opposite hemispheres requirement*, whereas Section 9.4 reports about a multi-dimensional optimization of the VBF selection.

9.3.1. Definition of the Opposite Hemispheres Requirement

The opposite hemispheres requirement is one selection cut which is commonly applied in the context of a VBF selection. It triggers the rejection of an event if the two tagging jets are reconstructed within the same rapidity hemisphere. It can be expressed in a formal way by

$$\eta_{\mathrm{j1}} \cdot \eta_{\mathrm{j2}} < 0,$$

where η_{j1} and η_{j2} are the pseudo-rapidities of the first and the second tagging jet, respectively. In conjunction with the requirements on the invariant mass m_{jj} of the two tagging jets, on their pseudo-rapidity separation $\Delta\eta_{\mathrm{jj}}$ to exceed certain thresholds, as well as a veto on jet activity in the central region of the detector (see also Section 8.2.2), the opposite hemispheres requirement constitutes the fundamental VBF selection.

In fact, the opposite hemispheres requirement can be considered as part of the forward jet tagging procedure (see also Section 8.2.1) and has in the context of the $H \to WW^{(*)} \to \ell\nu\ell\nu$ analysis for the first time been studied in Ref. [161]. Following several studies on the feasibility and prospects of the detection of a Higgs boson VBF signal at the LHC experiments [171–173], and in particular in the $H \to WW^{(*)} \to \ell\nu\ell\nu$ decay mode [161–167], the opposite hemispheres requirement has been adopted by the 2010 version of the $H \to WW^{(*)} \to \ell\nu\ell\nu$ analysis performed by the ATLAS Collaboration [134] and has been preserved for the 2011 version [24].

9.3.2. Performance of the Opposite Hemispheres Requirement

The performance of the opposite hemispheres requirement has been investigated using MC simulation corresponding to the 2011 dataset. Figure 9.9(a) shows the distributions of the product $\eta_{\mathrm{j1}} \cdot \eta_{\mathrm{j2}}$ of the pseudo-rapidities of the two tagging jets in a simulated sample of events passing the event preselection as described in Section 7.2.1 and featuring at least two jets selected according to Section 7.1.3. In the quantity $\eta_{\mathrm{j1}} \cdot \eta_{\mathrm{j2}}$ the total background as well as the $H \to WW^{(*)} \to \ell\nu\ell\nu$ signal with $m_H = 125$ GeV produced via gluon fusion or WH/ZH are almost symmetrically distributed around zero, whereas the VBF signal exhibits an asymmetric tendency towards negative values. Indeed, this appears like a strong motivation for the application of the opposite hemispheres requirement.

However, the quantity $\eta_{\mathrm{j1}} \cdot \eta_{\mathrm{j2}}$ strongly interferes with a cut on the pseudo-rapidity separation $\Delta\eta_{\mathrm{jj}} = |\eta_{\mathrm{j1}} - \eta_{\mathrm{j2}}|$ between the two tagging jets, which is part of the default VBF selection. Therefore, an unbiased assessment of the performance of the opposite hemispheres requirement has to include all cuts that affect the underlying distributions. As illustrated in Figure 9.9(b), imposing the $\Delta\eta_{\mathrm{jj}} > 3.8$ requirement forces the bulk of the distributions of $\eta_{\mathrm{j1}} \cdot \eta_{\mathrm{j2}}$ in both the $H \to WW^{(*)} \to \ell\nu\ell\nu$ signal as well as the total background below the

Selection	$H \to WW^{(*)} \to \ell\nu\ell\nu$ ($m_H = 125$ GeV)		Total Background
	VBF	ggF, WH/ZH	
Preselection			
+ $N_{\text{jets}} \geq 2$	≈ 17 %	≈ 59 %	≈ 56 %
+ $\Delta\eta_{\text{jj}} > 3.8$	0.51 %	0.83 %	1.61 %
+ $m_{\text{jj}} > 500$ GeV	0.07 %	0.13 %	0.50 %

Table 9.2: Rejection efficiencies of the opposite hemispheres requirement $\eta_{\text{j1}} \cdot \eta_{\text{j2}} < 0$ for the $H \to WW^{(*)} \to \ell\nu\ell\nu$ signal with $m_H = 125$ GeV split into the VBF production mode and the sum of gluon fusion (ggF) and WH/ZH production modes as well as of the total background. The numbers are given for different stages of the event selection. Due to an interference between the opposite hemispheres requirement and the cuts on $\Delta\eta_{\text{jj}}$ and m_{jj}, the latter two reduce the rejection efficiencies of the first to less than one percent in both signal and background samples. The numbers are obtained from MC simulation corresponding to the 2011 dataset and represent the sum of same and opposite flavor channels.

threshold at zero, thereby considerably diminishing the impact of the opposite hemispheres requirement.

Table 9.2 provides an overview of the efficiencies of events from different samples to be rejected by the opposite hemispheres requirement. In the sample of events passing the event preselection and featuring at least two jets (see also Figure 9.9(a)), the opposite hemispheres requirement rejects of the order of 56 % and 17 % of background events and VBF signal events at $m_H = 125$ GeV, respectively. Applying the $\Delta\eta_{\text{jj}} > 3.8$ requirement to the event sample, the corresponding efficiencies drop to approximately 1.6 % and 0.5 %, respectively. The effect is further suppressed if additionally the $m_{\text{jj}} > 500$ GeV cut is applied, which results in an efficiency to fail the opposite hemispheres requirement of the order of 0.5 % for the total background and approximately 0.07 % for the VBF signal.

An alternative illustration of the interdependence between the $\eta_{\text{j1}} \cdot \eta_{\text{j2}} < 0$ and the $\Delta\eta_{\text{jj}} > 3.8$ requirements is given in Figure 9.10, which displays the two-dimensional distributions of η_{j1} versus η_{j2} for VBF signal events with $m_H = 125$ GeV as well as for background events passing the same selection as in Figure 9.9(a). In the (η_{j1}-η_{j2})-plane the opposite hemispheres requirement vacates two diagonal quarters, whereas the $\Delta\eta_{\text{jj}} > 3.8$ cut vacates the regions covered by a diagonal band. The borders of the corresponding regions are indicated in the figures through red and green lines, respectively, and reveal an extensive overlap of the two rejection regions. The regions, which are accepted by the $\Delta\eta_{\text{jj}} > 3.8$ cut but rejected by the opposite hemispheres requirement $\eta_{\text{j1}} \cdot \eta_{\text{j2}} < 0$, is given by four tiny triangles corresponding to a configuration where one jet is almost central and the other is very forward. This topology is very unlikely in both the background as well as in the $H \to WW^{(*)} \to \ell\nu\ell\nu$ VBF signal.

9.3.3. Consequences for the Analysis

For the sake of a simplified analysis and in light of the marginal impact of the opposite hemispheres requirement, it has been decided to remove the latter from the list of VBF selection cuts applied in the $H \to WW^{(*)} \to \ell\nu\ell\nu$ analysis of the 2012 dataset. It should be mentioned, however, that this conclusion is based on two important facts: firstly, the jet acceptance is restricted to pseudo-rapidities $|\eta| < 4.5$, and secondly, the $\Delta\eta_{\text{jj}}$ requirement is

at least as tight as the default of $\Delta\eta_{\mathrm{jj}} > 3.8$. While the first can be considered as a fixed actuality, the second may be subject to changes during a revision of the VBF selection.

9.4. VBF Selection in the $\mathrm{H} + 2$ Jets Channel

In the context of the optimization of the VBF selection the sensitivity of the $H \to WW^{(*)} \to \ell\nu\ell\nu$ analysis to a signal from a SM Higgs boson with a mass of $m_H = 125$ GeV produced via vector-boson fusion is to be maximized by determining optimal cut thresholds on several distinctive quantities. In the following, Higgs boson mass hypothesis other than $m_H = 125$ GeV are not investigated explicitly.

9.4.1. Definition of the Optimization Problem

Based on the default VBF analysis in the $H + 2$ jets channel detailed in Chapter 8, several selection cuts are adopted directly and are treated as a fixed preselection in the optimization, while others are subject to a variation. Here, variables related to the selection specific to the VBF forward jet topology are natural candidates for an optimization. These are the invariant mass m_{jj} of the two tagging jets, their separation in rapidity or pseudo-rapidity space Δy_{jj} and $\Delta\eta_{\mathrm{jj}}$, as well as the opposite hemispheres requirement, which may support the VBF selection if the optimal cut on $\Delta\eta_{\mathrm{jj}}$ turns out to be looser than 3.8 units (see also Section 9.3).

Furthermore, the cut threshold on the projected missing transverse energy $E_{\mathrm{T,rel}}^{\mathrm{miss}}$ is chosen to be subject to the optimization. Even though a cut on $E_{\mathrm{T,rel}}^{\mathrm{miss}}$ is part of the event preselection (see also Section 7.2.1) which is common to the $H + 0$, $H + 1$, and $H + 2$ jets channels, the VBF specific selection features handles that may motivate a deviation of the cut threshold on $E_{\mathrm{T,rel}}^{\mathrm{miss}}$ in the context of the VBF analysis.

Figure 9.11 displays the distributions of $E_{\mathrm{T,rel}}^{\mathrm{miss}}$ in the $H + 2$ jets channel after the event preselection as described in Section 7.2.1 except for the cut on $E_{\mathrm{T,rel}}^{\mathrm{miss}}$ itself in the same and the opposite flavor channels individually. While in the same flavor channels a manifest separation between the $H \to WW^{(*)} \to \ell\nu\ell\nu$ VBF signal and the total background is present due to contributions from $Z/\gamma^* + \mathrm{jets}$, this is not the case in the opposite flavor channels. In the latter the total background is distributed similarly to the $H \to WW^{(*)} \to \ell\nu\ell\nu$ signal for both the sums of the gluon fusion and WH/ZH production modes as well as for the VBF production mode. This is of particular interest in the context of the optimization and can be attributed to two facts. First, every process contributing to the total background in the opposite flavor channels constitutes a source of real missing transverse energy. Second, the presence of at least two additional jets gives rise to a significantly increased probability in the calculation of $E_{\mathrm{T,rel}}^{\mathrm{miss}}$ (see Equation (7.2)) to find an object within the azimuthal hemisphere defined by the direction of the missing transverse energy. This thereby reduces the magnitude of $E_{\mathrm{T,rel}}^{\mathrm{miss}}$ in the $H + 2$ jets channel for every process.

Given these variables and their correlations, the optimization has to be performed in four dimensions simultaneously. In opposition to the optimization of the topological selection in the $H + 0$ and $H + 1$ jet channels presented in Section 9.2, which is a computational problem of only two dimensions and can be performed by integrating two-dimensional distributions, a four-dimensional optimization calls for a dedicated implementation. Several different algorithmic approaches exist that allow to deal with more than two dimensions in an optimization. For instance, the optimization of the VBF selection performed in Ref. [163] employs a *genetic algorithm* which mimics a genetic evolution of elements in a randomly created population and

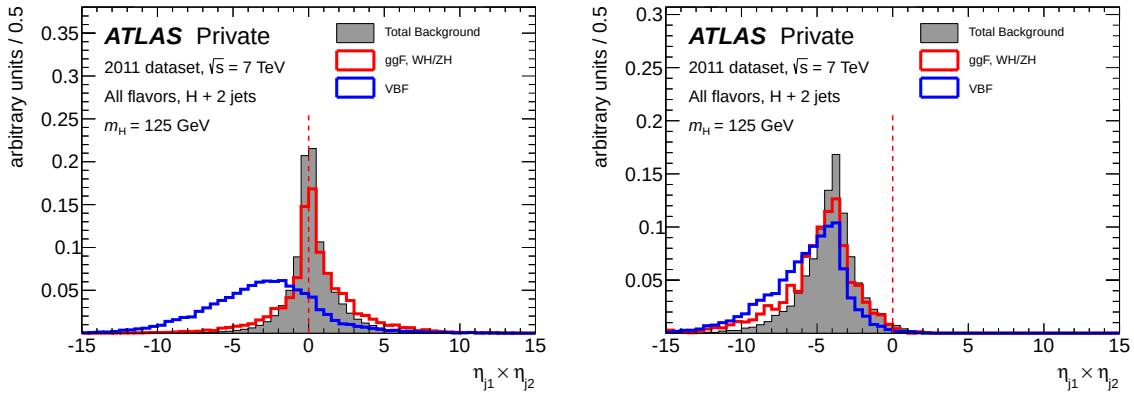

(a) Before $\Delta\eta_{jj} > 3.8$ cut

(b) After $\Delta\eta_{jj} > 3.8$ cut

Figure 9.9: Distributions of the product of the pseudo-rapidities of the two tagging jets $\eta_{j1} \cdot \eta_{j2}$. The total background is represented by gray solid histograms, while the $H \to WW^{(*)} \to \ell\nu\ell\nu$ signal with $m_H = 125$ GeV is shown as red (sums of ggF and WH/ZH production modes) and blue (VBF production mode) histograms. The opposite hemispheres requirement rejects an event if this quantity is equal or greater than zero. The distributions are obtained from MC simulation corresponding to the 2011 dataset and are normalized such that the total background as well as the individual $H \to WW^{(*)} \to \ell\nu\ell\nu$ signal contributions correspond to unit area. (a) Distribution for events passing the event preselection (see Section 7.2.1) and featuring at least two jets selected according to Section 7.1.3. (b) Distribution for events additionally passing the $\Delta\eta_{jj} > 3.8$ cut.

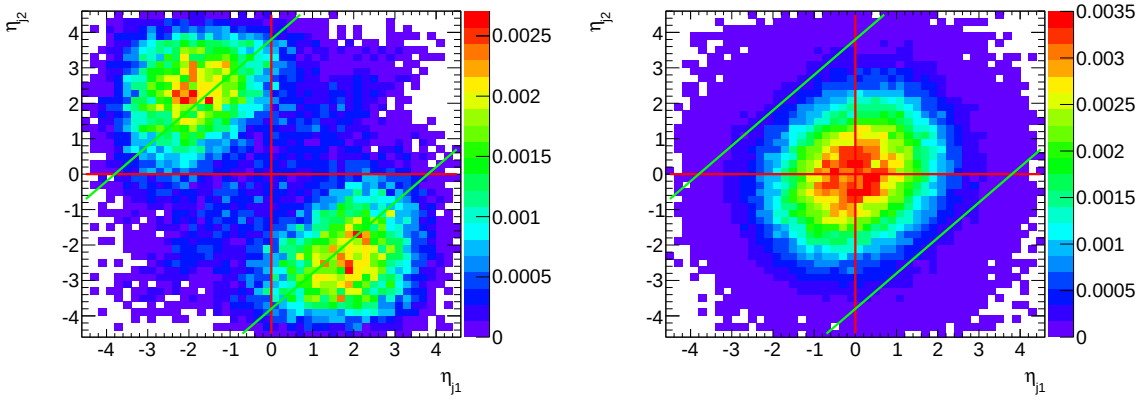

(a) VBF Signal, $m_H = 125$ GeV

(b) Total Background

Figure 9.10: Two-dimensional distributions of η_{j1} versus η_{j2}. The opposite hemispheres requirement ($\eta_{j1} \cdot \eta_{j2} < 0$) rejects events in the upper right and the lower left quarter (indicated by red lines). The $\Delta\eta_{jj} > 3.8$ requirement rejects events in the diagonal band enclosed by the green lines. This figure illustrates that the two rejection regions largely overlap. The distributions are normalized to unity and are produced from the same events as Figure 9.9(a).

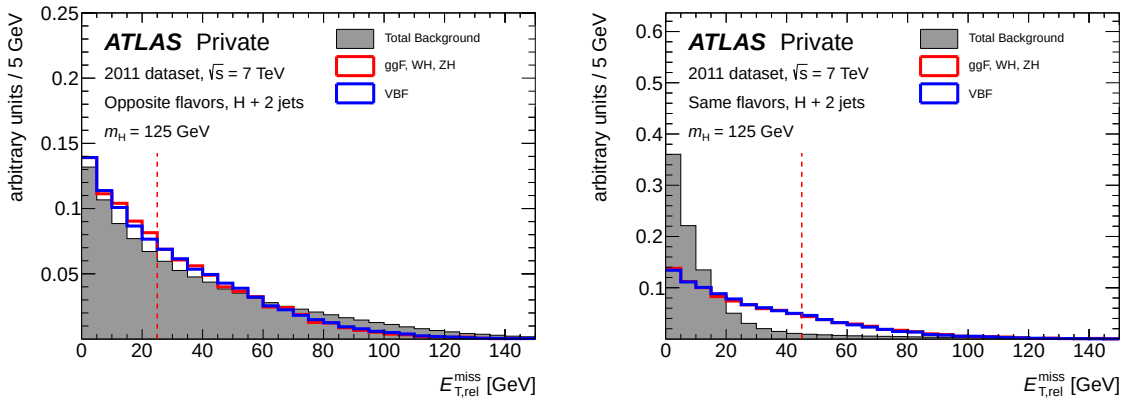

(a) Opposite flavor (b) Same flavor

Figure 9.11: Distributions of the projected missing transverse energy $E_{\mathrm{T,rel}}^{\mathrm{miss}}$ in the $H+2$ jets channel after the event preselection as described in Section 7.2.1 except for the cut on $E_{\mathrm{T,rel}}^{\mathrm{miss}}$ itself. The distributions are shown for the same flavor channels (a) and the opposite flavor channels (b). The total background is represented by the gray solid histograms, while the $H \to WW^{(*)} \to \ell\nu\ell\nu$ signal is shown as red (sums of ggF and WH/ZH production modes) and blue (VBF production mode) histograms. The nominal thresholds of $E_{\mathrm{T,rel}}^{\mathrm{miss}} > 25$ (45) GeV for the opposite (same) flavor channels are indicated as a vertical red dashed lines. The distributions are obtained from MC simulation corresponding to the 2011 dataset and are normalized such that the total background as well as the individual signal contributions correspond to unit area.

selects the best element with respect to some quality measure after several iterations (generations). Here and in the following, an *element* is a representation of a certain combination of event selection requirements, in conjunction constituting one instance of a candidate event selection.

For the optimization presented in the following a *grid scan approach* is chosen. This approach is sometimes referred to as a *brute-force* technique since it iteratively probes all elements defined by a grid in the space spanned by the intervals of possible cut thresholds on event variables subject to the optimization. Apart from being computationally expensive, one drawback of this approach is that the elements to be considered in the optimization are discrete and explicitly have to be specified in advance. However, as a consequence, a grid scan allows an easy implementation and is quite robust compared to other numerical optimization techniques which require a numerical convergence in a continuous space of possible solutions.

The grid scan optimization is based on MC simulation corresponding to the 2011 dataset and is performed for the same and the opposite flavor channels separately. The $W+$jets contributions are determined using a data-driven estimation technique outlined in Section 7.3.1. The MC event samples are preselected by requiring events to pass the default event preselection (see Section 7.2.1) except for the cut on $E_{\mathrm{T,rel}}^{\mathrm{miss}}$. Furthermore, events have to pass several additional selection requirements specific to the $H + 2$ jets channel:

- at least two jets, $N_{\mathrm{jets}} \geq 2$, including forward jet tagging (see Section 8.2.1),
- central jet veto (see Section 8.2.2),
- b-jet veto, and $Z \to \tau\tau$ veto (see Section 8.2.3).

These cuts are implemented in the same way as it is done for the default $H \to WW^{(*)} \to \ell\nu\ell\nu$ analysis of the 2011 dataset.

Since the MC simulation only comprises a limited number of events, no additional selection requirements are applied in order to avoid large statistical uncertainties on the predicted event yields. That is, with respect to the default analysis in the $H + 2$ jets channel the cuts $p_{\mathrm{T}}^{\mathrm{tot}} < 30$ GeV, $m_{\ell\ell} < 80$ GeV, and $\Delta\phi_{\ell\ell} < 1.8$ rad are omitted.

The distributions of $E_{\mathrm{T,rel}}^{\mathrm{miss}}$, $\Delta\eta_{\mathrm{jj}}$ m_{jj}, and $\eta_{\mathrm{j1}} \cdot \eta_{\mathrm{j2}}$, which are each subject to variable cuts in the scope of the grid scan optimization, in MC simulation after applying the grid scan preselection cuts are shown in Figures B.3 and B.4 in the appendix.

Based on the grid scan preselection, additional cuts with variable thresholds are applied in the scope of the optimization. These are $E_{\mathrm{T,rel}}^{\mathrm{miss}} > (E_{\mathrm{T,rel}}^{\mathrm{miss}})^{\mathrm{min}}$, $\Delta\eta_{\mathrm{jj}} > \Delta_{\eta_{\mathrm{jj}}}^{\mathrm{min}}$, $m_{\mathrm{jj}} > m_{\mathrm{jj}}^{\mathrm{min}}$, and $\eta_{\mathrm{j1}} \cdot \eta_{\mathrm{j2}} < \Pi_{\eta_{\mathrm{jj}}}^{\mathrm{max}}$. The cut thresholds $(E_{\mathrm{T,rel}}^{\mathrm{miss}})^{\mathrm{min}}$, $\Delta_{\eta_{\mathrm{jj}}}^{\mathrm{min}}$, and $m_{\mathrm{jj}}^{\mathrm{min}}$ are scanned within the intervals

$$
\begin{array}{rcccll}
10\ \mathrm{GeV} & \leq & (E_{\mathrm{T,rel}}^{\mathrm{miss}})^{\mathrm{min}} & \leq & 60\ \mathrm{GeV} & \text{in 10 steps of 5 GeV,} \\
2 & \leq & \Delta_{\eta_{\mathrm{jj}}}^{\mathrm{min}} & \leq & 5 & \text{in 15 steps of 0.2 units, and} \\
200\ \mathrm{GeV} & \leq & m_{\mathrm{jj}}^{\mathrm{min}} & \leq & 600\ \mathrm{GeV} & \text{in 16 steps of 25 GeV.}
\end{array}
$$

The effect of the opposite hemispheres requirement is probed by means of two possible values of $\Pi_{\eta_{\mathrm{jj}}}^{\mathrm{max}}$ considered in the optimization. Apart from $\Pi_{\eta_{\mathrm{jj}}}^{\mathrm{max}} = 0$, which corresponds to applying the opposite hemispheres requirement, the value $\Pi_{\eta_{\mathrm{jj}}}^{\mathrm{max}} = 100$ is used as a representation of omitting the opposite hemispheres requirement. This kind of implementation is possible since for any event it is $\eta_{\mathrm{j1}} \cdot \eta_{\mathrm{j2}} < 4.5^2 = 20.25 < 100$ as a result of the jet selection requirement $|\eta| < 4.5$ (see Section 7.1.3). The grid is chosen such that the default cut thresholds used in the $H + 2$ jets channel are exactly represented by one grid element whose proximity is sufficiently covered by the grid in each dimension.

According to the definitions mentioned above, the grid to scan is given by $11 \cdot 16 \cdot 17 \cdot 2 = 5984$ individual elements per lepton flavor channel. Each element corresponds to a certain combination of cut thresholds $(E_{\mathrm{T,rel}}^{\mathrm{miss}})^{\mathrm{min}}$, $\Delta_{\eta_{\mathrm{jj}}}^{\mathrm{min}}$, $m_{\mathrm{jj}}^{\mathrm{min}}$, and $\Pi_{\eta_{\mathrm{jj}}}^{\mathrm{max}}$. For each grid element the expected numbers of events from the $H \to WW^{(*)} \to \ell\nu\ell\nu$ signal produced via vector-boson fusion as well as from the total background are determined and used to calculate the Poisson significance according to Equation (9.2). The expected event yields are normalized to an integrated luminosity of 1 fb^{-1}.

It should be emphasized that contributions from a $H \to WW^{(*)} \to \ell\nu\ell\nu$ signal produced via gluon fusion or WH/ZH are neither taken into account as signal nor as background.

9.4.2. Results of the Optimization

The distributions of the resulting Poisson significances for all elements considered in the grid scan optimization are presented in Figures 9.12(a) and (b) for the same as well as for the opposite flavor channel, respectively. As expected, the full set of considered grid elements is widely distributed in the estimated signal sensitivity. The positions of the grid elements corresponding to the default VBF selection cuts used in the $H + 2$ jets channel are indicated as vertical red dashed lines. The default selection feature values of the estimated sensitivity somewhat below the highest values obtained in the grid scan.

The selection efficiency $\varepsilon_{\mathrm{vbf}}$ is defined as the fraction of events in a simulated sample of events from a $H \to WW^{(*)} \to \ell\nu\ell\nu$ signal for $m_H = 125$ GeV produced via vector-boson fusion and passing the grid scan preselection to additionally pass the four variable cuts on $E_{\mathrm{T,rel}}^{\mathrm{miss}}$, $\Delta\eta_{\mathrm{jj}}$, m_{jj}, and $\eta_{\mathrm{j1}} \cdot \eta_{\mathrm{j2}}$. Figures 9.12(c) and (d) provide an instructive illustration of the

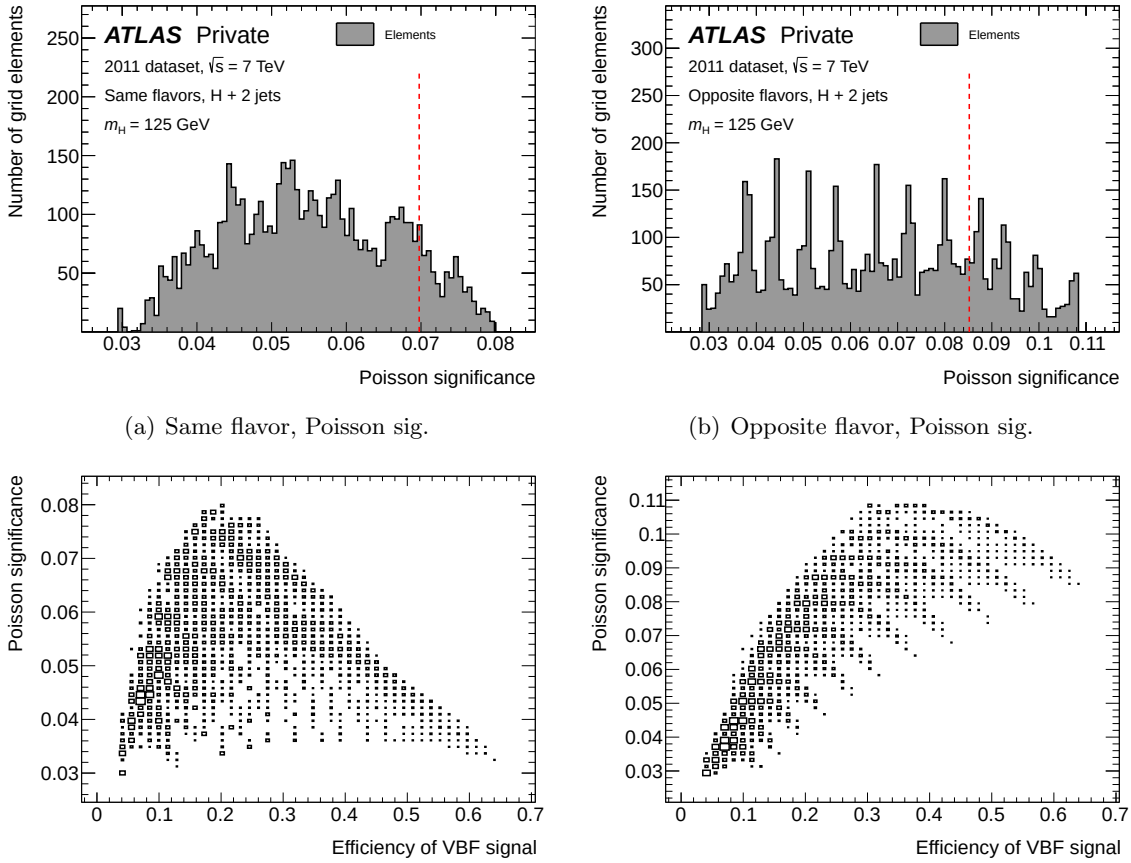

(a) Same flavor, Poisson sig.

(b) Opposite flavor, Poisson sig.

(c) Same flavor, ε_{vbf} versus Poisson sig.

(d) Opposite flavor, ε_{vbf} versus Poisson sig.

Figure 9.12: Distributions of several properties of all grid elements considered in the grid scan optimization. The distributions are shown for the same flavor channels (left) and the opposite flavor channels (right) individually. (a), (b) Distributions of the Poisson significances according to Equation (9.2) for an hypothesized integrated luminosity of 1 fb^{-1}. The vertical red dashed lines indicate the Poisson significances corresponding to the default VBF selection cuts in the $H+2$ jets channel. (c), (d) Selection efficiencies of the VBF signal ε_{vbf} versus the Poisson significances. The selection efficiencies ε are defined as the fraction of events passing the grid scan preselection to additionally

global performance of considered grid elements. It displays the two-dimensional distributions of the efficiencies ε_{vbf} versus the resulting Poisson significances for all elements considered in the grid scan.

The response of the same flavor channels is considerably different compared to the one of the opposite flavor channels. While in the latter the maximum Poisson significance is achieved for a VBF signal efficiency of the order of 35 %, the optimal grid element in the same flavor channels has a VBF signal efficiency of the order of 20 %.

A comprehensive comparison of the default cut thresholds $(E_{\text{T,rel}}^{\text{miss}})^{\text{min}}$, $\Delta_{\eta_{\text{jj}}}^{\text{min}}$, $m_{\text{jj}}^{\text{min}}$, and $\Pi_{\eta_{\text{jj}}}^{\text{max}}$ with the optimal ones obtained from the grid scan optimization is presented in Table 9.3. In the opposite flavor channels, the optimal cut on $E_{\text{T,rel}}^{\text{miss}}$ is given by $E_{\text{T,rel}}^{\text{miss}} > 10$ GeV, which is significantly looser than the default one of $E_{\text{T,rel}}^{\text{miss}} > 25$ GeV. This certainly has to be attributed to different sample compositions as well as to the features of $E_{\text{T,rel}}^{\text{miss}}$ mentioned in

	Opposite flavor		Same flavor	
	Default	Optimal	Default	Optimal
Cut thresholds				
$(E_{\mathrm{T,rel}}^{\mathrm{miss}})^{\mathrm{min}}$ [GeV]	25	10	45	30
$\Delta_{\eta_{\mathrm{jj}}}^{\mathrm{min}}$	3.8	2.8	3.8	2.8
$m_{\mathrm{jj}}^{\mathrm{min}}$ [GeV]	500	525	500	550
Opp. hem. req.	see text	no	see text	yes
Expected event yields				
VBF Signal	0.14	0.22	0.14	0.12
Total Background	2.7 ± 0.2	4.1 ± 0.2	4.2 ± 0.5	2.4 ± 0.3
Sensitivity				
Poisson significance	0.085	0.108	0.070	0.080
S/B	0.052	0.054	0.034	0.052

Table 9.3: Comparison of the default cut thresholds $(E_{\mathrm{T,rel}}^{\mathrm{miss}})^{\mathrm{min}}$, $\Delta_{\eta_{\mathrm{jj}}}^{\mathrm{min}}$, $m_{\mathrm{jj}}^{\mathrm{min}}$, and $\Pi_{\eta_{\mathrm{jj}}}^{\mathrm{max}}$ with the optimal ones obtained from the grid scan optimization for a VBF signal with $m_H = 125$ GeV. The optimization is based on MC simulation corresponding to the 2011 dataset and is performed for the opposite and the same flavor channels separately. The expected event yields are normalized to an integrated luminosity of 1 fb^{-1} and the uncertainties quoted for the total background reflect the statistical component only. The statistical uncertainties of the expected number of events from a VBF signal are less than 0.01 and are therefore not shown. The Poisson significance is calculated according to Equation (9.2).

Section 9.4.1 (see also Figure 9.11(a)). Indeed, for the same flavor channel the optimal lower bound on $E_{\mathrm{T,rel}}^{\mathrm{miss}}$ is lower than the default one, given by $E_{\mathrm{T,rel}}^{\mathrm{miss}} > 30$ GeV and $E_{\mathrm{T,rel}}^{\mathrm{miss}} > 45$ GeV, respectively.

In both the same and the opposite flavor channels the optimal cut on $\Delta\eta_{\mathrm{jj}}$ is looser than the default one of $\Delta\eta_{\mathrm{jj}} > 3.8$ and is given by $\Delta\eta_{\mathrm{jj}} > 2.8$. In contrast to that, the optimal cut on m_{jj} is tighter than the default one of $m_{\mathrm{jj}} > 500$ GeV and is given by $m_{\mathrm{jj}} > 525$ GeV and $m_{\mathrm{jj}} > 550$ GeV for the opposite and the same flavor channels, respectively.

The default analysis in the $H + 2$ jets channel requires the two tagging jets to be reconstructed in opposite rapidity hemispheres (opposite hemispheres requirement) for the analysis of the 2011 dataset, whereas this requirement is omitted for the analysis of the 2012 dataset (see Section 9.3). The optimal VBF selection determined here includes the opposite hemispheres requirement in the same flavor channels, where as it is not included in the optimal VBF selection of the opposite flavor channels.

Given the optimal cut thresholds, the Poisson significance obtained using the default selection in the opposite and the same flavor channels can be increased by approximately 25 % and 15 %, respectively. While the resulting signal-to-background ratios S/B are increased in both channels, the expected event yields of the VBF signal and the total background are larger (smaller) in the opposite (same) flavor channels.

It has to be noted again that both the expected event yields and the resulting estimated sensitivities do not include the residual cuts $p_{\mathrm{T}}^{\mathrm{tot}} < 30$ GeV, $m_{\ell\ell} < 80$ GeV, and $\Delta\phi_{\ell\ell} < 1.8$ rad, which are applied in the default analysis. Given the large statistical uncertainties

on the background predictions, which are a result of low numbers of simulated MC events passing the selection, applying additional selection requirements as a preselection appears to jeopardize reliable optimization results.

9.4.3. Stability of the Results

In order to assess the stability of the obtained optimal cut thresholds, the properties of elements which feature a Poisson significance close to the global maximum (*close-to-optimal* elements) are investigated. For this purpose, Figures 9.13 and 9.14 show the distributions of the cut thresholds for close-to-optimal elements for the opposite and the same flavor channels, respectively. Three different categories of close-to-optimal elements are defined by the fractions of the numbers of grid elements they comprise with respect to the total number. Here, these fractions are chosen to be 2 %, 1 %, and 0.1 %.

The highest stability is present in the optimal cut thresholds on $E_{\mathrm{T,rel}}^{\mathrm{miss}}$, where only a very small fraction of close-to-optimal elements deviate from the optimal threshold. Thus, since the optimal thresholds on $E_{\mathrm{T,rel}}^{\mathrm{miss}}$ differ from the default ones this has to be considered as strong evidence that it is worthwhile to decouple the event preselection in the $H + 2$ jets channel from the $H + 0/1$ jets channels.

In fact, the results for the cuts on $\Delta\eta_{\mathrm{jj}}$ and m_{jj} as well as for the opposite hemispheres requirement are not as definite as for $E_{\mathrm{T,rel}}^{\mathrm{miss}}$. Here, the most stable cut thresholds are obtained on $\Delta\eta_{\mathrm{jj}}$ in the opposite flavor channels and on m_{jj} in both the same and the opposite flavor channels. Furthermore, there is a clear indication that the opposite hemispheres requirement has a beneficial effect in the same flavor channels. The largest instabilities are present in the cut thresholds on $\Delta\eta_{\mathrm{jj}}$ in the same flavor channels and the application of the opposite hemispheres requirement in the opposite flavor channels.

Several effects may be the source of these instabilities. A quite natural candidate is the large statistical uncertainty on the background predictions, which may cause large acceptance variations for marginal changes of the event selection. Furthermore, given the four-dimensional optimization which is based on a one-dimensional quality measure, the optimal solution may be insufficiently defined and thereby be particularly susceptible to such statistical effects.

9.4.4. Consequences for the Analysis

As outlined in the previous section, the grid scan optimization features glaring evidence for the tight requirements on $E_{\mathrm{T,rel}}^{\mathrm{miss}}$ imposed in the context of the VBF selection to be non-optimal. This applies to both the same and the opposite flavor channels, though being most prominent in the opposite flavor channels. Here, the cut threshold on $E_{\mathrm{T,rel}}^{\mathrm{miss}}$ determined to be optimal is at the lower boundary of the interval considered in the optimization ($(E_{\mathrm{T,rel}}^{\mathrm{miss}})^{\mathrm{min}} = 10$ GeV). In order to avoid putting the analysis on risk by means of unknown effects potentially present for low values of $E_{\mathrm{T,rel}}^{\mathrm{miss}}$, it has been decided to adopt a moderate decrease of the $E_{\mathrm{T,rel}}^{\mathrm{miss}}$ cut threshold in the opposite flavor channels while keeping the remaining event selection unmodified.

The expected numbers of events in the opposite flavor channels obtained for this alternative event selection are presented in Table 9.4 for the total background as well as for the $H \to WW^{(*)} \to \ell\nu\ell\nu$ signal with $m_H = 125$ GeV split into the VBF and gluon fusion components. The numbers are obtained purely from MC simulation corresponding to the 2012 dataset and are normalized to the integrated luminosity in the 2012 data ($\mathcal{L} = 5.8$ fb^{-1}). The W + jets

	$E_{\mathrm{T,rel}}^{\mathrm{miss}} > 20$ GeV	$E_{\mathrm{T,rel}}^{\mathrm{miss}} > 25$ GeV	Ratio
Total Background	1.49 ± 0.37	1.39 ± 0.37	1.07
Signal			
$m_H = 125$ GeV			
ggF	0.18 ± 0.03	0.13 ± 0.02	1.12
VBF	0.58 ± 0.02	0.51 ± 0.02	1.36

Table 9.4: Expected numbers of events from backgrounds as well as from the $H \to WW^{(*)} \to \ell\nu\ell\nu$ signal for $m_H = 125$ GeV split into gluon fusion ("ggF") and vector-boson fusion ("VBF") components passing all selection cuts in the opposite flavor channels of the $H+2$ jets channel. The numbers are quoted for the alternative cut of $E_{\mathrm{T,rel}}^{\mathrm{miss}} > 20$ GeV as well as for the default cut of $E_{\mathrm{T,rel}}^{\mathrm{miss}} > 25$ GeV. The numbers are obtained purely from MC simulation corresponding to the 2012 dataset and are normalized to the integrated luminosity in the 2012 data ($\mathcal{L} = 5.8$ fb^{-1}). The quoted uncertainties reflect the statistical component only. The $W+$ jets contributions are assumed to be zero since the data-driven technique described in Section 7.3.1 yields negative estimates. The last column reflects the ratio of the expected event yields for the two $E_{\mathrm{T,rel}}^{\mathrm{miss}}$ selections. Since the contributions from top backgrounds are taken from MC simulation the estimated total background for the default selection deviates from the one presented in Chapter 8.

contributions are assumed to be zero since the data-driven technique for this process yields negative estimates (see Section 7.3.1).

Relaxing the cut on the projected missing transverse energy for the opposite flavor final states in the $H + 2$ jets channel from $E_{\mathrm{T,rel}}^{\mathrm{miss}} > 25$ GeV to $E_{\mathrm{T,rel}}^{\mathrm{miss}} > 20$ GeV results in an increase of the expected total background of approximately 7 %, whereas the VBF signal is enhanced by about 12 % and the component from gluon fusion by $\mathcal{O}(35\ \%)$. Considering the component from gluon fusion as background, the increase of the sum of both is approximately 10 % and thus still below the increase of the component from vector-boson fusion.

An independent statistical analysis similar to the one outlined in Section 7.5.1 and taking into account all relevant experimental and theoretical systematic uncertainties [174] is performed to obtain a comparison between the default ($E_{\mathrm{T,rel}}^{\mathrm{miss}} > 25$ GeV) and the alternative ($E_{\mathrm{T,rel}}^{\mathrm{miss}} > 20$ GeV) versions of the VBF candidate event selection in the opposite flavor channels. Only considering the $H + 2$ jets channel in the 2012 dataset and a Higgs boson mass hypothesis of $m_H = 125$ GeV, the independent analysis yields for the default selection 95 % CL upper limits on the Higgs boson production cross section which are compatible with the official results presented in Section 8.5 within $\mathcal{O}(10\ \%)$. This setup is used to get equitable and comparable estimates of the sensitivity for both variants of the VBF selection. In fact, an improvement of the order of 10 % in terms of the expected 95 % CL upper limit on the Higgs boson production cross section using the opposite flavor final states of the $H + 2$ jets channel in the 2012 dataset is obtained,

$$95\ \%\ \text{CL upper limit on } \sigma/\sigma_{\mathrm{SM}} = \begin{cases} 5.10 & \text{for } E_{\mathrm{T,rel}}^{\mathrm{miss}} > 20\ \text{GeV} \\ 5.67 & \text{for } E_{\mathrm{T,rel}}^{\mathrm{miss}} > 25\ \text{GeV}. \end{cases}$$

Here, σ denotes the hypothesized cross section $\sigma(pp \to H)$ times the branching ratio $\mathrm{BR}(H \to WW^{(*)} \to \ell\nu\ell\nu)$ and σ_{SM} denotes the corresponding SM expectation. Using the alternative $E_{\mathrm{T,rel}}^{\mathrm{miss}}$ selection, the expected upper limit on the relative cross section is numerically reduced and thus stronger compared to the default selection.

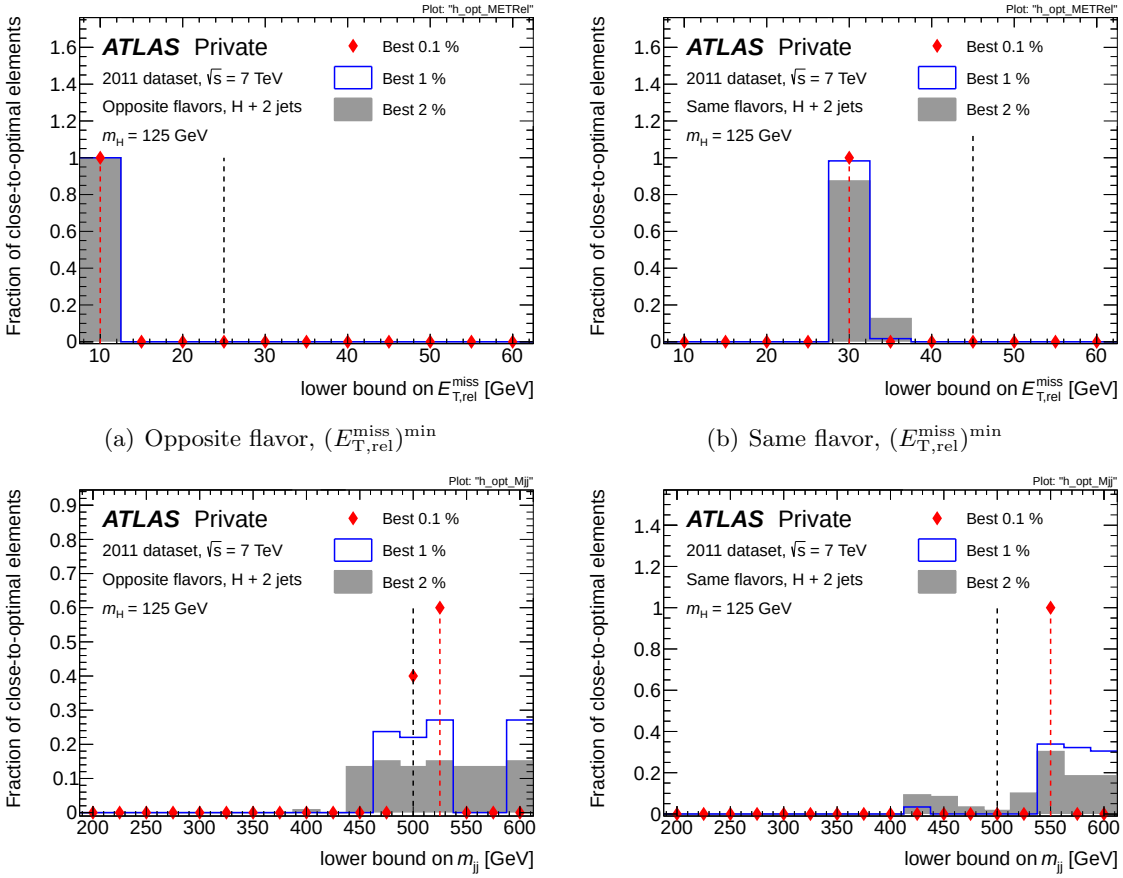

(a) Opposite flavor, $(E_{\mathrm{T,rel}}^{\mathrm{miss}})^{\mathrm{min}}$

(b) Same flavor, $(E_{\mathrm{T,rel}}^{\mathrm{miss}})^{\mathrm{min}}$

(c) Opposite flavor, $m_{\mathrm{jj}}^{\mathrm{min}}$

(d) Same flavor, $m_{\mathrm{jj}}^{\mathrm{min}}$

Figure 9.13: Distributions of cut thresholds in three different categories of close-to-optimal grid elements, which comprise the 2 % (gray solid histograms), 1 % (blue histograms), and 0.1 % (red diamond markers) grid elements featuring the highest Poisson significance out of all grid elements. The distributions are shown for the opposite flavor channels (left) and the same flavor channels (right) as well as for the cut thresholds on $E_{\mathrm{T,rel}}^{\mathrm{miss}}$ (top) and on m_{jj}. The values of the default and the optimal cut thresholds are indicated as vertical black and red dashed lines, respectively.

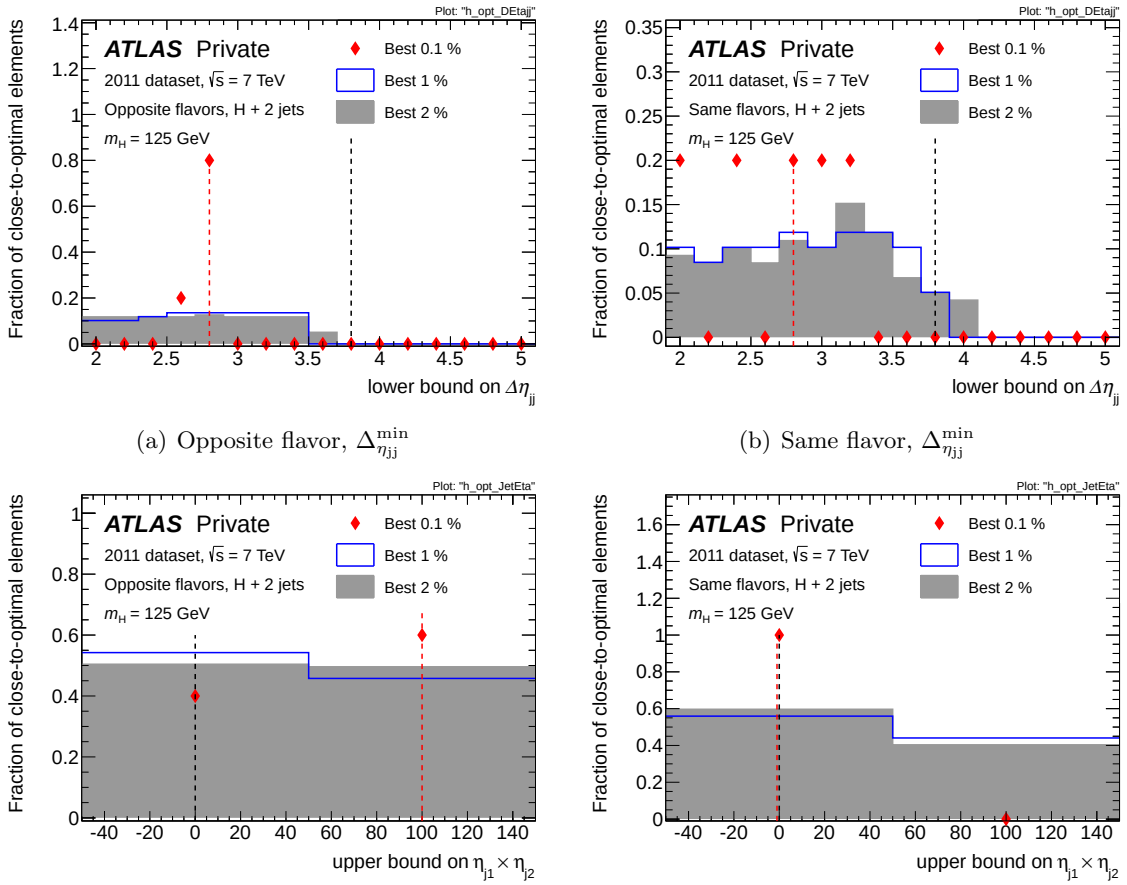

(a) Opposite flavor, $\Delta^{\min}_{\eta_{jj}}$

(b) Same flavor, $\Delta^{\min}_{\eta_{jj}}$

(c) Opposite flavor, $\Pi^{\max}_{\eta_{jj}}$

(d) Same flavor, $\Pi^{\max}_{\eta_{jj}}$

Figure 9.14: Distributions of cut thresholds in three different categories of close-to-optimal grid elements, which comprise the 2 % (gray solid histograms), 1 % (blue histograms), and 0.1 % (red diamond markers) grid elements featuring the highest Poisson significance out of all grid elements. The distributions are shown for the opposite flavor channels (left) and the same flavor channels (right) as well as for the cut thresholds on $\Delta\eta_{jj}$ (top) and on $\eta_{j1} \cdot \eta_{j2}$. The values of the default and the optimal cut thresholds are indicated as vertical black and red dashed lines, respectively.

10 Summary and Conclusion

The Standard Model (SM) of particle physics, comprising today's well-established knowledge of fundamental interactions, is a story of sustained success, though suffering from an integral defect. In conflict with observations it keeps fundamental particles massless unless an explicit mechanism spontaneously breaking the electroweak symmetry is incorporated. Albeit not yet verified, the Higgs mechanism has been incorporated in and become a cornerstone of the SM. The Higgs mechanism brings about the prediction of a new particle of unknown mass m_H, the SM Higgs boson.

The hypothetical Higgs boson H is of transient nature and a direct experimental confirmation has to rely on the observation of characteristic decay products. The ATLAS experiment at the LHC searched different decay channels for a signature of the Higgs boson. Out of these the $H \to \gamma\gamma$ and $H \to ZZ^{(*)} \to 4\ell$ channels drove the observation of an until then unknown particle with a mass of approximately 126 GeV, being supported by results of an analysis in the $H \to WW^{(*)} \to \ell\nu\ell\nu$ channel. The properties of the observed particle are compatible with the SM Higgs boson.

In this thesis a search for the SM Higgs boson in the $H \to WW^{(*)} \to \ell\nu\ell\nu$ decay channel, where the charged leptons are required to be an electrically neutral combination of electrons and muons ($\ell = e, \mu$), has been presented. The analysis is based on proton-proton (pp) collision data collected in the years 2011 and 2012 with the ATLAS detector at the LHC at center-of-mass energies of $\sqrt{s} = 7$ TeV and $\sqrt{s} = 8$ TeV, respectively. The dataset in total corresponds to an integrated luminosity of approximately $\mathcal{L} = 10.5$ fb^{-1}. While the analysis of the 2011 dataset used both same and opposite flavor combinations of the charged leptons, the analysis of the 2012 dataset had to refrain from using the same flavor combination. This is due to the fact that the same flavor channels received a significantly increased contribution from $Z/\gamma^* \to \ell\ell$ decays as a result of an increased instantaneous luminosity degrading the resolution of the missing transverse energy measurement.

In the full dataset an excess of events was observed which is compatible with the expected signal from a SM Higgs boson with a mass of $m_H = 125$ GeV, which has been chosen as a reference hypothesis. An analysis employing statistical methods which take into account data-driven background estimations as well as systematic uncertainties yielded a minimal probability for a fluctuation of the background at $m_H = 125$ GeV which is equivalent to 2.8 standard deviations.

Driven by a significant difference in the composition of both backgrounds and signal production mechanisms, the $H \to WW^{(*)} \to \ell\nu\ell\nu$ analysis is split into three different categories distinguished according to the number of reconstructed jets in an event. The $H + 0$ and $H + 1$ jet channels are dominated by the Higgs boson production via gluon fusion and feature the bulk of the sensitivity. The $H + 2$ jets channel, comprising events with at least two reconstructed jets, is geared towards the vector-boson fusion (VBF) Higgs boson production mode and can be considered as complementary to the $H + 0$ and $H + 1$ jet channels by allowing to purely probe Higgs boson couplings to massive vector bosons. Given the low signal cross section and the large background to be suppressed, the expected 95 % confidence level (CL) exclusion limit on the Higgs boson production cross section using the $H + 2$ jets channel alone

is of the order of four and of the order of 5.5 times the SM expectation at $m_H = 125$ GeV using the 2011 and the 2012 dataset, respectively. The observed cross section limits are well compatible with the expect ones assuming the absence of a signal.

The studies related to this thesis had a twofold focus. On the one hand, an essential component of the Common Analysis Framework (CAF), the `HWWAnalysisCode`, was designed and developed. The CAF is a software framework implementing the entire $H \to WW^{(*)} \to \ell\nu\ell\nu$ analysis chain in a way providing easy access for any member of the ATLAS Collaboration. It has become the default analysis software setup of the Higgs-to-WW sub-group and was used to obtain results for all recent publications related to the $H \to WW^{(*)} \to \ell\nu\ell\nu$ analysis. In the scope of the commissioning and maintenance of the `HWWAnalysisCode` a number of aspects of the analysis were investigated.

In addition, several optimization studies were performed aiming for an improvement of the sensitivity of the analysis to a Higgs boson signal. Due to spin correlations and the coupling structure of W bosons to leptons, the spin-0 nature of the SM Higgs boson induces a distinctive event topology in $H \to WW^{(*)} \to \ell\nu\ell\nu$ events, which strongly depends on m_H. This topology is exploited by placing cuts on the invariant mass $m_{\ell\ell}$ of the two charged leptons as well as their azimuthal separation angle $\Delta\phi_{\ell\ell}$. Based on Monte Carlo (MC) simulation, these cuts were optimized by maximizing the Poisson significance of a Higgs boson signal for 24 different mass points in the range 110 GeV $\leq m_H \leq$ 300 GeV, taking into account all relevant signal and background contributions. The stability of the optimization results was investigated and the $m_{\ell\ell}$ variable was found to provide the predominant separation between signal and backgrounds. Based on these fine-grained results, three successive categories in m_H each with unified selection cuts on $m_{\ell\ell}$ and $\Delta\phi_{\ell\ell}$ were defined and adopted.

In the $H + 2$ jets channel, the VBF topology, given by two jets with large transverse momenta in the forward regions of the detector (tagging jets), provides unique handles to suppress a large fraction of background contributions. The commonly imposed opposite hemispheres requirement, demanding the tagging jets to be reconstructed within opposite rapidity hemispheres, was found to have negligible impact in cooperation with the default requirement on the pseudo-rapidity gap $\Delta\eta_{\mathrm{jj}}$ between the two tagging jets, and therefore was removed for the analysis of the 2012 dataset.

Aiming for a comprehensive optimization of the VBF candidate event selection for the $m_H = 125$ GeV hypothesis, a grid scan approach was used to probe the performance of variable but discrete cut thresholds in four dimensions. Here, cuts on the projected missing transverse energy $E_{\mathrm{T,rel}}^{\mathrm{miss}}$, the invariant mass m_{jj} of the two tagging jets, as well as on $\Delta\eta_{\mathrm{jj}}$ were considered. The application of the opposite hemispheres requirement was included as the fourth dimension to account for a variable $\Delta\eta_{\mathrm{jj}}$ cut. The sensitivity was estimated using the Poisson significance obtained on MC simulation. The optimization yielded clear evidence for a potential improvement of the VBF signal sensitivity to be taken advantage of by decreasing the thresholds on $E_{\mathrm{T,rel}}^{\mathrm{miss}}$. The optimal cuts on m_{jj} and $\Delta\eta_{\mathrm{jj}}$ as well as the application of the opposite hemispheres requirement was not as definite as in the case of $E_{\mathrm{T,rel}}^{\mathrm{miss}}$.

A statistical analysis identified an increase of the sensitivity to a VBF signal at $m_H = 125$ GeV in the opposite flavor channels of the order of 10 % by lowering the cut threshold on $E_{\mathrm{T,rel}}^{\mathrm{miss}}$ from 25 GeV to 20 GeV while keeping other parameters of the event selection fixed.

In view of the presence of a Higgs boson-like signal with $m_H = 125$ GeV established in the channels $H \to \gamma\gamma$, $H \to ZZ^{(*)} \to 4\ell$, and $H \to WW^{(*)} \to \ell\nu\ell\nu$ it is an essential objective to determine the properties of the new boson. In doing so, the confirmation of the presence of the VBF process is a crucial element. Using the entire pp collision data recorded with the ATLAS detector in the year 2012, the VBF analysis presented herein may be able to provide first evidence for a VBF signal.

A Auxiliary Material for the Analysis in the $\mathrm{H}+0$ and $\mathrm{H}+1$ Jet Channels

This chapter provides auxiliary material related to the analysis in the $H+0$ and $H+1$ jet channels presented in Chapter 7.

- A more detailed version of Table 7.5 listing the efficiency of events from different physics processes to pass the cuts on $m_{\ell\ell}$ and $E_{\mathrm{T,rel}}^{\mathrm{miss}}$ in the context of the event preselection is presented in Table A.1.
- A version of Figure 7.2 illustrating the $E_{\mathrm{T,rel}}^{\mathrm{miss}}$ distribution in the same and the opposite flavor channels individually but in the 2012 dataset is given in Figure A.1.
- The distribution of the number of reconstructed jets in events from the 2012 dataset passing the event preselection is presented in Figure A.2.
- Tables A.2 to A.5 list the fraction of events with zero, one or at least two jets (*event fractions*) as well as the signal and background composition of event samples with zero, one or at least two jets (*sample composition*). Jets are counted according to the acceptance criteria described in Section 7.1.3 and events have to pass the preselection described in Section 7.2.1. While Table 7.6 lists numbers for the 2011 dataset inclusively in the same and opposite flavor channels, the following tables break the numbers down into datasets and same/opposite flavor final states.
- Figure A.3 displays the distributions of the transverse mass of $H \to WW^{(*)} \to \ell\nu\ell\nu$ signal events for $m_H = 125$ GeV in the 2011 and the 2012 datasets.

Process	2011 dataset		2012 dataset	
	SF	OF	SF	OF
Signal				
$m_H = 110$ GeV	25 %	59 %	26 %	57 %
$m_H = 125$ GeV	36 %	67 %	35 %	64 %
$m_H = 140$ GeV	43 %	71 %	42 %	69 %
$m_H = 170$ GeV	58 %	80 %	58 %	80 %
$m_H = 200$ GeV	42 %	76 %	42 %	75 %
$m_H = 240$ GeV	36 %	72 %	36 %	71 %
Backgrounds				
SM WW	30 %	63 %	30 %	63 %
$WZ/ZZ/W\gamma$	2.0 %	49 %	4.8 %	41 %
Single top	31 %	62 %	34 %	62 %
Top pairs	29 %	58 %	30 %	58 %
$Z/\gamma^* + \text{jets}$				
$Z/\gamma^* + \text{jets} \to ee, \mu\mu$	0.03 %	8.5 %	0.14 %	17 %
$Z/\gamma^* + \text{jets} \to \tau\tau$	0.48 %	7.5 %	1.6 %	15 %
$W + \text{jets}$	5.0 %	35 %	2.3 %	35 %

Table A.1: The efficiencies of events from different processes to pass the $m_{\ell\ell}$ and $E_{\mathrm{T,rel}}^{\mathrm{miss}}$ cuts of the preselection. "SF" refers to the sum of the same flavor channels and "OF" refers to the sum of the opposite flavor channels. The relative statistical uncertainties on the quoted numbers are less than 2.0 % in all cases.

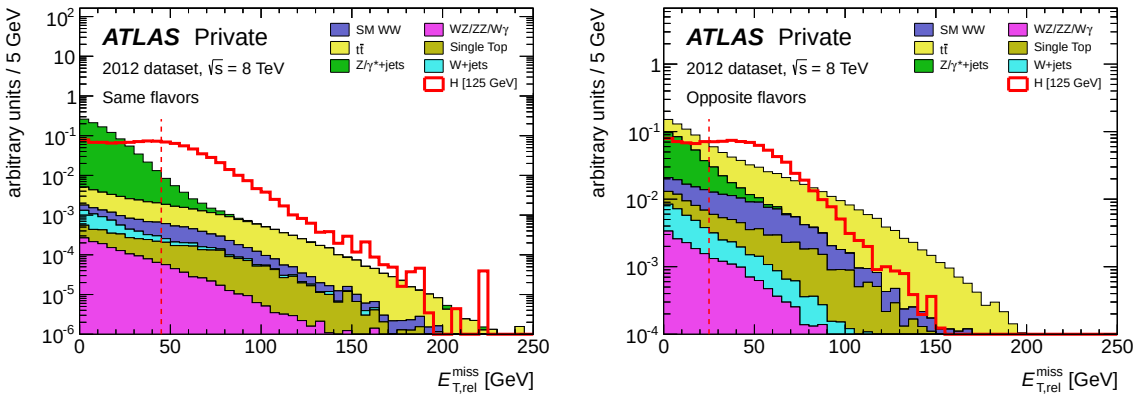

(a) Same flavor (b) Opposite flavor

Figure A.1: Distributions of the projected missing transverse energy $E_{\mathrm{T,rel}}^{\mathrm{miss}}$ after applying the selection criteria based on the invariant mass $m_{\ell\ell}$. The distributions are shown for the same flavor channels (a) and the opposite flavor channels (b). The solid histograms correspond to the total background, while the expected contributions from a $H \to WW^{(*)} \to \ell\nu\ell\nu$ signal with $m_H = 125$ GeV are superimposed as red hisograms. The distributions are obtained from MC simulation corresponding to the 2012 dataset and are normalized such that the total background as well as the $H \to WW^{(*)} \to \ell\nu\ell\nu$ signal correspond to unit area. The cut thresholds of $E_{\mathrm{T,rel}}^{\mathrm{miss}} > 45$ (25) GeV in the same (opposite) flavor channels are indicated as vertical red dashed lines. See Figure 7.2 for a version corresponding to the 2011 dataset.

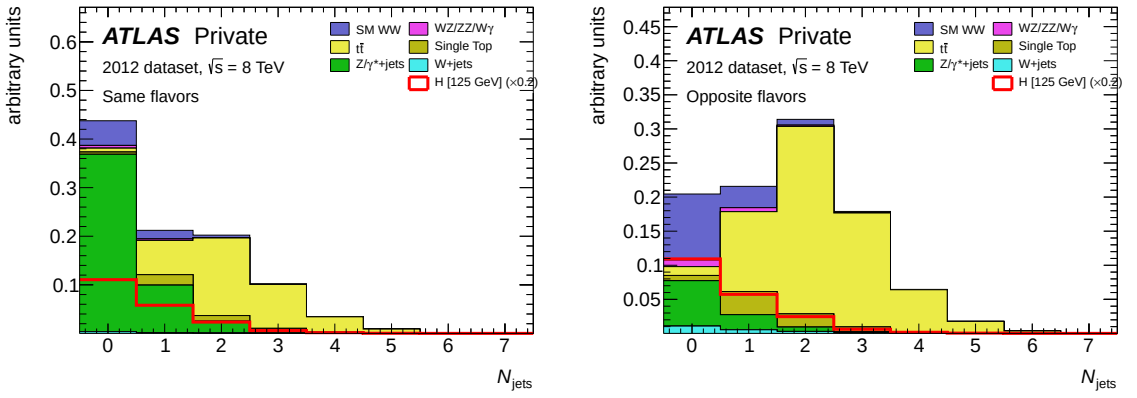

(a) Same flavor (b) Opposite flavor

Figure A.2: Distributions of the number of reconstructed jets N_{jets} according to the acceptance criteria described in Section 7.1.3 in events passing the event preselection as described in Section 7.2.1. The distributions are shown for the same flavor channels (a) and the opposite flavor channels (b). The solid histograms correspond to the total background, while the expected contributions from a $H \to WW^{(*)} \to \ell\nu\ell\nu$ signal with $m_H = 125$ GeV are superimposed as red hisograms. The distributions are obtained from MC simulation corresponding to the 2012 dataset and are normalized such that the total background as well as the $H \to WW^{(*)} \to \ell\nu\ell\nu$ signal correspond to unit area. See Figure 7.3 for a version corresponding to the 2011 dataset.

Process	Event fractions, $\sum(\ \cdots\ ) = 1$			Sample Compositions, $\sum(\ \vdots\ ) = 1$		
	$N_{\text{jets}} = 0$	$N_{\text{jets}} = 1$	$N_{\text{jets}} \geq 2$	$N_{\text{jets}} = 0$	$N_{\text{jets}} = 1$	$N_{\text{jets}} \geq 2$
Signal						
$m_H = 125$ GeV						
ggF	70 %	23 %	8 %	96 %	82 %	54 %
VBF	8 %	39 %	53 %	1 %	10 %	27 %
WH/ZH	29 %	32 %	39 %	3 %	8 %	18 %
Backgrounds						
SM WW	69 %	23 %	8 %	32 %	13 %	2 %
$WZ/ZZ/W\gamma$	55 %	32 %	14 %	2 %	2 %	0 %
Single top	12 %	51 %	37 %	3 %	14 %	5 %
Top pairs	3 %	20 %	77 %	5 %	48 %	89 %
$Z/\gamma^* + \text{jets}$	72 %	22 %	6 %	55 %	21 %	3 %
$W + \text{jets}$	64 %	26 %	11 %	4 %	2 %	0 %

Table A.2: Fraction of events with zero, one or at least two jets as well as the signal and background composition of event samples with zero, one or at least two jets. The numbers are determined from MC simulation corresponding to the 2011 dataset using events in the same flavor channels passing the event preselection (see Section 7.2.1). Jets are selected according to the criteria described in Section 7.1.3. The rounding of the quoted numbers may induce sums deviating from 100 %. The statistical uncertainties on the quoted numbers are less than 5 % in all cases.

Process	Event fractions, $\sum(\ \cdots\ ) = 1$			Sample Compositions, $\sum(\ \vdots\ ) = 1$		
	$N_{\text{jets}} = 0$	$N_{\text{jets}} = 1$	$N_{\text{jets}} \geq 2$	$N_{\text{jets}} = 0$	$N_{\text{jets}} = 1$	$N_{\text{jets}} \geq 2$
Signal						
$m_H = 125$ GeV						
ggF	68 %	24 %	8 %	97 %	83 %	55 %
VBF	8 %	37 %	54 %	1 %	10 %	28 %
WH/ZH	29 %	32 %	39 %	2 %	7 %	17 %
Backgrounds						
SM WW	70 %	22 %	8 %	53 %	16 %	2 %
$WZ/ZZ/W\gamma$	56 %	32 %	12 %	4 %	2 %	0 %
Single top	11 %	50 %	40 %	4 %	16 %	5 %
Top pairs	2 %	18 %	79 %	7 %	52 %	90 %
$Z/\gamma^* + \text{jets}$	64 %	26 %	11 %	22 %	8 %	1 %
$W + \text{jets}$	63 %	25 %	12 %	10 %	4 %	1 %

Table A.3: Fraction of events with zero, one or at least two jets as well as the signal and background composition of event samples with zero, one or at least two jets. The numbers are determined from MC simulation corresponding to the 2011 dataset using events in the opposite flavor channels passing the event preselection (see Section 7.2.1). Jets are selected according to the criteria described in Section 7.1.3. The rounding of the quoted numbers may induce sums deviating from 100 %. The statistical uncertainties on the quoted numbers are less than 6 % in all cases.

Process	Event fractions, $\sum(\ \cdots\ ) = 1$			Sample Compositions, $\sum(\ \vdots\ ) = 1$		
	$N_{\text{jets}} = 0$	$N_{\text{jets}} = 1$	$N_{\text{jets}} \geq 2$	$N_{\text{jets}} = 0$	$N_{\text{jets}} = 1$	$N_{\text{jets}} \geq 2$
Signal						
$m_H = 125$ GeV						
ggF	60 %	28 %	12 %	95 %	86 %	66 %
VBF	9 %	38 %	53 %	1 %	9 %	22 %
WH/ZH	36 %	29 %	35 %	3 %	5 %	12 %
Backgrounds						
SM WW	68 %	24 %	9 %	12 %	8 %	2 %
$WZ/ZZ/W\gamma$	58 %	31 %	11 %	1 %	1 %	0 %
Single top	11 %	50 %	40 %	1 %	10 %	5 %
Top pairs	2 %	19 %	79 %	2 %	33 %	83 %
$Z/\gamma^* + \text{jets}$	74 %	20 %	6 %	83 %	46 %	9 %
$W + \text{jets}$	45 %	22 %	33 %	1 %	1 %	1 %

Table A.4: Fraction of events with zero, one or at least two jets as well as the signal and background composition of event samples with zero, one or at least two jets. The numbers are determined from MC simulation corresponding to the 2012 dataset using events in the same flavor channels passing the event preselection (see Section 7.2.1). Jets are selected according to the criteria described in Section 7.1.3. The rounding of the quoted numbers may induce sums deviating from 100 %. The statistical uncertainties on the quoted numbers are less than 6 % in all cases.

Process	Event fractions, $\sum(\ \cdots\ ) = 1$			Sample Compositions, $\sum(\ \vdots\ ) = 1$		
	$N_{\text{jets}} = 0$	$N_{\text{jets}} = 1$	$N_{\text{jets}} \geq 2$	$N_{\text{jets}} = 0$	$N_{\text{jets}} = 1$	$N_{\text{jets}} \geq 2$
Signal						
$m_H = 125$ GeV						
ggF	60 %	28 %	12 %	97 %	85 %	64 %
VBF	9 %	38 %	54 %	1 %	9 %	22 %
WH/ZH	24 %	34 %	43 %	2 %	6 %	14 %
Backgrounds						
SM WW	70 %	23 %	8 %	47 %	15 %	2 %
$WZ/ZZ/W\gamma$	54 %	32 %	13 %	5 %	3 %	0 %
Single top	11 %	49 %	40 %	4 %	16 %	5 %
Top pairs	2 %	18 %	80 %	6 %	54 %	91 %
$Z/\gamma^* + \text{jets}$	69 %	23 %	8 %	33 %	10 %	1 %
$W + \text{jets}$	50 %	25 %	26 %	5 %	2 %	1 %

Table A.5: Fraction of events with zero, one or at least two jets as well as the signal and background composition of event samples with zero, one or at least two jets. The numbers are determined from MC simulation corresponding to the 2012 dataset using events in the opposite flavor channels passing the event preselection (see Section 7.2.1). Jets are selected according to the criteria described in Section 7.1.3. The rounding of the quoted numbers may induce sums deviating from 100 %. The statistical uncertainties on the quoted numbers are less than 6 % in all cases.

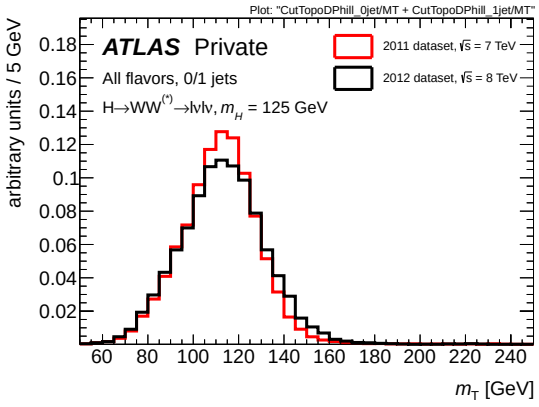

Figure A.3: Comparison of the distributions of the transverse mass m_{T} in simulated $H \to WW^{(*)} \to \ell\nu\ell\nu$ signal events for $m_H = 125$ GeV passing the final signal selection of the $H+0$ or $H+1$ jet channels in the 2011 dataset (red histogram) and the 2012 dataset (black histogram). The distributions correspond to the sum of the same and the opposite flavor channels for both datasets and are normalized to unit area.

B Auxiliary Material for the Optimization

This chapter provides auxiliary material related to the optimization of the event selection presented in Chapter 9.

- Section 9.2 presents an optimization of the topological selection in the H+0 and H+1 jet channels. The optimization is performed for the sum of the same and opposite flavor as well as the $H + 0$ and $H + 1$ jet channels. In order to ensure the validity of the results obtained from the combination of the individual channels the optimization procedure is also performed for these channels separately and presented in Figures B.1 and B.2. The results corresponding to individual channels are compatible with the ones corresponding to the combination of all channels.
- The grid scan optimization presented in Section 9.4 is based on a dedicated preselection including the default event preselection and additional cuts specific to the $H + 2$ jets channel. Figures B.3 and B.4 display distributions of quantities subject to the optimization in events of the same and the opposite flavor channel, respectively, passing the grid scan preselection.

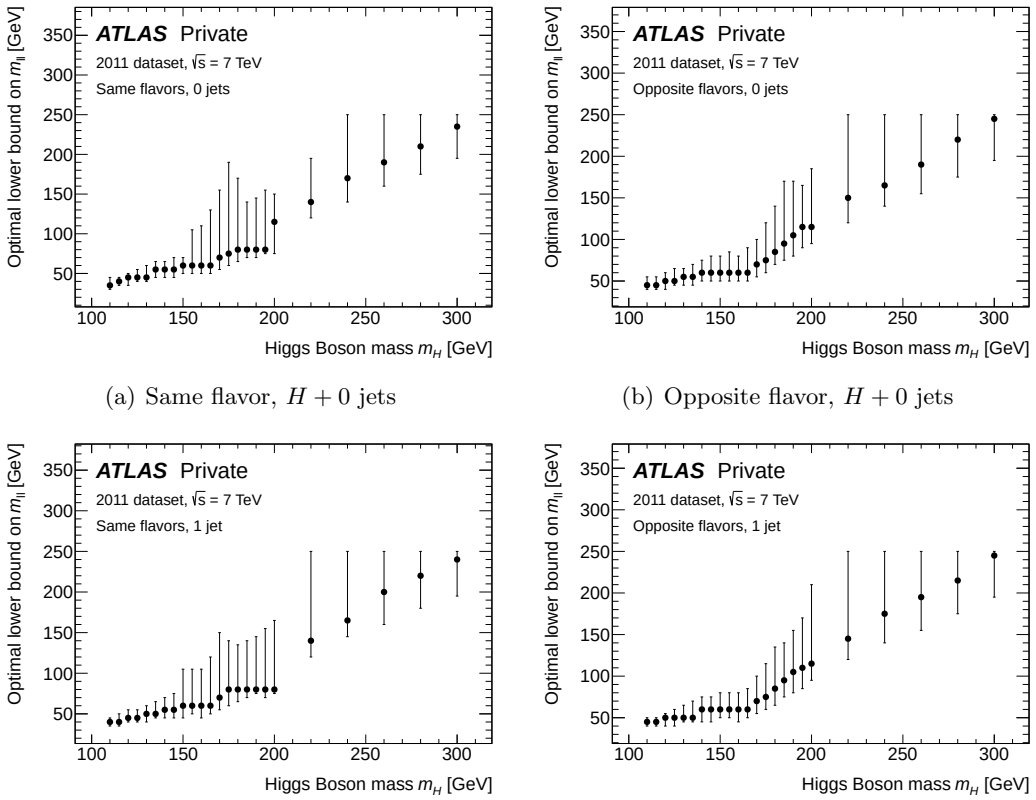

(a) Same flavor, $H + 0$ jets

(b) Opposite flavor, $H + 0$ jets

(c) Same flavor, $H + 1$ jet

(d) Opposite flavor, $H + 1$ jet

Figure B.1: Illustration of the optimal cut thresholds $m_{\ell\ell}^{\max}(m_H)$ obtained in the context of the optimization of the topological selection as a function of m_H for individual channels. The values are determined by maximizing the estimated sensitivity (Poisson significance) for each value of m_H individually. The vertical error bars indicate the interval which retains a sensitivity better than 95 % of the global maximum.

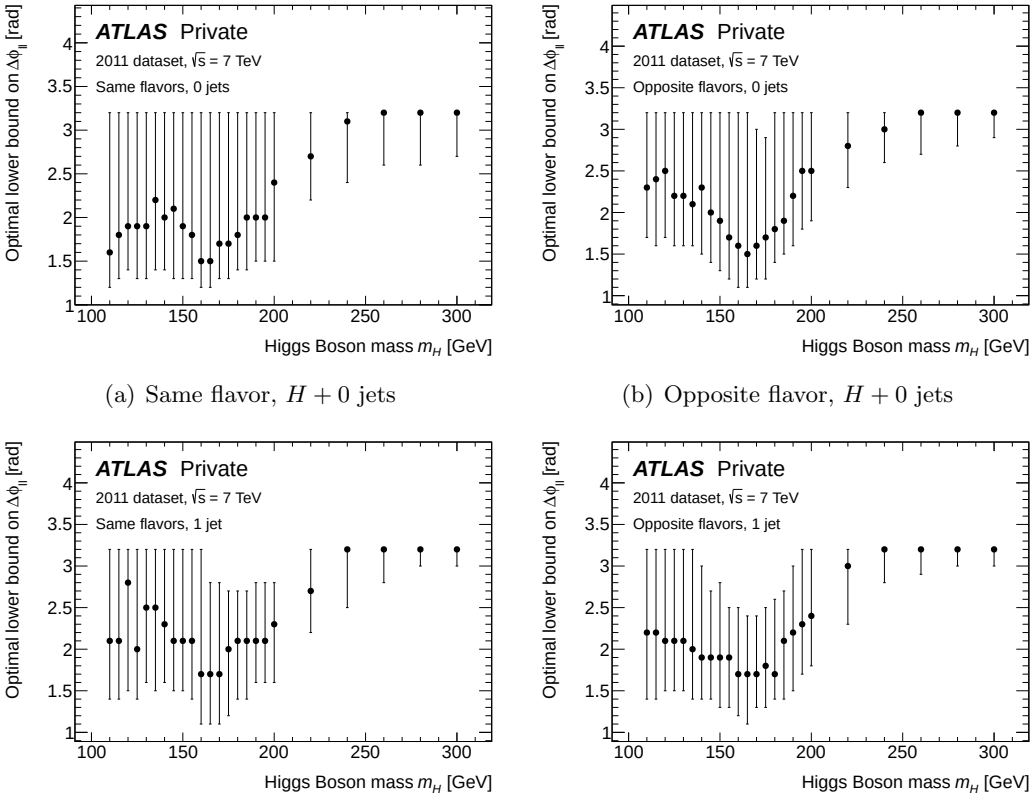

(a) Same flavor, $H + 0$ jets

(b) Opposite flavor, $H + 0$ jets

(c) Same flavor, $H + 1$ jet

(d) Opposite flavor, $H + 1$ jet

Figure B.2: Illustration of the optimal cut thresholds $\Delta^{\max}_{\phi_{\ell\ell}}(m_H)$ obtained in the context of the optimization of the topological selection as a function of m_H for individual channels. The values are determined by maximizing the estimated sensitivity (Poisson significance) for each value of m_H individually. The vertical error bars indicate the interval which retains a sensitivity better than 95 % of the global maximum.

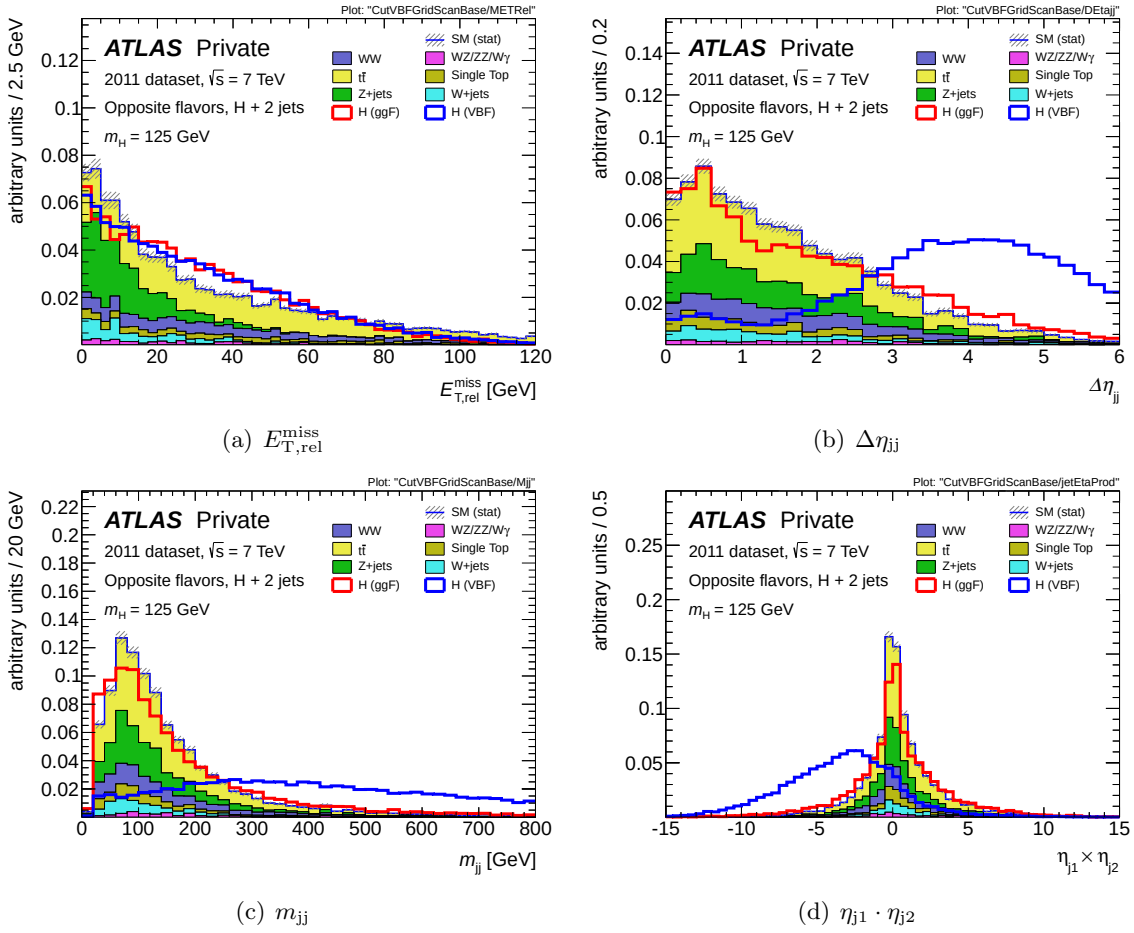

(a) $E_{\mathrm{T,rel}}^{\mathrm{miss}}$ (b) $\Delta\eta_{\mathrm{jj}}$

(c) m_{jj} (d) $\eta_{\mathrm{j1}} \cdot \eta_{\mathrm{j2}}$

Figure B.3: Distributions of the projected missing transverse energy $E_{\mathrm{T,rel}}^{\mathrm{miss}}$, the separation in pseudo-rapidity $\Delta\eta_{\mathrm{jj}}$ between the two tagging jets, their invariant mass m_{jj} and the product of their pseudo-rapdities $\eta_{\mathrm{j1}} \cdot \eta_{\mathrm{j2}}$ after passing the prselection for the grid scan optimization in the opposite flavor channel. The contribution from individual background processes is reflected by the solid colored histograms, while the contributions from a $H \to WW^{(*)} \to \ell\nu\ell\nu$ signal with $m_H = 125$ GeV produced in the ggF or the VBF mode are shown as red and blue histograms, respectively. The distributions are taken from Monte Carlo simulation corresponding to the 2011 dataset and are normalized such that the total background as well as the individual signal contributions correspond to unit area.

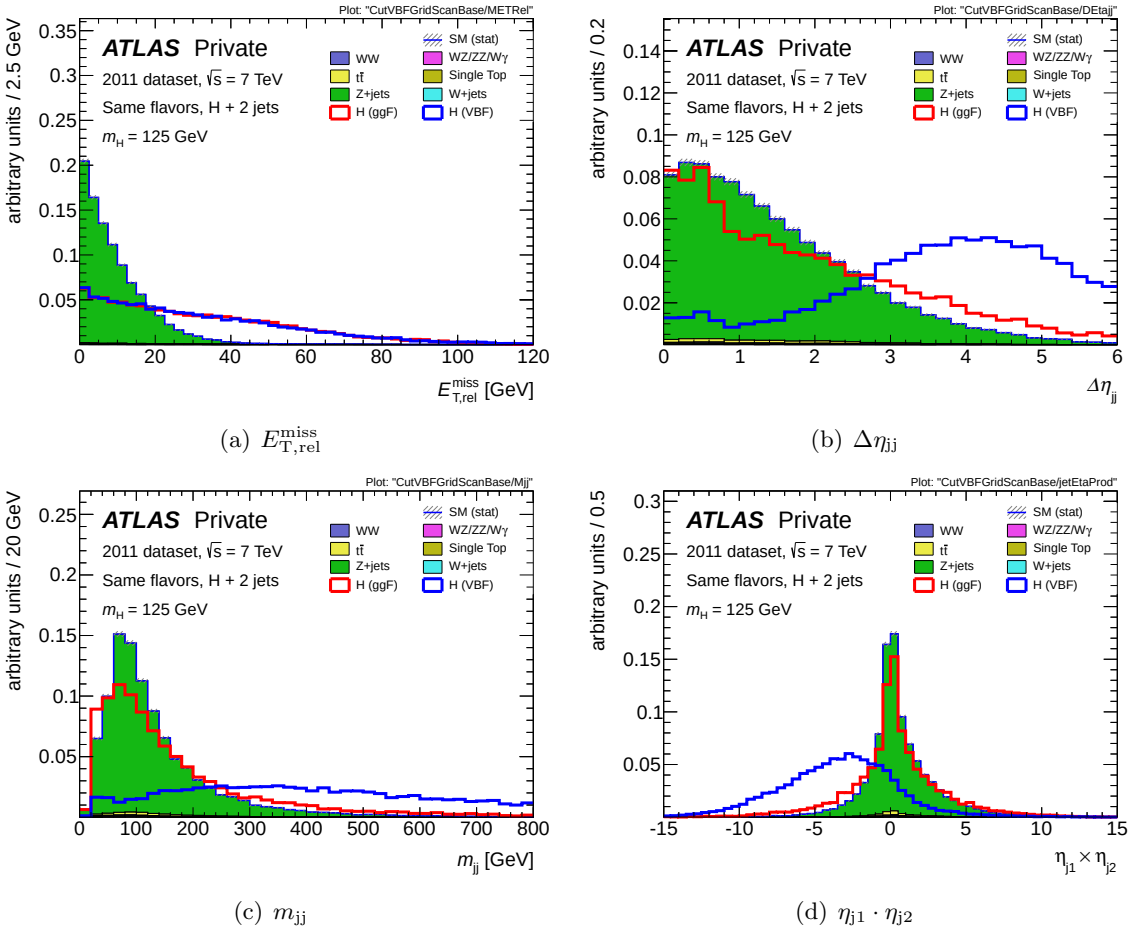

(a) $E_{\mathrm{T,rel}}^{\mathrm{miss}}$ (b) $\Delta\eta_{\mathrm{jj}}$

(c) m_{jj} (d) $\eta_{\mathrm{j1}} \cdot \eta_{\mathrm{j2}}$

Figure B.4: Distributions of the projected missing transverse energy $E_{\mathrm{T,rel}}^{\mathrm{miss}}$, the separation in pseudo-rapidity $\Delta\eta_{\mathrm{jj}}$ between the two tagging jets, their invariant mass m_{jj} and the product of their pseudo-rapdities $\eta_{\mathrm{j1}} \cdot \eta_{\mathrm{j2}}$ after passing the prselection for the grid scan optimization in the same flavor channel. The contribution from individual background processes is reflected by the solid colored histograms, while the contributions from a $H \to WW^{(*)} \to \ell\nu\ell\nu$ signal with $m_H = 125$ GeV produced in the ggF or the VBF mode are shown as red and blue histograms, respectively. The distributions are taken from Monte Carlo simulation corresponding to the 2011 dataset and are normalized such that the total background as well as the individual signal contributions correspond to unit area.

Bibliography

[1] "CERN to give update on Higgs search as curtain raiser to ICHEP conference." CERN Press Release, June 22nd, 2012.

[2] J. Ellis, M. K. Gaillard, and D. V. Nanopoulos, "A Historical Profile of the Higgs Boson", arXiv:1201.6045 [hep-ph].

[3] **ATLAS Collaboration**, "Combination of Higgs Boson Searches with up to 4.9 fb^{-1} of pp Collisions Data Taken at a center-of-mass energy of 7 TeV with the ATLAS Experiment at the LHC." ATLAS Note: ATLAS-CONF-2011-163.

[4] **CMS Collaboration**, S. Chatrchyan *et al.*, "Combined results of searches for the standard model Higgs boson in pp collisions at $\sqrt{s} = 7$ TeV", *Phys. Lett.* **B710** (2012) 26–48, arXiv:1202.1488 [hep-ex].

[5] **Tevatron New Physics Higgs Working Group, CDF Collaboration, DØ Collaboration**, "Updated Combination of CDF and DØ Searches for Standard Model Higgs Boson Production with up to 10.0 fb^{-1} of Data", arXiv:1207.0449 [hep-ex].

[6] F. Gianotti, "Status of Standard Model Higgs searches in ATLAS." Talk given at the scientific seminar on July 4th, 2012 at CERN.

[7] J. Incandela, "Status of the CMS SM Higgs Search." Talk given at the scientific seminar on July 4th, 2012 at CERN.

[8] **ATLAS Collaboration**, G. Aad *et al.*, "Observation of a new particle in the search for the Standard Model Higgs boson with the ATLAS detector at the LHC", *Phys. Lett. B* (2012) , arXiv:1207.7214 [hep-ex].

[9] **CMS Collaboration**, S. Chatrchyan *et al.*, "Observation of a new boson at a mass of 125 GeV with the CMS experiment at the LHC", *Phys. Lett.* **B716** (2012) 30–61, arXiv:1207.7235 [hep-ex].

[10] S. L. Glashow, "Partial-symmetries of weak interactions", *Nucl. Phys.* **22** no. 4, (1961) 579 – 588.

[11] S. Weinberg, "A Model of Leptons", *Phys. Rev. Lett.* **19** (1967) 1264–1266.

[12] A. Salam, "Weak and Electromagnetic Interactions", *Conf. Proc.* **C680519** (1968) 367–377.

[13] G. 't Hooft and M. Veltman, "Regularization and renormalization of gauge fields", *Nucl. Phys. B* **44** no. 1, (1972) 189 – 213.

[14] F. Englert and R. Brout, "Broken Symmetry and the Mass of Gauge Vector Mesons", *Phys. Rev. Lett.* **13** (1964) 321–323.

[15] P. Higgs, "Broken symmetries, massless particles and gauge fields", *Phys. Lett.* **12** no. 2, (1964) 132 – 133.

[16] P. W. Higgs, "Broken Symmetries and the Masses of Gauge Bosons", *Phys. Rev. Lett.* **13** (1964) 508–509.

[17] G. S. Guralnik, C. R. Hagen, and T. W. B. Kibble, "Global Conservation Laws and Massless Particles", *Phys. Rev. Lett.* **13** (1964) 585–587.

[18] P. W. Higgs, "Spontaneous Symmetry Breakdown without Massless Bosons", *Phys. Rev.* **145** (1966) 1156–1163.

[19] T. W. B. Kibble, "Symmetry Breaking in Non-Abelian Gauge Theories", *Phys. Rev.* **155** (1967) 1554–1561.

[20] **CDF Collaboration**, F. Abe *et al.*, "Evidence for top quark production in $\bar{p}p$ collisions at $\sqrt{s} = 1.8$ TeV", *Phys. Rev. Lett.* **73** (1994) 225–231, arXiv:hep-ex/9405005 [hep-ex].

[21] **D0 Collaboration**, S. Abachi *et al.*, "Observation of the top quark", *Phys. Rev. Lett.* **74** (1995) 2632–2637, arXiv:hep-ex/9503003 [hep-ex].

[22] **ALEPH, CDF, DØ, DELPHI, L3, OPAL and SLD Collaborations, LEP and Tevatron EWWG, SLD Electroweak and Heavy Flavour Groups**, "Precision Electroweak Measurements and Constraints on the Standard Model", arXiv:1012.2367 [hep-ex].

[23] **LEP Working Group for Higgs boson searches, ALEPH, DELPHI, L3 and OPAL Collaboration**, R. Barate *et al.*, "Search for the Standard Model Higgs boson at LEP", *Phys. Lett.* **B565** (2003) 61–75, arXiv:hep-ex/0306033 [hep-ex].

[24] **ATLAS Collaboration**, G. Aad *et al.*, "Search for the Standard Model Higgs boson in the $H \to WW^{(*)} \to \ell\nu\ell\nu$ decay mode with 4.7 fb^{-1} of ATLAS data at $\sqrt{s} = 7$ TeV", *Phys. Lett.* **B716** (2012) 62–81, arXiv:1206.0756 [hep-ex].

[25] **ATLAS Collaboration**, "Observation of an Excess of Events in the Search for the Standard Model Higgs Boson in the $H \to WW^{(*)} \to \ell\nu\ell\nu$ Channel with the ATLAS Detector." ATLAS Note: ATLAS-CONF-2012-098.

[26] F. Halzen and A. D. Martin, *Quarks and Leptons: An Introductory Course in Modern Particle Physics*. Wiley, 1984. ISBN: 0-471-88741-2.

[27] I. C. Brock and T. Schroeder-Sadenius, eds., *Physics at the Terascale*. Wiley, 2010. ISBN: 978-3-527-41001-9.

[28] A. Pich, "The Standard model of electroweak interactions", arXiv:0705.4264 [hep-ph].

[29] **Particle Data Group**, Beringer, J. and others, "The Review of Particle Physics", *Phys. Rev.* **D86** (2012) 010001. http://pdg.lbl.gov/.

[30] H. D. Politzer, "Reliable perturbative results for strong interactions?", *Phys. Rev. Lett.* **30** (1973) 1346–1349.

[31] D. J. Gross and F. Wilczek, "Ultraviolet behavior of non-abelian gauge theories", *Phys. Rev. Lett.* **30** (1973) 1343–1346.

[32] M. Kobayashi and T. Maskawa, "CP-Violation in the Renormalizable Theory of Weak Interaction", *Progress of Theoretical Physics* **49** no. 2, (1973) 652–657.

[33] G. Hooft, "Renormalizable Lagrangians for massive Yang-Mills fields", *Nucl. Phys. B* **35** no. 1, (1971) 167 – 188.

[34] A. Djouadi, "The Anatomy of electro-weak symmetry breaking. I: The Higgs boson in the standard model", *Phys. Rept.* **457** (2008) 1–216, arXiv:hep-ph/0503172 [hep-ph].

[35] T. Hambye and K. Riesselmann, "Matching conditions and Higgs mass upper bounds revisited", *Phys. Rev.* **D55** (1997) 7255–7262, arXiv:hep-ph/9610272 [hep-ph].

[36] The LEP Electroweak Working Group, "LEP/TEV EW WG Plots for Summer 2010." http://lepewwg.web.cern.ch/LEPEWWG/plots/summer2010.

[37] J. M. Campbell, J. Huston, and W. Stirling, "Hard Interactions of Quarks and Gluons: A Primer for LHC Physics", *Rept. Prog. Phys.* **70** (2007) 89, arXiv:hep-ph/0611148 [hep-ph].

[38] J. C. Collins, D. E. Soper, and G. F. Sterman, "Factorization of Hard Processes in QCD", *Adv. Ser. Direct. High Energy Phys.* **5** (1988) 1–91, arXiv:hep-ph/0409313 [hep-ph].

[39] A. Martin, W. Stirling, R. Thorne, and G. Watt, "Parton distributions for the LHC", *Eur. Phys. J.* **C63** (2009) 189–285, arXiv:0901.0002 [hep-ph].

[40] M. Dobbs, S. Frixione, E. Laenen, K. Tollefson, H. Baer, *et al.*, "Les Houches guidebook to Monte Carlo generators for hadron collider physics", arXiv:hep-ph/0403045 [hep-ph].

[41] A. Buckley, J. Butterworth, S. Gieseke, D. Grellscheid, S. Hoche, *et al.*, "General-purpose event generators for LHC physics", *Phys. Rept.* **504** (2011) 145–233, arXiv:1101.2599 [hep-ph].

[42] T. Sjostrand, S. Mrenna, and P. Z. Skands, "PYTHIA 6.4 Physics and Manual", *JHEP* **0605** (2006) 026, arXiv:hep-ph/0603175 [hep-ph].

[43] T. Sjostrand, S. Mrenna, and P. Z. Skands, "A Brief Introduction to PYTHIA 8.1", *Comput. Phys. Commun.* **178** (2008) 852–867, arXiv:0710.3820 [hep-ph].

[44] S. Frixione and B. R. Webber, "Matching NLO QCD computations and parton shower simulations", *JHEP* **0206** (2002) 029, arXiv:hep-ph/0204244 [hep-ph].

[45] S. Agostinelli *et al.*, "GEANT4 – A Simulation Toolkit", *Nuclear Instruments and Methods in Physics Research Section A: Accelerators, Spectrometers, Detectors and Associated Equipment* **506** no. 3, (2003) 250 – 303.

[46] **ATLAS Collaboration**, G. Aad *et al.*, "The ATLAS Simulation Infrastructure", arXiv:1005.4568 [hep-ex].

[47] L. Evans and P. Bryant, "LHC Machine", *JINST* **3** no. 08, (2008) S08001. http://stacks.iop.org/1748-0221/3/i=08/a=S08001.

[48] **ATLAS Collaboration**, G. Aad *et al.*, "The ATLAS Experiment at the CERN Large Hadron Collider", *JINST* **3** (2008) S08003.

[49] **ATLAS Collaboration**, G. Aad *et al.*, "Expected Performance of the ATLAS Experiment - Detector, Trigger and Physics", arXiv:0901.0512 [hep-ex].

[50] **ATLAS Collaboration**, "ATLAS computing: Technical design report." Scientific Committee Paper: CERN-LHCC-2005-022.

[51] T. Cornelissen, M. Elsing, S. Fleischmann, W. Liebig, E. Moyse, and A. Salzburger, "Concepts, Design and Implementation of the ATLAS New Tracking (NEWT)", Tech. Rep. ATL-SOFT-PUB-2007-007. ATL-COM-SOFT-2007-002, CERN, Geneva. CDS:1020106.

[52] **ATLAS Collaboration**, "Performance of primary vertex reconstruction in proton-proton collisions at $\sqrt{s} = 7$ TeV in the ATLAS experiment." ATLAS Note: ATLAS-CONF-2010-069.

[53] **ATLAS Collaboration**, G. Aad *et al.*, "Electron performance measurements with the ATLAS detector using the 2010 LHC proton-proton collision data", *Eur. Phys. J.* **C72** (2012) 1909, arXiv:1110.3174 [hep-ex].

[54] W. Lampl, S. Laplace, D. Lelas, P. Loch, H. Ma, S. Menke, S. Rajagopalan, D. Rousseau, S. Snyder, and G. Unal, "Calorimeter clustering algorithms: Description and performance", Tech. Rep. ATL-LARG-PUB-2008-002. ATL-COM-LARG-2008-003, CERN, Geneva. CDS:1099735.

[55] **ATLAS Collaboration**, "Performance of the Electron and Photon Trigger in *pp* Collisions at $\sqrt{s} = 7$ TeV." ATLAS Note: ATLAS-CONF-2011-114.

[56] **ATLAS Collaboration**, "Muon reconstruction efficiency in reprocessed 2010 LHC proton-proton collision data recorded with the ATLAS detector." ATLAS Note: ATLAS-CONF-2011-063.

[57] **ATLAS Collaboration**, "Muon Momentum Resolution in First Pass Reconstruction of *pp* Collision Data Recorded by ATLAS in 2010." ATLAS Note: ATLAS-CONF-2011-046.

[58] S. Ellis, J. Huston, K. Hatakeyama, P. Loch, and M. Tonnesmann, "Jets in hadron-hadron collisions", *Prog. Part. Nucl. Phys.* **60** (2008) 484–551, arXiv:0712.2447 [hep-ph].

[59] G. P. Salam, "Towards Jetography", *Eur. Phys. J.* **C67** (2010) 637–686, arXiv:0906.1833 [hep-ph].

[60] M. Cacciari, G. P. Salam, and G. Soyez, "The anti-k_t jet clustering algorithm", *JHEP* **2008** no. 04, (2008) 063. http://stacks.iop.org/1126-6708/2008/i=04/a=063.

[61] **ATLAS Collaboration**, G. Aad *et al.*, "Jet energy measurement with the ATLAS detector in proton-proton collisions at *sqrts* = 7 TeV", arXiv:1112.6426 [hep-ex].

[62] **ATLAS Collaboration**, "Selection of jets produced in proton-proton collisions with the ATLAS detector using 2011 data." ATLAS Note: ATLAS-CONF-2012-020.

[63] D. W. Miller, A. Schwartzman, and D. Su, "Jet-vertex association algorithm." ATLAS Internal Note: ATL-COM-PHYS-2008-008.

[64] **ATLAS Collaboration**, "Jet energy resolution and selection efficiency relative to track jets from in-situ techniques with the ATLAS Detector Using Proton-Proton Collisions at a Center of Mass Energy $\sqrt{s} = 7$ TeV." ATLAS Note: ATLAS-CONF-2010-054.

[65] **ATLAS Collaboration**, "Commissioning of the ATLAS high-performance b-tagging algorithms in the 7 TeV collision data." ATLAS Note: ATLAS-CONF-2011-102.

[66] G. Piacquadio and C. Weiser, "A new inclusive secondary vertex algorithm for b-jet tagging in ATLAS", *Journal of Physics: Conference Series* **119** no. 3, (2008) 032032. http://stacks.iop.org/1742-6596/119/i=3/a=032032.

[67] **ATLAS Collaboration**, "Measurement of the b-tag Efficiency in a Sample of Jets Containing Muons with 5 fb^{-1} of Data from the ATLAS Detector." ATLAS Note: ATLAS-CONF-2012-043.

[68] **ATLAS Collaboration**, G. Aad *et al.*, "Performance of Missing Transverse Momentum Reconstruction in Proton-Proton Collisions at 7 TeV with ATLAS", *Eur. Phys. J.* **C72** (2012) 1844, arXiv:1108.5602 [hep-ex].

[69] "LHC Higgs Cross Section Working Group." https://twiki.cern.ch/twiki/bin/view/LHCPhysics/CrossSections.

[70] **ATLAS Collaboration**, "ATLAS Sensitivity Prospects for Higgs Boson Production at the LHC Running at 7 TeV." ATLAS Note: ATL-PHYS-PUB-2010-009.

[71] **ATLAS Collaboration**, "ATLAS Sensitivity Prospects for Higgs Boson Production at the LHC Running at 7, 8 or 9 TeV." ATLAS Note: ATL-PHYS-PUB-2010-015.

[72] **ATLAS Collaboration**, "Search for the Higgs boson in the $H \to WW^{(*)} \to \ell\nu jj$ decay channel using 4.7 fb^{-1} of pp collisions at $\sqrt{s} = 7$ TeV with the ATLAS detector." ATLAS Note: ATLAS-CONF-2012-018.

[73] A. J. Barr, B. Gripaios, and C. G. Lester, "Measuring the Higgs boson mass in dileptonic W-boson decays at hadron colliders", *JHEP* **0907** (2009) 072, arXiv:0902.4864 [hep-ph].

[74] ATLAS Public Results, "ATLAS Physics Summary Plots." https://twiki.cern.ch/twiki/bin/view/AtlasPublic/CombinedSummaryPlots.

[75] **ATLAS Collaboration**, G. Aad *et al.*, "Measurement of the WW cross section in $\sqrt{s} = 7$ TeV pp collisions with the ATLAS detector and limits on anomalous gauge couplings", *Phys. Lett.* **B712** (2012) 289–308, arXiv:1203.6232 [hep-ex].

[76] J. M. Campbell, R. K. Ellis, and C. Williams, "Gluon-Gluon Contributions to W^+W^- Production and Higgs Interference Effects", *JHEP* **1110** (2011) 005, arXiv:1107.5569 [hep-ph].

[77] **ATLAS Collaboration**, G. Aad *et al.*, "Measurement of the cross section for top-quark pair production in pp collisions at $\sqrt{s} = 7$ TeV with the ATLAS detector using final states with two high-p_{T} leptons", *JHEP* **1205** (2012) 059, arXiv:1202.4892 [hep-ex].

[78] **ATLAS Collaboration**, G. Aad *et al.*, "Measurement of the t-channel single top-quark production cross section in pp collisions at $\sqrt{s} = 7$ TeV with the ATLAS detector", arXiv:1205.3130 [hep-ex].

[79] **ATLAS Collaboration**, G. Aad *et al.*, "Evidence for the associated production of a W boson and a top quark in ATLAS at $\sqrt{s} = 7$ TeV", arXiv:1205.5764 [hep-ex].

[80] **ATLAS Collaboration**, "Search for s-Channel Single Top-Quark Production in pp Collisions $\sqrt{s} = 7$ TeV." ATLAS Note: ATLAS-CONF-2011-118.

[81] **ATLAS Collaboration**, G. Aad *et al.*, "Measurement of the inclusive $W^{\pm}$ and Z/γ^{*} cross sections in the electron and muon decay channels in pp collisions at $\sqrt{s} = 7$ TeV with the ATLAS detector", *Phys.Rev.* **D85** (2012) 072004, arXiv:1109.5141 [hep-ex].

[82] **ATLAS Collaboration**, G. Aad *et al.*, "Measurement of WZ production in proton-proton collisions at $\sqrt{s} = 7$ TeV with the ATLAS detector", arXiv:1208.1390 [hep-ex].

[83] **ATLAS Collaboration**, G. Aad *et al.*, "Measurement of the ZZ production cross section and limits on anomalous neutral triple gauge couplings in proton-proton collisions at $\sqrt{s} = 7$ TeV with the ATLAS detector", *Phys. Rev. Lett.* **108** (2012) 041804, arXiv:1110.5016 [hep-ex].

[84] **ATLAS Collaboration**, G. Aad *et al.*, "Measurement of $W\gamma$ and Z/γ^{*} production cross sections in pp collisions at $\sqrt{s} = 7$ TeV and limits on anomalous triple gauge couplings with the ATLAS detector", arXiv:1205.2531 [hep-ex].

[85] ATLAS Public Results, "Online Luminosity Plots." https://twiki.cern.ch/twiki/bin/view/AtlasPublic/LuminosityPublicResults.

[86] J. Adelman *et al.*, "ATLAS offline data quality monitoring", *Journal of Physics: Conference Series* **219** no. 4, (2010) 042018. http://stacks.iop.org/1742-6596/219/i=4/a=042018.

[87] S. Alioli, P. Nason, C. Oleari, and E. Re, "NLO Higgs boson production via gluon fusion matched with shower in POWHEG", *JHEP* **0904** (2009) 002, arXiv:0812.0578 [hep-ph].

[88] P. Nason and C. Oleari, "NLO Higgs boson production via vector-boson fusion matched with shower in POWHEG", *JHEP* **1002** (2010) 037, arXiv:0911.5299 [hep-ph].

[89] D. de Florian, G. Ferrera, M. Grazzini, and D. Tommasini, "Transverse-momentum resummation: Higgs boson production at the Tevatron and the LHC", *JHEP* **1111** (2011) 064, arXiv:1109.2109 [hep-ph].

[90] **LHC Higgs Cross Section Working Group**, S. Dittmaier *et al.*, "Handbook of LHC Higgs Cross Sections: 1. Inclusive Observables", arXiv:1101.0593 [hep-ph].

[91] A. Djouadi, M. Spira, and P. Zerwas, "Production of Higgs bosons in proton colliders: QCD corrections", *Phys. Lett. B* **264** no. 34, (1991) 440 – 446.

[92] S. Dawson, "Radiative corrections to Higgs boson production", *Nucl. Phys. B* **359** no. 23, (1991) 283 – 300.

[93] M. Spira, A. Djouadi, D. Graudenz, and P. Zerwas, "Higgs boson production at the LHC", *Nucl. Phys.* **B453** (1995) 17–82, arXiv:hep-ph/9504378 [hep-ph].

[94] R. V. Harlander and W. B. Kilgore, "Next-to-next-to-leading order Higgs production at hadron colliders", *Phys. Rev. Lett.* **88** (2002) 201801, arXiv:hep-ph/0201206 [hep-ph].

[95] C. Anastasiou and K. Melnikov, "Higgs boson production at hadron colliders in NNLO QCD", *Nucl. Phys.* **B646** (2002) 220–256, arXiv:hep-ph/0207004 [hep-ph].

[96] V. Ravindran, J. Smith, and W. L. van Neerven, "NNLO corrections to the total cross-section for Higgs boson production in hadron hadron collisions", *Nucl. Phys.* **B665** (2003) 325–366, arXiv:hep-ph/0302135 [hep-ph].

[97] S. Catani, D. de Florian, M. Grazzini, and P. Nason, "Soft gluon resummation for Higgs boson production at hadron colliders", *JHEP* **0307** (2003) 028, arXiv:hep-ph/0306211 [hep-ph].

[98] U. Aglietti, R. Bonciani, G. Degrassi, and A. Vicini, "Two loop light fermion contribution to Higgs production and decays", *Phys. Lett.* **B595** (2004) 432–441, arXiv:hep-ph/0404071 [hep-ph].

[99] S. Actis, G. Passarino, C. Sturm, and S. Uccirati, "NLO Electroweak Corrections to Higgs Boson Production at Hadron Colliders", *Phys. Lett.* **B670** (2008) 12–17, arXiv:0809.1301 [hep-ph].

[100] C. Anastasiou, R. Boughezal, and F. Petriello, "Mixed QCD-electroweak corrections to Higgs boson production in gluon fusion", *JHEP* **0904** (2009) 003, arXiv:0811.3458 [hep-ph].

[101] D. de Florian and M. Grazzini, "Higgs production through gluon fusion: Updated cross sections at the Tevatron and the LHC", *Phys. Lett.* **B674** (2009) 291–294, arXiv:0901.2427 [hep-ph].

[102] J. Baglio and A. Djouadi, "Higgs production at the LHC", *JHEP* **1103** (2011) 055, arXiv:1012.0530 [hep-ph].

[103] C. Anastasiou, S. Buehler, F. Herzog, and A. Lazopoulos, "Inclusive Higgs boson cross-section for the LHC at 8 TeV", *JHEP* **1204** (2012) 004, arXiv:1202.3638 [hep-ph].

[104] D. de Florian and M. Grazzini, "Higgs production at the LHC: updated cross sections at $\sqrt{s} = 8$ TeV", arXiv:1206.4133 [hep-ph].

[105] E. Bagnaschi, G. Degrassi, P. Slavich, and A. Vicini, "Higgs production via gluon fusion in the POWHEG approach in the SM and in the MSSM", *JHEP* **1202** (2012) 088, arXiv:1111.2854 [hep-ph].

[106] P. Bolzoni, F. Maltoni, S.-O. Moch, and M. Zaro, "Higgs production via vector-boson fusion at NNLO in QCD", *Phys. Rev. Lett.* **105** (2010) 011801, arXiv:1003.4451 [hep-ph].

[107] M. Ciccolini, A. Denner, and S. Dittmaier, "Strong and electroweak corrections to the production of Higgs + 2 jets via weak interactions at the LHC", *Phys. Rev. Lett.* **99** (2007) 161803, arXiv:0707.0381 [hep-ph].

[108] M. Ciccolini, A. Denner, and S. Dittmaier, "Electroweak and QCD corrections to Higgs production via vector-boson fusion at the LHC", *Phys. Rev.* **D77** (2008) 013002, arXiv:0710.4749 [hep-ph].

[109] K. Arnold *et al.*, "VBFNLO: A parton level Monte Carlo for processes with electroweak bosons", *Comput. Phys. Commun.* **180** no. 9, (2009) 1661 – 1670.

[110] T. Han and S. Willenbrock, "QCD correction to the $pp \to WH$ and ZH total cross sections", *Phys. Lett. B* **273** no. 12, (1991) 167 – 172.

[111] O. Brein, A. Djouadi, and R. Harlander, "NNLO QCD corrections to the Higgs-strahlung processes at hadron colliders", *Phys. Lett.* **B579** (2004) 149–156, arXiv:hep-ph/0307206 [hep-ph].

[112] M. Ciccolini, S. Dittmaier, and M. Kramer, "Electroweak radiative corrections to associated WH and ZH production at hadron colliders", *Phys. Rev.* **D68** (2003) 073003, arXiv:hep-ph/0306234 [hep-ph].

[113] A. Djouadi, J. Kalinowski, and M. Spira, "HDECAY: A Program for Higgs boson decays in the standard model and its supersymmetric extension", *Comput. Phys. Commun.* **108** (1998) 56–74, arXiv:hep-ph/9704448 [hep-ph].

[114] M. L. Mangano, M. Moretti, F. Piccinini, R. Pittau, and A. D. Polosa, "ALPGEN, a generator for hard multiparton processes in hadronic collisions", *JHEP* **0307** (2003) 001, arXiv:hep-ph/0206293 [hep-ph].

[115] G. Corcella, I. Knowles, G. Marchesini, S. Moretti, K. Odagiri, *et al.*, "HERWIG 6: An Event generator for hadron emission reactions with interfering gluons (including supersymmetric processes)", *JHEP* **0101** (2001) 010, arXiv:hep-ph/0011363 [hep-ph].

[116] J. Butterworth, J. R. Forshaw, and M. Seymour, "Multiparton interactions in photoproduction at HERA", *Z. Phys.* **C72** (1996) 637–646, arXiv:hep-ph/9601371 [hep-ph].

[117] J. Alwall, S. Hoche, F. Krauss, N. Lavesson, L. Lonnblad, *et al.*, "Comparative study of various algorithms for the merging of parton showers and matrix elements in hadronic collisions", *Eur. Phys. J.* **C53** (2008) 473–500, arXiv:0706.2569 [hep-ph].

[118] T. Binoth, M. Ciccolini, N. Kauer, and M. Kramer, "Gluon-induced W-boson pair production at the LHC", *JHEP* **0612** (2006) 046, arXiv:hep-ph/0611170 [hep-ph].

[119] B. P. Kersevan and E. Richter-Was, "The Monte Carlo event generator AcerMC version 2.0 with interfaces to PYTHIA 6.2 and HERWIG 6.5", arXiv:hep-ph/0405247 [hep-ph].

[120] J. Alwall, P. Demin, S. de Visscher, R. Frederix, M. Herquet, *et al.*, "MADGRAPH/MADEVENT v4: The New Web Generation", *JHEP* **0709** (2007) 028, arXiv:0706.2334 [hep-ph].

[121] J. Alwall, M. Herquet, F. Maltoni, O. Mattelaer, and T. Stelzer, "MADGRAPH 5 : Going Beyond", *JHEP* **1106** (2011) 128, arXiv:1106.0522 [hep-ph].

[122] P. M. Nadolsky, H.-L. Lai, Q.-H. Cao, J. Huston, J. Pumplin, *et al.*, "Implications of CTEQ global analysis for collider observables", *Phys. Rev.* **D78** (2008) 013004, arXiv:0802.0007 [hep-ph].

[123] A. Sherstnev and R. Thorne, "Parton Distributions for LO Generators", *Eur. Phys. J.* **C55** (2008) 553–575, arXiv:0711.2473 [hep-ph].

[124] H.-L. Lai, M. Guzzi, J. Huston, Z. Li, P. M. Nadolsky, *et al.*, "New parton distributions for collider physics", *Phys. Rev.* **D82** (2010) 074024, arXiv:1007.2241 [hep-ph].

[125] R. Gavin, Y. Li, F. Petriello, and S. Quackenbush, "FEWZ 2.0: A code for hadronic Z production at next-to-next-to-leading order", *Comput. Phys. Commun.* **182** (2011) 2388–2403, arXiv:1011.3540 [hep-ph].

[126] S. Catani, L. Cieri, G. Ferrera, D. de Florian, and M. Grazzini, "Vector boson production at hadron colliders: A Fully exclusive QCD calculation at NNLO", *Phys. Rev. Lett.* **103** (2009) 082001, arXiv:0903.2120 [hep-ph].

[127] M. Aliev, H. Lacker, U. Langenfeld, S. Moch, P. Uwer, *et al.*, "HATHOR: HAdronic Top and Heavy quarks crOss section calculatoR", *Comput. Phys. Commun.* **182** (2011) 1034–1046, arXiv:1007.1327 [hep-ph].

[128] N. Kidonakis, "Next-to-next-to-leading-order collinear and soft gluon corrections for t-channel single top quark production", *Phys. Rev.* **D83** (2011) 091503, arXiv:1103.2792 [hep-ph].

[129] N. Kidonakis, "NNLL resummation for s-channel single top quark production", *Phys. Rev.* **D81** (2010) 054028, arXiv:1001.5034 [hep-ph].

[130] N. Kidonakis, "Two-loop soft anomalous dimensions for single top quark associated production with a W or H", *Phys. Rev.* **D82** (2010) 054018, arXiv:1005.4451 [hep-ph].

[131] J. M. Campbell and R. Ellis, "MCFM for the Tevatron and the LHC", *Nucl. Phys. Proc. Suppl.* **205-206** (2010) 10–15, arXiv:1007.3492 [hep-ph].

[132] **ATLAS Collaboration**, G. Aad *et al.*, "Combined search for the Standard Model Higgs boson in pp collisions at $\sqrt{s} = 7$ TeV with the ATLAS detector", arXiv:1207.0319 [hep-ex].

[133] Rene Brun et. al., "ROOT - An Object Oriented Data Analysis Framework." http://root.cern.ch/.

[134] **ATLAS Collaboration**, "Higgs Boson Searches using the $H \to WW^{(*)} \to \ell\nu\ell\nu$ Decay Mode with the ATLAS Detector at 7 TeV." ATLAS Note: ATLAS-CONF-2011-005.

[135] **ATLAS Collaboration**, "Performance of the ATLAS muon trigger in 2011." ATLAS Note: ATLAS-CONF-2012-099.

[136] **ATLAS Collaboration**, "Improved electron reconstruction in ATLAS using the Gaussian Sum Filter-based model for bremsstrahlung." ATLAS Note: ATLAS-CONF-2012-047.

[137] R. Aben *et al.*, "Selection for the search for the Higgs boson in the $H \to WW^{(*)} \to \ell\nu\ell\nu$ decay mode using 4.7 fb^{-1} of data collected with the ATLAS detector at $\sqrt{s} = 7$ TeV." ATLAS Internal Note: ATL-COM-PHYS-2011-1714.

[138] R. Aben *et al.*, "Object selection for the $H \to WW^{(*)}$ search with the ATLAS detector at $\sqrt{s} = 8$ TeV." ATLAS Internal Note: ATL-COM-PHYS-2012-861.

[139] **ATLAS Collaboration**, "Measurement of the Mistag Rate of b-tagging algorithms with 5 fb^{-1} of Data Collected by the ATLAS Detector." ATLAS Note: ATLAS-CONF-2012-040.

[140] **ATLAS Collaboration**, "Search for the Standard Model Higgs boson in the $H \to WW^{(*)} \to \ell\nu\ell\nu$ decay mode using Multivariate Techniques with 4.7 fb^{-1} of ATLAS data at $\sqrt{s} = 7$ TeV." ATLAS Note: ATLAS-CONF-2012-060.

[141] R. Ellis, I. Hinchliffe, M. Soldate, and J. V. D. Bij, "Higgs decay to $\tau^+\tau^-$: A possible signature of intermediate mass Higgs bosons at high energy hadron colliders", *Nucl. Phys. B* **297** no. 2, (1988) 221 – 243.

[142] R. Aben *et al.*, "Background estimates in the $H \to WW^{(*)} \to \ell\nu\ell\nu$ analysis with 4.2 fb^{-1} of data collected with the ATLAS detector at $\sqrt{s} = 8$ TeV." ATLAS Internal Note: ATL-COM-PHYS-2012-850.

[143] B. Mellado, X. Ruan, and Z. Zhang, "Extraction of Top Backgrounds in the Higgs Boson Search with the $H \to WW^{(*)} \to \ell\nu\ell\nu + E_{\mathrm{T}}^{\mathrm{miss}}$ Decay with a Full-Jet Veto at the LHC", *Phys. Rev.* **D84** (2011) 096005, `arXiv:1101.1383 [hep-ph]`.

[144] **LHC Higgs Cross Section Working Group**, S. Dittmaier *et al.*, "Handbook of LHC Higgs Cross Sections: 2. Differential Distributions", `arXiv:1201.3084 [hep-ph]`.

[145] M. H. Seymour, "The Higgs boson line shape and perturbative unitarity", *Phys. Lett.* **B354** (1995) 409–414, `arXiv:hep-ph/9505211 [hep-ph]`.

[146] G. Passarino, C. Sturm, and S. Uccirati, "Higgs Pseudo-Observables, Second Riemann Sheet and All That", *Nucl. Phys.* **B834** (2010) 77–115, `arXiv:1001.3360 [hep-ph]`.

[147] C. Anastasiou, S. Buehler, F. Herzog, and A. Lazopoulos, "Total cross-section for Higgs boson hadroproduction with anomalous Standard Model interactions", *JHEP* **1112** (2011) 058, `arXiv:1107.0683 [hep-ph]`.

[148] M. Botje, J. Butterworth, A. Cooper-Sarkar, A. de Roeck, J. Feltesse, *et al.*, "The `PDF4LHC` Working Group Interim Recommendations", `arXiv:1101.0538 [hep-ph]`.

[149] R. D. Ball, V. Bertone, F. Cerutti, L. Del Debbio, S. Forte, *et al.*, "Impact of Heavy Quark Masses on Parton Distributions and LHC Phenomenology", *Nucl. Phys.* **B849** (2011) 296–363, `arXiv:1101.1300 [hep-ph]`.

[150] R. Aben *et al.*, "Monte Carlo generators and theoretical aspects for the search of the Higgs boson in the $H \to WW^{(*)} \to \ell\nu\ell\nu$ decay mode using 4.7 fb^{-1} of data collected with the ATLAS detector at $\sqrt{s} = 7$ TeV." ATLAS Internal Note: ATL-COM-PHYS-2011-1726.

[151] **ATLAS Collaboration**, "Luminosity Determination in pp Collisions at $\sqrt{s} = 7$ TeV using the ATLAS Detector in 2011." ATLAS Note: ATLAS-CONF-2011-116.

[152] **ATLAS Collaboration**, G. Aad *et al.*, "Luminosity Determination in pp Collisions a $\sqrt{s} = 7$ TeV Using the ATLAS Detector at the LHC", *Eur. Phys. J.* **C71** (2011) 1630, `arXiv:1101.2185 [hep-ex]`.

[153] G. Cowan, K. Cranmer, E. Gross, and O. Vitells, "Asymptotic formulae for likelihood-based tests of new physics", `arXiv:1007.1727v2 [abs]`.

[154] A. L. Read, "Presentation of search results: the CL_s technique", *Journal of Physics G: Nuclear and Particle Physics* **28** no. 10, (2002) 2693. `http://stacks.iop.org/0954-3899/28/i=10/a=313`.

[155] **ATLAS Collaboration**, "Observation of an excess of events in the search for the Standard Model Higgs boson in the $\gamma\gamma$ channel with the ATLAS detector." ATLAS Note: ATLAS-CONF-2012-091.

[156] **ATLAS Collaboration**, "Observation of an excess of events in the search for the Standard Model Higgs boson in the $H \to ZZ^{(*)} \to 4\ell$ channel with the ATLAS detector." ATLAS Note: ATLAS-CONF-2012-092.

[157] M. Duehrssen, "Prospects for the measurement of Higgs boson coupling parameters in the mass range from $110 - 190$ GeV." ATLAS Note: ATL-PHYS-2003-030.

[158] M. Duehrssen, S. Heinemeyer, H. Logan, D. Rainwater, G. Weiglein, *et al.*, "Extracting Higgs boson couplings from CERN LHC data", *Phys. Rev.* **D70** (2004) 113009, `arXiv:hep-ph/0406323 [hep-ph]`.

[159] C. Ruwiedel, M. Schumacher, and N. Wermes, "Prospects for the Measurement of the Structure of the Coupling of a Higgs Boson to Weak Gauge Bosons in Weak Boson Fusion with the ATLAS Detector." ATLAS Note: SN-ATLAS-2007-060.

[160] A. Djouadi, "Precision Higgs coupling measurements at the LHC through ratios of production cross sections", `arXiv:1208.3436 [hep-ph]`.

[161] D. L. Rainwater and D. Zeppenfeld, "Observing $H \to W^*W^* \to e^{\pm}\mu^{\mp}\not{p}_{\mathrm{T}}$ in weak boson fusion with dual forward jet tagging at the CERN LHC", *Phys. Rev.* **D60** (1999) 113004, `arXiv:hep-ph/9906218 [hep-ph]`.

[162] C. M. Buttar, R. Harper, and K. Jakobs, "Weak boson fusion $H \to WW^{(*)} \to \ell^+\ell^- p_{\mathrm{T}}^{\mathrm{miss}}$ as a search mode for an intermediate mass SM Higgs boson at ATLAS." ATLAS Note: ATL-PHYS-2002-033.

[163] K. Cranmer, Y. Fang, B. Mellado, S. Paganis, W. Quayle, and W. S. Lan, "Analysis of VBF $H \to WW^{(*)} \to \ell\nu\ell\nu$." ATLAS Note: ATL-PHYS-2004-019.

[164] K. Cranmer, P. McNamara, B. Mellado, Y. Pan, W. Quayle, and W. S. Lan, "Neural Network Based Search for Higgs Boson Produced via VBF with $H \to W^+W^- \to \ell^+\ell^-\not{p}_{\mathrm{T}}$ for 115 GeV $\leq m_H \leq$ 130 GeV." ATLAS Note: ATL-PHYS-2003-007.

[165] K. Cranmer, P. McNamara, B. Mellado, W. Quayle, and W. S. Lan, "Search for Higgs Bosons Decay $H \to W^+W^- \to \ell^+\ell^-\not{p}_{\mathrm{T}}$ for 115 GeV $\leq m_H \leq$ 130 GeV Using Vector Boson Fusion." ATLAS Note: ATL-PHYS-2003-002.

[166] S. Asai, G. Azuelos, C. Buttar, V. Cavasinni, D. Costanzo, *et al.*, "Prospects for the search for a Standard Model Higgs boson in ATLAS using vector boson fusion", *Eur. Phys. J.* **C32S2** (2004) 19–54, `arXiv:hep-ph/0402254 [hep-ph]`.

[167] **ATLAS Collaboration**, "Prospects for Higgs Boson Searches using the $H \to WW^{(*)} \to \ell\nu\ell\nu$ Decay Mode with the ATLAS Detector for 10 TeV." ATLAS Note: ATL-PHYS-PUB-2010-005.

[168] R. Aben *et al.*, "Background estimates in the $H \to WW^{(*)} \to \ell\nu\ell\nu$ analysis with 4.7 fb^{-1} of data collected with the ATLAS detector at $\sqrt{s} = 7$ TeV." ATLAS Internal Note: ATL-COM-PHYS-2012-288.

[169] R. Aben *et al.*, "Theoretical inputs to the $H \to WW^{(*)}$ search with the ATLAS detector at $\sqrt{s} = 8$ TeV", tech. rep.

[170] R. Aben *et al.*, "Nominal $H \to WW^{(*)} \to \ell\nu\ell\nu$ analysis with 5.8 fb^{-1} of data collected with the ATLAS detector at $\sqrt{s} = 8$ TeV in 2012." ATLAS Internal Note: ATL-COM-PHYS-2012-875.

[171] T. Plehn, D. L. Rainwater, and D. Zeppenfeld, "A Method for identifying $H \to \tau^+\tau^- \to e^{\pm}\mu^{\mp}\not{p}_{\mathrm{T}}$ at the CERN LHC", *Phys. Rev.* **D61** (2000) 093005, `arXiv:hep-ph/9911385 [hep-ph]`.

[172] D. L. Rainwater and D. Zeppenfeld, "Searching for $H \to \gamma\gamma$ in weak boson fusion at the LHC", *JHEP* **9712** (1997) 005, `arXiv:hep-ph/9712271 [hep-ph]`.

[173] K. Cranmer, Y. Fang, B. Mellado, S. Paganis, W. Quayle, *et al.*, "Prospects for Higgs searches via VBF at the LHC with the ATLAS detector", `arXiv:hep-ph/0401148 [hep-ph]`.

[174] T. Vu Anh. *Private Communication*.

List of Acronyms

BR	Branching Ratio
CAF	Common Analysis Framework
CDF	Collider Detector at Fermilab
CERN	European Organization for Nuclear Research
CJV	Central Jet Veto
CL	Confidence Level
CMS	Compact Muon Solenoid
CR	Control Region
CSC	Cathode Strip Chambers
DGLAP	Dokshitzer-Gribov-Lipatov-Altarelli-Parisi
EF	Event Filter
EM	Electromagnetic
FCal	Forward calorimeter
ggF	Gluon Fusion
GSF	Gaussian Sum Filter
GWS	Glashow-Weinberg-Salam (model)
HEC	Hadronic End-cap Calorimeter
HI	Heavy Ion
ICHEP	International Conference on High Energy Physics
ID	Inner Detector
	or Identification
JER	Jet Energy Resolution
JES	Jet Energy Scale
JVF	Jet Vertex Fraction
JVSP	Jet Veto Survival Probability
LAr	Liquid Argon
LEP	Large Electron-Positron collider
LHC	Large Hadron Collider
LO	Leading Order
MC	Monte Carlo
MDT	Monitored Drift Tubes
MS	Muon System (*or* Muon Spectrometer)
MVA	Multivariate Algorithm
NF	Normalization Factor

NLO	Next-to-Leading Order
NNLL	Next-to-Next-to-Leading Logarithm
NNLO	Next-to-Next-to-Leading Order
OF	Opposite Flavor
PDF	Parton Distribution Function
pp	Proton-Proton
QCD	Quantum Chromodynamics
QED	Quantum Electrodynamics
RoI	Region-of-Interest
RPC	Resistive Plate Chambers
SCT	Semiconductor Tracker
SF	Scale Factor
	or Same flavor
SM	Standard Model (of particle physics)
SR	Signal Region
TGC	Thin Gap Chambers
TRT	Transition Radiation Tracker
VBF	Vector-Boson Fusion
VR	Validation Region

List of Symbols

$\mathscr{L}$	Lagrange density (see e.g. Equation 1.1)
L	Instantaneous luminosity
$\mathcal{L}$	Integrated luminosity
	or Likelihood function
$\sqrt{s}$	Center-of-mass energy
p_{T}	Transverse momentum
θ	Polar angle
η	Pseudo-rapidity (see Equation (2.1))
$m_{\ell\ell}$	Invariant mass of the two charged leptons
$\Delta\phi_{\ell\ell}$	Azimuthal separation angle between the two charged leptons
$p_{\mathrm{T}}^{\ell\ell}$	Transverse momentum of the two charged leptons (see Equation (7.3))
$p_{\mathrm{T}}^{\mathrm{tot}}$	Total transverse momentum (see Equation (7.4))
$E_{\mathrm{T}}^{\mathrm{miss}}$	Missing transverse energy
$E_{\mathrm{T},x}^{\mathrm{miss}}$	Missing transverse energy along the x-axis of the detector
$E_{\mathrm{T,rel}}^{\mathrm{miss}}$	Projected missing transverse energy (see Equation (7.2))
m_{T}	Transverse mass (see Equation (4.1))
m_{jj}	Invariant mass of the two tagging jets
$\Delta\eta_{\mathrm{jj}}$, Δy_{jj}	Separation of the two tagging jets in pseudo-rapidity, rapidity (see Equation (8.1))
N_{jets}	Number of reconstructed jets
$N_{\mathrm{jets}}^{b-\mathrm{tagged}}$	Number of reconstructed jets that are b-tagged
N_{vxp}	Number of reconstructed primary interaction vertices
$\langle\mu\rangle$	Mean number of interactions per bunch crossing
p_0	Probability of a fluctuation of the background at least as incompatible as the observation

List of Figures

List of Tables

Acknowledgment

This is the place to express my gratefulness to everyone who has a share in allowing me to begin, carry out and finish this thesis successfully. First and foremost I would like to thank Prof. Karl Jakobs for giving me the opportunity to work in his group on a topic which I could not imagine to be more interesting and exciting. Thanks to his support I was enabled to work in an environment of excellent scientists and interesting and enjoyable people at the same time. A also very much appreciate that he took the time to proofread the draft of my thesis despite his enormous workload.

Certainly, it was an extraordinary coincidence that I joined the effort searching for the Higgs boson at exactly that period of time when an almost 50 years lasting endeavor was concluding. Having been at CERN several times in the course of this thesis, I extremely enjoyed the unique atmosphere one can find there working in cooperation with people from all over the world. Still, any expression of my profound gratitude for getting the chance to be at CERN on July 4^{th}, 2012, when a new chapter of physics' history has been written, is understating. It was an unforgettable event only very few people get the chance to experience in their lifetime.

Ralf Bernhard deserves an enormous gratitude for his support during my time working on the $H \to WW^{(*)} \to \ell\nu\ell\nu$ analysis. He did a great job introducing me to and guiding me through the subject and thereby became a friend to spend my time with also beyond scientific work. Experiencing very exciting times and going through more than one sleepless night ("the sun never sets in Germany"), writing thousands of lines of code, generating an incredible number of plots and never-ending cutflow tables, it was a great pleasure to work with Evelyn Schmidt, who was an irreplaceable and pleasant workmate. I am also deeply grateful for all the support Tuan Vu Anh has provided, regardless of whether he was at CERN or in Freiburg. He has always been available for any kind of question, and in particular has spent quite some time setting up the complex machinery for a statistical analysis I took advantage of.

A very big thank I owe the whole Common Analysis Team, in particular Magda Chelstowska, Elina Berglund, Jonathan Long, Johanna Bronner, and Evelyn Schmidt, for working extremely hard, tending thousands of jobs on the grid to provide the much-in-demand common ntuples for everyone's use. Most of the things I presented would have been virtually impossible without their diligent work. I also ought to highlight Jonathan's prompt assistance in producing the input necessary to prove the benefit of my optimization proposal.

Furthermore, I would like to thank Jianming Qian, who as the convener guided the Higgs-to-WW sub-group during rousing times towards an important contribution to a momentous discovery and yet always offered young members of the group the chance to take responsibility for crucial aspects of the analysis. In doing so, it was his utmost concern to spotlight the contributions of every individual analyzer and thereby provided the opportunity to be given credit for hard and sometimes exhausting work. Jianming, thank you very much for all your confidence.

There are many others who deserve to be mentioned here: many thanks to Jochen Hartert for being a pleasant and competent office mate, and in particular for providing his nice-

looking LaTeX-template for this thesis. I also would like to thank Paul Günther for many fruitful discussions we had about many aspects of the analysis. I have to apologize to my office mate Philip Sommer for neglecting my promise to cite his diploma thesis (the analysis would not have been the same without your electron scale factors). I would not have survived a single day without the generous donation of numerous bars of Nespresso coffee capsules I received from Matti Werner. I also very much would like to thank Christian Weiser and Ulrich Parzefall for their positive and entertaining nature which I extremely enjoyed at many opportunities. Many thanks also to Kristin Lohwasser for her support. Not to forget Christina Skorek who deserves a big "Thank You" for professionally and patiently assisting with any kind of administrative issue.

Last but not least I would like to thank, and somehow apologize to my beloved girlfriend Anne, who has had hard times watching me sitting in front of my computer rather than giving my best attention to her. Too often she heard me saying things like "I only need ten more minutes to finish this", but then had to wait three more hours until I shut down the laptop. There are no words to express my thank for her to be by my side!

Erklärung der Selbstständigkeit

Hiermit versichere ich, dass ich die vorliegende Diplomarbeit selbstständig verfasst und keine anderen als die angegebenen Quellen und Hilfsmittel verwendet habe.

Freiburg, den

Ort, Datum

Andreas Walz